Breedband multiniveau snelle multipoolmethodes

Broadband Multilevel Fast Multipole Methods

Ignace Bogaert

Promotor: prof. dr. ir. F. Olyslager
Proefschrift ingediend tot het behalen van de graad van
Doctor in de Ingenieurswetenschappen: Toegepaste Natuurkunde

Vakgroep Informatietechnologie
Voorzitter: prof. dr. ir. P. Lagasse
Faculteit Ingenieurswetenschappen
Academiejaar 2007 - 2008

UNIVERSITEIT
GENT

ISBN 978-90-8578-206-3
NUR 928, 959
Wettelijk depot: D/2008/10.500/25

Dankwoord

Ah, ik herinner hem mij nog goed, de tijd die ik doorbracht in de terminalzaal, ook bekend onder de naam 'het thesiskot'. Ja, dat lokaal op de eerste verdieping van het Technicum waar het ofwel ijskoud (wanneer de airco werkte) ofwel tropisch warm (wanneer de airco niet werkte) was. De plek waar niet alleen naarstig gewerkt werd, maar ook vollen bak gezeverd. De plek waar Dries en Davy ons steeds te hulp snelden als we weer eens te maken kregen met een onvindbare programmeerfout. Het was ook gedurende deze thesistijd dat Femke de toch wel prangende vraag stelde: "Ben jij geïnteresseerd in het doen van een doctoraat?" Mijn antwoord laat zich raden, want zoals je misschien wel weet lees je momenteel het dankwoord van voorgenoemd doctoraat.

Jaja, een dankwoord. Hoe is het toch zover kunnen komen? Awel, in de eerste plaats is dit te danken aan mijn promotor, Femke, aan wie ik dan ook een dikke merci richt. Dankzij haar had ik de vrijheid om het onderzoek te doen dat mij het meest interesseerde, maar week ik ook niet te ver af van het pad naar het doctoraat. Ook bedank ik haar voor de vele lezingen en herlezingen van mijn schrijfsels, en voor de algemene mijmeringen over fysica en wetenschap. Ook Daniël, die nog steeds tegelijkertijd decaan én wetenschapper is, wens ik te bedanken voor alle levendige discussies over eindige geleidbaarheden, draaiende bollen en wiggen. Er is duidelijk nog heel wat werk te doen in het elektromagnetisme! Luk Knockaert, jou bedank ik voor het verviervoudigen van het aantal voor mij gekende integraaltransformaties, en voor nog een hele rist andere fantastische technieken waar ik anders nooit van zou gehoord hebben. Hendrik en Ann, met jullie heb ik minder wetenschap bedreven, maar ik wil jullie samen met Femke, Daniël en Luk bedanken voor het aangename gezelschap in blok 3 van het Technicum, op conferenties en tijdens de onvergetelijke INTEC-avondfeesten! Nog binnen INTEC gaat mijn dank uit naar de voorzitter Paul Lagasse, en de mensen van het administratief en IT team. Merci voor al jullie inspanningen om onze administratie- en computerzorgen weg te nemen!

Ook de collega's, die de sfeer in onze gang zo goed maken, mogen hier niet ontbreken: Frederick Declercq, Pieterjan Demarcke, Thomas Demeester, Dirk De Schrijver, Wouter Dullaert, Francesco Ferranti, Carla Hertleer, Gunther Lippens, Maria Lucia Scarpello, Luigi Vallozzi, Sara Van den Bulcke en Ben Van de Wiele: merci! Speciale dank heb ik voor Davy Pissoort en Dries Vande Ginste, die kilos en kilos van mijn teksten kritisch onder handen namen. Ook een dikke merci aan Jan Fostier, Peter Lewyllie en Joris Peeters, die mij geregeld bijstonden bij gevallen van acute

computermiserie.

En dan zijn er natuurlijk mijn maten, waarvan er velen collega-doctoraatsstudent zijn. Kristof, michiganmakker, merci voor de vele grappige anekdotes, scherpe wiskundige inzichten en Tex-Mex bezoeken. Menig schaap bezweek aan onze pitahonger! Samen met Kristof wil ik ook nog een paar anderstalige michiganmakkers bedanken. When I was in Michigan, I learned of the difference between felonies and misdemeanors, of the thoughts of ancient Greek philosophers and many other interesting topics. Francesco, Hakan and Karl, whose motto seems to be "to boldly discuss what no one has discussed before": thanks for all the polemical lunch, dinner, coffee and other breaks! Terug naar België. Guillaume, meer bekend als Guido, bedankt voor die talloze avonden op café en in de poolzaal, alwaar de eeuwige interesses van mannen steeds uitgebreid aan bod kwamen. Jürgen, bedankt om mijn 'partner in gezever' te zijn. Zonder jou zou het allemaal een pak serieuzer, en dus minder tof, verlopen zijn. Roald, bedankt voor je relativerende en heldere kijk op de zaken des levens, en voor de vele toffe momenten op (ski)reizen en feestjes. Lieven, merci voor de vele discussies en je gezelschap op reis. Weet je nog, onze foto met Pumo Ri op de achtergrond... Wim, Filip en Jo, jullie wil ik bedanken voor het toffe gezelschap in den Bleau, maar nog veel meer voor de vele avonden op café, waar menig zieltje blootgelegd werd. Je hebt het ongetwijfeld gemerkt, de woorden 'tof gezelschap' en 'café' zijn meerdere malen gevallen. Dit doctoraat zal door mij dan ook niet als een verzameling formules onthouden worden, maar vooral als een tijd waarin er heel wat afgediscussieerd, afgezien, afgedronken, en afgelachen is. Merci maten!

Laatst maar niet minst, wil ik mijn ouders bedanken. Jullie zijn er in geslaagd om mij de kansen te geven die jullie zelf nooit hebben gehad. Kansen die mij hebben toegelaten om mijn interesses te ontwikkelen, verre reizen te maken, een job te doen die ik zeer graag doe en nog zoveel meer. Ook weet ik dat ik bij jullie altijd terecht kan, en daarom wil ik jullie nu eens plechtig zeggen: merci voor jullie nooit aflatende steun, voor alles.

Ignace Bogaert
Gent, 29 Mei, 2008

...that, in a few years, all great physical constants will have been approximately estimated, and that the only occupation which will be left to men of science will be to carry these measurements to another place of decimals.

JAMES C. MAXWELL (1831-1879)
SCOTTISH MATHEMATICIAN

Contents

Samenvatting

Sinds ze in 1861 voor het eerst werden neergeschreven, vormen Maxwells vergelijkingen een bijzonder succesvolle beschrijving van macroscopische elektromagnetische velden. Echter, ze kunnen slechts voor een klein aantal eenvoudige geometriëen analytisch opgelost worden. Voor een brede waaier van moderne elektromagnetische toepassingen, zoals het ontwerp van antennes, draadloze communicatiesystemen, optische systemen, hoogfrequente circuits, enzovoort, volstaan deze analytische oplossingen niet. Om deze reden zijn numerieke simulaties tegenwoordig zeer belangrijk, en wordt er veel onderzoek verricht naar efficiënte oplossingsmethodes voor Maxwells vergelijkingen. Een belangrijke klasse van oplossingsmethodes wordt bijvoorbeeld gevormd door de eindige elementen methodes. In dit werk zullen we ons echter concentreren op een andere zeer belangrijke klasse van methodes, namelijk de zogenaamde randintegraalvergelijkingstechnieken, die het voordeel hebben dat de stralingsvoorwaarde a priori kan voldaan worden, i.e. zonder het gebruik van absorberende randvoorwaarden. Een tweede voordeel is dat voor geometriëen die opgebouwd zijn uit een aantal homogene gebieden, enkel de randen van die gebieden moeten meegenomen worden in de simulatie.

Gewoonlijk worden zogenaamde snelle multipool methodes (Fast Multipole Methods - FMMs) gebruikt om randintegraalvergelijkingen efficiënt op te lossen. Deze methodes gebruiken een hiërarchische opdeling van de geometrie in groepen op meerdere niveaus, in combinatie met een decompositie van de Greense functie. De efficiëntie van een FMM hangt echter sterk af van het type decompositie dat gebruikt wordt. Over het algemeen zijn FMMs gebaseerd op een multipool decompositie het minst efficiënt, terwijl de meest efficiënte FMM (vooral bekend als Multilevel Fast Multipole Algorithm (MLFMA)) gebaseerd is op een propagerende vlakke golven decompositie. FMMs die gebruik maken van de spectrale decompositie van de Greense functie liggen er ergens tussenin. Het probleem is echter dat het MLFMA door een numerieke instabiliteit faalt indien de groepen kleiner worden dan een bepaalde kritische elektrische grootte. Indien de geometrie onderdelen bevat die significant kleiner zijn dan de golflengte, kan de simulatie ervan bijgevolg niet gebeuren door middel van enkel het MLFMA. Een mogelijke oplossing bestaat erin een hybride methode te construeren, die het MLFMA gebruikt wanneer de groepen groot genoeg zijn (HF interacties) en één van de minder efficiënte decompositie gebruikt wanneer dat niet het geval is (LF interacties). Het volledige algoritme is echter maar zo snel als het traagste onderdeel, waardoor deze hybride methodes suboptimaal zijn. Dit brengt ons tot de

inhoud van dit werk: het verbeteren en vinden van alternatieven voor de multipool- en spectrale decomposities.

Deze nieuwe methodes vormen vooral een verbetering voor LF en breedband simulaties. Dit zijn simulaties waarbij de kleinste onderdelen van de geometrie elektrisch klein zijn. Voor breedbandproblemen is de volledige geometrie bovendien elektrisch groot. Breedband simulaties zijn echter belangrijk, zoals bijvoorbeeld bij hoogfrequente printed circuit boards en microgolfcircuiten, metamaterialen of de verstrooiing van radargolven aan complexe vormen. Het feit dat de sneller wordende computers steeds grotere simulaties toelaten versterkt deze trend omdat zelfs zeer fijn gediscretiseerde structuren significant groter dan de golflengte kunnen zijn.

Dit werk is als volgt georganiseerd: in hoofdstuk 1 worden de vergelijkingen van Maxwell gegeven, samen met de constitutieve vergelijkingen en de stralingsvoorwaarde. Een aantal eigenschappen die hieruit volgen worden eveneens gegeven. Daarna worden de analytische oplossingen van Maxwells vergelijkingen in een oneindig homogeen isotroop medium in Cartesische en sferische coordinaten opgesteld, alsook de verbanden tussen deze twee soorten oplossingen. In hoofdstuk 2 worden de resultaten van het eerste hoofdstuk toegepast voor de oplossing van problemen waarin inhomogeniteiten voorkomen. Onder andere wordt de meervoudige verstrooiings vergelijking (multiple scattering equation) opgesteld, die gebruikt wordt in hoofdstuk 7. Tenslotte wordt ook de noodzakelijkheid van het gebruik van FMMs aangetoond.

De vijf daaropvolgende hoofdstukken corresponderen met artikels die uit het doctoraatsonderzoek zijn voortgevloeid. In hoofdstuk 3 wordt een verbetering voorgesteld die van toepassing is op FMMs gebaseerd op de spectrale voorstelling van de Greense functie. Deze techniek laat in het beste geval toe om de (des)aggregatie stap in het algoritme te versnellen met een factor 6. Verder wordt ook een nieuwe toepassing van de Beltrami decompositie van het elektromagnetische veld voorgesteld. Het blijkt namelijk mogelijk om, via deze decompositie, de twee stralingpatronen van een vectoriële FMM nog vóór (ná) de (des)aggregatie te ontkoppelen.

De resultaten van hoofdstuk 3 laten toe om FMMs gebaseerd op de spectrale voorstelling van de Greense functie te versnellen. In hoofdstuk 4 wordt voor een andere aanpak gekozen, die toegepast wordt op de tweedimensionale Greense functie. In plaats van te vertrekken van de numeriek stabiele spectrale decompositie en deze zo efficiënt mogelijk te maken, gaan we uit van het efficiënte maar onstabiele MLFMA en proberen we de instabiliteit weg te werken. Dit doel wordt bereikt door de diagonalisatie van de multipool decompositie uit te stellen tot een zogenaamde normalisatiefactor geïntroduceerd is. Het nieuwe additietheorema dat hieruit resulteert is stabiel voor alle frequenties en leidt dus tot een breedband FMM. Het wordt ook aangetoond dat deze nieuwe FMM efficiënter is dan de multipool decompositie. De stabiliteit van de methode is te verklaren door het feit dat ze, zij het op een verdoken manier, evanescente vlakke golven in rekening brengt.

In hoofdstuk 5 wordt in zekere zin de techniek die werd voorgesteld in hoofdstuk

4 uitgebreid naar drie dimensies, met als resultaat het NSPWMLFMA (Nondirective Stable Plane Wave Multilevel Fast Multipole Algorithm). Zoals in het tweedimensionaal geval gebruikt het NSPWMLFMA evanescente vlakke golven, terwijl het convergentiegebied nog steeds het complement van een bol is. Er zijn echter ook een aantal belangrijke verschillen tussen het tweedimensionaal en driedimensionaal algoritme. Zo is er slechts één stralingspatroon, in vergelijking met twee in hoofdstuk 4. Dit maakt het NSPWMLFMA erg efficiënt. Ook zijn de discretisatiepunten van het vlakke golven additietheorema niet langer analytisch gekend, maar wordt het QR-algoritme gebruikt voor de bepaling ervan. Dit heeft als nadelig gevolg dat de interpolaties met volle matrices moeten gebeuren. Dit limiteert de bruikbaarheid van het NSPWMLFMA tot LF interacties. Een breedband methode gebaseerd op het NSPWMLFMA kan echter nog steeds geconstrueerd worden door een naadloze koppeling met het MLFMA.

Een aantal nadelen van het NSPWMLFMA worden in hoofdstuk 6 verholpen door een volledig analytische decompositie van de Greense functie in te voeren, gebaseerd op zogenaamde pseudosferische harmonieken. De speciale eigenschappen van de pseudosferische harmonieken maken het mogelijk om deze decompositie numeriek stabiel te maken voor LF interacties. De discretisatiepunten kunnen uniform gespreid gekozen worden, hetgeen interpolaties met behulp van discrete Fourier transformaties mogelijk maakt. De prijs die betaald wordt voor deze voordelen is het relatief hoge aantal discretisatiepunten en een numerieke instabiliteit voor HF interacties. Dit laatste kan opnieuw ondervangen worden door een koppeling met het MLFMA.

Tenslotte worden in hoofdstuk 7 de FMMs uit hoofdstukken 3 en 5 gebruikt om de effectieve materiaalparameters van metamaterialen te bepalen. Dit wordt gedaan door de T-matrix van een sferisch stuk metamateriaal te berekenen met behulp van numerieke simulaties, waarna deze T-matrix vergeleken wordt met de analytische uitdrukking voor een homogene sfeer. Hierdoor bekomt men een stelsel van transcendente vergelijkingen voor de effectieve materiaalparameters. Dit niet-lineair stelsel kan omgezet worden naar een kwadratische vergelijking voor de materiaalparameters. Er wordt enerzijds aangetoond dat deze homogenisatieprocedure goed werkt maar dat ze anderzijds ook haar beperkingen heeft bij bepaalde frequenties en types van materialen.

Summary

Since 1861, when they were for the first time written down, Maxwell's equations have provided an extremely successful description of macroscopic electromagnetic fields. However, they can only be solved analytically for a few simple geometries. For a plethora of modern applications, like antenna design, wireless communication systems, optical systems, high-frequency circuits and so on, these analytical solutions are insufficient. Therefore, numerical simulations are very important, and a great deal of effort is put in the search for computationally efficient algorithms for solving Maxwell's equations. One important class of solution techniques for example, is formed by the finite element methods. However, the focus of this work will be on the so-called integral equation methods, which have the advantage that the radiation condition can be satisfied a priori, i.e. without introducing absorbing boundary conditions. Another advantage is that when the geometry consists of a number of homogeneous regions, only the boundaries of those regions need to be taken into account.

Usually, integral equations are efficiently solved using so-called Fast Multipole Methods (FMMs). These methods use a subdivision of the geometry into boxes on multiple levels, in combination with some kind of decomposition of the Green function. However, the efficiency of the FMM strongly depends on the type of decomposition used. Generally speaking, the least efficient method is based on a multipole decomposition, while the most efficient method (widely known as the Multilevel Fast Multipole Algorithm (MLFMA)) is based on a propagating plane wave decomposition. The spectral decomposition of the Green function lies somewhere in between. The problem with the MLFMA is that it suffers from a numerical breakdown when the boxes get smaller than a certain critical electrical size. Therefore, if the geometry contains features that are significantly smaller than the wavelength, the simulation cannot be efficiently done using the MLFMA alone. A possible solution is the construction of a hybrid method, which uses the MLFMA when the boxes are large enough (HF interactions) and use one of the less efficient methods when they are not (LF interactions). However, this algorithm is only as fast as the slowest algorithm, so these hybrids are suboptimal. This brings us to the focus of this work: improving and finding more efficient alternatives for the multipole and spectral decomposition methods.

These new methods mainly improve the efficiency of low-frequency and broadband simulations. These are simulations for which the smallest features of the geometry are electrically small. For broadband simulations, the entire geometry is also electrically large. Broadband simulations are important, for example in the simulation

of HF printed circuit boards and microwave circuits, metamaterials or the scattering of radar waves off complex shapes. The increasing capabilities of computers also adds to this trend because they allow huge, yet still densely discretized, structures.

This work is organized as follows: in chapter 1 Maxwell's equations are postulated, along with the constitutive equations and the radiation condition. A few general properties, of Maxwell's equations are given as well. Subsequently, the analytical solution of Maxwell's equations in an infinite homogeneous medium are derived in both Cartesian and spherical coordinates. Relations linking the solutions in the two coordinate systems are derived as well. chapter 2 outlines the methodology to solve problems with inhomogeneities, using the results obtained in the first chapter. In particular, the electric field integral equation and the multiple scattering equation are derived. Finally, the necessity of using FMMs is also explained.

The five ensuing chapters correspond to five articles that resulted from the performed research. In chapter 3, an improvement to the spectral decomposition based FMM is presented. This improvement allows a reduction by a factor of at most 6 of the computational cost of the (dis)aggregation step in this FMM. Furthermore, a new application of the well-known Beltrami decomposition of electromagnetic fields is presented. It allows the decoupling of the two radiation patterns of any vectorial FMM, even before(after) the (dis)aggregation stage has been entered.

The results from chapter 3 allow a significant acceleration of FMMs based on the spectral decomposition. In chapter 4, another approach is used on the two dimensional case. Instead of starting from the numerically stable spectral decomposition and trying to make it more efficient, we start from the efficient but unstable MLFMA and attempt to make it numerically stable. This goal is achieved by postponing the diagonalization of the multipole decomposition until a so-called normalization factor has been introduced. The novel addition theorem resulting form this approach is stable for all frequencies, hence it leads to a broadband FMM. It is also shown that this new FMM is more efficient than the multipole based FMM. This novel addition theorem can be interpreted as one using evanescent plane waves, which explains the stability of the decomposition.

In chapter 5, the two dimensional technique developed in chapter 4 is more or less generalized to three dimensions, resulting in the so-called NSPWMLFMA (Nondirective Stable Plane Wave Multilevel Fast Multipole Algorithm). Similar to the two dimensional case, the NSPWMLFMA uses evanescent plane waves, while still having the complement of a sphere as convergence region. However, there are several differences too. For starters, there is only one radiation pattern, compared to the two radiation patterns for the two dimensional case. This makes the NSPWMLFMA a very efficient FMM. Also, the discretization points of the plane wave decomposition are not known analytically anymore. Instead they are determined by means of the QR-algorithm. This has the unfortunate side effect that the interpolations must be performed using dense matrices. This in turn limits the applicability of the NSP-

WMLFMA to LF interactions. However, a broadband FMM can still be constructed by seamlessly coupling the NSPWMLFMA with the MLFMA.

A number of disadvantages of the NSPWMLFMA are resolved in chapter 6 by means of a fully analytical decomposition of the Green function which is based on the so-called pseudospherical harmonics. The special properties of the pseudospherical harmonics allow the numerical stabilization of this decomposition for LF interactions. The discretization points can be chosen in a uniformly spaced manner, which allows the interpolations to be performed using Fast Fourier Transforms (FFTs). The price we have to pay for this is a large number of discretization points and a numerical instability for HF interactions. The latter problem can again be solved by using a coupling with the MLFMA.

Finally, in chapter 7, the FMMs developed in chapters 3 and 5 are put to use for the determination of effective parameters of metamaterials. This is done by calculating the T-matrix of a spherical sample of the metamaterial by means of full-wave solutions. This T-matrix is then compared to the analytical expression for a homogeneous sphere. This results in a set of two transcendental equations for the effective parameters. This set of nonlinear equations can be reduced to a simple quadratic equation for the effective material parameters. This procedure is shown to work well, although the method does encounter some problems for certain frequencies and for certain types of materials.

List of Abbreviations

FMM	Fast Multipole Method
MLFMA	Multilevel Fast Multipole Algorithm
SPWM	Stable Plane Wave Method
NPWM	Normalized Plane Wave Method
PWM	Plane Wave Method
UMLFMA	Uniform Multilevel Fast Multipole Algorithm
NSPWMLFM	Nondirective Stable Plane Wave Multilevel Fast Multipole Algorithm
LF	low-frequency
HF	high-frequency
2-D	two dimensional
3-D	three dimensional
EFIE	Electric Field Integral Equation
PEC	Perfect Electrically Conducting
SVD	Singular Value Decomposition
MoM	Method of Moments
RWG	Rao-Wilton-Glisson
BICGSTAB	Biconjugate Gradients Stabilized Method
FFT	Fast Fourier Transform

List of Symbols

Vectors and matrices

Vectors are denoted by boldface letters, while matrices are denoted by letters in the sans serif font. Unit vectors are denoted by a hat. Usually the norm $||a||$ of a vector $\boldsymbol{a}$ is denoted by a.

$\boldsymbol{r}$	The position vector in three dimensions
$\hat{\boldsymbol{r}}$	The normalized position vector in three dimensions
r	The norm of the position vector in three dimensions
$\boldsymbol{\rho}$	The position vector in two dimensions
$\hat{\boldsymbol{\rho}}$	The normalized position vector in two dimensions
ρ	The norm of the position vector in two dimensions
M	A matrix

Operators

Linear operators containing derivatives are denoted by means of an inverted hat.

$\check{\boldsymbol{\nabla}}$	The nabla operator
$\check{\boldsymbol{\nabla}}\times$	The curl operator
$\check{\boldsymbol{\nabla}}\cdot$	The divergence operator
$\check{\boldsymbol{L}}$	The angular momentum operator
$*$	Denotes complex conjugation
$Y_{l,m}\left(\frac{\check{\boldsymbol{\nabla}}}{-jk}\right)$	The scalar spherical wave operator
$\boldsymbol{X}_{l,m}\left(\frac{\check{\boldsymbol{\nabla}}}{-jk}\right)$	The vector spherical wave operator of first type
$\boldsymbol{W}_{l,m}\left(\frac{\check{\boldsymbol{\nabla}}}{-jk}\right)$	The vector spherical wave operator of second type

Electromagnetism

ω	2π times the frequency
ε	Permittivity of a medium
μ	Permeability of a medium
k	Wavenumber of a medium
Z	Impedance of a medium

$\boldsymbol{E}(\boldsymbol{r},t), \boldsymbol{e}(\boldsymbol{r})$	Electric field in the time and frequency domain
$\boldsymbol{H}(\boldsymbol{r},t), \boldsymbol{h}(\boldsymbol{r})$	Magnetic field in the time and frequency domain
$\boldsymbol{D}(\boldsymbol{r},t), \boldsymbol{d}(\boldsymbol{r})$	Electric induction in the time and frequency domain
$\boldsymbol{B}(\boldsymbol{r},t), \boldsymbol{b}(\boldsymbol{r})$	Magnetic induction in the time and frequency domain
$\boldsymbol{J}(\boldsymbol{r},t), \boldsymbol{j}(\boldsymbol{r})$	Electric current in the time and frequency domain
$\boldsymbol{M}(\boldsymbol{r},t), \boldsymbol{m}(\boldsymbol{r})$	Magnetic current in the time and frequency domain
$\rho(\boldsymbol{r},t), \rho(\boldsymbol{r})$	Electric charge in the time and frequency domain
$\pi(\boldsymbol{r},t), \pi(\boldsymbol{r})$	Magnetic charge in the time and frequency domain
$G_0(\boldsymbol{r})$	Scalar Green function in the frequency domain
$\mathsf{G}_e(\boldsymbol{r})$	Electric Green dyadic in the frequency domain
$\mathsf{G}_m(\boldsymbol{r})$	Magnetic Green dyadic in the frequency domain

Special functions

$h_l^{(2)}(z)$	Spherical Hankel function of the second kind and lth order
$j_l(z)$	Spherical Bessel function of the second kind and lth order
$H_l^{(2)}(z)$	Cylindrical Hankel function of the second kind and lth order
$J_l(z)$	Cylindrical Bessel function of the second kind and lth order
$P_l(z)$	Legendre polynomial of degree l
$Y_{l,m}(\hat{\boldsymbol{r}})$	Spherical harmonic
$Z_{l,m}^f(\hat{\boldsymbol{r}})$	Scalar multipole
$\boldsymbol{X}_{l,m}(\hat{\boldsymbol{r}})$	Vector spherical harmonic of first type
$\boldsymbol{W}_{l,m}(\hat{\boldsymbol{r}})$	Vector spherical harmonic of second type
$\boldsymbol{M}_{l,m}^f(\hat{\boldsymbol{r}})$	Vector multipole of first type
$\boldsymbol{N}_{l,m}^f(\hat{\boldsymbol{r}})$	Vector multipole of second type
$\delta_{p,q}$	Kronecker delta: $\delta_{p,q} = 1$ if $p = q$, otherwise $\delta_{p,q} = 0$
$D_{m_1,m_2}^l(\mathsf{R})$	Element of the Wigner rotation matrix associated with R
$\Gamma(z)$	Gamma function
$\mathrm{sign}(x)$	Sign function

Miscellaneous

j	Denotes $\sqrt{-1}$
$\sum_{l,m}$	Sum over all $l \in [0,\infty]$ and $m \in [-l,l]$
$\mathcal{O}(x)$	Complexity measure: cost $= Cx$, with C a constant called the prefactor.
$\mathbb{1}$	The 3 by 3 identity matrix

List of Publications

Articles in international journals

- I. Bogaert, D. Pissoort, and F. Olyslager, "A normalized plane wave method for 2-D Helmholtz problems", *Microwave and Optical Technology Letters*, vol. 48, no. 2, pp. 237–243, February 2006.

- I. Bogaert, D. Pissoort, and F. Olyslager, "A faster aggregation for 3-D fast evanescent wave solvers using rotations", *Journal of Computational Physics*, vol. 227, no. 1, pp. 557–573, November 2007.

- J. De Zaeytijd, I. Bogaert, and A. Franchois, "An efficient hybrid MLFMA-FFT solver for the volume integral equation in case of sparse 3-D inhomogeneous dielectric scatterers", *In press for Journal of Computational Physics*.

- I. Bogaert, J. Peeters, and F. Olyslager, "A nondirective plane wave MLFMA stable at low frequencies", *Accepted for IEEE Transactions on Antennas and Propagation*.

- I. Bogaert, J. Peeters, and F. Olyslager, "Homogenization of metamaterials using full-wave simulations", *Provisionally accepted for Metamaterials (Invited paper)*.

- I. Bogaert and F. Olyslager, "A low frequency stable plane wave addition theorem", *Submitted to Journal of Computational Physics*.

Articles in conference proceedings

- I. Bogaert and F. Olyslager, "Full-wave analysis of a finite piece of metamaterial", in *Proceedings of the International Student Seminar on Microwave Applications of Novel Physical Phenomena*, Rovaniemi, Finland, 24-25 August 2006, pp. 47–49.

- I. Bogaert and F. Olyslager, "Exact modelling of a finite sample of metamaterial", in *Proceedings of the Applied Computational Electromagnetics Society*, Verona, Italy, 19-23 March 2007, pp. 273–278.

- I. Bogaert, L. Knockaert, and F. Olyslager, "Efficient calculation of moment integrals for tensor product basis functions", in *Proceedings of the IEEE Symposium on Antennas and Propagation*, Honolulu, USA, 10-15 June 2007, pp. 5636–5639.

- I. Bogaert, L. Meert, and F. Olyslager, "Fast full-wave validation of a metamaterial luneberg lens", in *Proceedings of the IEEE Symposium on Antennas and Propagation*, Honolulu, USA, 10-15 June 2007, pp. 3476–3479.

- I. Bogaert, F. Olyslager, Y. Ariën, and D. Pissoort, "Modeling and optimization of advanced multilayered absorbers", in *Proceedings of the European Microwave Conference*, Munich, Germany, 9-12 October 2007, pp. 214–217.

- I. Bogaert and F. Olyslager, "Exact full-wave simulation of finite pieces of metamaterials and extraction of effective material parameters", in *Proceedings of Metamaterials*, Rome, Italy, 22-26 October 2007, pp. 609–612.

- J. Peeters, I. Bogaert, J. Fostier, and F. Olyslager, "Accurate wideband evaluation of the shielding effectiveness of complex enclosures using an asynchronous parallel NSPWMLFMA", *Accepted for the 19th International Zurich Symposium on Electromagnetic Compatibility*, Singapore, 19-23 May 2008.

- F. Olyslager, K. Cools, I. Bogaert, J. Fostier, and J. Peeters, "Recent advances in fast multipole methods to simulate ever larger and more complex structures", *Accepted for the 19th International Zurich Symposium on Electromagnetic Compatibility*, Singapore, 19-23 May 2008.

- I. Bogaert, J. Peeters, J. Fostier, and F. Olyslager, "NSPWMLFMA: A low frequency stable formulation of the MLFMA in three dimensions", *Accepted for the IEEE Symposium on Antennas and Propagation*, San Diego, USA, 5-12 July 2008.

- J. Peeters, I. Bogaert, J. Fostier, and F. Olyslager, "Full-wave 3-D simulations using the broadband NSPWMLFMA", *Submitted to the URSI General Assembly*, Chicago, USA, 7-16 August 2008.

- Y. Ariën, I. Bogaert, F. Olyslager, and K. Cools, "Creating a design platform for the modeling and optimization of advanced multilayered absorbers", *Accepted for Journées de Charactérisation de Matériaux Micro-ondes*, Limoges, France, April 2008.

- I. Bogaert and F. Olyslager, "New plane wave addition theorems", *Accepted for the International Conference on Mathematical Modeling of Wave Phenomena*, Växjö, Sweden, June 2008.

Conference abstracts

- F. Olyslager, J. De Zaeytijd, K. Cools, I. Bogaert, L. Meert, D. Vande Ginste, and D. Pissoort, "Applications of complex coordinates to the MLFMA", in *Proceedings of the USNC/URSI National Radio Science Meeting*, Monterey, USA, 20-25 June 2004, p. 206.

- I. Bogaert, J. De Zaeytijd, D. Vande Ginste, D. Pissoort, F. Olyslager, and E. Michielssen, "Simulation of extremely large 2D electromagnetic problems", in *Proceedings of the 5th Ugent-FTW PhD Symposium*, Ghent, Belgium, 1 Dec. 2004, Paper 2.

- F. Olyslager, D. Pissoort, J. Fostier, I. Bogaert, J. De Zaeytijd, and E. Michielssen, "Efficient and accurate techniques to simulate large electromagnetic crystals", in *Proceedings of the URSI National Radio Science Meeting*, Boulder, USA, 4-7 Jan. 2006, p. 58.

- I. Bogaert, D. Pissoort, and F. Olyslager, "Accelerating the aggregation and disaggregation in the stable plane wave method", in *Proceedings of the URSI Benelux Meeting*, Eindhoven, The Netherlands, 12 May 2006, p. 7.

- I. Bogaert, D. Pissoort, and F. Olyslager, "Accelerating the aggregation and disaggregation in the stable plane wave method", in *Proceedings of the USNC/URSI National Radio Science Meeting*, Albuquerque, USA, 9-14 July 2006, p. 302.

- I. Bogaert and F. Olyslager, "A low frequency stable formulation of the MLFMA in two dimensions", *Accepted for the USNC/URSI National Radio Science Meeting*, San Diego, USA, 5-12 July 2008.

- J. Fostier, J. Peeters, I. Bogaert, and F. Olyslager, "An open-source, kernel-independent, asynchronous, parallel MLFMA framework", *Accepted for the USNC/URSI National Radio Science Meeting*, San Diego, USA, 5-12 July 2008.

BROADBAND MULTILEVEL FAST MULTIPOLE METHODS

CHAPTER 1

Introduction: Maxwell's equations and multipoles in free space

★★★

Maxwell's equations, supplemented with the constitutive equations of the materials involved and a suitable boundary condition at infinity, provide a complete description of macroscopic electromagnetic fields. In this chapter, solutions of Maxwell's equations in an infinitely large homogeneous isotropic medium will be derived. Although in practice, no such medium exists, these solutions are essential for the solution of Maxwell's equations in more general geometries. How this is done is explained in the next chapter. In an infinitely large homogeneous isotropic medium, Maxwell's equations are translationally and rotationally invariant, and analytical solutions exist in both Cartesian and spherical coordinates. In this chapter, these analytical solutions will be derived as well as the connection between the solutions in Cartesian and spherical coordinates. Much of the material presented here has already been derived, but is scattered throughout the literature [1–5] and uses various notations. Therefore the aim of this chapter is to give a coherent derivation and provide a solid foundation for the rest of this work.

1.1 Maxwell's equations

Maxwell's equations [6] in the time domain are given by

$$\check{\boldsymbol{\nabla}} \times \boldsymbol{E}(\boldsymbol{r},t) = -\frac{\partial}{\partial t}\boldsymbol{B}(\boldsymbol{r},t), \tag{1.1a}$$

$$\check{\boldsymbol{\nabla}} \times \boldsymbol{H}(\boldsymbol{r},t) = \frac{\partial}{\partial t}\boldsymbol{D}(\boldsymbol{r},t) + \boldsymbol{J}(\boldsymbol{r},t), \tag{1.1b}$$

$$\check{\boldsymbol{\nabla}} \cdot \boldsymbol{D}(\boldsymbol{r},t) = \rho(\boldsymbol{r},t), \tag{1.1c}$$

$$\check{\boldsymbol{\nabla}} \cdot \boldsymbol{B}(\boldsymbol{r},t) = 0. \tag{1.1d}$$

In this, $\boldsymbol{E}(\boldsymbol{r},t)$ and $\boldsymbol{H}(\boldsymbol{r},t)$ are the electric and magnetic fields, while $\boldsymbol{D}(\boldsymbol{r},t)$ and $\boldsymbol{B}(\boldsymbol{r},t)$ are the electric and magnetic inductions. Equations (1.1a) and (1.1b) are the curl equations while Eqns. (1.1c) and (1.1d) are called the divergence equations. Taking the divergence of (1.1b) and using (1.1c) in the result yields the law of charge conservation

$$\frac{\partial}{\partial t}\rho(\boldsymbol{r},t) + \check{\boldsymbol{\nabla}} \cdot \boldsymbol{J}(\boldsymbol{r},t) = 0. \tag{1.2}$$

By means of Fourier transformation, defined here as

$$\mathcal{F}_{t\to\omega} f(t) = F(\omega) = \int_{-\infty}^{\infty} e^{-j\omega t} f(t)\mathrm{d}t, \tag{1.3}$$

with inverse

$$\mathcal{F}^{-1}_{\omega\to t} F(\omega) = f(t) = \frac{1}{2\pi}\int_{-\infty}^{\infty} e^{j\omega t} F(\omega)\mathrm{d}\omega, \tag{1.4}$$

Maxwell's equations in the frequency domain are obtained

$$\check{\boldsymbol{\nabla}} \times \boldsymbol{e}(\boldsymbol{r},\omega) = -j\omega\boldsymbol{b}(\boldsymbol{r},\omega), \tag{1.5a}$$

$$\check{\boldsymbol{\nabla}} \times \boldsymbol{h}(\boldsymbol{r},\omega) = j\omega\boldsymbol{d}(\boldsymbol{r},\omega) + \boldsymbol{j}(\boldsymbol{r},\omega), \tag{1.5b}$$

$$\check{\boldsymbol{\nabla}} \cdot \boldsymbol{d}(\boldsymbol{r},\omega) = \rho(\boldsymbol{r},\omega), \tag{1.5c}$$

$$\check{\boldsymbol{\nabla}} \cdot \boldsymbol{b}(\boldsymbol{r},\omega) = 0. \tag{1.5d}$$

The law of charge conservation becomes

$$j\omega\rho(\boldsymbol{r},\omega) + \check{\boldsymbol{\nabla}} \cdot \boldsymbol{j}(\boldsymbol{r},\omega) = 0. \tag{1.6}$$

Because Maxwell's equations in the time domain are real, the quantities appearing in (1.5) all have the symmetry property $\boldsymbol{w}(\boldsymbol{r},-\omega) = \boldsymbol{w}^*(\boldsymbol{r},\omega)$. Therefore, the information contained in $\boldsymbol{w}(\boldsymbol{r},\omega)$ for $\omega \geq 0$ is sufficient to construct the entire time domain

signal by means of inverse Fourier transform. Hence we will restrict ourselves to positive ω. Furthermore, we will from now on omit the explicit dependence of the various quantities on ω, since it only fulfills the role of a parameter in Maxwell's equations, and no derivatives are taken with respect to ω. Also, in many practical situations, one is only interested in a single frequency, making the explicit dependence obsolete.

Maxwell's equations in their own right are not sufficient to produce a unique solution. An appropriate boundary condition and constitutive equations must be added to get a unique solution. Here, we will assume constitutive relations of the simplest form

$$\boldsymbol{d}(\boldsymbol{r}) = \varepsilon \boldsymbol{e}(\boldsymbol{r}), \tag{1.7}$$

$$\boldsymbol{b}(\boldsymbol{r}) = \mu \boldsymbol{h}(\boldsymbol{r}), \tag{1.8}$$

where the constants ε and μ are respectively the permittivity and permeability of the medium. Other parameters associated with ε and μ are the wavenumber k and the impedance Z

$$k = \omega\sqrt{\varepsilon\mu} \;\; \Im k \leq 0, \tag{1.9}$$

$$Z = \frac{\omega\mu}{k}. \tag{1.10}$$

The condition on the imaginary part of k is introduced to make sure that a wave decays in the direction of its propagation (the direction of the Poynting vector), i.e. it expresses the passivity of the medium. With constitutive equations (1.7) and (1.8) it becomes possible to eliminate $\boldsymbol{d}(\boldsymbol{r})$ and $\boldsymbol{b}(\boldsymbol{r})$ from Maxwell's equations. The curl equations then become

$$\check{\boldsymbol{\nabla}} \times \boldsymbol{e}(\boldsymbol{r}) = -j\omega\mu \boldsymbol{h}(\boldsymbol{r}), \tag{1.11a}$$

$$\check{\boldsymbol{\nabla}} \times \boldsymbol{h}(\boldsymbol{r}) = j\omega\varepsilon \boldsymbol{e}(\boldsymbol{r}) + \boldsymbol{j}(\boldsymbol{r}). \tag{1.11b}$$

With the constitutive relations known, a unique solution is obtained when an appropriate boundary condition at infinity is used. Throughout this work, the Sommerfeld radiation condition is used

$$\lim_{r\to\infty} r\left(\frac{\partial}{\partial r} + jk\right)\boldsymbol{e}(\boldsymbol{r}) = 0, \tag{1.12}$$

which expresses the fact that no radiation is coming from infinity. In the time domain, the radiation condition manifests itself as the causality principle. The radiation condition (1.12) is also used for the other fields occurring in Maxwell's equations.

Maxwell's equations can be written in terms of potentials. Indeed, since

$$\check{\boldsymbol{\nabla}} \cdot \boldsymbol{b}(\boldsymbol{r}) = 0, \tag{1.13}$$

there exists a so-called vector potential $\boldsymbol{a}(\boldsymbol{r})$ satisfying

$$\boldsymbol{b}(\boldsymbol{r}) = \check{\boldsymbol{\nabla}} \times \boldsymbol{a}(\boldsymbol{r}). \tag{1.14}$$

Therefore (1.11a) can be written as

$$\check{\boldsymbol{\nabla}} \times [\boldsymbol{e}(\boldsymbol{r}) + j\omega \boldsymbol{a}(\boldsymbol{r})] = 0. \tag{1.15}$$

A curl-free vector field can be written as the gradient of a scalar function, the so-called scalar potential

$$\boldsymbol{e}(\boldsymbol{r}) = -j\omega \boldsymbol{a}(\boldsymbol{r}) - \check{\boldsymbol{\nabla}}\phi(\boldsymbol{r}). \tag{1.16}$$

Using the Lorenz gauge

$$\check{\boldsymbol{\nabla}} \cdot \boldsymbol{a}(\boldsymbol{r}) + j\omega\varepsilon\mu\phi(\boldsymbol{r}) = 0, \tag{1.17}$$

substitution of (1.14) and (1.16) in the divergence equations yields

$$\check{\boldsymbol{\nabla}}^2 \boldsymbol{a}(\boldsymbol{r}) + k^2 \boldsymbol{a}(\boldsymbol{r}) = -\mu \boldsymbol{j}(\boldsymbol{r}), \tag{1.18}$$

$$\check{\boldsymbol{\nabla}}^2 \phi(\boldsymbol{r}) + k^2 \phi(\boldsymbol{r}) = \frac{\check{\boldsymbol{\nabla}} \cdot \boldsymbol{j}(\boldsymbol{r})}{j\omega\varepsilon}. \tag{1.19}$$

The vector components of Eqn. (1.18) can be seen as three separate scalar Helmholtz equations. Indeed, once the vector potential is known, it is a simple matter to determine the scalar potential by means of (1.17). This potential automatically satisfies (1.19). Determining the vector potential can be done using the scalar multipoles, introduced in 1.2.

Maxwell's equations can also be written as Helmholtz equations of the fields themselves. Taking the curl of (1.11a) and substituting the second equation yields

$$\check{\boldsymbol{\nabla}} \times (\check{\boldsymbol{\nabla}} \times \boldsymbol{e}(\boldsymbol{r})) = \check{\boldsymbol{\nabla}}(\check{\boldsymbol{\nabla}} \cdot \boldsymbol{e}(\boldsymbol{r})) - \check{\boldsymbol{\nabla}}^2 \boldsymbol{e}(\boldsymbol{r}) = \omega^2\varepsilon\mu \boldsymbol{e}(\boldsymbol{r}) - j\omega\mu \boldsymbol{j}(\boldsymbol{r}) \tag{1.20}$$

or by means of the divergence equation (1.5c) and charge conservation (1.6)

$$\check{\boldsymbol{\nabla}}^2 \boldsymbol{e}(\boldsymbol{r}) + k^2 \boldsymbol{e}(\boldsymbol{r}) = j\omega\mu \left[\boldsymbol{j}(\boldsymbol{r}) + \frac{1}{k^2} \check{\boldsymbol{\nabla}}(\check{\boldsymbol{\nabla}} \cdot \boldsymbol{j}(\boldsymbol{r})) \right]. \tag{1.21}$$

with $k^2 = \omega^2\varepsilon\mu$. In a similar way an equation can be found for $\boldsymbol{h}(\boldsymbol{r})$

$$\check{\boldsymbol{\nabla}}^2 \boldsymbol{h}(\boldsymbol{r}) + k^2 \boldsymbol{h}(\boldsymbol{r}) = -\check{\boldsymbol{\nabla}} \times \boldsymbol{j}(\boldsymbol{r}). \tag{1.22}$$

Equations (1.21) and (1.22) could in principle be solved by solving a scalar Helmholtz equation for each of the vector components. However, the conditions imposed by the

divergence equations are not easily incorporated in such a solution. Instead Eqns. (1.21) and (1.22) should be solved by means of the vector multipoles, introduced in 1.3.

1.2 The scalar Helmholtz equation

In this section we will construct the general solution of the scalar Helmholtz equation, along with a number of properties of these solutions that are useful for the rest of this work. The scalar Helmholtz equation is given by

$$\boldsymbol{\nabla}^2 f(\boldsymbol{r}) + k^2 f(\boldsymbol{r}) = 0. \tag{1.23}$$

This equation is separable in Cartesian and spherical coordinates. In the Cartesian coordinate system, separation of variables leads to plane wave solutions

$$f(\boldsymbol{r}) = \sum_n F(\boldsymbol{k}_n) e^{-j\boldsymbol{k}_n \cdot \boldsymbol{r}}, \tag{1.24}$$

where all the so-called wavevectors $\boldsymbol{k}_n$ satisfy

$$\boldsymbol{k}_n \cdot \boldsymbol{k}_n = k^2. \tag{1.25}$$

In spherical coordinates, separation of variables leads to the following general solution

$$f(\boldsymbol{r}) = \sum_{l,m} \left[a_{l,m} Z^j_{l,m}(k\boldsymbol{r}) + b_{l,m} Z^h_{l,m}(k\boldsymbol{r}) \right] \tag{1.26}$$

with the so-called multipoles defined as

$$Z^j_{l,m}(k\boldsymbol{r}) = j_l(kr)\, Y_{l,m}(\hat{\boldsymbol{r}}), \tag{1.27}$$

$$Z^h_{l,m}(k\boldsymbol{r}) = h^{(2)}_l(kr)\, Y_{l,m}(\hat{\boldsymbol{r}}). \tag{1.28}$$

and the notation

$$\sum_{l,m} = \sum_{l=0}^{\infty} \sum_{m=-l}^{l}. \tag{1.29}$$

The multipoles containing the spherical Bessel functions are well-behaved at the origin. In contrast, the multipoles containing the spherical Hankel functions are singular at the origin. However, they satisfy the radiation condition at infinity. In general, a function satisfying (1.23) can be expanded in both plane waves and multipoles.

1.2.1 The scalar Green function

The scalar Green function will now be determined. This function is useful for example for determining the vector potential from a given electric current. The scalar Green function is defined by the following equation

$$\check{\boldsymbol{\nabla}}^2 G_0(\boldsymbol{r}) + k^2 G_0(\boldsymbol{r}) = -\delta(\boldsymbol{r}). \tag{1.30}$$

Since the source term (the right hand side), the boundary conditions at infinity and the Helmholtz equation are all rotationally invariant, the solution must be rotationally invariant as well, i.e. a linear combination of $j_0(kr)$ and $h_0^{(2)}(kr)$. We choose a solution that satisfies the radiation condition, i.e. $Ch_0^{(2)}(kr)$, to be able to interpret the Green function as a field radiated from the source to infinity. Using the divergence theorem, the constant C can be determined to be $-\frac{jk}{4\pi}$. Then

$$G_0(\boldsymbol{r}) = -\frac{jk}{4\pi} h_0^{(2)}(kr) = \frac{e^{-jkr}}{4\pi r}. \tag{1.31}$$

The same result can also be obtained by spatially Fourier transforming (1.30), which yields

$$G_0(\boldsymbol{r}) = \mathcal{F}^{-1}_{k_x\to x}\mathcal{F}^{-1}_{k_y\to y}\mathcal{F}^{-1}_{k_z\to z}\left[\frac{1}{k_x^2+k_y^2+k_z^2-k^2}\right], \tag{1.32}$$

$$= \frac{1}{2\pi^2}\int_0^\infty \frac{j_0(tr)}{t^2-k^2} t^2 \mathrm{d}t, \tag{1.33}$$

$$= \frac{1}{4ir\pi^2}\int_0^\infty \frac{e^{itr}-e^{-itr}}{t^2-k^2} t\mathrm{d}t, \tag{1.34}$$

$$= \frac{1}{4ir\pi^2}\int_{-\infty}^\infty \frac{e^{itr}}{t^2-k^2} t\mathrm{d}t. \tag{1.35}$$

If we assume k to have a slightly negative imaginary part (corresponding to a passive material), this integral can be evaluated using contour integration

$$G_0(\boldsymbol{r}) = \frac{e^{-jkr}}{4\pi r}. \tag{1.36}$$

Equation (1.30) allows the simple expansion of $h_0^{(2)}(kr)$ in plane waves. Indeed, taking the spatial Fourier transform in the x- and y-direction yields

$$\frac{\mathrm{d}^2}{\mathrm{d}z^2} w(k_x,k_y,z) + (k^2-k_x^2-k_y^2) w(k_x,k_y,z) = \frac{4\pi}{jk}\delta(z). \tag{1.37}$$

with

$$w(k_x, k_y, z) = \mathcal{F}_{x\to k_x}\mathcal{F}_{y\to k_y} h_0^{(2)}(kr) \tag{1.38}$$

Taking the radiation condition into account, this yields the solution in the half-spaces $z \gtrless 0$

$$w(k_x, k_y, z) = 2\pi \frac{1}{kk_z} e^{\mp jk_z z}, \tag{1.39}$$

with $K^2 = k_x^2 + k_y^2$

$$k_z = \begin{cases} \sqrt{k^2 - K^2}, & k \geq K \\ -j\sqrt{K^2 - k^2}, & K > k. \end{cases} \tag{1.40}$$

Taking the inverse spatial Fourier transform finally yields, $\forall z > 0$

$$h_0^{(2)}(kr) = \frac{1}{2\pi} \int_{-\infty}^{\infty}\int_{-\infty}^{\infty} \frac{1}{kk_z} e^{-j\boldsymbol{k}\cdot\boldsymbol{r}} \mathrm{d}k_x \mathrm{d}k_y. \tag{1.41}$$

This can be simplified by substituting (k_x, k_y) with $(k\sin\theta\cos\phi, k\sin\theta\sin\phi)$

$$h_0^{(2)}(kr) = \frac{1}{2\pi} \int_0^{2\pi}\int_\Gamma e^{-jk\hat{\boldsymbol{k}}(\theta,\phi)\cdot\boldsymbol{r}} \sin\theta \mathrm{d}\theta\mathrm{d}\phi \tag{1.42}$$

where the integration path $\Gamma = \Gamma_1 + \Gamma_2$ is defined as shown in Figure 1.1. After this substitution, $k_z = k\cos\theta$. It is convenient to introduce the following notation

$$\int_{\mathcal{E}} F(\hat{\boldsymbol{k}}) \mathrm{d}\hat{\boldsymbol{k}} = \int_0^{2\pi}\int_\Gamma F(\hat{\boldsymbol{k}}(\theta,\phi)) \sin\theta \mathrm{d}\theta\mathrm{d}\phi \tag{1.43}$$

which then allows to write

$$h_0^{(2)}(kr) = \frac{1}{2\pi} \int_{\mathcal{E}} e^{-jk\hat{\boldsymbol{k}}\cdot\boldsymbol{r}} \mathrm{d}\hat{\boldsymbol{k}}. \tag{1.44}$$

It should be noted that (1.44) is only valid for $z > 0$. However, since the left hand side is rotationally invariant, an integral representation that converges in any half space of choice can be easily found.

A plane wave expansion of $j_0(kr)$ can also be found. It is given by

$$j_0(kr) = \frac{1}{4\pi} \int_{\mathcal{S}_2} e^{-jk\hat{\boldsymbol{k}}\cdot\boldsymbol{r}} \mathrm{d}\hat{\boldsymbol{k}}. \tag{1.45}$$

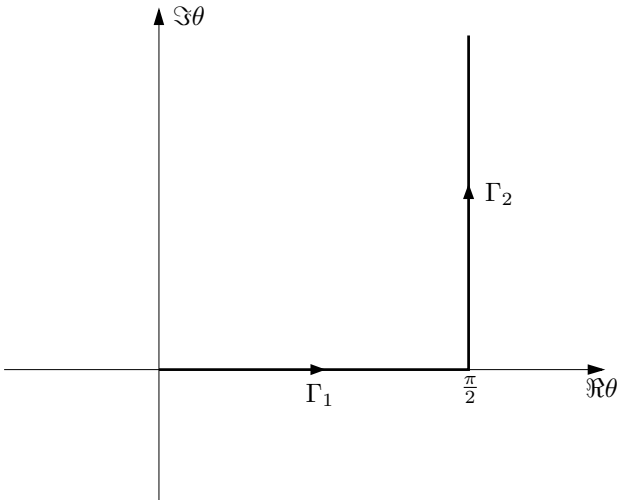

Figure 1.1: The integration path $\Gamma = \Gamma_1 + \Gamma_2$ for Eqn. (1.42).

where the integral with subscript $\mathcal{S}_2$ stands for integration over the unit sphere

$$\int_{\mathcal{S}_2} F(\hat{\boldsymbol{k}})\mathrm{d}\hat{\boldsymbol{k}} = \int_0^{2\pi}\int_0^{\pi} F(\hat{\boldsymbol{k}}(\theta,\phi))\sin\theta\mathrm{d}\theta\mathrm{d}\phi. \tag{1.46}$$

Equation (1.45) can then be proved by rotating the unit sphere such that $\boldsymbol{r}$ is rotated into $r\hat{\boldsymbol{e}}_z$

$$\frac{1}{4\pi}\int_{\mathcal{S}_2} e^{-jkr\hat{\boldsymbol{k}}\cdot\hat{\boldsymbol{e}}_z}\mathrm{d}\hat{\boldsymbol{k}} = \frac{1}{2}\int_{-1}^{1} e^{-jkru}\mathrm{d}u, \tag{1.47}$$

$$= \frac{\sin(kr)}{kr} = j_0\left(kr\right). \tag{1.48}$$

1.2.2 Alternative definition of the multipoles

The scalar multipoles (1.27) and (1.28) can also be defined using the so-called scalar spherical wave operators, defined in Appendix A

$$Z^j_{l,m}\left(k\boldsymbol{r}\right) = j^l Y_{l,m}\left(\frac{\check{\boldsymbol{\nabla}}}{-jk}\right) j_0\left(kr\right), \tag{1.49}$$

$$Z^h_{l,m}\left(k\boldsymbol{r}\right) = j^l Y_{l,m}\left(\frac{\check{\boldsymbol{\nabla}}}{-jk}\right) h_0^{(2)}\left(kr\right). \tag{1.50}$$

This definition is equivalent due to Theorem B.1.1. A direct consequence of (1.49), (1.50), (1.45) and (1.44) is

$$Z_{l,m}^{j}\left(k\boldsymbol{r}\right)=\frac{j^{l}}{4\pi}\int_{\mathcal{S}_{2}}Y_{l,m}\left(\hat{\boldsymbol{k}}\right)e^{-jk\hat{\boldsymbol{k}}\cdot\boldsymbol{r}}\mathrm{d}\hat{\boldsymbol{k}}, \tag{1.51}$$

$$Z_{l,m}^{h}\left(k\boldsymbol{r}\right)=\frac{j^{l}}{2\pi}\int_{\mathcal{E}}Y_{l,m}\left(\hat{\boldsymbol{k}}\right)e^{-jk\hat{\boldsymbol{k}}\cdot\boldsymbol{r}}\mathrm{d}\hat{\boldsymbol{k}}. \tag{1.52}$$

1.2.3 Multipole expansion of a plane wave

A plane wave is a solution of the Helmholtz equation, therefore it can be expanded in multipoles. More precisely it can be expanded in the regular multipoles, since a plane wave is regular at the origin. The expansion can be obtained by using the completeness of the spherical harmonics (A.18) and integral representation (1.51)

$$e^{-j\boldsymbol{k}\cdot\boldsymbol{r}}=\sum_{l,m}Y_{l,m}\left(\hat{\boldsymbol{k}}\right)\int_{\mathcal{S}_{2}}e^{-jk\hat{\boldsymbol{k}}'\cdot\boldsymbol{r}}Y_{l,m}^{*}\left(\hat{\boldsymbol{k}}'\right)\mathrm{d}\hat{\boldsymbol{k}}', \tag{1.53}$$

$$=4\pi\sum_{l,m}(-1)^{m}j^{-l}Y_{l,-m}\left(\hat{\boldsymbol{k}}\right)Z_{l,m}^{j}\left(k\boldsymbol{r}\right). \tag{1.54}$$

This converges for all $\boldsymbol{r}$. Using the spherical harmonic addition theorem (A.10) this can also be written as

$$e^{-j\boldsymbol{k}\cdot\boldsymbol{r}}=\sum_{l=0}^{\infty}j^{-l}(2l+1)j_{l}\left(kr\right)P_{l}\left(\hat{\boldsymbol{k}}\cdot\hat{\boldsymbol{r}}\right). \tag{1.55}$$

1.2.4 Multipole expansion of a general field

The expansion of a plane wave can now be used to expand a general field that satisfies (1.23) into multipoles. In a region where $f(\boldsymbol{r})$ satifies (1.23), it can be written as a superposition of plane waves, as in (1.24). By expanding every plane wave as in (1.54), the multipole expansion is obtained as

$$f(\boldsymbol{r})=4\pi\sum_{l,m}(-1)^{m}j^{-l}\left[\sum_{n}F(\boldsymbol{k}_{n})Y_{l,-m}\left(\hat{\boldsymbol{k}}_{n}\right)\right]Z_{l,m}^{j}\left(k\boldsymbol{r}\right). \tag{1.56}$$

This series converges in a spherical region with a radius determined by the distance between the origin and the nearest point where $\left[\check{\boldsymbol{\nabla}}^{2}+k^{2}\right]f(\boldsymbol{r})\neq0$. Using the scalar

spherical wave operators, this can also be written as

$$\sum_n F(\boldsymbol{k}_n) Y_{l,-m}\left(\hat{\boldsymbol{k}}_n\right) = \left[\sum_n F(\boldsymbol{k}_n) Y_{l,-m}\left(\frac{\check{\boldsymbol{\nabla}}''}{-jk}\right) e^{-j\boldsymbol{k}_n\cdot\boldsymbol{r}''}\right]_{\boldsymbol{r}''=\boldsymbol{0}},$$
$$= \left[Y_{l,-m}\left(\frac{\check{\boldsymbol{\nabla}}''}{-jk}\right) f(\boldsymbol{r}'')\right]_{\boldsymbol{r}''=\boldsymbol{0}}, \tag{1.57}$$

where $\check{\boldsymbol{\nabla}}''$ denotes the gradient with respect to $\boldsymbol{r}''$. Apparently, the scalar spherical wave operators can be used to calculate the coefficients of the multipole expansion (1.56). A generalization of (1.56) is obtained by replacing $f(\boldsymbol{r})$ with $g(\boldsymbol{r}+\boldsymbol{r}')$

$$g(\boldsymbol{r}+\boldsymbol{r}') = \sum_{l,m} 4\pi j^{-l}(-1)^m Z^j_{l,m}(k\boldsymbol{r})\, Y_{l,-m}\left(\frac{\check{\boldsymbol{\nabla}}'}{-jk}\right) g(\boldsymbol{r}'). \tag{1.58}$$

The following special case for $g(\cdot) = h_0^{(2)}(k\,||\cdot||)$ deserves special attention, since it is widely known

$$h_0^{(2)}(k\,||\boldsymbol{r}+\boldsymbol{r}'||) = \sum_{l,m} 4\pi(-1)^l Z^h_{l,-m}(k\boldsymbol{r}')\,(-1)^{-m} Z^j_{l,m}(k\boldsymbol{r}), \tag{1.59}$$
$$= \sum_{l=0}^{\infty}(2l+1)(-1)^l h_l^{(2)}(kr')\, j_l(kr)\, P_l\left(\hat{\boldsymbol{r}}\cdot\hat{\boldsymbol{r}}'\right). \tag{1.60}$$

1.2.5 Translation matrices

An application of (1.58) is the calculation of the scalar translation operator. This is a matrix $\alpha^f(k\boldsymbol{r}')$ defined by the property

$$Z^f_{l_1,m_1}(k(\boldsymbol{r}+\boldsymbol{r}')) = \sum_{l_2,m_2}\left[\alpha^f(k\boldsymbol{r}')\right]_{l_2,m_2;l_1,m_1} Z^j_{l_2,m_2}(k\boldsymbol{r}). \tag{1.61}$$

If the regular spherical Bessel functions are used, i.e. $f = j$, the left hand side satisfies (1.23) everywhere. Therefore, Eqn. (1.61) converges for all $\boldsymbol{r}$. If $f = h$, the left hand side does not satisfy the Helmholtz equation in the point $\boldsymbol{r} = -\boldsymbol{r}'$, yielding convergence if $r < r'$. The translation matrix is required when a field, known in terms of multipoles around the origin, has to be expanded in regular multipoles around the

point $\boldsymbol{r}'$. Clearly, the elements of this matrix are given by

$$\left[\alpha^f(k\boldsymbol{r}')\right]_{l_2,m_2;l_1,m_1}$$

$$= 4\pi j^{-l_2}(-1)^{m_2} Y_{l_2,-m_2}\left(\frac{\check{\boldsymbol{\nabla}}'}{-jk}\right) Z^f_{l_1,m_1}(k\boldsymbol{r}'), \tag{1.62}$$

$$= 4\pi j^{l_1-l_2}(-1)^{m_2} Y_{l_2,-m_2}\left(\frac{\check{\boldsymbol{\nabla}}'}{-jk}\right) Y_{l_1,m_1}\left(\frac{\check{\boldsymbol{\nabla}}'}{-jk}\right) f_0(kr'). \tag{1.63}$$

Since the scalar spherical wave operators are applied to $f_0(kr')$, which is a solution of the Helmholtz equation, Eqn. (A.26) can be used to evaluate this

$$\left[\alpha^f(k\boldsymbol{r}')\right]_{l_2,m_2;l_1,m_1} = 4\pi j^{l_1-l_2}$$

$$\times \sum_{l_3,m_3} (-1)^{m_2+m_3} \mathcal{A}_{l_1,m_1;l_2,-m_2;l_3,-m_3} Y_{l_3,m_3}\left(\frac{\check{\boldsymbol{\nabla}}'}{-jk}\right) f_0(kr'), \tag{1.64}$$

$$= 4\pi \sum_{l_3,m_3} j^{l_1-l_2-l_3}(-1)^{m_2+m_3} \mathcal{A}_{l_1,m_1;l_2,-m_2;l_3,-m_3} Z^f_{l_3,m_3}(k\boldsymbol{r}'). \tag{1.65}$$

These expressions were first derived in [4]. Another consequence of Eqn. (1.63) is a set of recurrence relations, first obtained in [7]. They are derived in a very straightforward manner by multiplying (1.63) with $Y_{1,m}\left(\frac{\check{\boldsymbol{\nabla}}'}{-jk}\right)$ and absorbing this factor once in $Y_{l_2,-m_2}\left(\frac{\check{\boldsymbol{\nabla}}'}{-jk}\right)$ and once in $Y_{l_1,m_1}\left(\frac{\check{\boldsymbol{\nabla}}'}{-jk}\right) f_0(kr')$ by means of Eqns. (A.23). Equating the two results yields the recurrences. These recurrences can be used for a very efficient calculation of the scalar translation matrices.

1.2.6 A plane wave addition theorem

The translation matrices described above can be diagonalized in a plane wave basis, as is done in [3]. Here, this diagonalized form will be proved in a more direct way, using (1.59) and the integral representation (1.51)

$$h_0^{(2)}(k\,||\boldsymbol{r}+\boldsymbol{r}'||) = \sum_{l=0}^{\infty}\sum_{m=-l}^{l} j^{-l} Z^h_{l,m}(k\boldsymbol{r}')(-1)^m \int_{\mathcal{S}_2} Y_{l,-m}\left(\hat{\boldsymbol{k}}\right) e^{-jk\hat{\boldsymbol{k}}\cdot\boldsymbol{r}} \mathrm{d}\hat{\boldsymbol{k}}, \tag{1.66}$$

$$= \frac{1}{4\pi}\int_{\mathcal{S}_2} T(k\boldsymbol{r}', \hat{\boldsymbol{k}}) e^{-jk\hat{\boldsymbol{k}}\cdot\boldsymbol{r}} \mathrm{d}\hat{\boldsymbol{k}}, \tag{1.67}$$

with the so-called translation operator defined by

$$T(k\boldsymbol{r}',\hat{\boldsymbol{k}}) = 4\pi \sum_{l=0}^{\infty} \sum_{m=-l}^{l} j^{-l} Z_{l,m}^{h}\left(k\boldsymbol{r}'\right)(-1)^{m} Y_{l,-m}\left(\hat{\boldsymbol{k}}\right), \tag{1.68}$$

$$= \sum_{l=0}^{\infty} j^{-l}(2l+1) h_{l}^{(2)}\left(kr'\right) P_{l}\left(\hat{\boldsymbol{r}}' \cdot \hat{\boldsymbol{k}}\right). \tag{1.69}$$

The sum over l in (1.69) does not converge, therefore it has to be interpreted in the distributional sense. For practical use, the sum is usually truncated at $l = L$, with L chosen such that (1.67) still holds within a certain accuracy. This 'practical' version of the addition theorem is the basis of the MLFMA [8].

1.3 The vector Helmholtz equation

Equations (1.21) and (1.22) are vectorial Helmholtz equations. These can be interpreted as three scalar Helmholtz equations, and can thus be solved with the theory developed in 1.2. Unfortunately, the divergence equations impose an additional constraint on the solutions. Indeed, in source free regions, the electric and magnetic fields are divergence free. Incorporating this condition is done by means of the so-called vector multipoles, defined as

$$\boldsymbol{M}_{l,m}^{j}\left(k\boldsymbol{r}\right) = \frac{j^{l}}{4\pi} \int_{\mathcal{S}_2} \boldsymbol{X}_{l,m}\left(\hat{\boldsymbol{k}}\right) e^{-jk\hat{\boldsymbol{k}}\cdot\boldsymbol{r}} \mathrm{d}\hat{\boldsymbol{k}}, \tag{1.70}$$

$$\boldsymbol{N}_{l,m}^{j}\left(k\boldsymbol{r}\right) = \frac{j^{l-1}}{4\pi} \int_{\mathcal{S}_2} \boldsymbol{W}_{l,m}\left(\hat{\boldsymbol{k}}\right) e^{-jk\hat{\boldsymbol{k}}\cdot\boldsymbol{r}} \mathrm{d}\hat{\boldsymbol{k}}, \tag{1.71}$$

$$\boldsymbol{M}_{l,m}^{h}\left(k\boldsymbol{r}\right) = \frac{j^{l}}{2\pi} \int_{\mathcal{E}} \boldsymbol{X}_{l,m}\left(\hat{\boldsymbol{k}}\right) e^{-jk\hat{\boldsymbol{k}}\cdot\boldsymbol{r}} \mathrm{d}\hat{\boldsymbol{k}}, \tag{1.72}$$

$$\boldsymbol{N}_{l,m}^{h}\left(k\boldsymbol{r}\right) = \frac{j^{l-1}}{2\pi} \int_{\mathcal{E}} \boldsymbol{W}_{l,m}\left(\hat{\boldsymbol{k}}\right) e^{-jk\hat{\boldsymbol{k}}\cdot\boldsymbol{r}} \mathrm{d}\hat{\boldsymbol{k}}. \tag{1.73}$$

or the equivalent

$$\boldsymbol{M}_{l,m}^{j}\left(k\boldsymbol{r}\right) = j^{l} \boldsymbol{X}_{l,m}\left(\frac{\check{\boldsymbol{\nabla}}}{-jk}\right) j_{0}\left(kr\right), \tag{1.74}$$

$$\boldsymbol{N}_{l,m}^{j}\left(k\boldsymbol{r}\right) = j^{l-1} \boldsymbol{W}_{l,m}\left(\frac{\check{\boldsymbol{\nabla}}}{-jk}\right) j_{0}\left(kr\right), \tag{1.75}$$

$$\boldsymbol{M}_{l,m}^{h}\left(k\boldsymbol{r}\right) = j^{l} \boldsymbol{X}_{l,m}\left(\frac{\check{\boldsymbol{\nabla}}}{-jk}\right) h_{0}^{(2)}\left(kr\right), \tag{1.76}$$

$$\boldsymbol{N}_{l,m}^{h}\left(k\boldsymbol{r}\right) = j^{l-1} \boldsymbol{W}_{l,m}\left(\frac{\check{\boldsymbol{\nabla}}}{-jk}\right) h_{0}^{(2)}\left(kr\right), \tag{1.77}$$

where the so-called vector spherical wave operators, defined in Appendix A, are used. Due to properties (A.64) and (A.65), the vector multipoles are divergence free for $r > 0$

$$\check{\boldsymbol{\nabla}} \cdot \boldsymbol{M}^{f}_{l,m}(k\boldsymbol{r}) = 0, \tag{1.78}$$

$$\check{\boldsymbol{\nabla}} \cdot \boldsymbol{N}^{f}_{l,m}(k\boldsymbol{r}) = 0. \tag{1.79}$$

A representation of $\boldsymbol{M}^{j}_{l,m}(k\boldsymbol{r})$ without integrals or spherical wave operators can be obtained by expanding each component of vector spherical harmonic $\boldsymbol{X}_{l,m}\left(\hat{\boldsymbol{k}}\right)$ in spherical harmonics by means of (A.86)

$$\boldsymbol{M}^{j}_{l,m}(k\boldsymbol{r}) = \frac{j^l}{4\pi}\frac{1}{\sqrt{l(l+1)}}\mathsf{M}^{H} \cdot \int_{\mathcal{S}_2} \begin{bmatrix} \frac{\lambda^{-}_{lm}}{\sqrt{2}} Y_{l,m-1}\left(\hat{\boldsymbol{k}}\right) \\ m Y_{l,m}\left(\hat{\boldsymbol{k}}\right) \\ -\frac{\lambda^{+}_{lm}}{\sqrt{2}} Y_{l,m+1}\left(\hat{\boldsymbol{k}}\right) \end{bmatrix} e^{-jk\hat{\boldsymbol{k}}\cdot\boldsymbol{r}} \mathrm{d}\hat{\boldsymbol{k}}, \tag{1.80}$$

$$= \frac{1}{\sqrt{l(l+1)}}\mathsf{M}^{H} \cdot \begin{bmatrix} \frac{\lambda^{-}_{lm}}{\sqrt{2}} Z^{j}_{l,m-1}(k\boldsymbol{r}) \\ m Z^{j}_{l,m}(k\boldsymbol{r}) \\ -\frac{\lambda^{+}_{lm}}{\sqrt{2}} Z^{j}_{l,m+1}(k\boldsymbol{r}) \end{bmatrix}, \tag{1.81}$$

$$= j_l(kr)\,\boldsymbol{X}_{l,m}(\hat{\boldsymbol{r}}). \tag{1.82}$$

Similarly

$$\boldsymbol{M}^{h}_{l,m}(k\boldsymbol{r}) = h^{(2)}_{l}(kr)\,\boldsymbol{X}_{l,m}(\hat{\boldsymbol{r}}). \tag{1.83}$$

An expression for $\boldsymbol{N}^{j}_{l,m}(k\boldsymbol{r})$ can be found by expanding $\boldsymbol{W}_{l,m}(\hat{\boldsymbol{r}})$ in spherical harmonics, by means of (A.87). However, a more convenient expression can be found by using the definition of $\boldsymbol{W}_{l,m}(\hat{\boldsymbol{r}})$ (A.59)

$$\boldsymbol{N}^{j}_{l,m}(k\boldsymbol{r}) = \frac{j^l}{4\pi}\int_{\mathcal{S}_2} (-j\hat{\boldsymbol{k}}) \times \boldsymbol{X}_{l,m}\left(\hat{\boldsymbol{k}}\right) e^{-jk\hat{\boldsymbol{k}}\cdot\boldsymbol{r}} \mathrm{d}\hat{\boldsymbol{k}}, \tag{1.84}$$

$$= \frac{1}{k}\check{\boldsymbol{\nabla}} \times \boldsymbol{M}^{j}_{l,m}(k\boldsymbol{r}). \tag{1.85}$$

It is interesting to note that applying the curl once more yields the reverse expression

$$\boldsymbol{M}^{j}_{l,m}(k\boldsymbol{r}) = \frac{1}{k}\check{\boldsymbol{\nabla}} \times \boldsymbol{N}^{j}_{l,m}(k\boldsymbol{r}). \tag{1.86}$$

Evaluating the curl in Eqn. (1.85) yields

$$k\boldsymbol{N}^{j}_{l,m}(k\boldsymbol{r}) = \left[\check{\boldsymbol{\nabla}} j_l(kr)\right] \times \boldsymbol{X}_{l,m}(\hat{\boldsymbol{r}}) + j_l(kr)\,\check{\boldsymbol{\nabla}} \times \boldsymbol{X}_{l,m}(\hat{\boldsymbol{r}}), \tag{1.87}$$

$$= \frac{\mathrm{d}}{\mathrm{d}r} j_l(kr)\,\boldsymbol{W}_{l,m}(\hat{\boldsymbol{r}}) - j\frac{j_l(kr)}{\sqrt{l(l+1)}}\check{\boldsymbol{\nabla}} \times \left[\boldsymbol{r} \times \check{\boldsymbol{\nabla}} Y_{l,m}(\hat{\boldsymbol{r}})\right]. \tag{1.88}$$

With

$$\check{\boldsymbol{\nabla}} \times \left[\boldsymbol{r} \times \check{\boldsymbol{\nabla}} Y_{l,m}(\hat{\boldsymbol{r}})\right] = \boldsymbol{r}\check{\boldsymbol{\nabla}}^2 Y_{l,m}(\hat{\boldsymbol{r}}) - \check{\boldsymbol{\nabla}} Y_{l,m}(\hat{\boldsymbol{r}}), \tag{1.89}$$

$$= -\frac{l(l+1)}{r^2}\boldsymbol{r} Y_{l,m}(\hat{\boldsymbol{r}}) - \frac{\sqrt{l(l+1)}}{jr}\boldsymbol{W}_{l,m}(\hat{\boldsymbol{r}}), \tag{1.90}$$

this becomes

$$\boldsymbol{N}^{j}_{l,m}(k\boldsymbol{r}) = \mathcal{J}_l(kr)\,\boldsymbol{W}_{l,m}(\hat{\boldsymbol{r}}) + j\sqrt{l(l+1)}\frac{j_l(kr)}{kr}\hat{\boldsymbol{r}} Y_{l,m}(\hat{\boldsymbol{r}}), \tag{1.91}$$

with

$$\mathcal{J}_l(x) = \frac{1}{x}\frac{\mathrm{d}}{\mathrm{d}x}\left[x j_l(x)\right] = j_{l-1}(x) - \frac{l}{x} j_l(x). \tag{1.92}$$

Analogously,

$$\boldsymbol{N}^{h}_{l,m}(k\boldsymbol{r}) = \mathcal{H}^{(2)}_l(kr)\,\boldsymbol{W}_{l,m}(\hat{\boldsymbol{r}}) + j\sqrt{l(l+1)}\frac{h^{(2)}_l(kr)}{kr}\hat{\boldsymbol{r}} Y_{l,m}(\hat{\boldsymbol{r}}), \tag{1.93}$$

with

$$\mathcal{H}^{(2)}_l(x) = \frac{1}{x}\frac{\mathrm{d}}{\mathrm{d}x}\left[x h^{(2)}_l(x)\right] = h^{(2)}_{l-1}(x) - \frac{l}{x} h^{(2)}_l(x). \tag{1.94}$$

Together, formulas (1.82), (1.83), (1.91) and (1.93) allow the efficient calculation of the vector multipoles.

1.3.1 The vectorial Green functions

The Green function of Eqns. (1.21) and (1.22) will now be determined. This means that the electric and magnetic field due to an elementary dipole current

$$\boldsymbol{j}_d(\boldsymbol{r}) = \boldsymbol{p}\delta(\boldsymbol{r}), \tag{1.95}$$

with $\boldsymbol{p}$ a constant vector, will be calculated. For the magnetic field this can be easily done by multiplying the defining equation (1.30) of the scalar Green function with $\boldsymbol{p}$

and applying the curl

$$\check{\boldsymbol{\nabla}}^2 \mathsf{G}_m(\boldsymbol{r}) \cdot \boldsymbol{p} + k^2 \mathsf{G}_m(\boldsymbol{r}) \cdot \boldsymbol{p} = -\check{\boldsymbol{\nabla}} \times \boldsymbol{j}_d(\boldsymbol{r}). \tag{1.96}$$

with the magnetic Green dyadic defined as

$$\mathsf{G}_m(\boldsymbol{r}) = \check{\boldsymbol{\nabla}} \times [\mathbb{1} G_0(\boldsymbol{r})] \tag{1.97}$$

In the above, $\mathbb{1}$ is the 3 by 3 identity matrix and the fact that the Laplace operator and the curl commute is used. Obtaining the electric field can be done using the curl equation (1.11b)

$$\mathsf{G}_e(\boldsymbol{r}) \cdot \boldsymbol{p} = \frac{1}{j\omega\varepsilon} \left[\check{\boldsymbol{\nabla}} \times \mathsf{G}_m(\boldsymbol{r}) \cdot \boldsymbol{p} - \boldsymbol{j}_d(\boldsymbol{r}) \right] \tag{1.98}$$

$$= \frac{1}{j\omega\varepsilon} \left[\check{\boldsymbol{\nabla}}\check{\boldsymbol{\nabla}} \cdot [\mathbb{1} G_0(\boldsymbol{r})] \cdot \boldsymbol{p} + k^2 [\mathbb{1} G_0(\boldsymbol{r})] \cdot \boldsymbol{p} \right]. \tag{1.99}$$

Therefore the electric Green dyadic is given by

$$\mathsf{G}_e(\boldsymbol{r}) = -j\omega\mu \left[\mathbb{1} + \frac{1}{k^2} \check{\boldsymbol{\nabla}}\check{\boldsymbol{\nabla}} \right] G_0(\boldsymbol{r}) \tag{1.100}$$

The derivatives can be evaluated using the recurrences of the spherical Hankel function

$$\mathsf{G}_e(\boldsymbol{r}) = -j\omega\mu G_0(\boldsymbol{r}) \left[\left(\frac{2j}{kr} + \frac{2}{(kr)^2} \right) \hat{\boldsymbol{r}}\hat{\boldsymbol{r}} + \left(1 - \frac{j}{kr} - \frac{1}{(kr)^2} \right) (1 - \hat{\boldsymbol{r}}\hat{\boldsymbol{r}}) \right] \tag{1.101}$$

Interestingly, the eigenvalues of the electric Green dyadic are immediately known from this

$$\lambda_1 = -j\omega\mu G_0(\boldsymbol{r}) \left(\frac{2j}{kr} + \frac{2}{(kr)^2} \right), \tag{1.102}$$

$$\lambda_2 = \lambda_3 = -j\omega\mu G_0(\boldsymbol{r}) \left(1 - \frac{j}{kr} - \frac{1}{(kr)^2} \right). \tag{1.103}$$

1.3.2 Vector multipole expansion of a vector plane wave

The vectorial Helmholtz equations have plane wave solutions of the form $\boldsymbol{E}_0 e^{-j\boldsymbol{k}\cdot\boldsymbol{r}}$ with the vector $\boldsymbol{E}_0$ completely free to chose. The condition that the divergence must be zero yields the following constraint

$$\boldsymbol{k} \cdot \boldsymbol{E}_0 = 0. \tag{1.104}$$

From their definitions (1.70), (1.71), (1.72) and (1.73) it is immediately seen that the vector multipoles are all superpositions of vector plane waves satisfying condition (1.104). The reverse is also true

$$\boldsymbol{E}_0 e^{-j\boldsymbol{k}\cdot\boldsymbol{r}} = \sum_{l,m} \left[a_{l,m} \boldsymbol{M}^j_{l,m}(k\boldsymbol{r}) + b_{l,m} \boldsymbol{N}^j_{l,m}(k\boldsymbol{r}) \right]. \tag{1.105}$$

for all $\boldsymbol{r}$. The coefficients $a_{l,m}$ and $b_{l,m}$ can be determined by means of the completeness (A.72) of the vector spherical harmonics

$$\begin{aligned}\boldsymbol{E}_0 e^{-j\boldsymbol{k}\cdot\boldsymbol{r}} = \sum_{l,m} \int_{\mathcal{S}_2} \boldsymbol{E}_0 \cdot \Big[& \boldsymbol{X}_{l,m}\left(\hat{\boldsymbol{k}}'\right) \boldsymbol{X}^*_{l,m}\left(\hat{\boldsymbol{k}}\right) \\ & + \boldsymbol{W}_{l,m}\left(\hat{\boldsymbol{k}}'\right) \boldsymbol{W}^*_{l,m}\left(\hat{\boldsymbol{k}}\right) \Big] e^{-jk\hat{\boldsymbol{k}}'\cdot\boldsymbol{r}} \mathrm{d}\hat{\boldsymbol{k}}',\end{aligned} \tag{1.106}$$

which, by means of (1.70) and (1.71), yields

$$a_{l,m} = 4\pi j^{-l}(-1)^{m+1} \boldsymbol{E}_0 \cdot \boldsymbol{X}_{l,-m}\left(\hat{\boldsymbol{k}}\right), \tag{1.107}$$

$$b_{l,m} = 4\pi j^{-l+1}(-1)^{m+1} \boldsymbol{E}_0 \cdot \boldsymbol{W}_{l,-m}\left(\hat{\boldsymbol{k}}\right). \tag{1.108}$$

1.3.3 Vector multipole expansion of a general vectorial field

The expansion of a vector plane wave can now be used to expand a general vector field $\boldsymbol{F}(\boldsymbol{r})$, that satisfies the vector Helmholtz equation and is divergence free inside a region, into multipoles

$$\boldsymbol{F}(\boldsymbol{r}+\boldsymbol{r}') = \sum_{l,m} \left[a_{l,m}(\boldsymbol{r}') \boldsymbol{M}^j_{l,m}(k\boldsymbol{r}) + b_{l,m}(\boldsymbol{r}') \boldsymbol{N}^j_{l,m}(k\boldsymbol{r}) \right]. \tag{1.109}$$

The convergence radius of this series is again dictated by the point nearest to $\boldsymbol{r}'$ where $\left[\check{\boldsymbol{\nabla}}^2 + k^2\right] \boldsymbol{F}(\boldsymbol{r}+\boldsymbol{r}') \neq 0$. The determination of $a_{l,m}$ and $b_{l,m}$ is completely analogous to the one used in (1.2.4) and yields

$$a_{l,m}(\boldsymbol{r}') = 4\pi j^{-l}(-1)^{m+1} \boldsymbol{X}_{l,-m}\left(\frac{\check{\boldsymbol{\nabla}}'}{-jk}\right) \cdot \boldsymbol{F}(\boldsymbol{r}'), \tag{1.110}$$

$$b_{l,m}(\boldsymbol{r}') = 4\pi j^{-l+1}(-1)^{m+1} \boldsymbol{W}_{l,-m}\left(\frac{\check{\boldsymbol{\nabla}}'}{-jk}\right) \cdot \boldsymbol{F}(\boldsymbol{r}'). \tag{1.111}$$

An alternative way of expanding a general field in regular vector multipoles is by means of the orthogonality properties of the vector spherical harmonics. Taking the

dot product of Eqn. (1.109) with $\boldsymbol{X}^*_{l',m'}(\hat{\boldsymbol{r}})$ and $\boldsymbol{W}^*_{l',m'}(\hat{\boldsymbol{r}})$ and integrating yields

$$j_{l'}(kr)\, a_{l',m'}(\boldsymbol{r}') = \int_{\mathcal{S}_2} \boldsymbol{X}^*_{l',m'}(\hat{\boldsymbol{r}}) \cdot \boldsymbol{F}(\boldsymbol{r}+\boldsymbol{r}')\mathrm{d}\hat{\boldsymbol{r}} \tag{1.112}$$

$$\mathcal{J}_{l'}(kr)\, b_{l',m'}(\boldsymbol{r}') = \int_{\mathcal{S}_2} \boldsymbol{W}^*_{l',m'}(\hat{\boldsymbol{r}}) \cdot \boldsymbol{F}(\boldsymbol{r}+\boldsymbol{r}')\mathrm{d}\hat{\boldsymbol{r}} \tag{1.113}$$

It should be noted that although the integration is over the unit sphere, the argument of $\boldsymbol{F}(\boldsymbol{r}+\boldsymbol{r}')$ still contains r as a free parameter, since

$$\int_{\mathcal{S}_2} \boldsymbol{F}(\boldsymbol{r}+\boldsymbol{r}')\mathrm{d}\hat{\boldsymbol{r}} = \int_0^{2\pi}\int_0^{\pi} \boldsymbol{F}(r\hat{\boldsymbol{r}}(\theta,\phi)+\boldsymbol{r}')\sin\theta \mathrm{d}\theta\mathrm{d}\phi. \tag{1.114}$$

Therefore r can be chosen such that the integration domain falls within the convergence radius of (1.109).

1.3.4 Vector multipole expansion of the Green dyadics

Equations (1.110) and (1.111) will now be used to expand the electric Green dyadic in vector multipoles. This is easiest by means of the integral representation (1.44)

$$\mathsf{G}_e(\boldsymbol{r}+\boldsymbol{r}') = -\frac{k\omega\mu}{8\pi^2}\int_{\mathcal{E}} \left[\mathbb{1} - \hat{\boldsymbol{k}}\hat{\boldsymbol{k}}\right] e^{-jk\hat{\boldsymbol{k}}\cdot(\boldsymbol{r}+\boldsymbol{r}')}\mathrm{d}\hat{\boldsymbol{k}}. \tag{1.115}$$

Since

$$\boldsymbol{X}_{l,m}\left(\hat{\boldsymbol{k}}\right)\cdot\left[\mathbb{1} - \hat{\boldsymbol{k}}\hat{\boldsymbol{k}}\right] = \boldsymbol{X}_{l,m}\left(\hat{\boldsymbol{k}}\right), \tag{1.116}$$

$$\boldsymbol{W}_{l,m}\left(\hat{\boldsymbol{k}}\right)\cdot\left[\mathbb{1} - \hat{\boldsymbol{k}}\hat{\boldsymbol{k}}\right] = \boldsymbol{W}_{l,m}\left(\hat{\boldsymbol{k}}\right), \tag{1.117}$$

this becomes

$$a_{l,m}(\boldsymbol{r}') = -k\omega\mu(-1)^{m+1}\boldsymbol{M}^h_{l,-m}(-k\boldsymbol{r}'), \tag{1.118}$$

$$b_{l,m}(\boldsymbol{r}') = -k\omega\mu(-1)^{m+1}\boldsymbol{N}^h_{l,-m}(-k\boldsymbol{r}'). \tag{1.119}$$

Written out, and replacing $\boldsymbol{r}'$ with $-\boldsymbol{r}'$, this becomes

$$\mathsf{G}_e(\boldsymbol{r}-\boldsymbol{r}') = -k\omega\mu\sum_{l,m}(-1)^{m+1}\Big[\boldsymbol{M}^h_{l,-m}(k\boldsymbol{r}')\,\boldsymbol{M}^j_{l,m}(k\boldsymbol{r}) + \boldsymbol{N}^h_{l,-m}(k\boldsymbol{r}')\,\boldsymbol{N}^j_{l,m}(k\boldsymbol{r})\Big]. \tag{1.120}$$

Since the electric Green dyadic corresponds to a source located at $\boldsymbol{r} = \boldsymbol{r}'$, the inequality $r < r'$ must hold converge for convergence. Simply exchanging $\boldsymbol{r}$ and $\boldsymbol{r}'$ in

(1.120) thus yields a series that converges in the region where $r > r'$

$$\mathsf{G}_e(\boldsymbol{r}-\boldsymbol{r}') = -k\omega\mu\sum_{l,m}(-1)^{m+1}\Big[\boldsymbol{M}^h_{l,-m}(k\boldsymbol{r})\,\boldsymbol{M}^j_{l,m}(k\boldsymbol{r}') + \boldsymbol{N}^h_{l,-m}(k\boldsymbol{r})\,\boldsymbol{N}^j_{l,m}(k\boldsymbol{r}')\Big], \tag{1.121}$$

which can be interpreted as an expansion in the singular vector multipoles. The vector multipole expansion of the magnetic Green dyadic can be easily obtained by applying $-\frac{1}{j\omega\mu}\check{\boldsymbol{\nabla}}\times$ to (1.120) and (1.121) and using (1.85) and (1.86).

The limit of the vector multipole expansion of the electric Green dyadic (1.120) for $r \to 0$ can be taken. In this way, an expression is obtained that is valid for all r'. Since $j_l(0) = 0\ \forall l \neq 0$, the limit of $\boldsymbol{M}^j_{l,m}(k\boldsymbol{r})$ is zero. For the same reason, only the $l = 1$ terms remain of those containing $\boldsymbol{N}^j_{l,m}(k\boldsymbol{r})$ and the electric Green dyadic is given by

$$\mathsf{G}_e(\boldsymbol{r}') = -k\omega\mu\sum_{m=-1}^{1}(-1)^{m+1}\boldsymbol{N}^h_{1,-m}(k\boldsymbol{r}')\,\boldsymbol{N}^j_{1,m}(\boldsymbol{0}), \tag{1.122}$$

with the $\boldsymbol{N}^j_{1,m}(\boldsymbol{0})$ given by

$$\boldsymbol{N}^j_{1,-1}(\boldsymbol{0}) = j\sqrt{\frac{1}{12\pi}}(\hat{\boldsymbol{e}}_x - j\hat{\boldsymbol{e}}_y), \tag{1.123}$$

$$\boldsymbol{N}^j_{1,0}(\boldsymbol{0}) = j\sqrt{\frac{1}{6\pi}}\hat{\boldsymbol{e}}_z, \tag{1.124}$$

$$\boldsymbol{N}^j_{1,1}(\boldsymbol{0}) = -j\sqrt{\frac{1}{12\pi}}(\hat{\boldsymbol{e}}_x + j\hat{\boldsymbol{e}}_y). \tag{1.125}$$

1.3.5 Vector translation matrices

As was done for the scalar case, the translation matrices for vectorial fields will now be determined. The vector translation matrices are defined as

$$\boldsymbol{M}^f_{l_1,m_1}(k(\boldsymbol{r}+\boldsymbol{r}')) = \sum_{l_2,m_2}\Big[\Big[\alpha^f_{MM}(k\boldsymbol{r}')\Big]_{l_2,m_2;l_1,m_1}\boldsymbol{M}^j_{l_2,m_2}(k\boldsymbol{r}) + \Big[\alpha^f_{MN}(k\boldsymbol{r}')\Big]_{l_2,m_2;l_1,m_1}\boldsymbol{N}^j_{l_2,m_2}(k\boldsymbol{r})\Big], \tag{1.126}$$

$$\boldsymbol{N}^f_{l_1,m_1}\left(k\left(\boldsymbol{r}+\boldsymbol{r}'\right)\right) = \sum_{l_2,m_2}\left[\left[\alpha^f_{NM}(k\boldsymbol{r}')\right]_{l_2,m_2;l_1,m_1}\boldsymbol{M}^j_{l_2,m_2}\left(k\boldsymbol{r}\right) + \left[\alpha^f_{NN}(k\boldsymbol{r}')\right]_{l_2,m_2;l_1,m_1}\boldsymbol{N}^j_{l_2,m_2}\left(k\boldsymbol{r}\right)\right]. \quad (1.127)$$

Again, the convergence radius is infinite or r' for $f = j$ respectively $f = h$. Since the vector multipoles are orthogonal (with respect to integration of the angular part over the unit sphere), taking the curl of the the first equation must yield the second equation. Therefore

$$\alpha^f_{MM}(k\boldsymbol{r}') = \alpha^f_{NN}(k\boldsymbol{r}') \quad (1.128)$$

$$\alpha^f_{MN}(k\boldsymbol{r}') = \alpha^f_{NM}(k\boldsymbol{r}') \quad (1.129)$$

By means of (1.110) and (1.111), the remaining matrices are easily found

$$\left[\alpha^f_{MM}(k\boldsymbol{r}')\right]_{l_2,m_2;l_1,m_1} = 4\pi j^{l_1-l_2}(-1)^{m_2+1}\boldsymbol{X}_{l_2,-m_2}\left(\frac{\check{\boldsymbol{\nabla}}'}{-jk}\right)\cdot\boldsymbol{X}_{l_1,m_1}\left(\frac{\check{\boldsymbol{\nabla}}'}{-jk}\right)f_0(kr'), \quad (1.130)$$

$$\left[\alpha^f_{MN}(k\boldsymbol{r}')\right]_{l_2,m_2;l_1,m_1} = 4\pi j^{l_1-l_2+1}(-1)^{m_2+1}\boldsymbol{W}_{l_2,-m_2}\left(\frac{\check{\boldsymbol{\nabla}}'}{-jk}\right)\cdot\boldsymbol{X}_{l_1,m_1}\left(\frac{\check{\boldsymbol{\nabla}}'}{-jk}\right)f_0(kr'). \quad (1.131)$$

To evaluate the product of two vector spherical wave operators in $\alpha^f_{MM}(k\boldsymbol{r}')$, Eqn. (A.84) can be used

$$\left[\alpha^f_{MM}(k\boldsymbol{r}')\right]_{l_2,m_2;l_1,m_1} = 4\pi\sum_{l_3,m_3} j^{l_1-l_2-l_3}(-1)^{m_2+m_3+1}\mathcal{B}_{l_1,m_1;l_2,-m_2;l_3,-m_3}Z^f_{l_3,m_3}\left(k\boldsymbol{r}'\right). \quad (1.132)$$

Evaluating the product in $\alpha^f_{MN}(k\boldsymbol{r}')$ is more complicated. Using Eqn. (A.83) and the integral representation of the spherical Hankel function, Eqn. (1.131) becomes

$$\begin{aligned}\frac{1}{2}j^{-l_1+l_2-1}(-1)^{m_2+1}&\left[\alpha^f_{MN}(k\boldsymbol{r}')\right]_{l_2,m_2;l_1,m_1}\\ &= \int_{\mathcal{E}} \boldsymbol{W}_{l_2,-m_2}\left(\hat{\boldsymbol{k}}\right)\cdot\boldsymbol{X}_{l_1,m_1}\left(\hat{\boldsymbol{k}}\right)e^{-jk\hat{\boldsymbol{k}}\cdot\boldsymbol{r}'}\mathrm{d}\hat{\boldsymbol{k}}, \qquad (1.133)\\ &= \frac{-jk}{\sqrt{l_1(l_1+1)}}\int_{\mathcal{E}}\check{\boldsymbol{\nabla}}_{\boldsymbol{k}}\cdot\left[\boldsymbol{X}_{l_2,-m_2}\left(\hat{\boldsymbol{k}}\right)Y_{l_1,m_1}\left(\hat{\boldsymbol{k}}\right)\right]e^{-jk\hat{\boldsymbol{k}}\cdot\boldsymbol{r}'}\mathrm{d}\hat{\boldsymbol{k}}. \qquad (1.134)\end{aligned}$$

Here, $\check{\boldsymbol{\nabla}}_{\boldsymbol{k}}\cdot$ is the divergence operator with respect to $\boldsymbol{k}$. Since the expression between brackets depends only on $\hat{\boldsymbol{k}}$, only the angular derivatives remain when this operator is expressed in spherical coordinates. Partial integration then yields

$$\begin{aligned}\frac{1}{2}j^{-l_1+l_2-1}(-1)^{m_2+1}&\left[\alpha^f_{MN}(k\boldsymbol{r}')\right]_{l_2,m_2;l_1,m_1}\\ &= \frac{-k\boldsymbol{r}'}{\sqrt{l_1(l_1+1)}}\cdot\int_{\mathcal{E}}\boldsymbol{X}_{l_2,-m_2}\left(\hat{\boldsymbol{k}}\right)Y_{l_1,m_1}\left(\hat{\boldsymbol{k}}\right)e^{-jk\hat{\boldsymbol{k}}\cdot\boldsymbol{r}'}\mathrm{d}\hat{\boldsymbol{k}}. \qquad (1.135)\end{aligned}$$

This integral can be evaluated by means of Eqn. (A.86) and (A.26)

$$\begin{aligned}&\left[\alpha^f_{MN}(k\boldsymbol{r}')\right]_{l_2,m_2;l_1,m_1}\\ &\quad= \frac{-jk\boldsymbol{r}'\cdot\mathsf{M}^H}{\sqrt{l_1(l_1+1)l_2(l_2+1)}}\cdot\begin{bmatrix}\frac{\lambda^+_{l_2,m_2}}{\sqrt{2}}\left[\alpha^f(k\boldsymbol{r}')\right]_{l_2,m_2+1;l_1,m_1}\\ m_2\left[\alpha^f(k\boldsymbol{r}')\right]_{l_2,m_2;l_1,m_1}\\ -\frac{\lambda^-_{l_2,m_2}}{\sqrt{2}}\left[\alpha^f(k\boldsymbol{r}')\right]_{l_2,m_2-1;l_1,m_1}\end{bmatrix}, \qquad (1.136)\end{aligned}$$

where $\alpha^f(k\boldsymbol{r}')$ is the scalar translation matrix (1.65).

Bibliography

[1] J. Van Bladel. *Electromagnetic Fields*. Electrical and Electronic Engineering. McGraw-Hill, New-York, 1964.

[2] B. Carrascal and G.A. Estévez and Peilian Lee and V. Lorenzo. Vector spherical harmonics and their application to classical electrodynamics. *European Journal of Physics*, 12(4):184–191, Jul 1991.

[3] W.C. Chew, S. Koc, J.M. Song, C.C. Lu, and E. Michielssen. A succinct way to diagonalize the translation matrix in three dimensions. *Microwave and Optical Technology Letters*, 15(3):144–147, December 1998.

[4] R.C. Wittmann. Spherical wave operators and the translation formulas. *IEEE Transactions on Antennas and Propagation*, 36(8):1078–1087, Aug 1988.

[5] W.C. Chew. Vector addition theorem and its diagonalization. *Communications in Computational Physics*, 3(2):330–341, Feb 2008.

[6] James Clerk Maxwell. *A Treatise on Electricity and Magnetism*, volume 1&2. Dover Publications, Inc., New York, 3rd edition, 1954.

[7] W.C. Chew. Recurrence Relations for the Three-Dimensional Scalar Addition Theorem. *Journal of Electromagnetic Waves and Applications*, 6(2):133–142, 1992.

[8] J. Song, C.C. Lu, and W.C. Chew. Multilevel fast multipole algorithm for electromagnetic scattering by large complex objects. *IEEE Transactions on Antennas and Propagation*, 45(10):1488–1493, October 1997.

CHAPTER 2

Maxwell's Equations in the Presence of Scatterers

★★★

In the previous chapter, Maxwell's equations were solved in an infinitely large homogeneous isotropic medium. In this chapter, these results will be used to obtain the solution of Maxwell's equations in an environment containing a number of homogeneous regions. An example of such an environment is shown in Figure 2.1. Solving Maxwell's equations in such a geometry is generally done by using the equivalence theorem, proved in Section 2.2, to find the general solution of Maxwell's equations in each homogeneous region. Then the remaining degrees of freedom are tuned such that the boundary conditions, derived in Section 2.1, are met. First we will use this general methodology to derive the electric field integral equation. Secondly, the scattering off a homogeneous dielectric sphere will be solved and the result will be generalized to an equation that can be used when an arbitrary number of spheres are present. Thirdly this equation will be further generalized such that it also applies to a collection of objects whose circumscribed spheres do not overlap. This equation is widely known as the T-matrix or multiple scattering equation [1]. Finally, an analysis of the computational cost of solving this equation is made to illustrate the need for fast multipole methods (FMMs).

2.1 Boundary conditions

Boundary conditions are equations relating jumps in the fields to current and charge densities present at the jump. They are useful in many ways, for example in the derivation of the equivalence theorem and in the solution of Maxwell's equations in

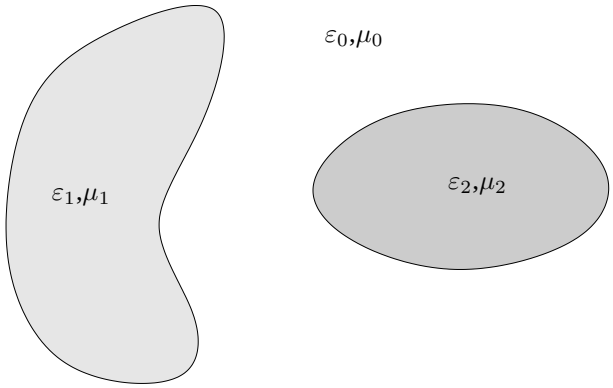

Figure 2.1: An example geometry consisting of homogeneous regions.

geometries containing sharp material boundaries. In the last case, the boundary conditions are used to 'glue' two solutions in different regions of space together such that their union satisfies Maxwell's equations.

Usually the boundary conditions are derived from the integral form of Maxwell's equations. However, here we will use an alternative, more direct approach. Consider the following two situations: the first situation is the entire space filled with a medium with parameters ε_1, μ_1 and the second situation is the entire space filled with a medium with parameters ε_2, μ_2. In space p, with $p \in \{1, 2\}$, the currents $\boldsymbol{j}_p(\boldsymbol{r})$, charges $\rho_p(\boldsymbol{r})$, electric fields $\boldsymbol{e}_p(\boldsymbol{r})$, magnetic fields $\boldsymbol{h}_p(\boldsymbol{r})$, electric inductions $\boldsymbol{d}_p(\boldsymbol{r})$ and magnetic inductions $\boldsymbol{b}_p(\boldsymbol{r})$ exist, all satisfying Maxwell's equations. Let $g(\boldsymbol{r})$ denote the real continuous function that is negative inside a region A, and positive in the complement of A, say region B. Now consider the situation where the medium parameters, currents and fields from the space 1 and 2 are used inside region A and region B respectively

$$\varepsilon = H\left[-g(\boldsymbol{r})\right]\varepsilon_1 + H\left[g(\boldsymbol{r})\right]\varepsilon_2, \tag{2.1}$$

$$\boldsymbol{e}(\boldsymbol{r}) = H\left[-g(\boldsymbol{r})\right]\boldsymbol{e}_1(\boldsymbol{r}) + H\left[g(\boldsymbol{r})\right]\boldsymbol{e}_2(\boldsymbol{r}), \tag{2.2}$$

and the same for μ, $\boldsymbol{h}$, $\boldsymbol{j}$, ρ, $\boldsymbol{d}$ and $\boldsymbol{b}$. Also, $H\left[\cdot\right]$ denotes the Heaviside function. This basically means that the two fields and media have been put next to each other at the interface defined by $g(\boldsymbol{r}) = 0$, thus creating a jump. Substituting the new fields and currents in Maxwell's equations immediately yields the so-called boundary conditions

$$\check{\boldsymbol{\nabla}} H\left[g(\boldsymbol{r})\right] \times \left[\boldsymbol{e}_2(\boldsymbol{r}) - \boldsymbol{e}_1(\boldsymbol{r})\right] = 0, \tag{2.3a}$$

$$\check{\boldsymbol{\nabla}} H\left[g(\boldsymbol{r})\right] \times \left[\boldsymbol{h}_2(\boldsymbol{r}) - \boldsymbol{h}_1(\boldsymbol{r})\right] = 0, \tag{2.3b}$$

$$\check{\boldsymbol{\nabla}} H\left[g(\boldsymbol{r})\right] \cdot \left[\boldsymbol{d}_2(\boldsymbol{r}) - \boldsymbol{d}_1(\boldsymbol{r})\right] = 0, \tag{2.3c}$$

$$\check{\boldsymbol{\nabla}} H\left[g(\boldsymbol{r})\right] \cdot \left[\boldsymbol{b}_2(\boldsymbol{r}) - \boldsymbol{b}_1(\boldsymbol{r})\right] = 0. \tag{2.3d}$$

Because $\check{\boldsymbol{\nabla}} g(\boldsymbol{r})$ is proportional to the external normal $\hat{\boldsymbol{n}}$ of region A, $\check{\boldsymbol{\nabla}} H\left[g(\boldsymbol{r})\right]$ can be written as

$$\check{\boldsymbol{\nabla}} H\left[g(\boldsymbol{r})\right] = \delta(g(\boldsymbol{r}))\check{\boldsymbol{\nabla}} g(\boldsymbol{r}), \tag{2.4}$$

$$= \hat{\boldsymbol{n}}\delta(g(\boldsymbol{r}))\frac{\partial}{\partial n} g(\boldsymbol{r}). \tag{2.5}$$

The factor $\delta(g(\boldsymbol{r}))\frac{\partial}{\partial n} g(\boldsymbol{r})$ is a function that differs from zero only on the interface. Actually it represents a δ distribution in the normal direction. Indeed, if $\boldsymbol{r}_s$ is a point on the interface and ϵ is a small positive number

$$\int_{-\epsilon}^{\epsilon} \delta(g(t\hat{\boldsymbol{n}} + \boldsymbol{r}_s))\frac{\mathrm{d}}{\mathrm{d}t} g(t\hat{\boldsymbol{n}} + \boldsymbol{r}_s)\mathrm{d}t = 1. \tag{2.6}$$

Applying this integration to Eqns. (2.3a), (2.3b), (2.3c) and (2.3d) yields the familiar expressions

$$\hat{\boldsymbol{n}} \times \left[\boldsymbol{e}_2(\boldsymbol{r}_s) - \boldsymbol{e}_1(\boldsymbol{r}_s)\right] = 0, \tag{2.7a}$$

$$\hat{\boldsymbol{n}} \times \left[\boldsymbol{h}_2(\boldsymbol{r}_s) - \boldsymbol{h}_1(\boldsymbol{r}_s)\right] = 0, \tag{2.7b}$$

$$\hat{\boldsymbol{n}} \cdot \left[\boldsymbol{d}_2(\boldsymbol{r}_s) - \boldsymbol{d}_1(\boldsymbol{r}_s)\right] = 0, \tag{2.7c}$$

$$\hat{\boldsymbol{n}} \cdot \left[\boldsymbol{b}_2(\boldsymbol{r}_s) - \boldsymbol{b}_1(\boldsymbol{r}_s)\right] = 0, \tag{2.7d}$$

which state that the tangential components of the electric and magnetic field, and the normal components of the electric and magnetic induction must be continuous.

When the fields do not satisfy these boundary conditions (2.7), Maxwell's equations can only be satisfied by introducing additional electric and magnetic surface currents and charges

$$\check{\boldsymbol{\nabla}} \times \boldsymbol{e}(\boldsymbol{r}) = -j\omega\boldsymbol{b}(\boldsymbol{r}) - \boldsymbol{m}'(\boldsymbol{r}), \tag{2.8a}$$

$$\check{\boldsymbol{\nabla}} \times \boldsymbol{h}(\boldsymbol{r}) = j\omega\boldsymbol{d}(\boldsymbol{r}) + \boldsymbol{j}(\boldsymbol{r}) + \boldsymbol{j}'(\boldsymbol{r}), \tag{2.8b}$$

$$\check{\boldsymbol{\nabla}} \cdot \boldsymbol{d}(\boldsymbol{r}) = \rho(\boldsymbol{r}) + \rho'(\boldsymbol{r}), \tag{2.8c}$$

$$\check{\boldsymbol{\nabla}} \cdot \boldsymbol{b}(\boldsymbol{r}) = \pi'(\boldsymbol{r}). \tag{2.8d}$$

which leads to the more general boundary conditions

$$\hat{\boldsymbol{n}} \times \left[\boldsymbol{e}_2(\boldsymbol{r}_s) - \boldsymbol{e}_1(\boldsymbol{r}_s)\right] = -\boldsymbol{m}'_s(\boldsymbol{r}_s), \tag{2.9}$$

$$\hat{\boldsymbol{n}} \times \left[\boldsymbol{h}_2(\boldsymbol{r}_s) - \boldsymbol{h}_1(\boldsymbol{r}_s)\right] = \boldsymbol{j}'_s(\boldsymbol{r}_s), \tag{2.10}$$

$$\hat{\boldsymbol{n}} \cdot \left[\boldsymbol{d}_2(\boldsymbol{r}_s) - \boldsymbol{d}_1(\boldsymbol{r}_s)\right] = \rho'_s(\boldsymbol{r}_s), \tag{2.11}$$

$$\hat{\boldsymbol{n}} \cdot \left[\boldsymbol{b}_2(\boldsymbol{r}_s) - \boldsymbol{b}_1(\boldsymbol{r}_s)\right] = \pi'_s(\boldsymbol{r}_s). \tag{2.12}$$

Here, the subscript s means that the quantity has been integrated across the interface as in Eqn. (2.6). It can be shown that, using the law of conservation of magnetic charge

$$\check{\boldsymbol{\nabla}} \cdot \boldsymbol{m}'(\boldsymbol{r}) = -j\omega\pi'(\boldsymbol{r}), \tag{2.13}$$

Eqns. (2.11) and (2.12) follow from Eqns. (2.10) and (2.9) respectively. This allows the usage of (2.9) and (2.10) as the only boundary conditions, since the two other ones are necessarily fulfilled.

2.2 The equivalence theorem

Using the boundary conditions derived in the previous section, it is possible to prove the so-called equivalence theorem. This theorem states that it is possible to replace any object by the following equivalent electric and magnetic surface current distribution on its surface

$$\boldsymbol{j}_s(\boldsymbol{r}_s) = \hat{\boldsymbol{n}} \times \boldsymbol{h}(\boldsymbol{r}_s), \tag{2.14}$$

$$\boldsymbol{m}_s(\boldsymbol{r}_s) = -\hat{\boldsymbol{n}} \times \boldsymbol{e}(\boldsymbol{r}_s), \tag{2.15}$$

where $\boldsymbol{r}_s$ denotes a point on the surface, $\hat{\boldsymbol{n}}$ is the external normal and the fields inside the surface are zero. To prove the theorem, we need only to show that this new field configuration constitutes a solution of Maxwell's equations. The fields inside the surface are zero and the fields outside of the surface are left unchanged. Clearly this field configuration solves Maxwell's equations inside and outside of the surface. Additionally, the boundary conditions (2.9) and (2.10) are satisfied because of the presence of currents (2.14) and (2.15). As was mentioned in 2.1, this guarantees that boundary conditions (2.11) and (2.12) are also satisfied. As a consequence Maxwell's equations are satisfied everywhere, which by the uniqueness of the solution proves the equivalence theorem.

The equivalence theorem can be used to replace scatterers with equivalent currents, so that in the region where the fields are now zero, the scatterer can be harmlessly replaced by free space. This in turn allows the use of the free space Green function for the evaluation of the fields associated with the equivalent and source currents.

2.3 The electric field integral equation

Here, the equivalence theorem will be used to derive the so-called electric field integral equation (EFIE). This equation can be used to solve the scattering off perfect electrically conducting (PEC) targets. A perfect electrically conducting surface has the property that the tangential electric field must be zero. Indeed, if this were not

the case, the current running on the PEC target would become infinite. Now apply the equivalence theorem to the surface of the PEC target. Because the tangential electric field is zero, no magnetic current (2.15) is required to represent the fields outside. Therefore the most general possible form of the electric field outside of the PEC is given by

$$\boldsymbol{e}(\boldsymbol{r}) = \boldsymbol{e}^{sco}(\boldsymbol{r}) + \int_S \mathsf{G}_e(\boldsymbol{r}-\boldsymbol{r}')\boldsymbol{j}_s(\boldsymbol{r}')\mathrm{d}S'. \tag{2.16}$$

The term $\boldsymbol{e}^{sco}(\boldsymbol{r})$ is added because the equivalent currents are not the only currents; there are also source currents, that illuminate the PEC target. The EFIE is then obtained by setting the total tangential field to zero

$$\hat{\boldsymbol{n}} \times \boldsymbol{e}^{sco}(\boldsymbol{r}) = -\hat{\boldsymbol{n}} \times \int_S \mathsf{G}_e(\boldsymbol{r}-\boldsymbol{r}')\boldsymbol{j}_s(\boldsymbol{r}')\mathrm{d}S'. \tag{2.17}$$

When this equation is properly discretized, the surface current $\boldsymbol{j}_s(\boldsymbol{r}')$ can be found by solving a system of linear equations.

2.4 The multiple scattering equation

Another important equation is the so-called multiple scattering equation [1]. It is used to solve problems consisting of a collection of objects whose circumscribed spheres do not overlap. To arrive at the equation, the analytical solution of one sphere will be determined, after which this result will be used to construct an equation for the scattering problem with many spheres. This equation is then further generalized to support other objects than spheres.

2.4.1 Analytical solution of a homogeneous sphere

Using boundary conditions (2.7), the analytic solution of Maxwell's equations in the presence of a dielectric sphere will now be derived. The analytical solution of a homogeneous sphere was first derived by Gustav Mie [2], after whom a 104km wide crater on Mars is named. However, the derivation will be repeated here using the conventions and definitions used in this work. Assume that a spherical region with radius a and centered around the origin is comprised of a material with permittivity ε_i, permeability μ_i, impedance Z_i and wavenumber k_i. The subscript i stands for 'inside'. The medium outside the sphere has permittivity ε_o, permeability μ_o, impedance Z_o and wavenumber k_o, where the subscript o has the obvious meaning 'outside'. Now assume that an electromagnetic field, generated by sources outside the sphere, impinges on the sphere. Due to the equivalence theorem, the sphere can be replaced by tangential electric and magnetic currents $\boldsymbol{j}_s(a\hat{\boldsymbol{r}})$ and $\boldsymbol{m}_s(a\hat{\boldsymbol{r}})$ on its surface. These currents

generate the so-called scattered field of the sphere. Because the currents are tangential, they can always be written as a superposition of vector spherical harmonics. This in turn leads to the conclusion that the scattered field must have the following form

$$\begin{aligned}\boldsymbol{e}^{sca}(\boldsymbol{r}) = &\sum_{l,m}\left[a^{sca}_{l,m}\boldsymbol{M}^{h}_{l,m}\left(k_o\boldsymbol{r}\right) + b^{sca}_{l,m}\boldsymbol{N}^{h}_{l,m}\left(k_o\boldsymbol{r}\right)\right] \\ &+ \sum_{l,m}\left[c^{sca}_{l,m}\boldsymbol{M}^{j}_{l,m}\left(k_o\boldsymbol{r}\right) + d^{sca}_{l,m}\boldsymbol{N}^{j}_{l,m}\left(k_o\boldsymbol{r}\right)\right].\end{aligned} \tag{2.18}$$

However, this field has to satisfy the radiation condition. Therefore the sum over the regular multipoles must be omitted and the scattered field has the following most general form

$$\boldsymbol{e}^{sca}(\boldsymbol{r}) = \sum_{l,m}\left[a^{sca}_{l,m}\boldsymbol{M}^{h}_{l,m}\left(k_o\boldsymbol{r}\right) + b^{sca}_{l,m}\boldsymbol{N}^{h}_{l,m}\left(k_o\boldsymbol{r}\right)\right]. \tag{2.19}$$

The source field is known and regular since the sources are assumed to be known and located outside of the sphere. It can therefore be expanded in regular multipoles centered around the origin

$$\boldsymbol{e}^{sco}(\boldsymbol{r}) = \sum_{l,m}\left[a^{sco}_{l,m}\boldsymbol{M}^{j}_{l,m}\left(k_o\boldsymbol{r}\right) + b^{sco}_{l,m}\boldsymbol{N}^{j}_{l,m}\left(k_o\boldsymbol{r}\right)\right]. \tag{2.20}$$

The electric field inside the sphere $\boldsymbol{e}^{i}(\boldsymbol{r})$ has to be regular, again because there are no sources in the sphere. Using the equivalence theorem to set the fields outside of the sphere to zero then yields the following most general form

$$\boldsymbol{e}^{i}(\boldsymbol{r}) = \sum_{l,m}\left[a^{i}_{l,m}\boldsymbol{M}^{j}_{l,m}\left(k_i\boldsymbol{r}\right) + b^{i}_{l,m}\boldsymbol{N}^{j}_{l,m}\left(k_i\boldsymbol{r}\right)\right]. \tag{2.21}$$

The magnetic fields are then easily obtained in both regions by means of curl equations (1.86), (1.85) and (1.11b)

$$\boldsymbol{h}^{sco}(\boldsymbol{r}) = \frac{j}{Z_o}\sum_{l,m}\left[b^{sco}_{l,m}\boldsymbol{M}^{j}_{l,m}\left(k_o\boldsymbol{r}\right) + a^{sco}_{l,m}\boldsymbol{N}^{j}_{l,m}\left(k_o\boldsymbol{r}\right)\right], \tag{2.22}$$

$$\boldsymbol{h}^{sca}(\boldsymbol{r}) = \frac{j}{Z_o}\sum_{l,m}\left[b^{sca}_{l,m}\boldsymbol{M}^{h}_{l,m}\left(k_o\boldsymbol{r}\right) + a^{sca}_{l,m}\boldsymbol{N}^{h}_{l,m}\left(k_o\boldsymbol{r}\right)\right], \tag{2.23}$$

$$\boldsymbol{h}^{i}(\boldsymbol{r}) = \frac{j}{Z_i}\sum_{l,m}\left[b^{i}_{l,m}\boldsymbol{M}^{j}_{l,m}\left(k_i\boldsymbol{r}\right) + a^{i}_{l,m}\boldsymbol{N}^{j}_{l,m}\left(k_i\boldsymbol{r}\right)\right]. \tag{2.24}$$

Imposing the boundary conditions (2.7a) and (2.7b)

$$\hat{\boldsymbol{r}} \times [\boldsymbol{e}^{sco}(a\hat{\boldsymbol{r}}) + \boldsymbol{e}^{sca}(a\hat{\boldsymbol{r}})] = \hat{\boldsymbol{r}} \times \boldsymbol{e}^{i}(a\hat{\boldsymbol{r}}) \ \ \forall \hat{\boldsymbol{r}}, \tag{2.25}$$

$$\hat{\boldsymbol{r}} \times [\boldsymbol{h}^{sco}(a\hat{\boldsymbol{r}}) + \boldsymbol{h}^{sca}(a\hat{\boldsymbol{r}})] = \hat{\boldsymbol{r}} \times \boldsymbol{h}^{i}(a\hat{\boldsymbol{r}}) \ \ \forall \hat{\boldsymbol{r}}, \tag{2.26}$$

can be done by taking the dot product of both sides with $\boldsymbol{X}_{l,m}(\hat{\boldsymbol{r}})$ and $\boldsymbol{W}_{l,m}(\hat{\boldsymbol{r}})$ and integrating. For the electric field this yields

$$a^{sco}_{l,m} j_l(k_o a) + a^{sca}_{l,m} h^{(2)}_l(k_o a) = a^{i}_{l,m} j_l(k_i a), \tag{2.27}$$

$$b^{sco}_{l,m} \mathcal{J}_l(k_o a) + b^{sca}_{l,m} \mathcal{H}^{(2)}_l(k_o a) = b^{i}_{l,m} \mathcal{J}_l(k_i a), \tag{2.28}$$

while the magnetic field gives

$$b^{sco}_{l,m} Z_i j_l(k_o a) + b^{sca}_{l,m} Z_i h^{(2)}_l(k_o a) = b^{i}_{l,m} Z_o j_l(k_i a), \tag{2.29}$$

$$a^{sco}_{l,m} Z_i \mathcal{J}_l(k_o a) + a^{sca}_{l,m} Z_i \mathcal{H}^{(2)}_l(k_o a) = a^{i}_{l,m} Z_o \mathcal{J}_l(k_i a). \tag{2.30}$$

Elimination of the 'inside' coefficients $a^i_{l,m}$ and $b^i_{l,m}$ yields

$$b^{sco}_{l,m} \frac{\mathcal{J}_l(k_o a)}{\mathcal{J}_l(k_i a)} + b^{sca}_{l,m} \frac{\mathcal{H}^{(2)}_l(k_o a)}{\mathcal{J}_l(k_i a)} = b^{sco}_{l,m} \frac{Z_i j_l(k_o a)}{Z_o j_l(k_i a)} + b^{sca}_{l,m} \frac{Z_i h^{(2)}_l(k_o a)}{Z_o j_l(k_i a)}, \tag{2.31}$$

$$a^{sco}_{l,m} \frac{\mathcal{J}_l(k_o a)}{\mathcal{J}_l(k_i a)} + a^{sca}_{l,m} \frac{\mathcal{H}^{(2)}_l(k_o a)}{\mathcal{J}_l(k_i a)} = a^{sco}_{l,m} \frac{Z_o j_l(k_o a)}{Z_i j_l(k_i a)} + a^{sca}_{l,m} \frac{Z_o h^{(2)}_l(k_o a)}{Z_i j_l(k_i a)}. \tag{2.32}$$

This can be cast into

$$\frac{a^{sca}_{l,m}}{a^{sco}_{l,m}} = T^M_l = -\frac{Z_i \frac{\mathcal{J}_l(k_o a)}{j_l(k_o a)} - Z_o \frac{\mathcal{J}_l(k_i a)}{j_l(k_i a)}}{Z_i \frac{\mathcal{H}^{(2)}_l(k_o a)}{j_l(k_o a)} - Z_o \frac{\mathcal{J}_l(k_i a)}{j_l(k_i a)} \frac{h^{(2)}_l(k_o a)}{j_l(k_o a)}}, \tag{2.33}$$

$$\frac{b^{sca}_{l,m}}{b^{sco}_{l,m}} = T^N_l = -\frac{Z_o \frac{\mathcal{J}_l(k_o a)}{j_l(k_o a)} - Z_i \frac{\mathcal{J}_l(k_i a)}{j_l(k_i a)}}{Z_o \frac{\mathcal{H}^{(2)}_l(k_o a)}{j_l(k_o a)} - Z_i \frac{\mathcal{J}_l(k_i a)}{j_l(k_i a)} \frac{h^{(2)}_l(k_o a)}{j_l(k_o a)}}. \tag{2.34}$$

The knowledge of the multipole expansion of the source field thus yields the knowledge of the scattered field. In other words, the total field is known. The coefficients $a^i_{l,m}$ and $b^i_{l,m}$ and thus the fields inside the sphere are also easily calculated using Eqns. (2.27) and (2.28). For a perfect electrically conducting sphere, the fields inside

the sphere are identically zero, yielding the simpler expressions

$$\frac{a_{l,m}^{sca}}{a_{l,m}^{sco}} = -\frac{j_l\left(k_o a\right)}{h_l^{(2)}\left(k_o a\right)}, \tag{2.35}$$

$$\frac{b_{l,m}^{sca}}{b_{l,m}^{sco}} = -\frac{\mathcal{J}_l\left(k_o a\right)}{\mathcal{H}_l^{(2)}\left(k_o a\right)}. \tag{2.36}$$

2.4.2 The multiple scattering equation for homogeneous spheres

The results from the previous subsection allow the solution of Maxwell's equations in the presence of one homogeneous sphere. This result can be extended [1] to an environment with Q non-touching spheres, that have center $\boldsymbol{r}_n$ and radius a_n. The field generated by the source is now expanded around all the spheres

$$\boldsymbol{e}^{sco}(\boldsymbol{r}) = \sum_{l,m}\left[a_{n,l,m}^{sco}\boldsymbol{M}_{l,m}^{j}\left(k\left(\boldsymbol{r}-\boldsymbol{r}_n\right)\right) + b_{n,l,m}^{sco}\boldsymbol{N}_{l,m}^{j}\left(k\left(\boldsymbol{r}-\boldsymbol{r}_n\right)\right)\right]. \tag{2.37}$$

Assuming that the source is located outside of the spheres, this series converges in a spherical region around every sphere. However, the spheres feel not only the field from the source, but also the fields scattered by other spheres. The field scattered by the pth sphere can be determined with an argument similar to the one used in 2.4.1 and is given by

$$\boldsymbol{e}_p^{sca}(\boldsymbol{r}) = \sum_{l,m}\left[a_{p,l,m}^{sca}\boldsymbol{M}_{l,m}^{h}\left(k\left(\boldsymbol{r}-\boldsymbol{r}_p\right)\right) + b_{p,l,m}^{sca}\boldsymbol{N}_{l,m}^{h}\left(k\left(\boldsymbol{r}-\boldsymbol{r}_p\right)\right)\right]. \tag{2.38}$$

This holds for all $||\boldsymbol{r}-\boldsymbol{r}_p|| > a_p$ with unknown $a_{p,l,m}^{sca}$ and $b_{p,l,m}^{sca}$. Because the spheres do not touch, this field is regular in a finite spherical region around every sphere and can thus be expanded in regular multipoles around the nth sphere center

$$\boldsymbol{e}_p^{sca}(\boldsymbol{r}) = \sum_{l,m}\left[a_{p,n,l,m}\boldsymbol{M}_{l,m}^{j}\left(k\left(\boldsymbol{r}-\boldsymbol{r}_n\right)\right) + b_{p,n,l,m}\boldsymbol{N}_{l,m}^{j}\left(k\left(\boldsymbol{r}-\boldsymbol{r}_n\right)\right)\right]. \tag{2.39}$$

where the coefficients $a_{p,n,l,m}$ and $b_{p,n,l,m}$ are obtained by means of the vector translation matrices from 1.3.5

$$a_{p,n,l,m} = \sum_{l',m'} \left[\left[\alpha^f_{MM}(k\,(\boldsymbol{r}_n - \boldsymbol{r}_p)) \right]_{l,m;l',m'} a^{sca}_{p,l',m'} + \left[\alpha^f_{MN}(k\,(\boldsymbol{r}_n - \boldsymbol{r}_p)) \right]_{l,m;l',m'} b^{sca}_{p,l',m'} \right], \tag{2.40}$$

$$b_{p,n,l,m} = \sum_{l',m'} \left[\left[\alpha^f_{NM}(k\,(\boldsymbol{r}_n - \boldsymbol{r}_p)) \right]_{l,m;l',m'} a^{sca}_{p,l',m'} + \left[\alpha^f_{NN}(k\,(\boldsymbol{r}_n - \boldsymbol{r}_p)) \right]_{l,m;l',m'} b^{sca}_{p,l',m'} \right]. \tag{2.41}$$

By means of (2.37) and (2.39), the total field impinging on the nth sphere can thus be written as

$$\boldsymbol{e}^{imp}_n(\boldsymbol{r}) = \sum_{p\neq n} \sum_{l,m} \left[\left[a^{sco}_{n,l,m} + a_{p,n,l,m} \right] \boldsymbol{M}^j_{l,m}\,(k\,(\boldsymbol{r} - \boldsymbol{r}_n)) + \left[b^{sco}_{n,l,m} + b_{p,n,l,m} \right] \boldsymbol{N}^j_{l,m}\,(k\,(\boldsymbol{r} - \boldsymbol{r}_n)) \right]. \tag{2.42}$$

Clearly, the fields scattered by the spheres determine the fields impinging on them. However, the scattered fields are still unknown. They can be determined by enforcing the boundary conditions on the surfaces of all the spheres. Using the results from 2.4.1

$$a^{sca}_{n,l,m} = T^M_{n,l} \left[\sum_{p\neq n} a_{p,n,l,m} + a^{sco}_{n,l,m} \right] \tag{2.43}$$

$$b^{sca}_{n,l,m} = T^N_{n,l} \left[\sum_{p\neq n} b_{p,n,l,m} + b^{sco}_{n,l,m} \right] \tag{2.44}$$

with $T^M_{n,l}$ and $T^N_{n,l}$ defined in (2.33) and (2.33). Putting all this together yields the multiple scattering equation

$$T^M_{n,l} a^{sco}_{n,l,m} = a^{sca}_{n,l,m} - T^M_{n,l} \sum_{p \neq n} \sum_{l',m'} \left[\left[\alpha^f_{MM}(k\,(\boldsymbol{r}_n - \boldsymbol{r}_p)) \right]_{l,m;l',m'} a^{sca}_{p,l',m'} + \left[\alpha^f_{MN}(k\,(\boldsymbol{r}_n - \boldsymbol{r}_p)) \right]_{l,m;l',m'} b^{sca}_{p,l',m'} \right], \tag{2.45}$$

$$T^N_{n,l} b^{sco}_{n,l,m} = b^{sca}_{n,l,m} - T^N_{n,l} \sum_{p \neq n} \sum_{l',m'} \left[\left[\alpha^f_{NM}(k\,(\boldsymbol{r}_n - \boldsymbol{r}_p)) \right]_{l,m;l',m'} a^{sca}_{p,l',m'} + \left[\alpha^f_{NN}(k\,(\boldsymbol{r}_n - \boldsymbol{r}_p)) \right]_{l,m;l',m'} b^{sca}_{p,l',m'} \right]. \tag{2.46}$$

The left hand side is known, and if the sums over l, m are truncated so the maximum value for l is L, the coefficients $a^{sca}_{n,l,m}$ and $b^{sca}_{n,l,m}$ can be determined by solving a system of linear equations of order $2Q(L+1)^2$. Once the solution of this system has been obtained, it is easily shown that the corresponding fields solve Maxwell's equations. Indeed, the field in the space between the spheres is a superposition of the source field and the scattered fields of the spheres, both solutions of Maxwell's equations. In addition, the boundary conditions are met because Eqns. (2.43) and (2.44) are satisfied. By the uniqueness of the solution of Maxwell's equations, the obtained solution is the solution of the many-spheres scattering problem.

2.4.3 The multiple scattering equation for other objects

It should be noted that the reasoning that led to the scattered field of a sphere (2.38), can be repeated unchangedly for more complicated objects. Indeed, assume that object n can be circumscribed by a sphere with radius a_n and center $\boldsymbol{c}_n$. Then simply apply the equivalence theorem to each object's circumscribing sphere and use the radiation condition to obtain the most general scattered field for the nth object

$$\boldsymbol{e}^{sca}_n(\boldsymbol{r}) = \sum_{l,m} \left[a^{sca}_{n,l,m} \boldsymbol{M}^h_{l,m}\,(k\,(\boldsymbol{r} - \boldsymbol{c}_n)) + b^{sca}_{n,l,m} \boldsymbol{N}^h_{l,m}\,(k\,(\boldsymbol{r} - \boldsymbol{c}_n)) \right]. \tag{2.47}$$

Then, can the multiple scattering equation be generalized to arbitrary objects? The answer is no, because the other crucial part of the equation is the re-expansion of this scattered field in regular multipoles centered around the other objects. For this series to converge, the objects' circumscribing spheres must not touch nor overlap. When this condition is met, it is clear that only Eqns. (2.43) and (2.44) must be altered to accommodate for the extra generality. Basically, Eqns. (2.43) and (2.44) are replaced

with the more general

$$a^{sca}_{n,l,m} = \sum_{l',m'} \left[\left[\mathsf{T}^{MM}_n \right]_{l,m;l',m'} a_{n,l',m'} + \left[\mathsf{T}^{MN}_n \right]_{l,m;l',m'} b_{n,l',m'} \right], \tag{2.48}$$

$$b^{sca}_{n,l,m} = \sum_{l',m'} \left[\left[\mathsf{T}^{NM}_n \right]_{l,m;l',m'} a_{n,l',m'} + \left[\mathsf{T}^{NN}_n \right]_{l,m;l',m'} b_{n,l',m'} \right]. \tag{2.49}$$

$$\tag{2.50}$$

with $a_{n,l,m} = \sum_{p \neq n} a_{p,n,l,m} + a^{sco}_{n,l,m}$ and $b_{n,l,m} = \sum_{p \neq n} b_{p,n,l,m} + b^{sco}_{n,l,m}$. The matrices T^{MM}_n, T^{MN}_n, T^{NM}_n and T^{NN}_n are blocks of the so-called T-matrix of the nth object.

The T-matrix of an object can usually not be determined analytically. However, numerically this can be done as follows. Let $\boldsymbol{c}$ and a be the center and radius of the circumscribing sphere of the object. Then calculate the scattered field of the object for all the incoming fields given by the regular vector multipoles $\boldsymbol{M}^j_{l,m}\left(k\left(\boldsymbol{r}-\boldsymbol{c}\right)\right)$ and $\boldsymbol{N}^j_{l,m}\left(k\left(\boldsymbol{r}-\boldsymbol{c}\right)\right)$. These scattered fields $\boldsymbol{e}^{sca,M}_{l,m}(\boldsymbol{r})$ and $\boldsymbol{e}^{sca,N}_{l,m}(\boldsymbol{r})$ can be decomposed in singular vector multipoles by means of

$$h^{(2)}_l(ka)\left[\mathsf{T}^{MM}\right]_{l,m;l',m'} = \int_{\mathcal{S}_2} \boldsymbol{X}^*_{l,m}(\hat{\boldsymbol{r}}) \cdot \boldsymbol{e}^{sca,M}_{l',m'}(\boldsymbol{c}+a\hat{\boldsymbol{r}}) \mathrm{d}\hat{\boldsymbol{r}}, \tag{2.51}$$

$$\mathcal{H}^{(2)}_l(ka)\left[\mathsf{T}^{NM}\right]_{l,m;l',m'} = \int_{\mathcal{S}_2} \boldsymbol{W}^*_{l,m}(\hat{\boldsymbol{r}}) \cdot \boldsymbol{e}^{sca,M}_{l',m'}(\boldsymbol{c}+a\hat{\boldsymbol{r}}) \mathrm{d}\hat{\boldsymbol{r}}, \tag{2.52}$$

$$h^{(2)}_l(ka)\left[\mathsf{T}^{MN}\right]_{l,m;l',m'} = \int_{\mathcal{S}_2} \boldsymbol{X}^*_{l,m}(\hat{\boldsymbol{r}}) \cdot \boldsymbol{e}^{sca,N}_{l',m'}(\boldsymbol{c}+a\hat{\boldsymbol{r}}) \mathrm{d}\hat{\boldsymbol{r}}, \tag{2.53}$$

$$\mathcal{H}^{(2)}_l(ka)\left[\mathsf{T}^{NN}\right]_{l,m;l',m'} = \int_{\mathcal{S}_2} \boldsymbol{W}^*_{l,m}(\hat{\boldsymbol{r}}) \cdot \boldsymbol{e}^{sca,N}_{l',m'}(\boldsymbol{c}+a\hat{\boldsymbol{r}}) \mathrm{d}\hat{\boldsymbol{r}}, \tag{2.54}$$

which uniquely determines the T-matrix.

2.5 The necessity of fast multipole methods

As shown in the previous section, the multiple scattering equation for Q spheres, where multipoles up to order L are taken into account, becomes a dense system of linear equations of order $N = 2Q(l+1)^2$

$$\mathsf{Z} \cdot \mathsf{x} = \mathsf{y}, \tag{2.55}$$

where Z is the $N \times N$ system matrix, x is the $N \times 1$ vector containing the unknowns and y is the $N \times 1$ vector containing the source fields. Clearly, when a large number of spheres are involved or a high accuracy is required, N becomes very large. Solving the linear system using direct methods, e.g. LU decomposition, is then not

feasible anymore because direct methods have an $\mathcal{O}\left(N^3\right)$ computational and $\mathcal{O}\left(N^2\right)$ memory complexity. The fact that the system is dense is caused by the fact that every sphere (observer sphere) receives fields from every other sphere (source sphere). This in turn is because the vector translation matrices (and their special cases, the Green dyadics) are nonzero throughout the entire space. This problem is thus not specific to the multiple scattering equation: any integral equation method in electromagnetism suffers from this complexity problem.

The application of iterative solvers, such as the biconjugate gradient method [3], can somewhat improve this situation. These methods start from a guess of the solution x_0, and evaluate its correctness by multiplying it with Z and checking the difference $\mathsf{Z} \cdot \mathsf{x}_0 - \mathsf{y}$. Based on a set of rules that is specific to the type of iterative solver used, a new guess x_1 is determined, which is usually closer to the actual solution than x_0. This procedure is then repeated until, in the Pth iteration, the residual error $||\mathsf{Z} \cdot \mathsf{x}_P - \mathsf{y}||$ has been reduced below a preset threshold. Since in each iteration, a number of multiplications of the system matrix Z with test vectors is required, the computational complexity of an iterative solution method is P times the complexity of a matrix-vector multiplication, i.e. $\mathcal{O}\left(PN^2\right)$. For well-conditioned problems, the number of iterations P is small, so that this indeed means a reduction of the computational cost.

Naturally, the aim then becomes to perform the matrix-vector multiplications as efficiently as possible. In the past, many fast algorithms have been developed for this purpose [4–10]. Fast multipole methods (FMMs) are arguably one of the most important classes of these algorithms. FMMs can reduce the computational complexity of the multiplication of the system matrix with a vector from $\mathcal{O}\left(N^2\right)$ to $\mathcal{O}\left(N\right)$ or $\mathcal{O}\left(N \log N\right)$. This is accomplished by dividing the geometry of the problem into a hierarchy of boxes, the so-called tree, and invoking a decomposition of the Green function. The tree is constructed by taking the box that contains the entire geometry of the problem and recursively subdividing it until a stopping criterion (for example a given minimal box size) is violated. The expansions of the Green function are then used to let the boxes interact as a whole.

The various possible decompositions of the Green function give rise to different FMMs and different circumstances under which the FMMs provide an improvement in complexity. Some examples are

- multipole decomposition: this is the oldest FMM [4], and reduces the complexity of a matrix-vector multiplication to $\mathcal{O}\left(N\right)$ if kR, with R the size of the simulated structure, does not become much larger than 1, i.e. when the frequency is sufficiently low. Also, the prefactor is quite large.

- propagating plane wave decomposition [5, 11]: this decomposition yields an $\mathcal{O}\left(N \log^s N\right)$ complexity, where $s \in \{0, 1, 2\}$ depends on the problem geometry and some algorithmic details. Although in principle the most efficient decomposition, it suffers from a numerical instability and therefore fails to de-

liver accurate results when the smallest boxes become significantly smaller than one wavelength. As a consequence the frequency must be sufficiently high to be able to use this decomposition.

- spectral, or directive evanescent plane wave decomposition [9, 12]: as one of the more recent FMMs, this method works for both high and low frequencies. However, the decomposition converges in only one half-space. Therefore, six different decompositions are required to cover the entire space.

Clearly, these three methods all have their drawbacks. In the following chapters, efforts to alleviate or eliminate these drawbacks will be presented.

Bibliography

[1] M.I. Mishchenko, J.W. Hovenier, and L.D. Travis. *Light Scattering by Nonspherical Particles: Theory, Measurements, and Applications*. Academic Press, San Diego, 2000.

[2] G. Mie. Beiträge zur Optik trüber Medien, speziell kolloidaler Metallösungen. *Annalen der Physik*, 330(3):377–445, 1908.

[3] O. Axelsson. *Iterative Solution Methods*. Cambridge University Press, New York, USA, 1995.

[4] L. Greengard and V. Rokhlin. A fast algorithm for particle simulations. *Journal of Computational Physics*, 73(2):325–348, December 1987.

[5] R. Coifman, V. Rokhlin, and S. Wandzura. The fast multipole method for the wave equation: A pedestrian prescription. *IEEE Antennas and Propagation Magazine*, 35(3):7–12, June 1993.

[6] E. Bleszynski, M. Bleszynski, and T. Jaroszewicz. AIM: Adaptive integral method for solving large-scale electromagnetic scattering and radiation problems. *Radio Science*, 31:1225–1252, 1996.

[7] W.C. Chew, J.M. Jin, C.C. Lu, E. Michielssen, and J.M. Song. Fast solution methods in electromagnetics. *IEEE Transactions on Antennas and Propagation*, 45(3):533–543, March 1997.

[8] J.M. Song, C.C. Lu, W.C. Chew, and S.W. Lee. Fast Illinois solver code (FISC). *IEEE Antennas and Propagation Magazine*, 40(3):27–34, June 1998.

[9] E. Darve and P. Havé. Efficient fast multipole method for low-frequency scattering. *Journal of Computational Physics*, 197(1):341–363, June 2004.

[10] D. Vande Ginste, E. Michielssen, F. Olyslager, and D. De Zutter. An efficient perfectly matched layer based multilevel fast multipole algorithm for large planar microwave structures. *IEEE Transactions on Antennas and Propagation*, 54(5):1538–1548, May 2006.

[11] W.C. Chew, S. Koc, J.M. Song, C.C. Lu, and E. Michielssen. A succinct way to diagonalize the translation matrix in three dimensions. *Microwave and Optical Technology Letters*, 15(3):144–147, December 1998.

[12] B. Hu and W.C. Chew. Fast Inhomogeneous Plane Wave Algorithm for Scattering from Objects Above the Multilayered Medium. *IEEE Transactions on Geoscience and Remote Sensing*, 39(5):1028–1038, May 2001.

CHAPTER 3

A Faster Aggregation for 3-D Fast Evanescent Wave Solvers Using Rotations

I. Bogaert, D. Pissoort, and F. Olyslager

Published in *Journal of Computational Physics,227 (1):557–573, Nov. 2007.*

★★★

The main drawback of using the spectral representation of the Green function in an FMM is the shape of the representation's convergence region, i.e. a half space. Therefore, to cover the entire space, six rotated versions of the representation are required. In this chapter, a novel technique to accelerate the aggregation and disaggregation stages in an FMM using the spectral representation of the Green function is presented. The new method calculates the six plane wave radiation patterns from a multipole expansion (aggregation) and calculates the multipole expansion of an incoming field from the six plane wave incoming field patterns. It is faster than the direct approach for multipole orders larger than one, and becomes six times faster for large multipole orders. The method relies on a connection between the discretizations of the six integral representations, and on the fact that the Wigner D-matrices become diagonal for rotations around the z-axis. The proposed technique can also be extended to the vectorial case in two different ways, one of which is very similar to the scalar case. The other method relies on a Beltrami decomposition of the fields and is faster than the direct approach for any multipole order. This Beltrami decomposition is also not limited to solvers using the spectral representation, but can be used in any vectorial FMM.

3.1 Introduction

Currently, several so-called Fast Multipole Algorithms (FMMs) exist [1–7]. These methods accelerate the matrix-vector multiplications required for the iterative solution of the systems of linear equations arising in Method of Moments based integral equation solvers. Unfortunately, most of these methods only apply to a specific type of problem. The multilevel fast multipole method (MLFMA) is based on a homogeneous plane wave expansion of the Green function to reduce the computation time and memory requirements for high frequency (HF) problems to $\mathcal{O}(N)$ - N denotes the number of unknowns - or $\mathcal{O}(N \log N)$. However it completely fails for low frequency (LF) problems due to roundoff errors. On the other hand, FMMs based on a multipole expansion of the Green function reduce both computation time and memory requirements to $\mathcal{O}(N)$ for LF problems, but not for HF problems. Hence, they are referred to as the low-frequency fast multipole methods (LF-FMMs). To mitigate this a new class of FMMs was introduced, which all somehow rely on a discretized version of the spectral representation of the Green function. These methods, most notably the stable plane wave method [6,8], are capable of delivering $\mathcal{O}(N)$ or $\mathcal{O}(N \log N)$ complexity for LF and HF problems respectively. However, as shown in [9], the MLFMA turns out to be the most efficient FMM if the frequency is high enough to reach the target accuracy. Therefore, the state of the art is to introduce a level in the FMM tree above (the HF part) which the MLFMA is used, and below (the LF part) which either the LF-FMM (as for example in [10]) or some form of evanescent plane wave method (as for example in [9]) is used. In [8, 9], it is argued that the evanescent wave technique is more efficient than the LF-FMM, especially for high accuracies. The reason for this is the diagonality of the translation operator, which reduces the cost of one translation from $\mathcal{O}\left(L^4\right)$ to $\mathcal{O}\left(L^2\right)$ with L the multipole order (of the LF-FMM). This shows that evanescent wave methods certainly are of practical importance for the LF part of FMMs.

However, their main drawback is that the underlying Green function's integral representation only converges in one half-space of choice. By consequence, in practice, six integral representations are needed to cover the entire space. For the propagating plane waves, all dependency on the half-space can be incorporated into the translation operator, thereby allowing to calculate all six integral representations starting from only one radiation pattern. Hence, for the propagating plane waves, only one radiation pattern is needed. For the evanescent plane waves up to now no such technique exists despite several attempts to solve this conundrum. For example, in [11], Jiang and Chew split the evanescent plane waves into so called 'shallow evanescent plane waves' and 'deep evanescent plane waves'. The shallow plane waves are obtained by extrapolating the propagating plane waves and improve the efficiency of the method at higher levels. However for very low frequencies or for very low levels in the tree, the extrapolation has little use, since virtually none of the evanescent plane waves will be

shallow. Indeed, if the extrapolation would still be effective at very low frequencies, the MLFMA would to some extent still work at those frequencies. Also, according to [11], it is not possible to calculate all six integral representations of the deep evanescent plane waves starting from only one radiation pattern. The need for six radiation patterns results in high memory requirements [10] and a high computational cost. As is done in [9, 12], the memory problem can be reduced by first calculating a multipole expansion of the radiated field, and then going to the plane wave basis. The calculation of the six evanescent radiation patterns from a multipole expansion will from here on be referred to as 'aggregation'. The reverse procedure, namely projecting the six evanescent incoming field patterns of an FMM group onto multipoles, will be referred to as 'disaggregation'. These procedures not only arise in the LF-part of [9], but can also be used when for example multiple scattering from a collection of spheres is considered (where the sources in every FMM group are multipoles). It is thus important to do the (dis)aggregation as efficiently as possible.

The main goal of this paper is to introduce an elegant, novel and exact method to do this (dis)aggregation. This new method relies on the use of Wigner rotation matrices and the fact that these matrices are diagonal for rotations around the z-axis. The computation time is lower than the direct computation if the maximal multipole order L is larger than one, which is true for all practical cases. Moreover, if a large enough number of multipoles are used, the computation time is reduced by a factor six compared to the direct case. It will also be shown that the proposed scheme applies to both the scalar (for example acoustics) and the vectorial (for example electromagnetics) case. In the latter case, two methods are provided, the second of which is faster than the direct approach for *any* multipole order. The proposed methods do not reduce the complexity however, so they can only be used for the LF-part of the FMM tree. A drawback of the method occurs when one is simulating a structure which is long in one direction. Only a few of the six radiation patterns are needed then, while the proposed method still calculates all six radiation patterns. Such inefficiencies can be avoided by switching to the direct method for these cases.

Notation: throughout this work all sources and fields are assumed time-harmonic with angular frequency ω; temporal dependencies $e^{j\omega t}$ are suppressed. Unit vectors are denoted by a hat $\hat{\boldsymbol{k}} = \frac{\boldsymbol{k}}{k}$, and the Cartesian unit vectors are $\boldsymbol{e}_\tau$, with $\tau = x, y, z$.

3.2 FMMs with evanescent plane waves

An FMM with evanescent plane waves [6, 8, 11], like all FMM codes, uses a hierarchical cubical subdivision of the computational domain. For the interaction between groups on a level, it relies upon the spectral decomposition of the spherical Hankel function of the second kind and of zeroth order (1.44), which is readily generalized to

both positive and negative z

$$h_0^{(2)}(kr) = \frac{1}{2\pi}\int_{\mathcal{E}} e^{\mp j\boldsymbol{k}\cdot\boldsymbol{r}}\mathrm{d}\hat{\boldsymbol{k}},\ z = \hat{\boldsymbol{e}}_z\cdot\boldsymbol{r} \gtrless 0. \tag{3.1}$$

Here, k is the free-space wavenumber, $\boldsymbol{k} = k\hat{\boldsymbol{k}} = (k_x, k_y, k_z)$ the wave vector, and $\boldsymbol{r}$ a global position vector. The integration with subscript $\mathcal{E}$ is defined in (1.43) and becomes

$$h_0^{(2)}(kr) = \frac{1}{2\pi}\int_0^{2\pi}\int_{\Gamma} e^{\mp j\boldsymbol{k}\cdot\boldsymbol{r}}\sin\theta\mathrm{d}\theta\mathrm{d}\phi \tag{3.2}$$

with $(k_x, k_y, k_z) = k(\cos\phi\sin\theta, \sin\phi\sin\theta, \cos\theta)$. The integration path Γ consists of two pieces, Γ_1 and Γ_2, depicted in Figure 1.1 and corresponding to propagating and evanescent plane waves respectively. Therefore the integral (3.1) can be split in a propagating and an evanescent part

$$h_0^{(2)}(kr) = \underbrace{\frac{1}{2\pi}\int_0^{2\pi}\int_{\Gamma_1} e^{\mp j\boldsymbol{k}\cdot\boldsymbol{r}}\sin\theta\mathrm{d}\theta\mathrm{d}\phi}_{Propagating} + \underbrace{\frac{1}{2\pi}\int_0^{2\pi}\int_{\Gamma_2} e^{\mp j\boldsymbol{k}\cdot\boldsymbol{r}}\sin\theta\mathrm{d}\theta\mathrm{d}\phi}_{Evanescent}. \tag{3.3}$$

Then both integrals are discretized separately, for example for the case $z > 0$:

$$h_0^{(2)}(kr) = \sum_{v_p=1}^{V_p} w_{v_p}^p e^{-j\boldsymbol{k}_{v_p}^p\cdot\boldsymbol{r}} + \sum_{v_e=1}^{V_e} w_{v_e}^e e^{-j\boldsymbol{k}_{v_e}^e\cdot\boldsymbol{r}} \tag{3.4}$$

where $w_{v_p}^p$, $\boldsymbol{k}_{v_p}^p$, $w_{v_e}^e$ and $\boldsymbol{k}_{v_e}^e$ are the weights and nodes of the propagating and evanescent part respectively. The discretization of the propagating part is straightforward [6]. The discretization of the evanescent part is more difficult, since the evanescent integral in (3.3) covers an infinite region. However, since Γ_2 is given by the parameter equation $\theta = \frac{\pi}{2} + jt, t \in [0, \infty]$ and $k_z = k\cos\theta$, the integral converges in an exponential manner if $z \gtrless 0$. This allows the discretization to be done with exponential accuracy. It can be done in many ways, for example with a singular value decomposition (SVD) based approach. A uniform discretization is also possible, albeit after some further coordinate transformations. Both the SVD and uniform discretizations are described in [6]. However, the details of the discretization are not important for the remainder of this paper.

An important property of (3.1) is that it is valid only if $z \gtrless 0$. In the plane $z = 0$, this integral representation does not converge. For the discretized version, matters are even worse, since series (3.4) will only converge if $\boldsymbol{r}$ remains *far enough* from the plane $z = 0$. A more rigorous criterium for convergence of (3.4) is given in [6], with

some positive constant C:

$$\sqrt{x^2 + y^2} < Cz, \tag{3.5}$$

As a consequence, only a cone-like region around the z-axis can be covered with this expansion of the Green function. This situation is remedied by introducing extra integral (series) representations which converge along the x- and y-axes. As a result, in total six integral representations are used, which will henceforth be denoted as $1\pm$, $2\pm$, and $3\pm$. This configuration has been ubiquitously used in the literature [6, 8, 11]. In [6], it is shown that in an oct-tree using these six integral representations, criterium (3.5) is always satisfied with $C = \sqrt{2}$, thus assuring convergence of the series. Figure 3.1 shows an example configuration in which the field in the point $\boldsymbol{d}_1$ due to sources $\boldsymbol{J}$ in the box must be calculated by means of the $3+$ expansion, while the fields in the point $\boldsymbol{d}_2$ must be calculated by means of the $1+$ expansion.

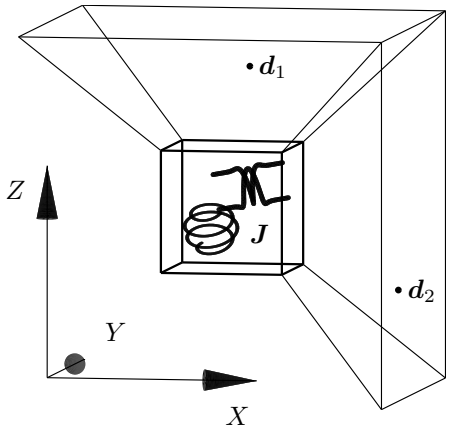

Figure 3.1: The radiated fields of the central box is given by different expansions in the different cone-like regions. For example, the fields in $\boldsymbol{d}_1$ must be calculated using the $3+$ expansion while the fields in $\boldsymbol{d}_2$ must be calculated by means of the $1+$ expansion.

The propagating parts of the six series are all integrations over one half of the Ewald sphere. As is shown in [6] this permits absorbing all directional dependence into the weights. As a consequence only one radiation pattern is needed for the propagating part. Unfortunately, this is not possible for the evanescent part [11]. Therefore, from now on, we will focus on the evanescent part only, so $w^e_{v_e}$ and $\boldsymbol{k}^e_{v_e}$ will henceforth be written as w_v and $\boldsymbol{k}_v$. In this paper, it will be shown that the six evanescent radiation patterns can be calculated from a multipole expansion with asymptotically the same computational cost as for one radiation pattern, thus gaining a factor six.

The essential element of this novel method is the fact that the nodes of the different representations are rotated versions of the nodes for the expansion around the positive z-axis $\boldsymbol{k}_v$ ($= \boldsymbol{k}_v^{3+}$):

$$\boldsymbol{k}_v^{1+} = \mathsf{R}_x^{-1} \cdot \boldsymbol{k}_v, \tag{3.6}$$

$$\boldsymbol{k}_v^{2+} = \mathsf{R}_y^{-1} \cdot \boldsymbol{k}_v, \tag{3.7}$$

$$\boldsymbol{k}_v^{3+} = \mathsf{R}_z^{-1} \cdot \boldsymbol{k}_v = \boldsymbol{k}_v, \tag{3.8}$$

In addition:

$$\boldsymbol{k}_v^{p-} = -\boldsymbol{k}_v^{p+} \ \ \forall p \in \{1,2,3\}. \tag{3.9}$$

with the matrices R_x, R_y and R_z defined as

$$\mathsf{R}_x = \mathsf{R}\left(-\frac{2\pi}{3}, \frac{1}{\sqrt{3}}(\hat{\boldsymbol{e}}_x + \hat{\boldsymbol{e}}_y + \hat{\boldsymbol{e}}_z)\right) = \begin{bmatrix} 0 & 1 & 0 \\ 0 & 0 & 1 \\ 1 & 0 & 0 \end{bmatrix}, \tag{3.10}$$

$$\mathsf{R}_y = \mathsf{R}\left(\frac{2\pi}{3}, \frac{1}{\sqrt{3}}(\hat{\boldsymbol{e}}_x + \hat{\boldsymbol{e}}_y + \hat{\boldsymbol{e}}_z)\right) = \begin{bmatrix} 0 & 0 & 1 \\ 1 & 0 & 0 \\ 0 & 1 & 0 \end{bmatrix}. \tag{3.11}$$

$$\mathsf{R}_z = \mathbb{1} \tag{3.12}$$

In this, the rotation matrix $\mathsf{R}(\alpha, \boldsymbol{u})$ is a 3 by 3 matrix which rotates a vector $\boldsymbol{c}$ around the axis $\boldsymbol{u}$ (with $\boldsymbol{u} \cdot \boldsymbol{u} = 1$) over the angle α into the vector $\boldsymbol{c}'$, viz. $\boldsymbol{c}' = \mathsf{R}(\alpha, \boldsymbol{u}) \cdot \boldsymbol{c}$. The direction of rotation is determined by means of the right hand rule. A graphical representation of this is given in Figure 3.2. It will now be shown that the relationships (3.6)-(3.9) can be unified in one symmetric expression. Begin by observing that R_x, R_y, and R_z are all rotations around the $\frac{1}{\sqrt{3}}(\hat{\boldsymbol{e}}_x + \hat{\boldsymbol{e}}_y + \hat{\boldsymbol{e}}_z)$-axis. This means they all can be converted into rotations around the z-axis by means of one similarity transform. With $\mathsf{R}_0 = \mathsf{R}\left(-\arccos(\frac{1}{\sqrt{3}}), \frac{1}{\sqrt{2}}(-\hat{\boldsymbol{e}}_x + \hat{\boldsymbol{e}}_y)\right)$, this yields

$$\mathsf{R}_x = \mathsf{R}_0^{-1} \cdot \mathsf{R}(-\frac{2\pi}{3}, \hat{\boldsymbol{e}}_z) \cdot \mathsf{R}_0, \tag{3.13}$$

$$\mathsf{R}_y = \mathsf{R}_0^{-1} \cdot \mathsf{R}(-\frac{4\pi}{3}, \hat{\boldsymbol{e}}_z) \cdot \mathsf{R}_0, \tag{3.14}$$

$$\mathsf{R}_z = \mathsf{R}_0^{-1} \cdot \mathsf{R}(-\frac{6\pi}{3}, \hat{\boldsymbol{e}}_z) \cdot \mathsf{R}_0. \tag{3.15}$$

This means that the discretization points for all six representations can be unified in one formula:

$$\boldsymbol{k}_v^{ps} = \mathsf{R}_0^{-1} \cdot \left[s\mathsf{R}(\frac{2p\pi}{3}, \hat{\boldsymbol{e}}_z)\right] \cdot \mathsf{R}_0 \cdot \boldsymbol{k}_v^{3+} \ \ \forall s \in \{-1,+1\} \ \ \forall p \in \{1,2,3\}. \tag{3.16}$$

When s is used as an index, for example in $\boldsymbol{k}_v^{ps}$, the $+1$ and -1 are denoted as $+$ and $-$ respectively. Formula (3.16) is a form in which the symmetry between the six radiation patterns is visible. This symmetry will be crucial in developing the accelerated scheme, since it will allow the six radiation patterns to be decomposed in six other patterns which require only one sixth of the amount of work to calculate. The derivations will be presented in the following sections.

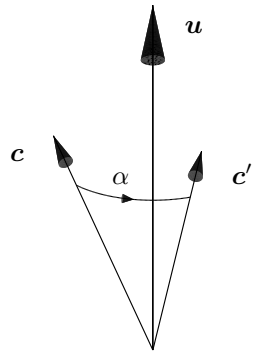

Figure 3.2: The rotation matrix $\mathsf{R}(\alpha, \boldsymbol{u})$ rotates a vector $\boldsymbol{c}$ around the axis $\boldsymbol{u}$ over the angle α into the vector $\boldsymbol{c}'$. The direction of the rotation is determined by the right hand rule.

3.3 A faster (dis)aggregation for the scalar case

As stated in the introduction, the aggregation denotes the calculation of the six evanescent radiation patterns from a multipole expansion. This process is used and elaborated in [9]. It consists of calculating

$$\Theta_v^{ps} = \sum_{l=0}^{L} \sum_{m=-l}^{l} a_{lm} j^l Y_{l,m}\left(\hat{\boldsymbol{k}}_v^{ps}\right) \qquad \forall p \in \{1,2,3\}, s \in \{-1,+1\}, \tag{3.17}$$

where the a_{lm} are the multipole coefficients, $Y_{l,m}\left(\hat{\boldsymbol{k}}\right)$ denotes a spherical harmonic and L is the maximum multipole order that is taken into account. The $\boldsymbol{k}_v^{ps}$ are the discretization nodes from the evanescent part in (3.4). The definition and some properties of the spherical harmonics are summarized in Appendix A. When Φ_v^{ps} denotes

the incoming field patterns in the six directions, the disaggregation is given by

$$b_{lm} = \sum_v w_v \sum_{p,s} \Phi_v^{ps} (-1)^m Y_{l,-m} \left(\hat{\boldsymbol{k}}_v^{ps} \right) \tag{3.18}$$

$$= \sum_v w_v \sum_{p,s} \Phi_v^{ps} Y_{l,m}^* \left(\hat{\boldsymbol{k}}_v^{ps*} \right). \tag{3.19}$$

Here, $*$ denotes the complex conjugate. The fact that - in contrast to the nodes - the weights w_v do not depend on p nor s has also been used. In the following sections, the accelerated scheme will be developed.

3.3.1 Aggregation

The accelerated scheme relies for a great deal on the connection (3.16) between the discretization points for the six representations. Substitution of (3.16) in Θ_v^{ps} yields:

$$\Theta_v^{ps} = \sum_{l=0}^{L} \sum_{m=-l}^{l} a_{lm} j^l Y_{l,m} \left(\mathsf{R}_0^{-1} \cdot \left[s\mathsf{R}(\frac{2p\pi}{3}, \hat{\boldsymbol{e}}_z) \right] \cdot \mathsf{R}_0 \cdot \hat{\boldsymbol{k}}_v^{3+} \right). \tag{3.20}$$

The outer rotation in the argument of the spherical harmonic can be brought outside the function by means of the Wigner D-matrices, defined in Section A.2 in Appendix A, as follows

$$\Theta_v^{ps} = \sum_{l=0}^{L} \sum_{m=-l}^{l} \sum_{m_1} a_{lm} j^l D_{m,m_1}^l \left(\mathsf{R}_0^{-1} \right) Y_{l,m_1} \left(s\mathsf{R}(\frac{2p\pi}{3}, \hat{\boldsymbol{e}}_z) \cdot \mathsf{R}_0 \cdot \hat{\boldsymbol{k}}_v^{3+} \right) \tag{3.21}$$

$$= \sum_{l=0}^{L} \sum_{m_1=-l}^{l} a'_{lm_1} j^l Y_{l,m_1} \left(s\mathsf{R}(\frac{2p\pi}{3}, \hat{\boldsymbol{e}}_z) \cdot \mathsf{R}_0 \cdot \hat{\boldsymbol{k}}_v^{3+} \right) \tag{3.22}$$

where

$$a'_{lm_1} = \sum_m a_{lm} D_{m,m_1}^l \left(\mathsf{R}_0^{-1} \right) \tag{3.23}$$

This sum runs over m only and thus can be done fast, compared to the full aggregation. After this operation, all sources are actually rotated to a reference system in which the former $\frac{1}{\sqrt{3}}(\hat{\boldsymbol{e}}_x + \hat{\boldsymbol{e}}_y + \hat{\boldsymbol{e}}_z)$ axis is the new z-axis. In a second step the dependence on p and s can be removed. According to equation (A.6) the spherical harmonics are eigenfunctions of the inversion operator (which replaces $\boldsymbol{r}$ by $-\boldsymbol{r}$) with eigenvalues $(-1)^l$, which allows for the removal of s. Moving the p-dependence out of the spherical harmonic can again be done using the Wigner D-matrices. However a crucial point here is that Wigner D-matrices for rotations around the z-axis are diagonal, as stated

in (A.44). This yields:

$$\Theta_v^{ps} = \sum_{l=0}^{L} \sum_{m=-l}^{l} a'_{lm} j^l s^l e^{im\frac{2p\pi}{3}} Y_{l,m}\left(\mathsf{R}_0 \cdot \hat{\boldsymbol{k}}_v^{3+}\right) \tag{3.24}$$

or after splitting the summations:

$$\Theta_v^{ps} = \sum_{r=0}^{1} \sum_{q=0}^{2} s^r e^{iq\frac{2p\pi}{3}} \sum_{r=l \bmod 2} \sum_{q=m \bmod 3} a'_{lm} j^l Y_{l,m}\left(\mathsf{R}_0 \cdot \hat{\boldsymbol{k}}_v^{3+}\right) \tag{3.25}$$

The inner summation runs over all m for which $q = m \bmod 3$ and all l for which $r = l \bmod 2$. 'mod' means modulo, so for example $1 = 7 \bmod 3$. Equation (3.25) shows that (3.17) can be re-expressed as an aggregation towards six new radiation patterns κ_v^{qr}

$$\kappa_v^{qr} = \sum_{r=l \bmod 2} \sum_{q=m \bmod 3} a'_{lm} j^l Y_{l,m}\left(\mathsf{R}_0 \cdot \hat{\boldsymbol{k}}_v^{3+}\right) \ \forall q \in \{0,1,2\},\ \forall r \in \{0,1\} \tag{3.26}$$

However, only one sixth of the multipoles contributes to each of these patterns. In this way, calculating these six new patterns costs as little as calculating one pattern with the direct formula (3.17). Of course, there is the extra cost of a postprocessing step, i.e., the summation over q and r in (3.25), but this cost has only an $\mathcal{O}\left(L^2\right)$ complexity and is negligible compared to the entire aggregation. Note that this whole scheme works totally independent from the choice of the discretization points $\boldsymbol{k}_v^{3+}$. Only the connection (3.16) is required. Another important point was brought up by one of the reviewers: very elongated structures require less than six radiation patterns to be computed. For example a long wire will need the FMM groups to have only two radiation patterns. In this case (3.25) will only yield an asymptotic factor two. If an FMM group needs only one radiation pattern, then a switch to the direct method should be made. The same considerations apply to the disaggregation and the first method for the vectorial case. The second method will be shown to be capable of accelerating by a factor 2 even if only one radiation pattern is required.

An explicit operation count will be done to show that the proposed method requires less multiplications than the direct approach for most practical cases. The operation count for doing the rotation on a_{lm} (3.23) is:

$$\sum_{l=0}^{L} (2l+1)^2 = \frac{1}{3}\left(4L^3 + 12L^2 + 11L + 3\right) \tag{3.27}$$

The operation count for the construction of the new radiation patterns κ_v^{qr} clearly is $V(L+1)^2$. V is the number of discretization points for the Green function's integral

representation. The postprocessing step requires $36V$ multiplications. Hence the total number of multiplications is:

$$\frac{1}{3}\left(4L^3+12L^2+11L+3\right)+V(L^2+2L+37) \tag{3.28}$$

The number of multiplications without acceleration is $6V(L+1)^2$. Therefore, the value of V for which the proposed method is faster than the one without acceleration is given by:

$$V > \frac{1}{3}\frac{4L^3+12L^2+11L+3}{5L^2+10L-31} \quad \forall\, L>1 \tag{3.29}$$

For the case where $L=1$, $>$ in equation (3.29) has to be replaced by $<$ because $5L^2+10L-31$ is negative. Therefore, if $L=1$, (3.29) is not satisfied and the new method is slower than the direct approach. For $L=2$, the right hand side becomes $\frac{35}{9}<4$. Since the number of discretization points is always more than 3, (3.29) is always satisfied. Moreover, $V=\mathcal{O}\left(L^2\right)$ because the multipole and plane wave expansion have approximately the same information content. This makes sure that equation (3.29) is also satisfied for larger L. Therefore it is safe to say that for any $L>1$, the method presented in 3.4.2 is faster than the direct approach. It has to be acknowledged that this operation count has to be put in the right perspective, because different optimizations and hardware can have a great influence on performance.

3.3.2 Disaggregation

The disaggregation can also be accelerated. The operations are analogous to the aggregation, but are done in reversed order. A short treatment is given below for completeness. The derivation is again started by using (3.16) in (3.19), which yields:

$$b_{lm}=\sum_v w_v \sum_{p,s}\Phi_v^{ps}Y_{l,m}^*\left(\mathsf{R}_0^{-1}\cdot\left[s\mathsf{R}(\frac{2p\pi}{3},\hat{\boldsymbol{e}}_z)\right]\cdot\mathsf{R}_0\cdot\hat{\boldsymbol{k}}_v^{3+*}\right). \tag{3.30}$$

As a first step it is possible to remove the last rotation by multiplying b_{lm} with $D_{m_2,m}^{l*}\left(\mathsf{R}_0\right)$ and summing over m:

$$b'_{lm_2}=\sum_m D_{m_2,m}^{l*}\left(\mathsf{R}_0\right)b_{lm}=\sum_v w_v\sum_{p,s}\Phi_v^{ps}Y_{l,m_2}^*\left(s\mathsf{R}(\frac{2p\pi}{3},\hat{\boldsymbol{e}}_z)\cdot\mathsf{R}_0\cdot\hat{\boldsymbol{k}}_v^{3+*}\right). \tag{3.31}$$

Again the rotation around the z-axis can be taken out of the spherical harmonics by using the diagonal Wigner D-matrices:

$$b'_{lm_2} = \sum_v w_v \sum_{p,s} \Phi_v^{ps} s^l \sum_{m_3=-l}^{l} D^{l*}_{m_2,m_3} \left(\mathsf{R}(\frac{2p\pi}{3}, \hat{\boldsymbol{e}}_z) \right) Y^*_{l,m_3} \left(\mathsf{R}_0 \cdot \hat{\boldsymbol{k}}_v^{3+*} \right) \quad (3.32)$$

$$= \sum_v w_v \sum_{p,s} \Phi_v^{ps} s^l e^{-im_2 \frac{2p\pi}{3}} Y^*_{l,m_2} \left(\mathsf{R}_0 \cdot \hat{\boldsymbol{k}}_v^{3+*} \right). \quad (3.33)$$

The summation over p, s gives rise to 6 distinct new disaggregation patterns:

$$\Xi_v^{k,r} = \sum_{p,s} \Phi_v^{ps} s^r e^{-ik \frac{2p\pi}{3}}, \forall k \in \{0,1,2\}, r \in \{0,1\}. \quad (3.34)$$

These new patterns allow for a faster disaggregation because they each only contribute to one sixth of the b'_{lm_1}:

$$b'_{lm_1} = \sum_v w_v \Xi_v^{m_1 \bmod 3, l \bmod 2} Y_{l,m_1} \left(\mathsf{R}_0 \cdot \hat{\boldsymbol{k}}_v^{3+*} \right). \quad (3.35)$$

In order to obtain the b_{lm}, the b'_{lm_1} have only to be rotated back:

$$b_{lm} = \sum_{m_3=-l}^{l} \sum_{m_1=-l}^{l} D^{l*}_{m,m_1} \left(\mathsf{R}_0^{-1} \right) D^{l*}_{m_1,m_3} \left(\mathsf{R}_0 \right) b_{l,m_3} \quad (3.36)$$

$$= \sum_{m_1=-l}^{l} D^{l*}_{m,m_1} \left(\mathsf{R}_0^{-1} \right) b'_{l,m_1} \quad (3.37)$$

$$= \sum_{m_1=-l}^{l} D^{l}_{m_1,m} \left(\mathsf{R}_0 \right) b'_{l,m_1}. \quad (3.38)$$

$$(3.39)$$

3.4 A faster (dis)aggregation for the vectorial case

The proposed technique can also be used in the vectorial case, as is needed for the general electromagnetic case. The vector multipoles $\boldsymbol{M}^f_{l,m}(k\boldsymbol{r})$ and $\boldsymbol{N}^f_{l,m}(k\boldsymbol{r})$ are defined in Section 1.3. Because there are two sets, the multipole coefficients associated with the vector multipoles will thus carry the label M or N besides the usual l and m. Because the vectorial case is less well-known, a short derivation of the formulas for the (dis)aggregation will be given here. Let $\boldsymbol{\Phi}(\boldsymbol{r})$ be the vectorial field generated by sources inside a sphere with center $\boldsymbol{r}_1$. This field can be expanded into outgoing

multipoles:

$$\boldsymbol{\Phi}(\boldsymbol{r}) = \sum_{l=0}^{L} \sum_{m=-l}^{l} \left[a_{lm}^{M} \boldsymbol{M}_{l,m}^{h} \left(k(\boldsymbol{r} - \boldsymbol{r}_1) \right) + a_{lm}^{N} \boldsymbol{N}_{l,m}^{h} \left(k(\boldsymbol{r} - \boldsymbol{r}_1) \right) \right] \tag{3.40}$$

$\boldsymbol{\Phi}(\boldsymbol{r})$ can now be expanded around $\boldsymbol{r}_2$ as:

$$\boldsymbol{\Phi}(\boldsymbol{r}) = \sum_{l=0}^{L} \sum_{m=-l}^{l} \left[b_{lm}^{M} \boldsymbol{M}_{l,m}^{j} \left(k(\boldsymbol{r} - \boldsymbol{r}_2) \right) + b_{lm}^{N} \boldsymbol{N}_{l,m}^{j} \left(k(\boldsymbol{r} - \boldsymbol{r}_2) \right) \right] \tag{3.41}$$

with $b_{l,m}^{M}$ and $b_{l,m}^{N}$ defined by means of the vector multipole translation matrix [13]:

$$\begin{bmatrix} \boldsymbol{b}^{M} \\ \boldsymbol{b}^{N} \end{bmatrix} = \begin{bmatrix} \alpha_{MM}^{h} \left(k(\boldsymbol{r}_2 - \boldsymbol{r}_1) \right) & \alpha_{NM}^{h} \left(k(\boldsymbol{r}_2 - \boldsymbol{r}_1) \right) \\ \alpha_{NM}^{h} \left(k(\boldsymbol{r}_2 - \boldsymbol{r}_1) \right) & \alpha_{MM}^{h} \left(k(\boldsymbol{r}_2 - \boldsymbol{r}_1) \right) \end{bmatrix} \cdot \begin{bmatrix} \boldsymbol{a}^{M} \\ \boldsymbol{a}^{N} \end{bmatrix} \tag{3.42}$$

with α_{MM}^{h} and α_{MN}^{h} defined by means of the vector spherical wave operators in (1.130) and (1.131)

$$\left[\alpha_{MM}^{h} \left(k\boldsymbol{d} \right) \right]_{l',m',l,m} = 2j^{l-l'} \int_{\mathcal{E}} \boldsymbol{X}_{l,m} \left(\hat{\boldsymbol{k}} \right) \cdot \boldsymbol{X}_{l',m'}^{*} \left(\hat{\boldsymbol{k}}^{*} \right) e^{-j\boldsymbol{k}\cdot\boldsymbol{d}} \mathrm{d}\hat{\boldsymbol{k}}, \tag{3.43}$$

$$\left[\alpha_{MN}^{h} \left(k\boldsymbol{d} \right) \right]_{l',m',l,m} = 2j^{l-l'+1} \int_{\mathcal{E}} \boldsymbol{X}_{l,m} \left(\hat{\boldsymbol{k}} \right) \cdot \boldsymbol{W}_{l',m'}^{*} \left(\hat{\boldsymbol{k}}^{*} \right) e^{-j\boldsymbol{k}\cdot\boldsymbol{d}} \mathrm{d}\hat{\boldsymbol{k}}, \tag{3.44}$$

if $\boldsymbol{d} \cdot \hat{\boldsymbol{e}}_z > 0$. Here, the $\boldsymbol{X}_{l,m}(\cdot)$ and $\boldsymbol{W}_{l,m}(\cdot)$ are the so-called vector spherical harmonics, defined in Section A.3 in Appendix A. Integrals (3.43) and (3.44) can again be split up in a propagating and an evanescent part and discretized. The propagating part will again be omitted. By means of (3.43), (3.44), and the formulas (A.66) and (A.67) in Appendix A, the aggregation toward the six evanescent radiation patterns can be written as follows:

$$\boldsymbol{\Theta}_{v}^{ps} = \sum_{l=0}^{L} \sum_{m=-l}^{l} j^{l} \left[a_{lm}^{M} \boldsymbol{X}_{l,m} \left(\hat{\boldsymbol{k}}_{v}^{ps} \right) - j a_{lm}^{N} \boldsymbol{W}_{l,m} \left(\hat{\boldsymbol{k}}_{v}^{ps} \right) \right] \tag{3.45}$$

The vector $\boldsymbol{\Theta}_{v}^{ps}$ has three Cartesian components. However, Eqns. (A.64) and (A.65) show that the radial component of $\boldsymbol{\Theta}_{v}^{ps}$ is zero. This permits representing the vector $\boldsymbol{\Theta}_{v}^{ps}$ with only the two components orthogonal to $\boldsymbol{k}_{v}^{ps}$. An obvious choice for these components is to take the part of $\boldsymbol{\Theta}_{v}^{ps}$ parallel with $\hat{\boldsymbol{e}}_{\phi,v}^{ps}$ and $\hat{\boldsymbol{e}}_{\theta,v}^{ps}$, which are defined as follows:

$$\hat{\boldsymbol{e}}_{\phi,v}^{ps} = \mathsf{R}_0^{-1} \cdot \mathsf{R}(\frac{2p\pi}{3}, \hat{\boldsymbol{e}}_z) \cdot \mathsf{R}_0 \cdot \hat{\boldsymbol{e}}_{\phi,v}^{3+} \tag{3.46}$$

$$\hat{\boldsymbol{e}}_{\theta,v}^{ps} = s\mathsf{R}_0^{-1} \cdot \mathsf{R}(\frac{2p\pi}{3}, \hat{\boldsymbol{e}}_z) \cdot \mathsf{R}_0 \cdot \hat{\boldsymbol{e}}_{\theta,v}^{3+} \tag{3.47}$$

Here $\hat{\boldsymbol{e}}^{3+}_{\phi,v}$ and $\hat{\boldsymbol{e}}^{3+}_{\theta,v}$ are the two usual nonradial unit vectors in the spherical coordinate system. Expression (3.46) does not contain an s in the right hand side for reasons that will be explained in Section 3.4.2. The aggregation to $\boldsymbol{\Theta}^{ps}_v$ is thus reduced to an aggregation to two scalar quantities namely to $\hat{\boldsymbol{e}}^{ps}_{\phi,v} \cdot \boldsymbol{\Theta}^{ps}_v$ and $\hat{\boldsymbol{e}}^{ps}_{\theta,v} \cdot \boldsymbol{\Theta}^{ps}_v$:

$$\hat{\boldsymbol{e}}^{ps}_{\phi,v} \cdot \boldsymbol{\Theta}^{ps}_v = \sum_{l=0}^{L} \sum_{m=-l}^{l} j^l \left[a^M_{lm} \hat{\boldsymbol{e}}^{ps}_{\phi,v} \cdot \boldsymbol{X}_{l,m}\left(\hat{\boldsymbol{k}}^{ps}_v\right) - j a^N_{lm} \hat{\boldsymbol{e}}^{ps}_{\phi,v} \cdot \boldsymbol{W}_{l,m}\left(\hat{\boldsymbol{k}}^{ps}_v\right)\right] \tag{3.48}$$

$$\hat{\boldsymbol{e}}^{ps}_{\theta,v} \cdot \boldsymbol{\Theta}^{ps}_v = \sum_{l=0}^{L} \sum_{m=-l}^{l} j^l \left[a^M_{lm} \hat{\boldsymbol{e}}^{ps}_{\theta,v} \cdot \boldsymbol{X}_{l,m}\left(\hat{\boldsymbol{k}}^{ps}_v\right) - j a^N_{lm} \hat{\boldsymbol{e}}^{ps}_{\theta,v} \cdot \boldsymbol{W}_{l,m}\left(\hat{\boldsymbol{k}}^{ps}_v\right)\right] \tag{3.49}$$

This aggregation for the vectorial case can now be accelerated in two ways. These will both be outlined below. In what follows we will only consider (3.48) because the formulas for (3.49) can be derived in a very similar fashion.

3.4.1 A Faster Aggregation for the Vectorial Case: Method 1

The rotations of the argument of the vector spherical harmonics can again be brought outside by means of the Wigner D-matrices which yields:

$$\begin{aligned}\hat{\boldsymbol{e}}^{ps}_{\phi,v} \cdot \boldsymbol{\Theta}^{ps}_v = \\ \left[\mathsf{R}(\frac{2p\pi}{3}, \hat{\boldsymbol{e}}_z) \cdot \mathsf{R}_0 \cdot \hat{\boldsymbol{e}}^{3+}_{\phi,v}\right] \cdot \sum_{l=0}^{L} \sum_{m=-l}^{l} \Bigg[\boldsymbol{X}_{l,m}\left(s\mathsf{R}(\frac{2p\pi}{3}, \hat{\boldsymbol{e}}_z) \cdot \mathsf{R}_0 \cdot \hat{\boldsymbol{k}}^{3+}_v\right) a'^M_{lm} \\ - j\boldsymbol{W}_{l,m}\left(s\mathsf{R}(\frac{2p\pi}{3}, \hat{\boldsymbol{e}}_z) \cdot \mathsf{R}_0 \cdot \hat{\boldsymbol{k}}^{3+}_v\right) a'^N_{lm}\Bigg]\end{aligned} \tag{3.50}$$

with:

$$a'^M_{lm_1} = \sum_m D^l_{m,m_1}(\mathsf{R}_0^{-1}) j^l a^M_{l,m} \tag{3.51}$$

$$a'^N_{lm_1} = \sum_m D^l_{m,m_1}(\mathsf{R}_0^{-1}) j^l a^N_{l,m} \tag{3.52}$$

To remove the dependence on s the properties of the vector spherical harmonics (A.60) and (A.61) can be used. The dependence on p can again be removed using the diagonal

Wigner D-matrices for rotations around the z-axis:

$$\hat{\boldsymbol{e}}^{ps}_{\phi,v} \cdot \boldsymbol{\Theta}^{ps}_{v} = \sum_{l=0}^{L} \sum_{m=-l}^{l} s^l e^{im\frac{2p\pi}{3}} \left[\left(\mathsf{R}_0 \cdot \hat{\boldsymbol{e}}^{3+}_{\phi,v} \right) \cdot \boldsymbol{X}_{l,m} \left(\mathsf{R}_0 \cdot \hat{\boldsymbol{k}}^{3+}_{v} \right) a'^{M}_{lm} \right. \tag{3.53}$$

$$\left. - js \left(\mathsf{R}_0 \cdot \hat{\boldsymbol{e}}^{3+}_{\phi,v} \right) \cdot \boldsymbol{W}_{l,m} \left(\mathsf{R}_0 \cdot \hat{\boldsymbol{k}}^{3+}_{v} \right) a'^{N}_{lm} \right] \tag{3.54}$$

or after splitting the summations:

$$\begin{aligned} \hat{\boldsymbol{e}}^{ps}_{\phi,v} \cdot \boldsymbol{\Theta}^{ps}_{v} = & \sum_{r=0}^{1} \sum_{q=0}^{2} s^r e^{iq\frac{2p\pi}{3}} \\ & \times \sum_{r=l \bmod 2} \sum_{q=m \bmod 3} \left[\left(\mathsf{R}_0 \cdot \hat{\boldsymbol{e}}^{3+}_{\phi,v} \right) \cdot \boldsymbol{X}_{l,m} \left(\mathsf{R}_0 \cdot \hat{\boldsymbol{k}}^{3+}_{v} \right) a'^{M}_{lm} \right. \\ & \left. -js \left(\mathsf{R}_0 \cdot \hat{\boldsymbol{e}}^{3+}_{\phi,v} \right) \cdot \boldsymbol{W}_{l,m} \left(\mathsf{R}_0 \cdot \hat{\boldsymbol{k}}^{3+}_{v} \right) a'^{N}_{lm} \right] \end{aligned} \tag{3.55}$$

Despite the splitting of the sums, there is still an s inside the brackets. This can be resolved by rewriting the sum as:

$$\begin{aligned} \hat{\boldsymbol{e}}^{ps}_{\phi,v} \cdot \boldsymbol{\Theta}^{ps}_{v} = & \sum_{r=0}^{1} \sum_{q=0}^{2} s^r e^{iq\frac{2p\pi}{3}} \\ & \times \sum_{q=m \bmod 3} \left[\sum_{r=l \bmod 2} \left(\mathsf{R}_0 \cdot \hat{\boldsymbol{e}}^{3+}_{\phi,v} \right) \cdot \boldsymbol{X}_{l,m} \left(\mathsf{R}_0 \cdot \hat{\boldsymbol{k}}^{3+}_{v} \right) a'^{M}_{lm} \right. \\ & \left. -j \sum_{l=(1-r) \bmod 2} \left(\mathsf{R}_0 \cdot \hat{\boldsymbol{e}}^{3+}_{\phi,v} \right) \cdot \boldsymbol{W}_{l,m} \left(\mathsf{R}_0 \cdot \hat{\boldsymbol{k}}^{3+}_{v} \right) a'^{N}_{lm} \right] \end{aligned} \tag{3.56}$$

Equation (3.56) again requires only one sixth of the amount of work that is needed for (3.48). Indeed, there are six new radiation patterns, but each of them requires six times less work. The disaggregation is entirely analogous to the aggregation.

3.4.2 A Faster Aggregation for the Vectorial Case: Method 2

The (dis)aggregation in the vectorial case can also be accelerated in a different way. This method does not use the inversion properties of the vector spherical harmonics, but rather uses the transformation properties under the curl operator. This method is easier to implement and slightly faster than method 1. The aggregation, given by

(3.48) and (3.49), can be concisely written as:

$$\begin{bmatrix} \hat{\boldsymbol{e}}_{\phi,v}^{ps} \cdot \boldsymbol{\Theta}_v^{ps} \\ \hat{\boldsymbol{e}}_{\theta,v}^{ps} \cdot \boldsymbol{\Theta}_v^{ps} \end{bmatrix} = \sum_{l=0}^{L} \sum_{m=-l}^{l} \begin{bmatrix} A_{\phi,v}^{M,p,s,l,m} & A_{\phi,v}^{N,p,s,l,m} \\ A_{\theta,v}^{M,p,s,l,m} & A_{\theta,v}^{N,p,s,l,m} \end{bmatrix} \cdot \begin{bmatrix} a_{l,m}^{M} \\ a_{l,m}^{N} \end{bmatrix}, \tag{3.57}$$

with:

$$A_{\theta,v}^{M,p,s,l,m} = j^l \hat{\boldsymbol{e}}_{\theta,v}^{ps} \cdot \boldsymbol{X}_{l,m}\left(\hat{\boldsymbol{k}}_v^{ps}\right), \tag{3.58}$$

$$A_{\theta,v}^{N,p,s,l,m} = j^l \hat{\boldsymbol{e}}_{\theta,v}^{ps} \cdot \left[-j\boldsymbol{W}_{l,m}\left(\hat{\boldsymbol{k}}_v^{ps}\right)\right], \tag{3.59}$$

$$A_{\phi,v}^{M,p,s,l,m} = j^l \hat{\boldsymbol{e}}_{\phi,v}^{ps} \cdot \boldsymbol{X}_{l,m}\left(\hat{\boldsymbol{k}}_v^{ps}\right), \tag{3.60}$$

$$A_{\phi,v}^{N,p,s,l,m} = j^l \hat{\boldsymbol{e}}_{\phi,v}^{ps} \cdot \left[-j\boldsymbol{W}_{l,m}\left(\hat{\boldsymbol{k}}_v^{ps}\right)\right]. \tag{3.61}$$

As stated before, the unit vectors $\hat{\boldsymbol{e}}_{\theta,v}^{ps}$ and $\hat{\boldsymbol{e}}_{\phi,v}^{ps}$ are orthogonal to each other and to $\boldsymbol{k}_v^{ps}$. As a consequence:

$$\hat{\boldsymbol{e}}_{\theta,v}^{ps} \times \left(\boldsymbol{k}_v^{ps} \times \hat{\boldsymbol{e}}_{\phi,v}^{ps}\right) = \boldsymbol{k}_v^{ps}\left(\hat{\boldsymbol{e}}_{\theta,v}^{ps} \cdot \hat{\boldsymbol{e}}_{\phi,v}^{ps}\right) - \hat{\boldsymbol{e}}_{\phi,v}^{ps}\left(\hat{\boldsymbol{e}}_{\theta,v}^{ps} \cdot \boldsymbol{k}_v^{ps}\right) \tag{3.62}$$

$$= 0 \tag{3.63}$$

which yields, with the fact that $\hat{\boldsymbol{e}}_{\phi,v}^{ps}$ and $\hat{\boldsymbol{e}}_{\theta,v}^{ps}$ have unit length:

$$\boldsymbol{k}_v^{ps} \times \hat{\boldsymbol{e}}_{\phi,v}^{ps} = \pm k \hat{\boldsymbol{e}}_{\theta,v}^{ps} \tag{3.64}$$

The sign can be chosen freely, but it is convenient to work with a plus sign, since that is similar to the usual unit vectors in spherical coordinates. As a consequence:

$$\boldsymbol{k}_v^{ps} \times \hat{\boldsymbol{e}}_{\phi,v}^{ps} = k \hat{\boldsymbol{e}}_{\theta,v}^{ps} \tag{3.65}$$

$$\hat{\boldsymbol{e}}_{\theta,v}^{ps} \times \boldsymbol{k}_v^{ps} = k \hat{\boldsymbol{e}}_{\phi,v}^{ps} \tag{3.66}$$

$$k\hat{\boldsymbol{e}}_{\phi,v}^{ps} \times \hat{\boldsymbol{e}}_{\theta,v}^{ps} = \boldsymbol{k}_v^{ps} \tag{3.67}$$

This particular choice explains why $\hat{\boldsymbol{e}}_{\theta,v}^{ps}$ has the additional factor s in (3.47):

$$\boldsymbol{k}_v^{ps} \times \hat{\boldsymbol{e}}_{\phi,v}^{ps} = k \hat{\boldsymbol{e}}_{\theta,v}^{ps} = \mathsf{R}_0^{-1} \cdot \mathsf{R}(\frac{2p\pi}{3}, \hat{\boldsymbol{e}}_z) \cdot \mathsf{R}_0 \cdot \left[s\boldsymbol{k}_v^{3+} \times \hat{\boldsymbol{e}}_{\phi,v}^{3+}\right] \tag{3.68}$$

$$= sk\mathsf{R}_0^{-1} \cdot \mathsf{R}(\frac{2p\pi}{3}, \hat{\boldsymbol{e}}_z) \cdot \mathsf{R}_0 \cdot \hat{\boldsymbol{e}}_{\theta,v}^{3+} \tag{3.69}$$

With this choice, it can be easily shown that:

$$A_{\phi,v}^{M,p,s,l,m} = -j^l(\frac{\boldsymbol{k}_v^{ps}}{k} \times \hat{\boldsymbol{e}}_{\theta,v}^{ps}) \cdot \boldsymbol{X}_{l,m}\left(\hat{\boldsymbol{k}}_v^{ps}\right) = jA_{\theta,v}^{N,p,s,l,m} \tag{3.70}$$

$$A_{\phi,v}^{N,p,s,l,m} = j^{l+1}(\frac{\boldsymbol{k}_v^{ps}}{k} \times \hat{\boldsymbol{e}}_{\theta,v}^{ps}) \cdot \boldsymbol{W}_{l,m}\left(\hat{\boldsymbol{k}}_v^{ps}\right) = jA_{\theta,v}^{M,p,s,l,m} \tag{3.71}$$

So (3.57) becomes:

$$\begin{bmatrix} -j\hat{\boldsymbol{e}}_{\phi,v}^{ps} \cdot \boldsymbol{\Theta}_v^{ps} \\ \hat{\boldsymbol{e}}_{\theta,v}^{ps} \cdot \boldsymbol{\Theta}_v^{ps} \end{bmatrix} = \sum_{l=0}^{L} \sum_{m=-l}^{l} \begin{bmatrix} A_{\theta,v}^{N,p,s,l,m} & A_{\theta,v}^{M,p,s,l,m} \\ A_{\theta,v}^{M,p,s,l,m} & A_{\theta,v}^{N,p,s,l,m} \end{bmatrix} \cdot \begin{bmatrix} a_{l,m}^M \\ a_{l,m}^N \end{bmatrix} \tag{3.72}$$

It is worthwhile to point out that the 2×2 matrix occurring in (3.72) is circulant and can thus be diagonalized by means of the 2×2 Fourier matrix. After some calculations, this yields:

$$(-j\hat{\boldsymbol{e}}_{\phi,v}^{ps} \pm \hat{\boldsymbol{e}}_{\theta,v}^{ps}) \cdot \boldsymbol{\Theta}_v^{ps} = \frac{1}{2} \sum_{l=0}^{L} \sum_{m=-l}^{l} \left(A_{\theta,v}^{N,p,s,l,m} \pm A_{\theta,v}^{M,p,s,l,m}\right) \left(a_{l,m}^M \pm a_{l,m}^N\right) \tag{3.73}$$

This expression allows to reduce the amount of work associated with the aggregations by a factor two. It also exposes some fundamental aspects of vector multipoles. For example consider the vector multipole translation matrix as given in (3.42). This matrix is block-circulant and can thus also be block-diagonalized by means of the 2×2 Fourier matrix. This yields

$$\begin{bmatrix} \boldsymbol{b}^M + \boldsymbol{b}^N \\ \boldsymbol{b}^M - \boldsymbol{b}^N \end{bmatrix} = \begin{bmatrix} \alpha_{MM}^h + \alpha_{NM}^h & 0 \\ 0 & \alpha_{MM}^h - \alpha_{NM}^h \end{bmatrix} \cdot \begin{bmatrix} \boldsymbol{a}^M + \boldsymbol{a}^N \\ \boldsymbol{a}^M - \boldsymbol{a}^N \end{bmatrix} \tag{3.74}$$

This allows a two times faster application of the vector multipole translation matrix. Another example can be found in [14]: the recurrences for the calculation of the vector multipole translation matrices α_{MM}^h and α_{MN}^h are coupled, but they can be decoupled by using $\alpha_{MM}^h \pm \alpha_{MN}^h$ instead. As for the vector multipoles themselves, this block-diagonalization of the vector multipole translation matrix is a change of basis which boils down to using using the combinations $\boldsymbol{M}_{lm}^f \pm \boldsymbol{N}_{lm}^f$ instead of $\boldsymbol{M}_{lm}^f$ and $\boldsymbol{N}_{lm}^f$. All this is caused by the transformation properties of $\boldsymbol{M}_{lm}^f \pm \boldsymbol{N}_{lm}^f$ under the curl operator:

$$\check{\boldsymbol{\nabla}} \times \left[\boldsymbol{M}_{lm}^f \pm \boldsymbol{N}_{lm}^f\right] = k\left[\boldsymbol{N}_{lm}^f \pm \boldsymbol{M}_{lm}^f\right] = \pm k\left[\boldsymbol{M}_{lm}^f \pm \boldsymbol{N}_{lm}^f\right] \tag{3.75}$$

Apparently $\boldsymbol{M}_{lm}^f + \boldsymbol{N}_{lm}^f$ and $\boldsymbol{M}_{lm}^f - \boldsymbol{N}_{lm}^f$ are eigenfunctions of the curl operator with eigenvalues $+k$ and $-k$ respectively. Any electromagnetic field in a source-free region is a superposition of vector multipoles $\boldsymbol{M}_{lm}^j$ and $\boldsymbol{N}_{lm}^j$ and can thus be decomposed

into a part with eigenvalue $+k$ and a part with eigenvalue $-k$ with respect to the curl operator. This is the so-called Beltrami-decomposition of the electromagnetic field [15, 16]. Because the curl operator commutes with the translation operator, these parts will remain separated under translation. Indeed, applying the curl before or after translation of one of the parts must yield the same result, so no mixing of the two parts can take place under translation. Therefore, the vector multipole translation matrix cannot contain coupling between $\boldsymbol{M}_{lm}^{f} + \boldsymbol{N}_{lm}^{f}$ and $\boldsymbol{M}_{lm}^{f} - \boldsymbol{N}_{lm}^{f}$ fields. For the aggregation, no mixing will occur if the plane waves (to which the aggregation is done) are also eigenfunctions of the curl operator. Although not explicitly visible, this is already the case in (3.73). To show this, Eqn. (3.73) is rewritten as:

$$\begin{aligned}&\left(-j\hat{\boldsymbol{e}}_{\phi,v}^{ps} \pm \hat{\boldsymbol{e}}_{\theta,v}^{ps}\right) \cdot \boldsymbol{\Theta}_{v}^{ps} \\ &\qquad = \frac{1}{4}\sum_{l=0}^{L}\sum_{m=-l}^{l} j^{l}\left(-j\hat{\boldsymbol{e}}_{\phi,v}^{ps} \pm \hat{\boldsymbol{e}}_{\theta,v}^{ps}\right) \cdot \boldsymbol{V}_{l,m}^{\mp}\left(\hat{\boldsymbol{k}}_{v}^{ps}\right)\left[a_{l,m}^{M} \pm a_{l,m}^{N}\right] \end{aligned} \tag{3.76}$$

with $\boldsymbol{V}_{l,m}^{\pm}(\cdot)$ defined in Eqn. (A.80). From this it is seen that the plane waves have the form

$$\boldsymbol{V}_{l,m}^{\mp}\left(\hat{\boldsymbol{k}}_{v}^{ps}\right) e^{-j\boldsymbol{k}_{v}^{ps}\cdot\boldsymbol{r}} \tag{3.77}$$

and it can be verified easily that these plane waves are eigenfunctions of the curl operator:

$$\check{\boldsymbol{\nabla}} \times \left[\boldsymbol{V}_{l,m}^{\mp}\left(\hat{\boldsymbol{k}}_{v}^{ps}\right) e^{-j\boldsymbol{k}_{v}^{ps}\cdot\boldsymbol{r}}\right] = \pm k\boldsymbol{V}_{l,m}^{\mp}\left(\hat{\boldsymbol{k}}_{v}^{ps}\right) e^{-j\boldsymbol{k}_{v}^{ps}\cdot\boldsymbol{r}} \tag{3.78}$$

A similar block-diagonalization as the one for the aggregation can also be done for the disaggregation, yielding an acceleration by a factor two. The dependencies (3.16) can now be used again to obtain further acceleration by a factor three, resulting in a total acceleration by a factor six. Unfortunately, the inversion properties (A.60) and (A.61) of the vector harmonics cannot be used any more because $\boldsymbol{M}_{lm}^{f} \pm \boldsymbol{N}_{lm}^{f}$ are *not* eigenfunctions of the inversion operator. Indeed, the inversion and curl operator do not commute, so their eigenfunctions cannot be the same.

The method described here is slightly faster than the method from Section 3.4.1. This is because the factor two from the block-diagonalization of the (dis)aggregation is almost completely free of any overhead. Just combine the $a_{l,m}^{M}$ and $a_{l,m}^{N}$ into $a_{l,m}^{M} \pm a_{l,m}^{N}$ before the start of the entire FMM and the two sets of coefficients remain completely independent until the FMM is finished. This also permits running the FMM on two processors without any communication between them, with perfect load balancing. Moreover, the second method is easier to implement. It is worthwhile to point out that the gain from using eigenfunctions of the curl operator is not limited to evanescent wave solvers. In fact it can be used in *any* vectorial FMM in

electromagnetics, including the MLFMA (faster (dis)aggregation if both electric and magnetic currents are present) and LF-FMMs (all translation matrices become block-diagonal, as shown in (3.74), yielding a factor two). Finally, in the method described here the $\boldsymbol{k}_v^{p+}$ and $\boldsymbol{k}_v^{p-}$ radiation patterns do not couple. So if for example only radiation pattern $\boldsymbol{k}_v^{2+}$ is required, only the three $\boldsymbol{k}_v^{p+}$ patterns will be calculated. As a consequence an asymptotic factor 2 is still gained compared to the direct method.

An operation count as in Section 3.3 will now be performed. The operation count for doing the rotation on the two sets of coefficients is:

$$2\sum_{l=1}^{L}(2l+1)^2 = \frac{2}{3}\left(4L^3+12L^2+11L\right) \tag{3.79}$$

The operation count for the construction of the new radiation patterns clearly is $4V(L^2+2L)$. The postprocessing step requires $36V$ multiplications. The total cost is thus:

$$\frac{2}{3}\left(4L^3+12L^2+11L\right)+4V(L^2+2L+9) \tag{3.80}$$

The cost without acceleration is $24V(L^2+2L)$. Therefore, the value of V for which the proposed method is faster than the one without acceleration is given by:

$$V > \frac{L}{6}\frac{4L^2+12L+11}{5L^2+10L-9} \tag{3.81}$$

Equation (3.81) is always satisfied if $L < 7$, because the right hand side is certainly smaller than 1 which is smaller than V. Moreover, $V = \mathcal{O}\left(L^2\right)$ again assures that equation (3.81) is also satisfied for larger L. Therefore it is safe to say that for any L, the method presented in 3.4.2 is faster than the direct approach. This will also be validated in section 3.6. The acceleration factor is given by:

$$\frac{24V(L^2+4L)}{\frac{3}{2}\left(4L^3+12L^2+11L\right)+4V(L^2+4L+9)} \tag{3.82}$$

Again for large L, $V = \mathcal{O}\left(L^2\right)$ so the acceleration factor becomes six.

3.5 Extension to N axes

The rotation method described in the above can be generalized to a case where N axes are located on a cone as in Figure 3.3. This generalization will be demonstrated for the scalar case only, but evidently it can be used for the vectorial case as well. The

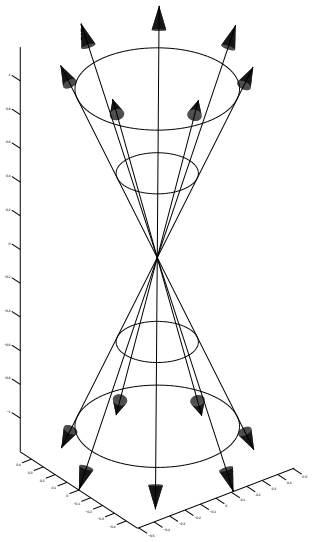

Figure 3.3: An example configuration with seven axes.

formula for $\boldsymbol{k}_v^{ps}$ becomes

$$\boldsymbol{k}_v^{ps} = \mathsf{R}_0^{-1} \cdot \left[s\mathsf{R}(\frac{2p\pi}{N}, \hat{\boldsymbol{e}}_z) \right] \cdot \mathsf{R}_0 \cdot \boldsymbol{k}_v^{N+} \;\; \forall s \in \{-1, +1\} \;\; \forall p \in \{1, ..., N\} \quad (3.83)$$

with R_0 the rotation matrix which rotates the reference frame to a new frame in which the symmetry axis of the cone is the new z-axis. When all the steps of the method are repeated, the following expression is obtained:

$$\Theta_v^{ps} = \sum_{r=0}^{1} \sum_{q=0}^{N} s^r e^{iq\frac{2p\pi}{N}} \Gamma_v^{rq} \quad (3.84)$$

Here, Γ_v^{rq} are $2N$ new radiation patterns, which each require $2N$ times less work than one 'normal' pattern. Therefore the total amount of work for evaluating the Γ_v^{rq} is independent of the number of axes N. The recombination step is the only remaining step and can be done with an FFT. Indeed, the sum over q represents precisely an inverse FFT.

3.6 Results

The vectorial stable plane wave method was applied to the scattering from spheres [17]. In particular the T-matrix method was used, described in detail in [18], which was then accelerated with the vectorial stable plane wave method. The multipole-to-plane-wave and plane-wave-to-multipole operations are natural parts of this algorithm. A uniform discretization of the evanescent integral in both of the integration variables was used. This technique is discussed briefly in [6]. The method from Section 3.4.2 was used to speed up the (dis)aggregation. Figure 3.4 shows the acceleration factor of the (dis)aggregation from the multipole sources on the spheres to the evanescent plane wave radiation patterns of the lowest-level boxes as a function of the multipole order L used on the spheres. The acceleration factor is defined here as the time needed for the direct scheme ((3.49) and (3.48)) divided by the time needed for the newly proposed method from Section 3.4.2. As can be seen, the curves show strong fluctuations. This

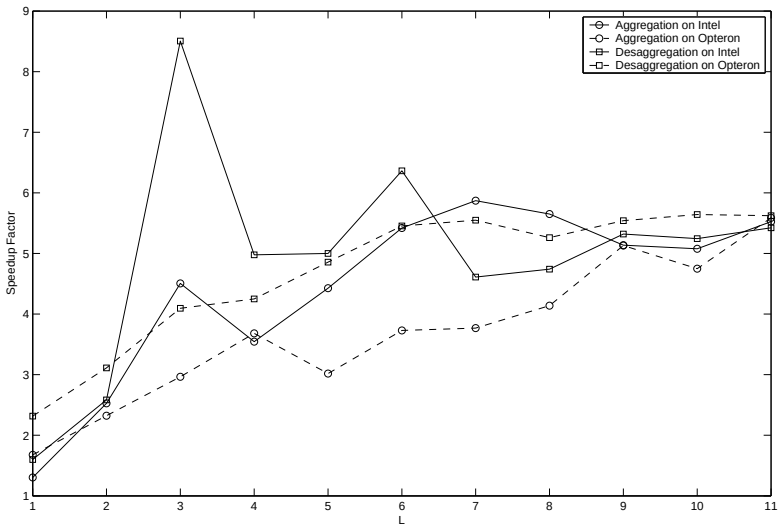

Figure 3.4: The acceleration factor of Method 2 for the vectorial case as a function of L. The Intel processor is a Pentium 4, 2.40GHz and the other processor is an Opteron 270.

is caused by peculiarities in the hardware because when the code is run on two different processors (an Intel Pentium 4, 2.40GHz and an AMD Opteron 270), the curves behave differently. However, it is clear that the acceleration factor grows towards six with increasing multipole order for all the curves.

In order to assess the acceleration directly in the context of the stable plane wave method, a typical multiple scattering problem was solved. The problem consists of $8 \times 4 \times 4 = 128$ spheres with radius 5cm on a rectangular grid with period 15cm. The spheres have a relative permittivity of 12 and a relative permeability of 1. Figure 3.5

shows the geometry of the problem. This scattering problem was solved for various accuracies at a frequency of 0.5GHz, so the aggregation is in the LF regime. The accuracy setting has an influence on both the stable plane wave method and on the multipole order that is necessary to represent the fields on the spheres. In this test, for every multipole order L between 1 and 9, the accuracy obtained by an exact solver was measured, and the stable plane wave method was set to deliver this accuracy. For each box, all the radiation patterns were calculated, so that the results would be more representative for larger scattering problems. The stable plane wave method used one level with translations. Figure 3.6 shows a logarithmic plot of the iteration time and accuracy as a function of the multipole order for both the direct aggregation method and the method from Section 3.4.2. From 3.6 it is visible that the acceleration in this problem saturates at approximately a factor four. This is caused by the fact that the other operations (near interactions, translation) also add computational cost. Since these operations are not accelerated, this has a negative effect on the acceleration.

3.7 Conclusion

A novel method has been proposed that accelerates the multipole-to-plane-wave and plane-wave-to-multipole operations in the stable plane wave method. The fact that the Wigner D-matrices become diagonal for rotations around the z-axis has been exploited to obtain a acceleration of a factor six. Apart from some overhead which becomes negligible for not-too-small multipole orders, this reduces the computational cost of the six (dis)aggregations of the stable plane wave method to the cost of only one. The method has also been extended to the vectorial case and to the case with N axes. For the vectorial case, two possible methods have been proposed. The first is very similar to the scalar case, the second uses the Beltrami decomposition of the electromagnetic field. This second method permits splitting the vectorial FMM into two completely independent FMMs, including the (dis)aggregation from multipoles. As a consequence, some of the overhead associated with the new method is eliminated and this results in a method which is faster than the direct approach for any multipole order. These results have been shown both theoretically and numerically. The Beltrami decomposition is also valid for any vectorial FMM, still yielding an acceleration of a factor two.

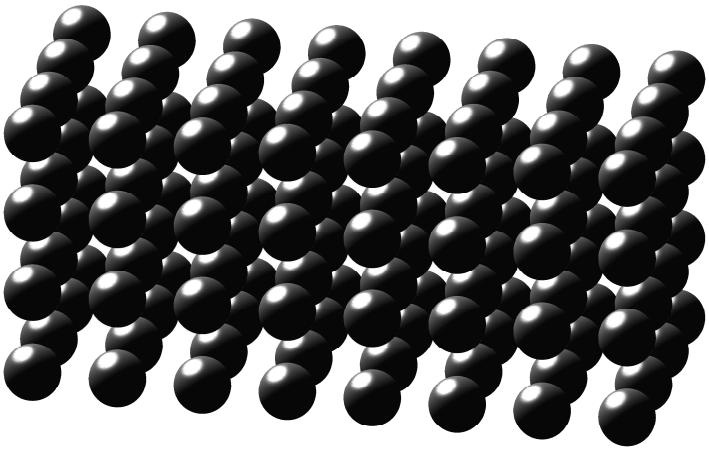

Figure 3.5: The geometry for testing the performance of the new method in the stable plane wave method. The spheres with radius 5cm and permittivity 12 are located on a $8 \times 4 \times 4$ grid with period 15cm. The frequency is 0.5GHz.

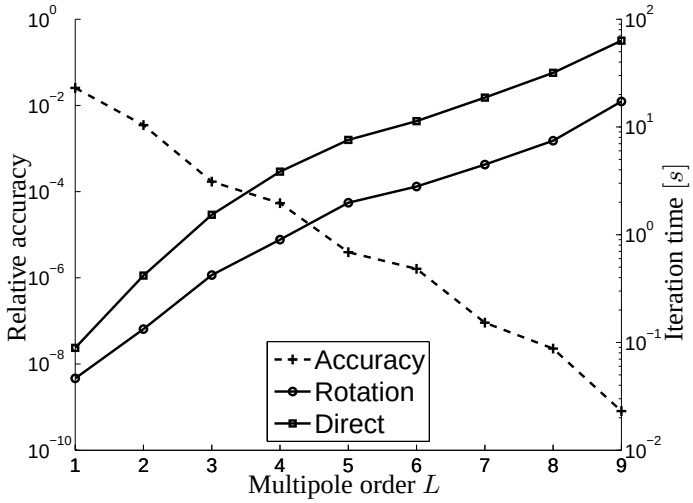

Figure 3.6: The accuracy and time required for 1 iteration as a function of the multipole order L. The scattering geometry is shown in 3.5.

Bibliography

[1] V. Rokhlin. *Rapid solution of integral equations of classical potential theory*, volume 60. J. Comp. Phys., 1985.

[2] L. Greengard. *The rapid evaluation of potential fields in particle systems*. The MIT Press, 1987.

[3] V. Rokhlin. Diagonal forms of translation operators for the helmholtz equation in three dimensions. *Applied and Computational Harmonic Analysis*, 1(1):82–93, 1993.

[4] L. Greengard, J. Huang, V. Rokhlin, and S. Wandzura. Accelerating Fast Multipole Methods for the Helmholtz Equation at Low Frequencies. *Computing in Science and Engineering*, 5(3):32–38, July-September 1998.

[5] W.C. Chew, J.M. Jin, E. Michielssen, and J. Song. *Fast and Efficient Algorithms in Computational Electromagnetics*. Artech House, 2001.

[6] E. Darve and P. Havé. A fast multipole method for Maxwell equations stable at all frequencies. *Philosophical Transactions of the Royal Society A*, 362(1816):603–628, Mar 2004.

[7] I. Bogaert, D. Pissoort, and F. Olyslager. A normalized plane wave method for 2-D Helmholtz problems. *Microwave and Optical Technology Letters*, 48(2):237–243, February 2006.

[8] E. Darve and P. Havé. Efficient fast multipole method for low-frequency scattering. *Journal of Computational Physics*, 197(1):341–363, June 2004.

[9] H. Cheng, W.Y. Crutchfield, Z. Gimbutas, L.F. Greengard, J.F. Ethridge, J. Huang, V. Rokhlin, N. Yarvin, and J. Zhao. A wideband fast multipole method for the Helmholtz equation in three dimensions. *Journal of Computational Physics*, 216(1):300–325, 2006.

[10] L.J. Jiang and W.C. Chew. A mixed-form fast multipole algorithm. *IEEE Transactions on Antennas and Propagation*, 53(12):4145–4156, Dec 2005.

[11] L.J. Jiang and W.C. Chew. Low-frequency fast inhomogeneous plane-wave algorithm (LF-FIPWA). *Microwave and Optical Technology Letters*, 40(2):117–122, Jan 2004.

[12] T.F. Eibert. A Diagonalized Multilevel Fast Multipole Method With Spherical Harmonics Expansion of the k-space integrals. *IEEE Trans. Antennas Propag.*, 53(2):814–817, February 2005.

[13] R.C. Wittmann. Spherical wave operators and the translation formulas. *IEEE Transactions on Antennas and Propagation*, 36(8):1078–1087, Aug 1988.

[14] W.C. Chew and Y.M. Wang. Efficient Ways to compute the Vector Addition Theorem. *Journal of Electromagnetic Waves and Applications*, 7(5):651–665, 1993.

[15] A. Lakhtakia. *Beltrami Fields in Chiral Media*. World Scientific Publishing Co. Pte. Ltd., P O Box 128, Farrer Road, Singapore 9128, 1994.

[16] A. Lakhtakia, V.K. Varadan, and V.V. Varadan. *Time-Harmonic Electromagnetic Fields in Chiral Media*. World Scientific Publishing Co. Pte. Ltd., P O Box 128, Farrer Road, Singapore 9128, 1994.

[17] I. Bogaert and F. Olyslager. Full-wave analysis of a finite piece of metamaterial. In *Proceedings of the International Student Seminar on Microwave Applications of Novel Physical Phenomena*, pages 47–49, Rovaniemi, Finland, 24-25 August 2006.

[18] M.I. Mishchenko, J.W. Hovenier, and L.D. Travis. *Light Scattering by Non-spherical Particles: Theory, Measurements, and Applications*. Academic Press, San Diego, 2000.

CHAPTER 4

A Normalized Plane Wave Method for 2-D Helmholtz Problems

I. Bogaert, D. Pissoort, and F. Olyslager

Published in *Microwave and Optical Technology Letters, 48 (2):237–243, Feb. 2006.*

★★★

Although the FMMs using the spectral decomposition of the Green function can be used for basically all frequencies, the fact that six radiation patterns are needed for each box limits the efficiency of these methods. Indeed, there is some overlap in the validity regions of the six representations of the radiated fields. As a consequence, some of the points in the six representations must be redundant. The MLFMA is nondirective, i.e. it requires only one radiation pattern, and is thus more efficient in this respect. However, the MLFMA fails due to numerical reasons if the boxes get too small compared to the wavelength. It is therefore useful to try to understand and control the numerical instability of the MLFMA. In this way, it is possible to find an intermediary algorithm that combines the stability of the spectral methods with the non-directivity of the MLFMA. In the following, such an algorithm for the 2-D case is developed.

4.1 Introduction

The basic problem that will be addressed in this work is the 2-D scattering of electromagnetic waves, i.e. a 2-D Helmholtz problem. This scattering problem can always be written as an integral equation in which a convolution occurs with the 2-D Green

function. All sources and fields are assumed time-harmonic; temporal dependencies $e^{j\omega t}$ are suppressed. Therefore, the 2-D Green function is given by the cylindrical Hankel function of the second kind and zeroth order [1]. The Method of Moments (MoM) reduces the continuous integral equation to a linear system of equations of dimension N. However, often, problems involve so many unknowns that direct methods to solve the linear system, e.g., LU-decomposition, are too slow because of their $\mathcal{O}\left(N^3\right)$ computational complexity. The brute-force application of iterative solvers, e.g., the biconjugate gradient method, permits to solve the linear system in $\mathcal{O}\left(PN^2\right)$ operations, where P is the number of iterations required by the iterative solver to reduce the residual error below a preset threshold. The computational cost can be reduced dramatically by applying a fast multiplication scheme, e.g. an FMM. At this point, a distinction has to be made between low-frequency problems (e.g., microwave integrated circuits), which are physically small compared to the wavelength but require many unknowns because of the small geometrical details, and high-frequency problems (e.g., antenna arrays), which are large in comparison to the wavelength.

Consider the configuration depicted in Fig. 4.1, comprising a source and an observation point residing at $\boldsymbol{\rho}_i$ and $\boldsymbol{\rho}_j$ which are part of square source and observation boxes centered about $\boldsymbol{\rho}_l$ and $\boldsymbol{\rho}_{l'}$, respectively. The core of the 2-D low-frequency fast multipole method (LF-FMM) is the multipole expansion of the Hankel function [2]

$$H_0^{(2)}(k\rho_{ji}) \approx \sum_{n=-K}^{K} \sum_{m=-K}^{K} \left[\beta(\boldsymbol{\rho}_{jl'})\right]_{0n} \left[\alpha(\boldsymbol{\rho}_{l'l}))\right]_{nm} \left[\beta(\boldsymbol{\rho}_{li})\right]_{m0}. \quad (4.1)$$

Here, $\boldsymbol{\rho}_{ab}$ is a shorthand notation for $\boldsymbol{\rho}_b - \boldsymbol{\rho}_a$, ρ and ϕ are defined by $\boldsymbol{\rho} = \rho\cos\phi\boldsymbol{u}_x + \rho\sin\phi\boldsymbol{u}_y$ and $k = \omega\sqrt{\epsilon\mu}$ is the wavenumber; K is the multipole order above which the series is truncated. The α and β matrices are defined in terms of Hankel and Bessel

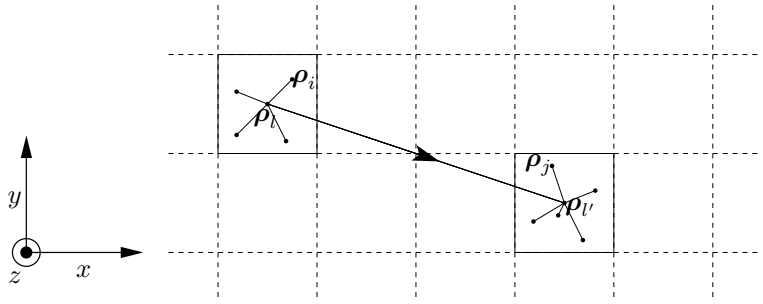

Figure 4.1: The arrangement of the position vectors for two interacting groups.

functions as

$$\left[\alpha(\boldsymbol{\rho})\right]_{nm} = H_{n-m}^{(2)}(k\rho)e^{j(n-m)\phi}, \quad (4.2a)$$

$$\left[\beta(\boldsymbol{\rho})\right]_{nm} = J_{n-m}(k\rho)e^{j(n-m)\phi}. \quad (4.2b)$$

Expression (4.1) can be generalized to the expansion of higher order Hankel functions as follows

$$\alpha(\boldsymbol{\rho}_{ji}) = \underbrace{\beta(\boldsymbol{\rho}_{jl'})}_{Disaggregation} \cdot \underbrace{\alpha(\boldsymbol{\rho}_{l'l})}_{Translation} \cdot \underbrace{\beta(\boldsymbol{\rho}_{li})}_{Aggregation} \tag{4.3}$$

For low-frequency problems the implementation of 4.3 into a multilevel scheme immediately leads to a matrix-vector multiplication with a computational complexity that scales as $\mathcal{O}(N)$. For very-low-frequency problems, i.e., very small $k\rho$, the Hankel and Bessel functions in (4.2a) and (4.2b) become very large and very small, respectively, resulting in overflow and underflow errors. However, this problem easily can be solved using an appropriate normalization [2]. Although the computational cost scales as $\mathcal{O}(N)$, this scheme is 'slow', i.e., has a large pre-factor, because translations and (dis)aggregations require matrix-vector multiplications with dense matrices α and β.

For the same reason, the application of (4.3) does not lead to a lower computational complexity for high-frequency problems. Indeed, for these problems, the required number of multipoles increases for higher levels according to the formula $K \approx kR + B$, where R is the radius of the circumscribed circle of the square boxes on that level and B is a constant. The cost needed to multiply the dense α or β matrices with a vector is proportional to the square of the number of multipoles. As a consequence, the computational complexity remains $\mathcal{O}\left(N^2\right)$ [2]. To obtain a lower computational complexity for high-frequency problems, it is necessary to use diagonal aggregation, translation, and disaggregation matrices. This can be achieved by expanding the Hankel function into plane waves (i.e. the MLFMA [3, 4])

$$H_0^{(2)}(k\rho_{ji}) = \frac{1}{2Q+1} \sum_{q=-Q}^{Q} e^{jk\rho_{jl'}\cos(\alpha_q - \phi_{jl'})} T_q(k, \rho_{l'l}, \phi_{l'l}) e^{jk\rho_{li}\cos(\alpha_q - \phi_{li})}, \tag{4.4}$$

$$T_q(k, \rho, \phi) = \sum_{p=-Q}^{Q} H_p^{(2)}(k\rho) e^{jp(\phi + \frac{\pi}{2} - \alpha_q)}, \tag{4.5}$$

$$\alpha_q = \frac{2\pi q}{2Q+1}. \tag{4.6}$$

Similar to the number of multipoles, the number of plane waves Q is related to the box size R through $Q \approx 2kR + B'$ with B' another constant.

To reduce the pre-factor for low-frequency problems, it would be very convenient to have diagonal operators for that case as well. Unfortunately, the MLFMA (4.4) breaks down at low frequencies because of a numerical instability caused by round-off errors. Indeed: $H_p^{(2)}(k\rho)$ diverges exponentially as a function of $|p|$ if $|p| > k\rho$. Hence, in (4.5), very large numbers, i.e., $H_p^{(2)}(k\rho)$ for large $|p|$, are added to numbers of the order of unity, i.e., $H_p^{(2)}(k\rho)$ for small $|p|$, and the information in the

smallest numbers is lost. In [5,6] this problem was tackled using inhomogeneous plane waves. In this work, an alternative, conceptually simpler scheme will be presented. In addition, the proposed scheme uses a lot of the machinery from the original LF-FMM, which means that existing low-frequency FMM solvers easily can be modified.

4.2 The MLFMA

In this section, an alternative formulation of the MLFMA will be derived which will allow to remove the numerical instability mentioned at the end of Section 4.1. This formulation starts directly from the truncated form of the addition theorem (4.1). A translation in the LF-FMM corresponds to calculating $\forall n \in [-K, K]$ something of the form

$$\begin{aligned}\Phi_n &= \sum_{m=-K}^{K} \left[\alpha(\boldsymbol{\rho}_{l'l})\right]_{nm} \left[\beta(\boldsymbol{\rho}_{li})\right]_{m0}, \\ &= \sum_{m=-K}^{K} H^{(2)}_{n-m}(k\rho_{l'l}) e^{j(n-m)\phi_{l'l}} J_m(k\rho_{li}) e^{jm\phi_{li}}. \end{aligned} \tag{4.7}$$

As the matrix $\alpha(\boldsymbol{\rho}_{l'l})$ clearly is Toeplitz, the required matrix-vector multiplication can be performed with Fast Fourier Transforms (FFTs). To show this, consider the following identities

$$1 \equiv \sum_{p=-2K}^{2K} \delta_{p,n-m} \quad \forall n, m \in [-K, K], \tag{4.8}$$

$$\delta_{p,n-m} \equiv \frac{1}{4K+1} \sum_{q=-2K}^{2K} e^{-j\frac{2\pi q}{4K+1}[p-(n-m)]} \quad \forall n, m \in [-K, K], \tag{4.9}$$

with $\delta_{i,j}$ the Kronecker delta. By means of (4.8), eq. (4.7) can be re-expressed as

$$\Phi_n = \sum_{m=-K}^{K} \sum_{p=-2K}^{2K} \delta_{p,n-m} H^{(2)}_p(k\rho_{l'l}) e^{jp\phi_{l'l}} J_m(k\rho_{li}) e^{jm\phi_{li}}. \tag{4.10}$$

Replacing $\delta_{p,n-m}$ by the sum in (4.9) and exchanging some summation signs yields a diagonalized form for the translation operator

$$\Phi_n = \sum_{q=-2K}^{2K} \left[\frac{1}{4K+1} \sum_{p=-2K}^{2K} H_p^{(2)}(k\rho_{l'l}) e^{jp\phi_{l'l}} e^{-j\frac{2\pi qp}{4K+1}} \right] \times \left[\sum_{m=-K}^{K} J_m(k\rho_{li}) e^{jm\phi_{li}} e^{-j\frac{2\pi qm}{4K+1}} \right] e^{j\frac{2\pi qn}{4K+1}}. \quad (4.11)$$

All the sums in (4.11) can be calculated using FFTs and, what is even more important, the translations themselves are pointwise multiplications of two functions of q. It is worthwhile to point out that formula (4.11) has the same physical meaning and computational cost as the MLFMA, but that it retains multipoles rather than plane waves as the basis functions for the radiation patterns.

However, this alternative formulation of the plane wave expansion still suffers from the same numerical instability as the original version (4.4). When looking at the summation over p in (4.11), it is obvious that, as $H_p^{(2)}(k\rho)$ grows exponentially larger as a function of p, the lower order terms become swamped in the higher order terms. A similar swamping, but this time of the higher order multipoles, occurs in the sum over m. These numerical instabilities eventually lead to the complete failure of (4.11) for low frequencies. In the original formulation of the MLFMA (4.4), this cannot be corrected [4]. However, the new formulation will allow to derive an expansion that is diagonal and stable at low frequencies.

4.3 A normalized plane wave method

Now we will show how the translation operator can be stably diagonalized in the low-frequency case. Identity (4.8) can be rewritten as

$$1 \equiv \sum_{p=-2K}^{-1} \delta_{p,n-m} t^{|p|} t^{(n-m)} + \sum_{p=0}^{2K} \delta_{p,n-m} t^{|p|} t^{-(n-m)} \quad \forall n, m \in [-K, K], \quad (4.12)$$

with t still a freely chosen number called the normalization factor. This new form of (4.8) has been opted for because of the factor $t^{|p|}$ that also occurs in the asymptotic behavior of $H_p^{(2)}(x)$ if x is small ($x < 1$)

$$\left| H_p^{(2)}(x) \right| \approx \begin{cases} \frac{2^{|p|}(|p|-1)!}{\pi x^{|p|}} & \forall p \neq 0, \\ \frac{2}{\pi} \ln x & p = 0. \end{cases} \quad (4.13)$$

Following the same steps as in the previous section with (4.12) instead of (4.8), the following expression for the matrix-vector-multiplication is found

$$\begin{aligned}\Phi_n = &\sum_{q=-2K}^{2K}\left[\sum_{p=-2K}^{-1}\frac{1}{4K+1}H_p^{(2)}(k\rho_{l'l})t^{|p|}e^{jp\phi_{l'l}}e^{-j\frac{2\pi qp}{4K+1}}\right]\\ &\qquad\times\left[\sum_{m=-K}^{K}J_m(k\rho_{li})e^{jm\phi_{li}}t^{-m}e^{-j\frac{2\pi qm}{4K+1}}\right]t^n e^{j\frac{2\pi qn}{4K+1}}\\ &+\sum_{q=-2K}^{2K}\left[\sum_{p=0}^{2K}\frac{1}{4K+1}H_p^{(2)}(k\rho_{l'l})t^{|p|}e^{jp\phi_{l'l}}e^{-j\frac{2\pi qp}{4K+1}}\right]\\ &\qquad\times\left[\sum_{m=-K}^{K}J_m(k\rho_{li})e^{jm\phi_{li}}t^{m}e^{-j\frac{2\pi qm}{4K+1}}\right]t^{-n}e^{j\frac{2\pi qn}{4K+1}}.\end{aligned}\tag{4.14}$$

This new form (4.14) can be made numerically stable with an appropriate choice of the normalization factor t. Indeed, every Hankel function is accompanied by a factor $t^{|p|}$, allowing it to be normalized. A remarkable feature of (4.14) is the fact that a good normalization for $H_p^{(2)}(x)$ also normalizes $J_m(x)$ relatively well. Consider the asymptotic expansion of the Bessel function for small x

$$|J_m(x)| \approx \frac{x^{|m|}}{2^{|m|}\,|m|!}.\tag{4.15}$$

In the first term of expression (4.14) the summation over m is normalized for $m \geq 0$. The $J_m(x)$ for which $m < 0$, are "anti-normalized", resulting in their rapid loss. However, as can be seen in (4.7), the terms for which $m < 0$ also very rapidly lose *importance* as $|m|$ increases. A detailed analysis shows that the loss of the $J_m(x)$ is approximately compensated by a comparable loss of importance of these terms in (4.7). Here, 'approximately' means that the nett loss does not depend on $k\rho$. In the second term of (4.14), the $J_m(x)$ for which $m \leq 0$, are normalized and the others are anti-normalized. For the same reason, this does not result in a dramatic loss of precision and the numerical instability associated with the summations over m in (4.14) is avoided.

In addition, the matrix-vector-multiplications associated with the aggregation and disaggregation steps in a multilevel scheme can also be diagonalized in a similar way by using variations on (4.8)

- for the aggregations, the following kind of matrix-vector multiplication must be done

$$\Phi_n = \sum_{m=-K}^{K}\left[\beta(\boldsymbol{\rho}_{l'l}))\right]_{nm}\left[\beta(\boldsymbol{\rho}_{li})\right]_{m0},\tag{4.16}$$

$$= \sum_{m=-K}^{K} J_{n-m}(k\rho_{l'l}) e^{j(n-m)\phi_{l'l}} J_m(k\rho_{li}) e^{jm\phi_{li}}. \tag{4.17}$$

The $\beta(\boldsymbol{\rho}_{l'l})$ matrices are also Toeplitz, but the Bessel functions *decay* exponentially as their order increases. Because of this, the powers of t have to be rearranged

$$1 \equiv \begin{cases} t^{|n|} \sum_{p=-2K}^{2K} \delta_{p,n-m} t^{-(p+m)} & \forall n \geq 0, \\ t^{|n|} \sum_{p=-2K}^{2K} \delta_{p,n-m} t^{(p+m)} & \forall n < 0, \end{cases} \tag{4.18}$$

which yields the following diagonal formula

$$\Phi_n = \begin{cases} t^{|n|} \sum\limits_{q=-2K}^{2K} \left[\sum\limits_{p=-2K}^{2K} \frac{1}{4K+1} J_p(k\rho_{l'l}) t^{-p} e^{jp\phi_{l'l}} e^{-j\frac{2\pi qp}{4K+1}} \right] \\ \qquad \times \left[\sum\limits_{m=-K}^{K} J_m(k\rho_{li}) e^{jm\phi_{li}} t^{-m} e^{-j\frac{2\pi qm}{4K+1}} \right] e^{j\frac{2\pi qn}{4K+1}} \quad \forall n \geq 0, \\ t^{|n|} \sum\limits_{q=-2K}^{2K} \left[\sum\limits_{p=-2K}^{2K} \frac{1}{4K+1} J_p(k\rho_{l'l}) t^{p} e^{jp\phi_{l'l}} e^{-j\frac{2\pi qp}{4K+1}} \right] \\ \qquad \times \left[\sum\limits_{m=-K}^{K} J_m(k\rho_{li}) e^{jm\phi_{li}} t^{m} e^{-j\frac{2\pi qm}{4K+1}} \right] e^{j\frac{2\pi qn}{4K+1}} \quad \forall n < 0. \end{cases} \tag{4.19}$$

- for the disaggregations, a similar approach can be applied. Since the multipole expansions that are to be disaggregated increase with growing multipole order, another form of (4.8) is in order

$$1 \equiv \begin{cases} \sum_{p=-2K}^{2K} \delta_{p,n-m} t^{-(n-p)} t^{|m|} & \forall m \geq 0, \\ \sum_{p=-2K}^{2K} \delta_{p,n-m} t^{(n-p)} t^{|m|} & \forall m < 0. \end{cases} \tag{4.20}$$

4.4 Determination of the optimal normalization factor

Having derived normalized diagonal forms for the aggregation, translation, and disaggregation operators, the task ahead is the selection of a suitable, if not optimal, normalization factor t. First consider the following sum, arising in the formula (4.14) for the diagonal translation

$$\sum_{p=0}^{2K} H_p^{(2)}(k\rho) t^{|p|} e^{jp\phi} e^{-j\frac{2\pi lp}{4K+1}}. \tag{4.21}$$

In comparison to the other sums, this sum is much more prone to numerical instability mostly because the Hankel functions $H_p^{(2)}(k\rho)$ *increase* with increasing p. As a con-

sequence, the lowest order terms which contribute the most in the addition theorem (4.3) are lost in the higher order terms. This suggests that (4.21) is the most 'dangerous' summation, and thus the one upon which to base the derivation of t. By choosing t as

$$t = \left| \frac{H_0^{(2)}(k\rho)}{H_{2K}^{(2)}(k\rho)} \right|^{\frac{1}{2K}}, \tag{4.22}$$

the highest and lowest order terms in (4.21) are of the same magnitude. It is worthwhile to point out that the asymptotic expression (4.13) for $H_p^{(2)}(k\rho)$ contains the factorial $(|p|-1)!$. A factorial never can be completely compensated with an exponential function and this implies that $t^{|p|}H_p^{(2)}(k\rho)$ possesses a minimum at $p = \pm p_{min}$. A straightforward calculation shows that this minimum is located at

$$p_{min} = \lceil \frac{k\rho}{2t} \rceil, \tag{4.23}$$

for small $k\rho$ ($k\rho < 1$). Here, $\lceil \cdot \rceil$ is the ceiling function. Since the largest term in (4.21) is $H_0^{(2)}(k\rho)$ which is of about the same magnitude as unity, the ratio of the smallest and largest term is approximately equal to

$$t^{\lceil \frac{k\rho}{2t} \rceil} H_{\lceil \frac{k\rho}{2t} \rceil}^{(2)}(k\rho) \approx \sqrt{\frac{2}{\pi \frac{k\rho}{2t}}} e^{-\frac{k\rho}{2t}}. \tag{4.24}$$

To obtain (4.24), expression (4.13) was used, together with Stirling's formula and the fact that $\lceil \frac{k\rho}{2t} \rceil \approx \frac{k\rho}{2t}$. Also, expression (4.22) for t can be crudely approximated as (again for small $k\rho$ and large K)

$$t \approx \frac{ek\rho}{4K}, \tag{4.25}$$

where e is Euler's number. From this it is clear that the ratio of the smallest and largest term, and thus the loss of precision, depends only upon the number of multipoles used and not on the argument $k\rho$

$$\sqrt{\frac{2}{\pi \frac{k\rho}{2t}}} e^{-\frac{k\rho}{2t}} \approx \sqrt{\frac{e}{\pi K}} e^{-\frac{2K}{e}}. \tag{4.26}$$

For K equal to 25 this yields a maximum loss of precision of about 10 digits for the multipole orders $p = \pm p_{min}$. This seems quite a lot but, as will be shown further on, the loss of precision for the addition theorem (4.1) will turn out to be much less than this because the higher order terms (the ones close to p_{min}) contribute much less to the 2-D Green function than the lower order terms. Hence they do not require the same accuracy.

Now, if the same value for t is used on an entire level, which is desirable because it eliminates the need to do the FFTs for every separate translation, it cannot be expected

that all of the diagonal operators are fully normalized. For example, consider the situation depicted in Fig. 4.2. Translations 1 and 2 respectively translate the multipole pattern over a distance ρ_1 and ρ_2. These distances satisfy the following relation

$$\frac{\rho_1}{\rho_2} = \frac{\sqrt{2}}{3}. \tag{4.27}$$

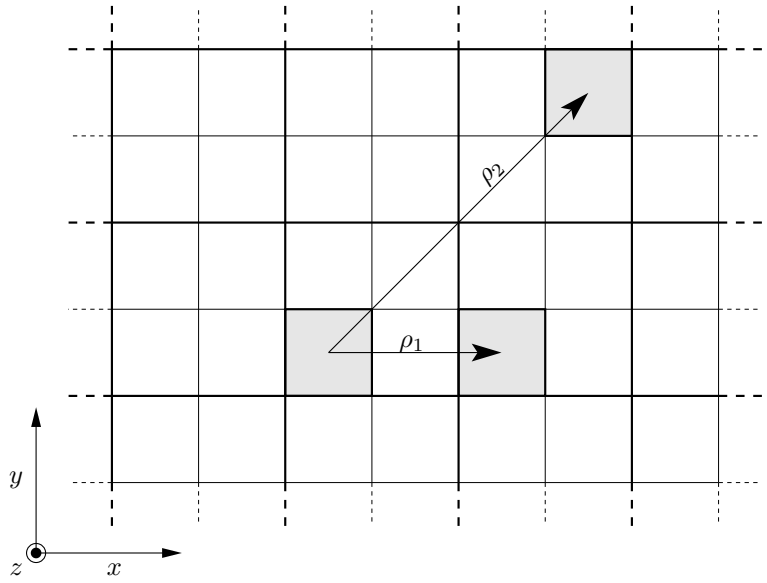

Figure 4.2: The two most extreme translations in 2-D FMM.

If t is chosen to be optimal for translation 2 according to formula (4.22), then t will not be optimal for translation 1. At this point it is important to realize that translation 2 requires less multipoles than translation 1 to achieve the same accuracy. This fact can be exploited by choosing t optimal for the translation over the shortest translation distance, i.e., translation 1. According to (4.22), this normalization factor will be too small for translation 2, resulting in an 'overnormalized' translation operator of which the multipole components *decay* with increasing multipole order. However, the loss of the higher order terms does not result in a loss of precision because we do not need as many multipoles for translation 2 as for translation 1.

This same value for t can also be used for the aggregations (4.18) and disaggregations (4.20). Since all translations on one level are over a distance at least twice as large as the radius of a box on that level, the diagonal aggregation and disaggregation operators will be undernormalized, again resulting in the favorable situation of decaying multipole components. Due to the fact that a value for t can be found which turns all multipole patterns occurring on a certain level in mildly decaying multipole

patterns, the error is controllable over a wide interval of possible values for K. This is illustrated in the next section.

4.5 Results

The method described above has been numerically tested on the situation sketched in Fig. 4.3. This Figure shows a two-level interaction between $\boldsymbol{\rho}_i$ and $\boldsymbol{\rho}_j$ corresponding

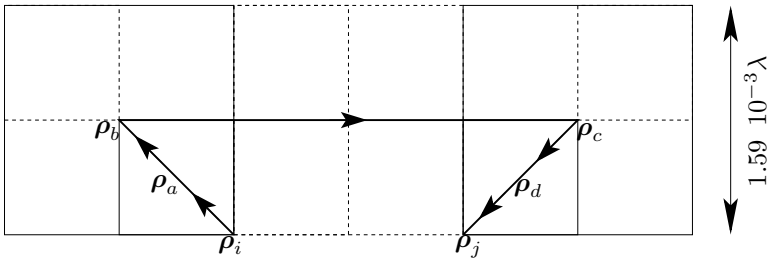

Figure 4.3: Geometry for accuracy testing.

to the following expansion of the Green function

$$H_0^{(2)ADD}(k\rho_{ji}) \approx \sum_{n=-K}^{K} \sum_{m=-K}^{K} \left[\beta(\boldsymbol{\rho}_{jd})\right]_{0n} \left[\beta(\boldsymbol{\rho}_{dc}) \cdot \alpha(\boldsymbol{\rho}_{cb}) \cdot \beta(\boldsymbol{\rho}_{ba})\right]_{nm} \left[\beta(\boldsymbol{\rho}_{ai})\right]_{m0} . \quad (4.28)$$

As all three stages of fast multipole methods occur in this expansion, this configuration is ideal for testing the accuracy of the normalized plane wave method (NPWM) with the diagonal aggregation, translation, and disaggregation stages. Figures 4.4 and 4.5 show the relative error between the direct application of (4.28) and the normalized plane wave method as a function of the normalization factor t for $K = 10$ and $K = 25$. The functions $\Delta(k\rho, t)$ and $\theta(k\rho)$ are relative errors defined as

$$\Delta(k\rho, t) = \left| \frac{H_0^{(2)NPWM}(k\rho, t)}{H_0^{(2)ADD}(k\rho)} - 1 \right|, \quad (4.29)$$

$$\theta(k\rho) = \left| \frac{H_0^{(2)ADD}(k\rho)}{H_0^{(2)}(k\rho)} - 1 \right|. \quad (4.30)$$

In both figures the errors for the shortest and the longest translation as in Fig. 4.2 are plotted. The shortest translation corresponds to translation 1 ($\rho_1 = 3.18\ 10^{-3}\lambda$) and longest translation corresponds to translation 2 ($\rho_2 = 6.75\ 10^{-3}\lambda$), with an additional diagonal aggregation and disaggregation. The two horizontal lines give the relative

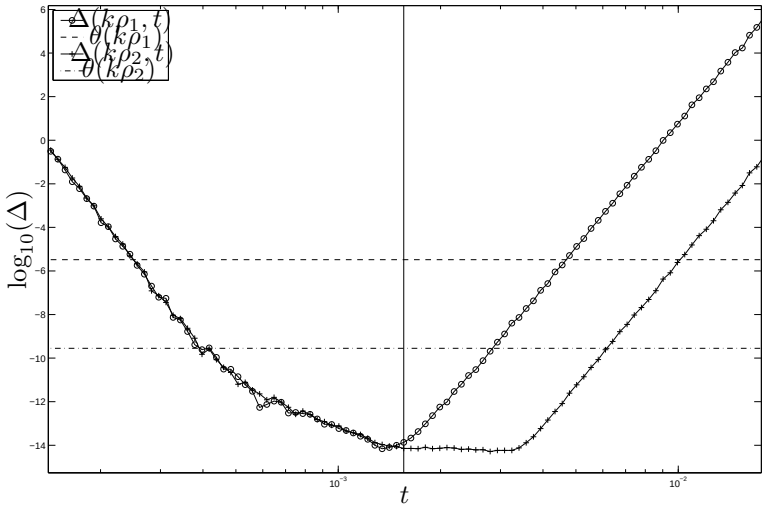

Figure 4.4: Comparison between the addition theorem and the diagonal form of the addition theorem as a function of the normalization factor t for $K = 10$.

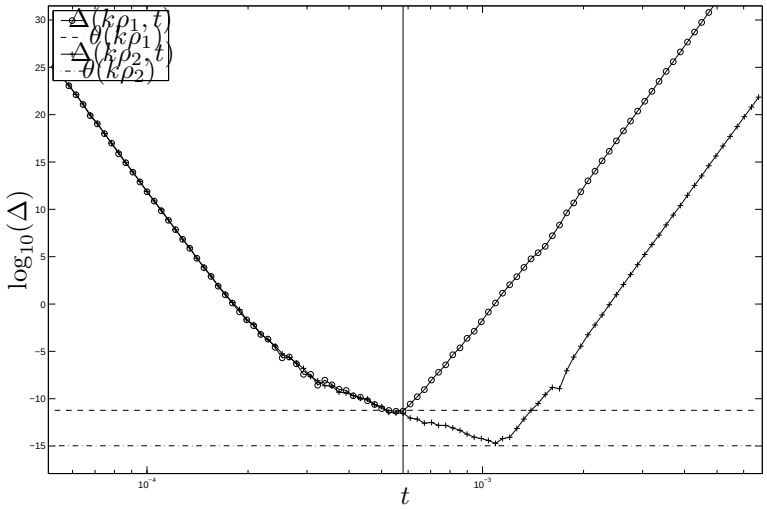

Figure 4.5: Comparison between the addition theorem and the diagonal form of the addition theorem as a function of the normalization factor t for $K = 25$.

errors between the addition theorem (truncated at K multipoles) and the Hankel function for the shortest and longest translations. The vertical line is the optimal value for t obtained with (4.22) and the 'shortest translation' prescription. From this it is clear that the proposed formula for t works very well, since it gives us the almost exact location of the minimum in the error curve. Fig. 4.5 also demonstrates that the achievable accuracy of the normalized plane wave method is high. Indeed, with $K = 25$ both Δ and θ reach 10^{-10}. As a consequence, the error between the normalized plane wave method and the Hankel function is on the order of 10^{-10}.

In the high-frequency regime, t becomes approximately equal to 1, rendering the method equivalent to the MLFMA. Since the normalized plane wave method entails only diagonal operators and FFTs, the method also has the same complexity ($\mathcal{O}(N)$) for the high-frequency regime as the plane wave method. However, in the region between the HF and LF regimes, some care is required. The reasoning which lead to the conclusion that the accuracy of the normalized plane wave method is high supposes that $k\rho < 1$ to make sure that the asymptotic forms (4.13) and (4.15) can be used. In the intermediate frequency zone this is no longer true, and error estimates cannot be easily made. Therefore we resorted to numerical testing. Fig. 4.6 shows Ψ, the best accuracy possible (optimized towards the number of multipoles K) with the normalized plane wave method, as a function of the translation distance $k\rho$

$$\Psi(k\rho) = \left| \frac{H_0^{(2)NPWM}(k\rho, t_{optimal})}{H_0^{(2)}(k\rho)} - 1 \right|. \tag{4.31}$$

This calculation was performed for a geometry similar to the one depicted in Fig. 4.3, but scaled up or down according to the translation distance. It is clear that the method's accuracy is high for both the HF and LF regime, and that the accuracy is slightly more limited in the intermediate region, but not dramatically.

The normalized plane wave method described above has been implemented in a multilevel scheme. For simplicity, only Perfect Electrically Conducting (PEC) targets were used, illuminated by a TM$_z$-polarized wave (for which the electric field is directed parallel with the targets). The simplest integral equation describing this problem is the well-known Electric Field Integral Equation (EFIE), which states that the total electric field vanishes on the surface of the targets

$$\lim_{\boldsymbol{\rho} \to C} \left[E_z^{\mathrm{i}}(\boldsymbol{\rho}) - \frac{\omega\mu}{4} \oint_C H_0^{(2)}(k|\boldsymbol{\rho} - \boldsymbol{\rho}'|) j_z(\boldsymbol{\rho}') \mathrm{d}c' = 0 \right]. \tag{4.32}$$

Here, C is the integration path on the surface of the PEC targets. The unknown quantity is the surface current j_z. The simulated structure consists of a dense arrangement of P^2 PEC cylinders inside a square with size 1 m such as in Fig. 4.7. For all the simulations to come, $P = 51$. The surface current is discretized in terms of a set of N pulse functions. The number of unknowns N then amounts to 65025. The wavelength

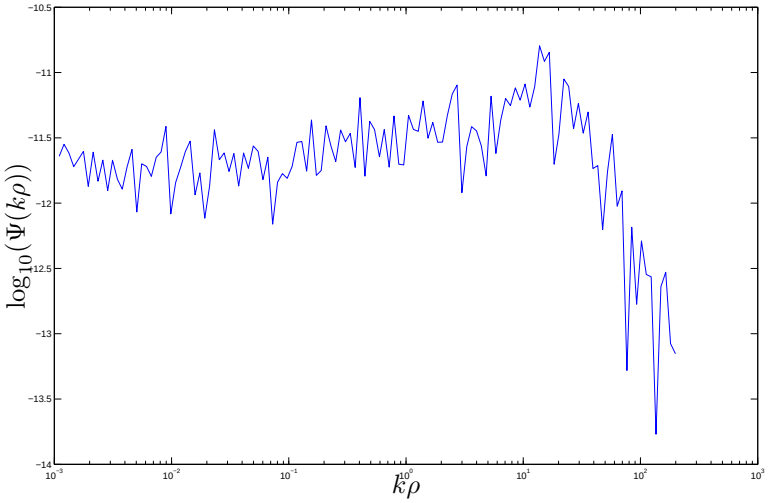

Figure 4.6: The minimal error achievable with the normalized plane wave method as a function of the translation distance.

K	FMM	NPWM
11	0.18	0.08
15	0.30	0.23
20	0.53	0.15

Table 4.1: The cost of the translation stage of the two methods and for different multipole orders.

is 6000 m. The normalized plane wave method is compared to a multipole solver, which acts as a reference. The multipole solver itself is also optimized in the sense that translations that are further away are done with less multipoles than translations that are closer. Table 4.1 shows the CPU time for the translation stage of both the fast multipole method (FMM) and the normalized plane wave method for different multipole orders K. This table shows that for $K = 15$, the cost of the translation stage is even larger than the cost with $K = 20$. This can be explained by looking at the corresponding dimension $4K + 1$ of the FFTs that are required: $4 \cdot 11 + 1 = 45 = 3 \cdot 3 \cdot 5$ and $4 \cdot 20 + 1 = 81 = 3 \cdot 3 \cdot 3 \cdot 3$. These are both products of small primes, but $4 \cdot 15 + 1 = 61$ is prime, so the FFTs will be significantly slower if $K = 15$. The FFTs were done with the FFTW library [7]. Table 4.2 shows the cost of the FFTs and the translations (pointwise multiplications as in (4.14)) This demonstrates that the cost of the translations is indeed rising linearly with the multipole order K. It has to be recognized that the cost associated with the FFTs can vary wildly as a function of K,

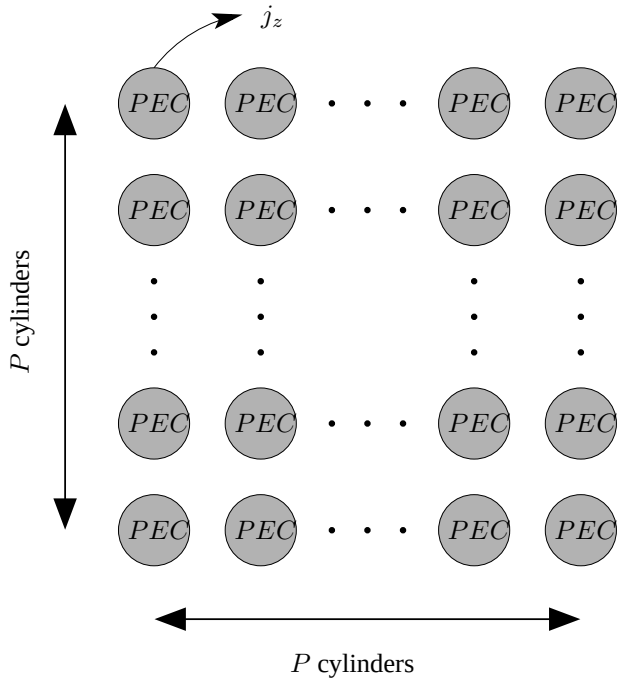

Figure 4.7: The geometry of the simulated structure.

K	FFTs	Transfers
11	0.025	0.06
15	0.15	0.08
20	0.045	0.105

Table 4.2: The cost of the FFTs and the diagonal transfers for different multipole orders.

but even if a value for K is chosen such that $4K + 1$ is prime, the diagonal method is still faster than the traditional fast multipole method.

4.6 Conclusion

In this work, a normalized diagonal form of the addition theorem for multipoles in 2-D is derived. This approach has several merits, such as being more efficient than the low-frequency fast multipole method in the low-frequency regime and having the same complexity as the MLFMA in the high-frequency regime. The normalized plane wave method should thus be interpreted as a generalization of the MLFMA to the intermediate- and low-frequency regime. Moreover, existing multipole solvers easily can be modified to use this new method, since multipoles remain an important part of the normalized plane wave method. The multilevel algorithm is implemented and the computer labor for the translation stage is shown to decrease considerably compared to an already optimized multipole solver. The extension of the presented normalized plane wave method to three dimensions is a possible area for future research. However, a similar normalization and diagonalization of the addition theorem as described for 2-D in this work may not be as straightforward in 3-D.

Bibliography

[1] M. Abramowitz and I.A. Stegun. *Handbook of Mathematical Functions with Formulas, Graphs and Mathematical Tables*. Advanced Mathematics. Dover Publications, Inc., New York, 1965.

[2] W.C. Chew, J.M. Jin, E. Michielssen, and J. Song. *Fast and Efficient Algorithms in Computational Electromagnetics*. Artech House, 2001.

[3] R. Coifman, V. Rokhlin, and S. Wandzura. The fast multipole method for the wave equation: A pedestrian prescription. *IEEE Antennas and Propagation Magazine*, 35(3):7–12, June 1993.

[4] E. Darve and P. Havé. Efficient fast multipole method for low-frequency scattering. *Journal of Computational Physics*, 197(1):341–363, June 2004.

[5] B. Hu and W.C. Chew. Fast Inhomogeneous Plane Wave Algorithm for Scattering from Objects Above the Multilayered Medium. *IEEE Transactions on Geoscience and Remote Sensing*, 39(5):1028–1038, May 2001.

[6] B. Hu and W.C. Chew. Fast Inhomogeneous Plane Wave Algorithm for electromagnetic solutions in layered medium structures, 2-D case. *Radio Sci.*, 35:31–43, Jan./Feb. 2000.

[7] M. Frigo and S. G. Johnson. *FFTW*, may 2004. www.fftw.org.

CHAPTER 5

A Nondirective Plane Wave MLFMA Stable at Low Frequencies

I. Bogaert, J. Peeters, and F. Olyslager

Accepted for *IEEE Transactions on Antennas and Propagation*.

★★★

The normalized plane wave method developed in the previous chapter allows an efficient treatment of two dimensional scattering problems. As was stated in the conclusion, applying the same ideas to the three dimensional case may not straightforwardly result in a workable algorithm. In compliance with this statement, any attempt to introduce a normalization factor t in the three dimensional addition theorem destroyed the intricate symmetries in the translation matrices that allow a diagonalization. Reinterpretation of the normalization factor as a rotation over a complex angle did not result in a three dimensional analogue either. Finally, progress was made by noticing that, when a uniform sampling is used in the θ integration of the addition theorem of the MLFMA and a suitable complex shift is applied, translations along the z-axis can be done in a stable manner. This line of research has resulted in a novel method, called the Nondirective Stable Plane Wave Multilevel Fast Multipole Algorithm (NSP-WMLFMA), which can be used to evaluate the low-frequency (LF) interactions that cannot be handled by the Multilevel Fast Multipole Algorithm (MLFMA). It uses a QR-based method to allow stable translations in all the directions, not only along the z-axis. The method combines error-controllability and diagonal translations through the use of evanescent plane waves. However, it also has the key advantage that only one radiation pattern is required.

5.1 Introduction

For the solution of three dimensional acoustic and electromagnetic time-harmonic scattering problems (assuming $e^{j\omega t}$ time dependence throughout this work), integral equations are of considerable practical importance. In general, these can often be cast as

$$\mathcal{F}(\boldsymbol{r}) = \int \mathcal{J}(\boldsymbol{r}')h_0^{(2)}(k\,||\boldsymbol{r}-\boldsymbol{r}'||)\mathrm{d}\boldsymbol{r}', \tag{5.1}$$

where k is the wavenumber and $h_0^{(2)}(k\,||\boldsymbol{r}||)$ is the spherical Hankel function of the second kind and zeroth order, defined on page 437 in [1], which is (neglecting a constant factor) also the Green function of the three dimensional scalar Helmholtz equation. The unknown $\mathcal{J}(\boldsymbol{r}')$ can be defined in a volume (leading to a Volume Integral Equation) or on a boundary (leading to a Boundary Integral Equation) or may consist of discrete point sources. By means of the method of moments [2], these problems are converted into a system of linear equations of dimension N

$$\boldsymbol{F} = \mathsf{Z}\cdot\boldsymbol{J}, \tag{5.2}$$

where Z is the $N\times N$ system matrix, $\boldsymbol{F}$ is the excitation vector and the vector $\boldsymbol{J}$ is unknown and has to be solved for. Using direct solution methods, such as an LU-decomposition, is often not feasible since N is usually very large and direct methods have an $\mathcal{O}\left(N^3\right)$ computational complexity. The application of iterative solvers, such as the biconjugate gradient method [3], permits to solve the linear system in $\mathcal{O}\left(PN^2\right)$ operations, where P is the number of iterations required by the iterative solver to reduce the residual error below a preset threshold. Since in each iteration, a number of multiplications of the system matrix Z with test vectors is required, the computational complexity of an iterative solution method can be reduced if these multiplications are accelerated. In the past, many fast algorithms have been developed for this purpose [4–10]. Fast multipole methods (FMMs) constitute an important class of such algorithms that reduce the computational complexity of the multiplication of the system matrix with a vector from $\mathcal{O}\left(N^2\right)$ to $\mathcal{O}\left(N\right)$ or $\mathcal{O}\left(N\log N\right)$. This is accomplished by dividing the geometry of the problem into a hierarchy of boxes (sometimes called a tree) and invoking some kind of decomposition of the Green function. Especially the MLFMA, which relies on a propagating plane wave decomposition of the Green function, has been extensively used. The MLFMA has allowed the simulation of electrically very large scattering problems [11] that do not contain much sub-wavelength geometrical detail.

However, structures containing considerable sub-wavelength geometrical detail cannot be simulated efficiently using only the MLFMA. This important drawback has been referred to as the LF breakdown of the MLFMA [12] and is caused by numerical roundoff error. Hence, broadband simulations require the integration of the MLFMA with another method that efficiently takes care of the subwavelength geometrical de-

tail [13, 14]. One such other method is based on a multipole decomposition of the Green function [15]. Although this method has $\mathcal{O}(N)$ computational complexity at LF, the translations in this method are not diagonal (even with point-and-shoot [16]), resulting in a relatively slow algorithm. The nondiagonal translations also lead to a rapidly increasing computational cost in the intermediate and high-frequency region, so that a coupling with the MLFMA is necessary to maintain the $\mathcal{O}(N \log N)$ scaling. As a response, methods based on the spectral representation of the Green function were developed [9, 12, 17], which exhibit diagonal translations. These methods use both propagating and evanescent plane waves and are faster than those based on multipoles. Due to the diagonal translations, these methods can also be used in the high-frequency (HF) regime. However, due to the directionality of the spectral representation of the Green function, they need six different expansions of the Green function in six different directions to cover the entire space. As a consequence the factor hidden in the $\mathcal{O}(N)$ is still quite large [13, 18]. Moreover, it is stated in [13] that whenever possible, the high-frequency method (MLFMA) should be used instead of the method based on the spectral representation. It thus seems worthwhile to try to tame the LF breakdown and extend the validity range of the MLFMA into the LF regime. In the past considerable work has been done to stabilize the MLFMA for LF applications. For example in [19], a new two dimensional MLFMA was derived which is stable and error-controllable for all frequencies. For the three dimensional case, the so-called Uniform Multilevel Fast Multipole Algorithm (UMLFMA) was constructed by Xuan *et al.* [20]. In the UMLFMA the integration is partly shifted into the complex plane and the appropriate translation operators are constructed numerically. The shift into the complex plane results in radiation patterns that contain more near field information. Unfortunately, the UMLFMA turned out to be only poorly error-controllable [21] and hence of limited use.

In this work, a novel FMM will be presented. This novel method, the NSPWMLFMA, is based on the same mathematics as the MLFMA, but is stable in the LF regime. It can be coupled with the MLFMA, yielding a broadband algorithm. The similarity of the NSPWMLFMA and the MLFMA makes this coupling and its implementation especially straightforward. First the MLFMA will be briefly revisited in order to introduce quantities and notations needed in the remainder of the paper. In particular the bandwidth properties of the translation, aggregation and disaggregation operators will be discussed, as well as the chosen spectral discretization. Then we will discuss in Section 5.3 the origin and nature of the LF breakdown of the MLFMA. The findings of Section 5.3 will then be used in Sections 5.4 and 5.5 to construct a stable FMM valid at low frequencies. In Section 5.4 translations along the z-axis are stabilized by using a shift into the complex plane somewhat similar as in the UMLFMA. However, unlike the UMLFMA, we will derive the translation operator in closed form and derive explicit formulas for the size of the shift in the complex plane to control the error. Section 5.5 extends the results of Section 5.4 to translations in other direc-

tions using a QR-decomposition. In Section 5.7 we investigate the DC-limit and show that the developed method remains valid for static problems. To conclude Section 5.8 contains a few numerical experiments to demonstrate the accuracy of the method.

5.2 The Multilevel Fast Multipole Algorithm

Consider two cubical regions, called boxes, with centers $\boldsymbol{r}_1$ and $\boldsymbol{r}_2$ respectively. Both boxes are of equal size, defined by their radius of the circumscribing sphere r_B. The first box contains $\mathcal{P}$ sources $\mathcal{J}_p$ at positions $\boldsymbol{r}_1 - \boldsymbol{a}_p$ and the second contains $\mathcal{Q}$ observation points at positions $\boldsymbol{r}_2 + \boldsymbol{d}_q$. The vectors $\boldsymbol{a}_p$, $\boldsymbol{d}_q$ and $\boldsymbol{r}_T = \boldsymbol{r}_2 - \boldsymbol{r}_1$ are called the aggregation, disaggregation and translation vector respectively and their sum $\boldsymbol{a}_p + \boldsymbol{d}_q + \boldsymbol{r}_T$ will be denoted as $\boldsymbol{r}_{pq}$. The length of this vector $r_{pq} = ||\boldsymbol{r}_{pq}||$ is the distance between the pth source and the qth observation point. The length of the translation vector $r_T = ||\boldsymbol{r}_T||$ is the translation distance. Also, the vector $\boldsymbol{a}_p + \boldsymbol{d}_q$ will be denoted as $\boldsymbol{r}_A^{pq}$. Suppose that the translation distance r_T is larger than $2r_B$. In that case the generated fields at all the observation points can be calculated by means of the addition theorem. This addition theorem is an expansion of the Green function into a continuous set of propagating plane waves, which is an integral over the Ewald sphere

$$h_0^{(2)}(kr_{pq}) = \frac{e^{-jkr_{pq}}}{-jkr_{pq}} = \frac{1}{4\pi}\int_0^{2\pi}\int_0^{\pi} e^{-j\boldsymbol{k}\cdot\boldsymbol{a}_p} T(k\boldsymbol{r}_T,\theta,\phi) e^{-j\boldsymbol{k}\cdot\boldsymbol{d}_q} \sin\theta \mathrm{d}\theta\mathrm{d}\phi, \quad (5.3)$$

with $\boldsymbol{k} = k\hat{\boldsymbol{k}} = k\cos\phi\sin\theta\hat{\boldsymbol{e}}_x + k\sin\phi\sin\theta\hat{\boldsymbol{e}}_y + k\cos\theta\hat{\boldsymbol{e}}_z$ the wavevector and $\hat{\boldsymbol{e}}_x$, $\hat{\boldsymbol{e}}_y$ and $\hat{\boldsymbol{e}}_z$ the Cartesian unit vectors. The representation (5.3) of the Green function converges if $||\boldsymbol{a}_p + \boldsymbol{d}_q|| < r_T$, which is obviously the case if $\tau > 1$, with $\tau = \frac{r_T}{2r_B}$. The translation operator $T(k\boldsymbol{r}_T,\theta,\phi)$ and the exponential $e^{-j\boldsymbol{k}\cdot\boldsymbol{r}_A^{pq}}$ have a similar structure

$$T(k\boldsymbol{r}_T,\theta,\phi) = \sum_{l=0}^{L}(2l+1)j^{-l}h_l^{(2)}(kr_T)P_l\left(\hat{\boldsymbol{k}}\cdot\hat{\boldsymbol{r}}_T\right), \quad (5.4)$$

$$e^{-j\boldsymbol{k}\cdot\boldsymbol{r}_A^{pq}} = \sum_{l=0}^{\infty}(2l+1)j^{-l}j_l(kr_A^{pq})P_l\left(\hat{\boldsymbol{k}}\cdot\hat{\boldsymbol{r}}_A^{pq}\right), \quad (5.5)$$

with $r_A^{pq} = ||\boldsymbol{r}_A^{pq}||$. The parameter L determines the relative accuracy ϵ of the addition theorem (5.3). In the literature [22–25], explicit formulas have been derived to determine L as a function of ϵ. However, here an implicit formula is presented, similar to formula (3.41) on page 86 in [16], which is more appropriate for further use in this work. It can be easily shown, by means of the addition theorem (A.10) and

orthonormality (A.17) of the spherical harmonics, that (5.3) can be reduced to

$$h_0^{(2)}(kr_{pq}) = \sum_{l=0}^{L}(-1)^l(2l+1)j_l(kr_A^{pq})h_l^{(2)}(kr_T)P_l\left(\hat{\boldsymbol{r}}_A^{pq}\cdot\hat{\boldsymbol{r}}_T\right). \tag{5.6}$$

This equation is well known, but is repeated here to emphasize its strong link with (5.3). By inspecting the worst case scenario, where $r_A^{pq} = 2r_B$ and $P_l\left(\hat{\boldsymbol{r}}_A^{pq}\cdot\hat{\boldsymbol{r}}_T\right) = 1$, Eqn. (5.6) can be used to determine L in order to obtain a specified target accuracy ϵ. This leads to the following condition

$$(2L+3)j_{L+1}(2kr_B)\left|h_{L+1}^{(2)}(kr_T)\right| \leq \epsilon\left|h_0^{(2)}(kr_{pq})\right| \approx \epsilon\left|h_0^{(2)}(kr_T)\right|. \tag{5.7}$$

To avoid the possibility of getting near a zero of the spherical Bessel function, the condition $L+1 > 2kr_B$ should be added. If the convergence condition $\tau > 1$ for (5.3) is satisfied, such an L can always be found. In practice the condition

$$\beta r_B < r_T, \tag{5.8}$$

is imposed on the translation vector, with $\beta > 2$ to limit the value of L obtained using (5.7). An obvious consequence of this is the existence of a minimal value for τ, denoted as $\tau_{\min} = \frac{\beta}{2}$. The parameter β is a setting for the MLFMA and is thus fixed and explicitly known. For example, if β is set to $\frac{4}{\sqrt{3}}$, then the nearest two boxes for which the addition theorem is used have one box in between them.

In the MLFMA the integral in (5.3) is discretized, i.e. the continuous superposition of plane waves is approximated by a finite sum of plane waves. From (5.6) it is clear that terms of a higher order than L in the expansion of the plane wave (5.5) do not contribute to $h_0^{(2)}(kr_{pq})$. Therefore, the summation in (5.5) can be truncated at $l = L$ whilst preserving the accuracy ϵ. Moreover it can be shown that $\left|\frac{h_l^{(2)}(kr_T)}{h_0^{(2)}(kr_T)}\right| \geq 1$ for all $l \geq 0$ if $\Im(kr_T) \leq 0$. Then from (5.7) it is easy to show that $(2L+3)j_{L+1}(2kr_B) \leq \epsilon$. Hence, the plane wave can be decomposed, with a relative accuracy ϵ, into spherical harmonics of degree not higher than L. Since the translation operator is also comprised of spherical harmonics of degree not higher than L, their product contains spherical harmonics of degree 0 to $2L$. This allows the discretization of the integral by means of $2L+1$ uniformly spaced points in the ϕ-direction and $L+1$ Gauss-Legendre quadrature points in the θ-direction. An alternative discretization which will be used throughout this work is a uniform discretization in both the ϕ-

and θ-direction

$$\theta_{n_\theta} = \frac{2\pi}{N_\theta} n_\theta, \ \ \forall n_\theta \in [1, N_\theta], \tag{5.9}$$

$$\phi_{n_\phi} = \frac{2\pi}{N_\phi} n_\phi, \ \ \forall n_\phi \in [1, N_\phi], \tag{5.10}$$

with $N_\theta = 2L + 1$ and $N_\phi = 2L + 2$. This guarantees an accurate integration of a function with a bandwidth $2L$. This discretization is based on the fact that $e^{-j\boldsymbol{k}\cdot\boldsymbol{r}_A^{pq}}$ is quasi-bandlimited with bandwidth L in trigonometric polynomials [26]. This means that the plane wave can be written as a Fourier series of θ and ϕ

$$e^{-j\boldsymbol{k}\cdot\boldsymbol{r}_A^{pq}} = \sum_{n=-L}^{L} \sum_{m=-L}^{L} a_{nm}^{pq} e^{j(n\theta + m\phi)}. \tag{5.11}$$

Hence, to use the uniform points (5.10) and (5.9), this discretization requires an extension of the integration domain to $[2\pi \times 2\pi]$. In addition, a smoothing of the product of the translation operator with $|\sin\theta|$ to a bandwidth L in trigonometric polynomials is required for optimal efficiency [21]. This smoothed product is denoted as $\tilde{T}(k\boldsymbol{r}_T, \theta, \phi)$

$$h_0^{(2)}(kr_{pq}) = \frac{1}{8\pi} \int_0^{2\pi} \int_0^{2\pi} e^{-j\boldsymbol{k}\cdot\boldsymbol{r}_A^{pq}} T(k\boldsymbol{r}_T, \theta, \phi) \, |\sin\theta| \, \mathrm{d}\theta \mathrm{d}\phi, \tag{5.12}$$

$$= \frac{\pi}{2N_\theta N_\phi} \sum_{n_\theta=1}^{N_\theta} \sum_{n_\phi=1}^{N_\phi} e^{-j\boldsymbol{k}_{n_\theta,n_\phi}\cdot\boldsymbol{r}_A^{pq}} \tilde{T}(k\boldsymbol{r}_T, \theta_{n_\theta}, \phi_{n_\phi}), \tag{5.13}$$

where $\boldsymbol{k}_{n_\theta,n_\phi} = \boldsymbol{k}\left(\theta_{n_\theta}, \phi_{n_\phi}\right)$. As explained in [26], compared to the Gauss-Legendre discretization, the extension of the integration domain initially yields a discretization with twice the number of points in the θ-direction, but this is a redundancy that can be easily removed by using the identity $\boldsymbol{k}(\theta, \phi) = \boldsymbol{k}(2\pi - \theta, \phi + \pi)$. The choice $N_\phi = 2L + 2$ facilitates the use of this identity. Moreover, this uniform discretization has the advantage that the inter- and anterpolations of the MLFMA can all be done using FFTs only.

Now consider the two boxes shown in Figure 5.1. Box 1 contains sources $\mathcal{J}_p$ at positions $\boldsymbol{r}_1 - \boldsymbol{a}_p$ that generate a field in the observation points at positions $\boldsymbol{r}_2 + \boldsymbol{d}_q$ in box 2. The discretized addition theorem (5.13) allows a fast evaluation of these fields. To do this, the fields in the observation points are written as

$$\sum_p \mathcal{J}_p h_0^{(2)}(kr_{pq}) = \frac{\pi}{2N_\theta N_\phi} \left(\boldsymbol{\Psi}^q\right)^T \cdot \tilde{\boldsymbol{T}}, \tag{5.14}$$

with the column vector $\boldsymbol{\Psi}^q$ defined by means of the function $\Psi^q\left(\boldsymbol{k}\right)$

$$\left[\boldsymbol{\Psi}^q\right]_{N_\phi(n_\theta-1)+n_\phi} = \Psi^q\left(\boldsymbol{k}_{n_\theta,n_\phi}\right), \tag{5.15}$$

$$\Psi^q\left(\boldsymbol{k}\right) = \underbrace{\sum_p \mathcal{J}_p e^{-j\boldsymbol{k}\cdot\boldsymbol{a}^p}}_{\text{Aggregation}} \underbrace{e^{-j\boldsymbol{k}\cdot\boldsymbol{d}^q}}_{\text{Disaggregation}} . \tag{5.16}$$

In the MLFMA, the calculations are not done in the order suggested by these formulas. First, the outgoing field of box 1 due to the currents is calculated ('Aggregation' in (5.16)). Then this outgoing field is multiplied element-wise with the translation operator $\tilde{\boldsymbol{T}}$ (translation) to obtain an incoming field on box 2. Finally, the actual field values in the observation points are obtained by multiplying the incoming field by the disaggregation exponential ('Disaggregation' in (5.16)) and summing over n_θ and n_ϕ. If the size of the boxes remains constant, the cost of evaluating the fields in all the observation points scales linearly with the number of sources and observation points. A multilevel version of this multiplication algorithm, using a tree-like hierarchical subdivision of the computational domain and a set of rules to make sure that (5.8) is satisfied [16], leads to a linear scaling for general geometries.

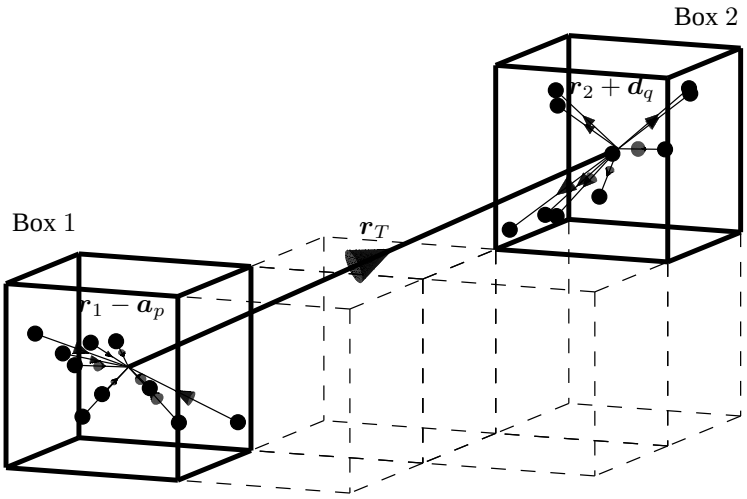

Figure 5.1: The three steps in calculating interactions between two boxes in the MLFMA: aggregation, translation and disaggregation.

5.3 The Low-Frequency Breakdown

It turns out that if the boxes in the tree become too small, the error on a fixed-precision implementation of (5.3) becomes much larger than the target accuracy ϵ, even when L is chosen such that (5.7) is satisfied. This is because of numerical roundoff error and this phenomenon is widely known as the 'LF breakdown' of the MLFMA. The LF breakdown of the addition theorem (5.3) can be attributed mainly to the exponential increase of the spherical Hankel function $h_l^{(2)}(x)$ as a function of its order if $l > x$. As a consequence the contributions of the low-order terms in (5.4) lose accuracy and finally drop below the numerical noise level that is set by the high-order terms. Another (less important) cause is the exponential decrease of the spherical Bessel function $j_l(x)$ as a function of its order if $l > x$. In (5.5) the higher order terms drop below the numerical noise level and do not contribute to the summation anymore. However, the integral representation of the Green function requires all those lost terms in both the plane wave as the translation operator. In a sense, the translation operator must extract near field information from the outgoing fields which are a far field radiation pattern, which is essentially ill-conditioned.

Now a crude but simple criterium for deciding whether the addition theorem is stable or not is deduced. If the floating-point precision is δ ($= 2.2\ \ 10^{-16}$ in double precision), it is clear from (5.4) that the zeroth-order term loses too much digits if

$$\delta(2L+1)\left|h_L^{(2)}(kr_T)\right| > \epsilon\left|h_0^{(2)}(kr_T)\right|. \tag{5.17}$$

Invoking (5.7) and the LF asymptotic forms of the spherical Hankel and Bessel functions, given on page 437 in [1]

$$h_l^{(2)}(x) \approx j\frac{(2l-1)!!}{x^{l+1}}, \tag{5.18}$$

$$j_l(x) \approx \frac{x^l}{(2l+1)!!}, \tag{5.19}$$

where the double factorial for positive integer values of n is defined as $(2n-1)!! = \frac{(2n)!}{2^n n!}$, allows for the simplification of (5.17)

$$j_L(2kr_B) < \delta\tau \approx \delta. \tag{5.20}$$

Similar to (5.17) a stability criterium for (5.5) can be derived

$$(2L+1)j_L(2kr_B) < \delta. \tag{5.21}$$

Due to the similarity of (5.20) and (5.21) we conclude that both contributions to the instability come into play below the same frequency, i.e. when $2kr_B$ becomes so small that $j_L(2kr_B)$ is lost in numerical roundoff error. This observation suggests that both

breakdowns might be remedied simultaneously. For the sake of completeness, it is stated again that the instability in the translation operator is more catastrophic than in the plane wave because the low-order terms are lost, which contribute the most to the addition theorem.

On the one hand, the LF breakdown is often regarded as a fundamental problem, because of the obvious physical explanation for the phenomenon: namely that the near field has to be reconstructed from far field information. As stated before, this operation is ill-conditioned. On the other hand, it is clear that in infinite precision no numerical roundoff errors are introduced and the addition theorem remains valid for arbitrarily low frequencies. As stated in the introduction, considerable research has already been devoted to the stabilization of the MLFMA for LF. A stable formulation in two dimensions was presented in [19]. For the three dimensional case, the UMLFMA was developed [20] which shifts the integration over θ in (5.3) into the complex plane (this requires an extension of the integration domain to 2π) and the appropriate translation operator is constructed numerically. The shift of the integration over θ results in outgoing fields that contain more near field information. Unfortunately, the UMLFMA's error-controllability is poor [21] making it of limited use.

5.4 A stable translation in the z-direction

5.4.1 An analytic translation operator

In this section a novel method is presented that allows stable translations in the z-direction. The method uses a similar shift into the complex plane as the UMLFMA, but since the construction of the novel method immediately leads to an explicit expression for the translation operator, its numerical construction is avoided. Moreover, we will gain more insight in how the LF breakdown is eliminated, which in turn results in a much better error control.

The derivation starts with the integral expression for the Green function with the extended integration domain (5.12). For translations in the z-direction, $\boldsymbol{r}_T$ is equal to $r_T\hat{\boldsymbol{e}}_z$ and the expression for the translation operator (5.4) simplifies to

$$T(kr_T\hat{\boldsymbol{e}}_z,\theta,\phi)=\sum_{l=0}^{L}(2l+1)j^{-l}h_l^{(2)}(kr_T)P_l\left(\cos\theta\right). \tag{5.22}$$

In Section 5.2 it was noted that the translation operator must be smoothed to a bandwidth L in trigonometric polynomials. In [21, 26], this is done by calculating the product of formula (5.22) with a smoothed version of $|\sin\theta|$ and truncating the result in Fourier space using an FFT. This method cannot be applied here, since simply evaluating formula (5.22) is already unstable at LF and destroys the information that is comprised in the low-order terms. Instead an analytic integration will be used for cal-

culating the Fourier spectrum of the smoothed operator $\tilde{T}(kr_T\hat{\boldsymbol{e}}_z, \theta, \phi)$. Since (5.22) does not depend on ϕ, only a Fourier series in θ is necessary

$$\tilde{T}(kr_T\hat{\boldsymbol{e}}_z, \theta, \phi) = \sum_{n=-L}^{L} b_n e^{jn\theta}, \tag{5.23}$$

with

$$b_n = \frac{1}{2\pi}\sum_{l=0}^{L}(2l+1)j^{-l}h_l^{(2)}(kr_T)f_n^l, \tag{5.24}$$

and

$$f_n^l = \int_0^{2\pi} P_l\left(\cos\theta\right)|\sin\theta|\, e^{-jn\theta}\mathrm{d}\theta. \tag{5.25}$$

$$\tag{5.26}$$

The presence of the absolute value in $|\sin\theta|$ makes this integral somewhat cumbersome. However on page 335 in [1], a formula for the Legendre polynomial of argument $\cos\theta$ is given which removes this problem. For $0 < \theta < \pi$ we have

$$P_l(\cos\theta) = \frac{2^{l+2}}{\pi}\sum_{k=0}^{\infty}\frac{(2k-1)!!(l+k)!}{k!(2l+2k+1)!!}\sin\left[(l+2k+1)\theta\right], \tag{5.27}$$

and for $\pi < \theta < 2\pi$

$$P_l(\cos\theta) = -\frac{2^{l+2}}{\pi}\sum_{k=0}^{\infty}\frac{(2k-1)!!(l+k)!}{k!(2l+2k+1)!!}\sin\left[(l+2k+1)\theta\right]. \tag{5.28}$$

Multiplying these expressions by $|\sin\theta|$ yields a single expression valid for all θ

$$P_l(\cos\theta)\,|\sin\theta| = \frac{2^{l+2}}{\pi}\sum_{k=0}^{\infty}\frac{(2k-1)!!(l+k)!}{k!(2l+2k+1)!!}\sin\left[(l+2k+1)\theta\right]\sin\theta, \tag{5.29}$$

where $(-1)!! = 1$. The product of the two sine functions can be written in terms of cosines which, if $l \neq 0$, yields after some manipulations

$$P_l(\cos\theta)\,|\sin\theta| = -\frac{2^{l+1}}{\pi}\sum_{k=0}^{\infty}(2k+l)\frac{(2k-3)!!(l+k-1)!}{k!(2l+2k+1)!!}\cos\left[(l+2k)\theta\right], \tag{5.30}$$

with $(-3)!! = -1$. Hence,

$$f_n^l = \begin{cases} l \neq 0 : -2^{l+1} \sum_{k=0}^{\infty} (2k+l) \frac{(2k-3)!!(l+k-1)!}{k!(2l+2k+1)!!} \left[\delta_{l+2k,n} + \delta_{l+2k,-n}\right] \\ l = 0, n \neq 0 : 4 \sum_{k=0}^{\infty} \frac{\delta_{2k,n} + \delta_{2k,-n}}{1-4k^2} \\ l = 0, n = 0 : 4 \end{cases} \tag{5.31}$$

From this, the Fourier spectrum of $\tilde{T}(kr_T\hat{\boldsymbol{e}}_z, \theta, \phi)$ can be easily calculated using (5.24). The coefficients f_n^l have the special property

$$f_n^l = 0 \quad \forall -l < n < l. \tag{5.32}$$

This means that the spherical Hankel function of order l is only present in the Fourier coefficients b_n with $n \geq l$. In other words: if $kr_T < 1$ the Fourier coefficients b_n approximately show the same behavior as the spherical Hankel functions themselves. Indeed, for $kr_T < 1$ the Hankel functions increase superexponentially as a function of their order, and the coefficients b_n can be approximated as

$$b_n \approx \frac{1}{2\pi} j^{-|n|} h_{|n|}^{(2)}(kr_T) \left[(2n+1) f_n^{|n|}\right]. \tag{5.33}$$

Here, $(2n+1)f_n^{|n|} \approx \sqrt{\pi(4n+1)}$ is a slowly varying function of n if $|n| >> 1$. As a consequence of the similarity between b_n and $h_n^{(2)}(kr_T)$, the magnitude of the spectrum increases superexponentially with rising $|n|$. Figure 5.2 shows the absolute value of the spectrum b_n for various values of kr_T. From the two dimensional case [19], it is known that a Fourier series with an exponentially increasing spectrum can be 'normalized' by means of an exponential factor designed to compensate for the increase of the spectrum. The introduction of this exponential factor can be done by shifting the integration path into the complex plane. It is worthwhile to point out that, although this shift can only compensate an exponential, the superexponentially increasing spherical Hankel function can be approximated by an exponential. We will come back to the validity of this approximation later on. First the integral representation of the Green function (5.12) is cast into a form only containing the increasing half ($n \geq 0$) of the spectrum

$$h_0^{(2)}(kr_{pq}) = \frac{1}{8\pi} \int_0^{2\pi} \int_0^{2\pi} e^{-j\boldsymbol{k}\cdot\boldsymbol{r}_A^{pq}} \left[\sum_{n=-L}^{L} b_n e^{jn\theta}\right] \mathrm{d}\theta \mathrm{d}\phi, \tag{5.34}$$

$$= \frac{1}{8\pi} \int_0^{2\pi} \int_0^{2\pi} e^{-j\boldsymbol{k}\cdot\boldsymbol{r}_A^{pq}} \left[\sum_{n=-L}^{0} q_n b_n e^{jn\theta} + \sum_{n=0}^{L} q_n b_n e^{jn\theta}\right] \mathrm{d}\theta \mathrm{d}\phi, \tag{5.35}$$

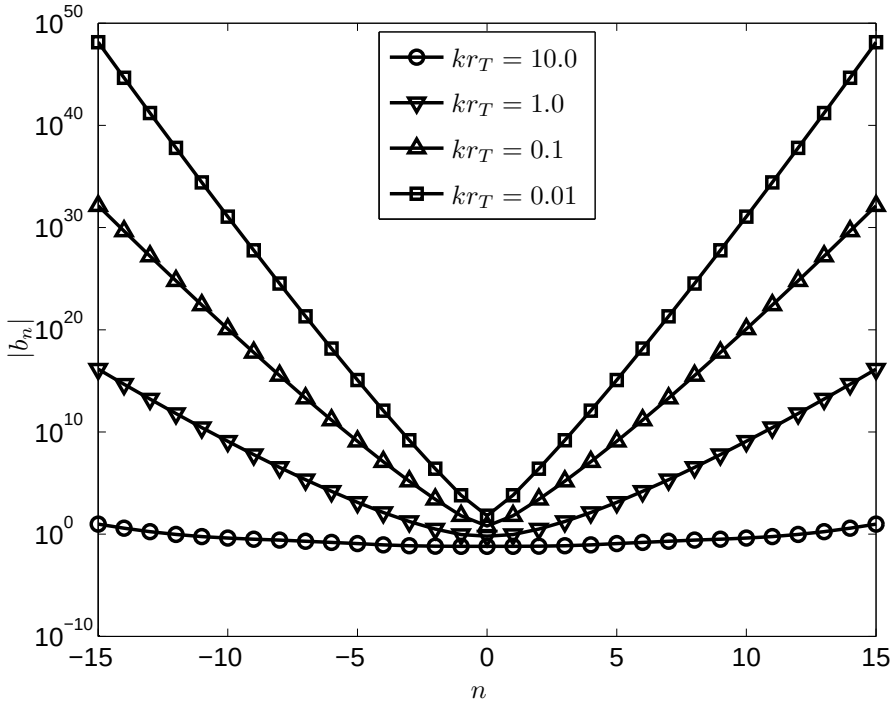

Figure 5.2: The absolute value of the Fourier coefficients b_n of the translation operator $\tilde{T}(kr_T\hat{\boldsymbol{e}}_z, \theta, 0)$ for various translation distances.

where $q_0 = \frac{1}{2}$ and $q_n = 1$ for $n \neq 0$. Since $b_n = b_{-n}$ we can apply the transformation $[\theta, \phi] \rightarrow [2\pi - \theta, \phi + \pi]$ to the first term to show that the two terms yield the same result. This leads to

$$h_0^{(2)}(kr_{pq}) = \frac{1}{4\pi} \int_0^{2\pi} \int_0^{2\pi} e^{-j\boldsymbol{k}\cdot\boldsymbol{r}_A^{pq}} \left[\sum_{n=0}^{L} q_n b_n e^{jn\theta} \right] \mathrm{d}\theta \mathrm{d}\phi. \tag{5.36}$$

The translation operator $\sum_{n=-L}^{L} b_n e^{jn\theta}$ has been replaced by a 'one-sided translation operator' $2\sum_{n=0}^{L} q_n b_n e^{jn\theta}$, which has a superexponentially increasing spectrum. The integrand in (5.36) is an entire function of θ. As a consequence the integration path C_0, shown in Figure 5.3 can be shifted into the complex plane. Because of the periodicity of the integrand contributions from C_1 and C_3 cancel and as a consequence integration along C_0 and C_2 yields the same value. The addition theorem then becomes:

$$h_0^{(2)}(kr_{pq}) = \frac{1}{4\pi} \int_0^{2\pi} \int_{0+j\chi}^{2\pi+j\chi} e^{-j\boldsymbol{k}\cdot\boldsymbol{r}_A^{pq}} \left[\sum_{n=0}^{L} q_n b_n e^{jn\theta} \right] \mathrm{d}\theta \mathrm{d}\phi. \tag{5.37}$$

It can be seen that this expression is similar to the one used in the UMLFMA. However, here the translation operator is known analytically. Moreover, the explicit knowledge of the translation operator will allow us to remove the instability by choosing a quasi-optimal value for χ. A disadvantage of the shift into the complex plane is that the symmetry $\boldsymbol{k}(\theta + j\chi, \phi) = \boldsymbol{k}(2\pi - \theta - j\chi, \phi + \pi)$ can no longer be exploited to reduce the number of discretization points as was possible without the shift. However, in Section 5.5, the excess number of points will be removed in another way.

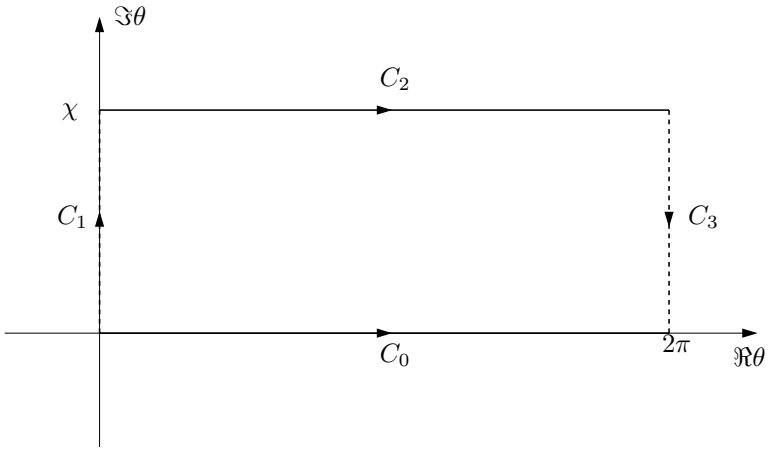

Figure 5.3: Shifting the integration path C_0 into the complex plane. The new integration path is C_2.

5.4.2 Determining χ

Integral (5.37) is readily discretized using the uniform points defined in (5.9) and (5.10), so the only undetermined parameter is χ. In order to determine χ, the relative error Λ between the discretized version of (5.37) and the explicit spherical Hankel function will be investigated

$$\Lambda(kr_T, k\boldsymbol{r}_A, \chi, \epsilon) = \left| \frac{\sum_{n_\theta=1}^{N_\theta} \sum_{n_\phi=1}^{N_\phi} \frac{\pi}{N_\theta N_\phi} e^{-j\boldsymbol{k}(\theta_{n_\theta}+j\chi,\phi_{n_\phi})\cdot\boldsymbol{r}_A} \left[\sum_{n=0}^{L} q_n b_n e^{jn\theta_{n_\theta}} e^{-n\chi}\right]}{h_0^{(2)}(k\,||r_T\hat{\boldsymbol{e}}_z + \boldsymbol{r}_A||)} - 1 \right|. \tag{5.38}$$

The dependence on ϵ is implicitly included in the determination of L, N_θ and N_ϕ. Figure 5.4 shows the relative error $\Lambda(0.015, -0.01\hat{\boldsymbol{e}}_z, \chi, \epsilon)$ as a function of χ for various target accuracies ϵ. As can be seen, for each plotted ϵ there exists a range for χ where the error becomes constant. This is the range of χ for which the error due to numerical roundoff-error is smaller than the error due to other sources (e.g. truncation of the translation operator at L, finite number of integration points,...). A good value of χ should thus be chosen in this 'stable' range. As can be seen, the size of this stable range decreases if a higher accuracy is required. Eventually, the stable region disappears and the target accuracy cannot be achieved anymore. However, as will be shown in Subsection 5.4.3, in that case there is still the option of increasing $\tau_{\min}$, i.e. increasing the parameter β. The cause of the disappearance of the stable region and the influence of kr_T and $k\boldsymbol{r}_A$ on Λ is also investigated in Subsection 5.4.3.

A necessary condition for χ to be in the stable region can be deduced by reasoning that it must be possible to numerically (for example by means of FFT) recover the coefficients b_n from the one-sided translation operator $\sum_{n=0}^{L} q_n b_n e^{jn\theta_{n_\theta}} e^{-n\chi}$ with sufficient accuracy. Using a similar reasoning as the one leading to (5.17), we find the following condition for χ

$$\epsilon \frac{|b_0|}{2} \geq \delta\,|b_L|\,e^{-L\chi}. \tag{5.39}$$

This condition provides a lower bound on χ

$$\chi \geq \frac{1}{L} \ln \frac{2\delta\,|b_L|}{\epsilon\,|b_0|}. \tag{5.40}$$

As can be seen from the positions of the dashed vertical lines in Figure 5.4, in practice this inequality is a neccesary condition but not a sufficient one for χ to be in the stable region.

How then to fix the value of χ? In the two dimensional case [19], χ is chosen such

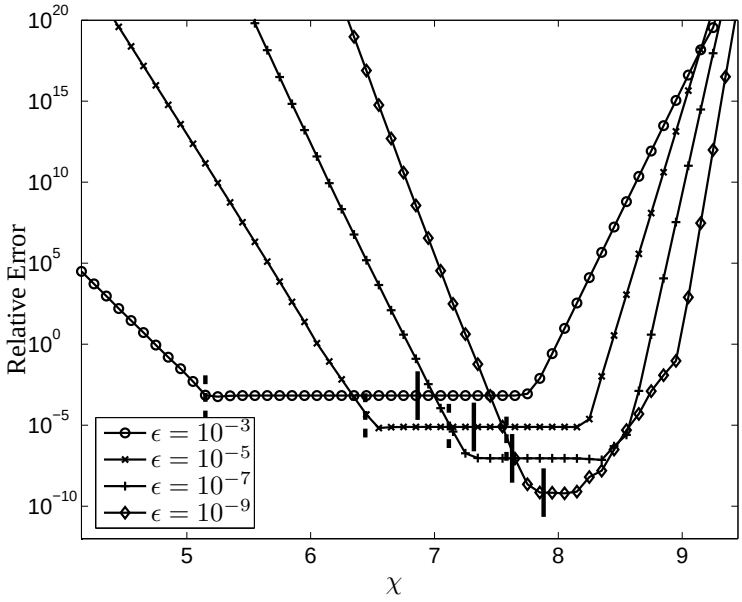

Figure 5.4: The relative error $\Lambda(0.015, -0.01\hat{e}_z, \chi, \epsilon)$, as defined in (5.38) on the normalized addition theorem (5.37) for various target accuracies ϵ. The dashed vertical lines show the lower limits for χ as determined with (5.40), while the solid vertical lines show the quasi-optimal choice for χ as defined in (5.41).

that the highest order term is of the same magnitude as the lowest-order term. This turned out to be a quasi-optimal value for the two dimensional case. The same reasoning can be repeated here, leading to a quasi-optimal value for the three dimensional case given by

$$\chi = \frac{1}{L} \ln \left| \frac{2b_L}{b_0} \right|. \tag{5.41}$$

This choice clearly satisfies (5.40). In Figure 5.4, the solid vertical lines denote the value of χ as determined with (5.41). It can be seen that, even for high target accuracies ϵ, this choice remains in the flat part of the curve. Figure 5.5 shows the nonzero part of the spectrum of the one-sided translation operator with a normalization based on (5.41). Clearly, the differences in magnitude are much smaller than in the unnormalized (i.e. $\chi = 0$) case in Figure 5.2. For use in an FMM, various translation distances r_T occur. Therefore it is not immediately clear which one to use in (5.41). Similar to the two dimensional case however, it can be easily seen that the *smallest translation distance* $r_T^{\min} \equiv \beta r_B \equiv 2\tau_{\min} r_B$ should be used. Indeed the radiation patterns contain enough information for the shortest translations, so they certainly contain enough information for the longer translations. In the translation operator higher-order b_n for longer translation distances might then get lost numerically, but that is not a problem since their contribution to the addition theorem is smaller than the accuracy. It can thus be concluded that it is possible to use one single value for χ on each FMM level, which is based on the smallest translation distance on that level.

Except for reducing the numerical instabilities in the translation operator, the choice (5.41) also normalizes the radiation and receiving pattern. Indeed, the product of the radiation and receiving pattern can be written as a sum of plane waves of the form $e^{-j\boldsymbol{k}\cdot\boldsymbol{r}_A^{pq}}$. When taking the trigonometric expansion of such a plane wave (5.11) and after some manipulations using (5.37), it follows that

$$h_0^{(2)}(kr_{pq}) = \pi \sum_{n=0}^{L} q_n a_{-n,0}^{pq} b_n. \tag{5.42}$$

Because the highest-order term in this sum must be of the order of the accuracy $\epsilon \left| h_0^{(2)}(kr_T) \right|$, it follows

$$\epsilon \left| h_0^{(2)}(kr_T) \right| \approx \left| a_{-L,0}^{pq} e^{L\chi} \right| \left| b_L e^{-L\chi} \right|, \tag{5.43}$$

$$\approx \left| a_{-L,0}^{pq} e^{L\chi} \right| \left| \frac{b_0}{2} \right|, \tag{5.44}$$

$$\approx \left| a_{-L,0}^{pq} e^{L\chi} \right| \frac{1}{\pi} \left| h_0^{(2)}(kr_T) \right|. \tag{5.45}$$

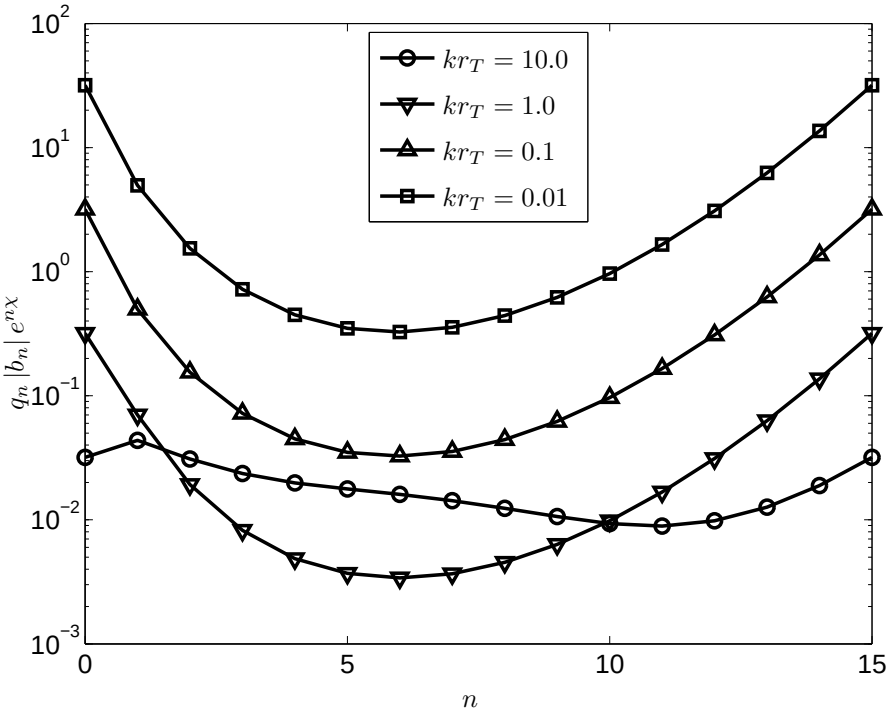

Figure 5.5: The Fourier coefficients of the 'one-sided translation operator' after the complex shift of the integration path. The coefficients for $n < 0$ are zero and are omitted for clarity. When compared to Figure 5.2, it is clear that the shift dramatically reduces the differences in magnitude between the coefficients.

As a consequence: $\epsilon \approx \frac{1}{\pi}\left|a_{-L,0}^{pq} e^{L\chi}\right|$. The normalization thus blows up the higher-order coefficients in the spectrum, so that they can still be retrieved numerically (for example by means of FFT). However, the spectrum still decays to the accuracy ϵ, which will make the interpolations in the multilevel version of this algorithm accurate. Therefore, in the remainder of this work, formula (5.41) will be used to determine χ.

5.4.3 A stability limit

One could argue that, although the differences in magnitude of the spectrum in the normalized case (see Fig. 5.5) are much smaller than in the unnormalized case (see Fig. 5.2), a dip in the former curve is still present. This dip is caused by the fact that the double factorial in the asymptotic form of the Hankel function increases superexponentially as a function of n. As a consequence it cannot be completely compensated for by a normalization as proposed here. Moreover the dip deepens for increasing L and could thus cause a numerical instability. This problem was encountered in the two dimensional case as well. A similar investigation for the three dimensional case is carried out in Appendix 5.A leading to the following criterium, valid if $2\tau_{\min} kr_B < 1$

$$\tau_{\min}^{n_{\min}-L} \frac{(n_{\min})!}{[L!]^{\frac{n_{\min}}{L}}} > \delta \tag{5.46}$$

with $n_{\min} = \left\lfloor \frac{\sqrt[L]{L!}}{\tau_{\min}} \right\rfloor$. If this criterium is not satisfied, the target accuracy ($\epsilon \approx \tau_{\min}^{-L}$) cannot be achieved because of numerical roundoff error. Used the other way around, it also gives a rough estimate of the region where (5.37) can be expected to give good results. The thick line in Figure 5.6 is found when the inequality in (5.46) is turned into an equality and $\delta = 2.2\ \ 10^{-16}$. Criterium (5.46) expresses that, in the region below this thick line, the target accuracy $\epsilon \approx \tau_{\min}^{-L}$ can be achieved. In the region above the thick line, this is not possible. To show the approximate validity of (5.46), Figure 5.6 also shows a contour plot of $-\log_{10}\Lambda(0.01\tau_{\min}, -0.01\hat{\boldsymbol{e}}_z, \chi, \tau_{\min}^{-L})$, with χ determined using the quasi-optimal (5.41) (based on a translation distance $\frac{0.01}{k}\tau_{\min}$). The contours can be divided in two regions. In the lower region the contours are smooth and approximate the contours of $\tau_{\min}^{-L}$, which leads to the conclusion that the target accuracy has been achieved in this region. In the upper region the contours are chaotic. It can be clearly seen that the criterium (5.46) effectively separates these two regions. The separation is not exact because of the various approximations made in the derivation of (5.46) and the fact that (5.46) is based solely on the translation operator. In Figure 5.6, it can also be seen that, as expected, for low values of the parameter $\tau_{\min}$, the achievable accuracy is limited. For example if $\tau_{\min} = 1.5$ and the calculations are done in double precision, the best possible accuracy is around $1.0\ \ 10^{-9}$, which is still more than acceptable for most applications. Higher accuracy is possible by increasing $\tau_{\min}$.

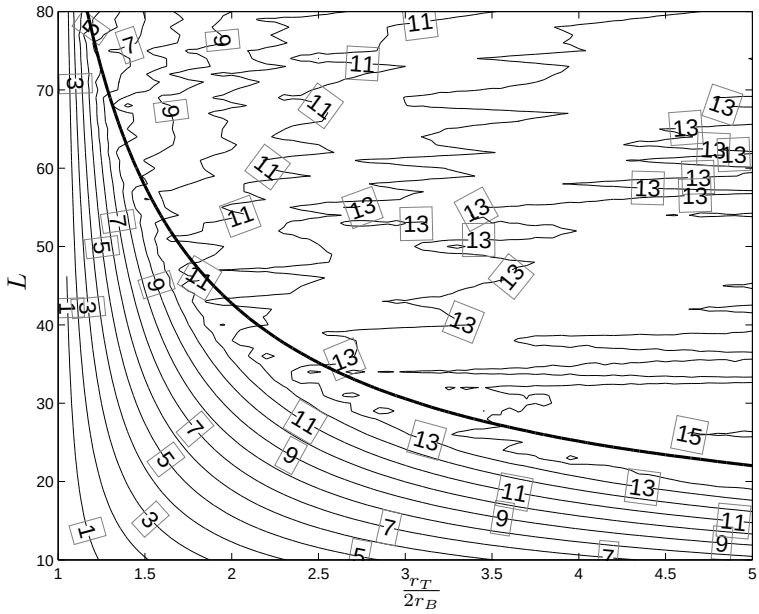

Figure 5.6: A contour plot of the relative error expressed in number of digits $-\log_{10}\Lambda(0.01\tau_{\min}, -0.01\hat{\boldsymbol{e}}_z, \chi, \tau_{\min}^{-L})$. The thick line is the line on which criterium (5.46) becomes an equality. The contours approximate the contours of $\tau_{\min}^{-L}$ in the region below this line, but become chaotic above it.

5.5 Stable translations in other directions

Extending the results from Section 5.4 to translation directions other than along the z-axis is not straightforward. The special property (5.32) which the spectrum of the smoothed translation operator $\tilde{T}(kr_T\hat{\boldsymbol{e}}_z, \theta, \phi)$ satisfies does not easily extend to other translations except the translation in the negative z-direction. Therefore, another technique is required that is derived in this section. The idea is that, if only translations along the z-axis can be stabilized, all translations should be rewritten as translations along the z-axis. Suppose there are V distinct translation vectors, given by $\boldsymbol{r}_T^v = r_T^v \mathsf{R}_v \cdot \boldsymbol{e}_z \; \forall v \in [1, V]$, with rotation matrices R_v. Then for each translation the original addition theorem of the MLFMA (5.3) can be easily rewritten by rotating the $\boldsymbol{k}$-space such that the translation is in the z-direction

$$h_0^{(2)}(kr_{pq}) = \frac{1}{4\pi}\int_0^{2\pi}\int_0^{\pi} e^{-j(\mathsf{R}_v\cdot\boldsymbol{k})\cdot\boldsymbol{r}_A^{pq}} T(kr_T^v\boldsymbol{e}_z, \theta, \phi)\sin\theta \mathrm{d}\theta\mathrm{d}\phi. \tag{5.47}$$

Following all the steps from Section 5.4 for a stable translation in the z-direction, the following expression is obtained

$$h_0^{(2)}(kr_{pq}) = \frac{1}{4\pi}\int_0^{2\pi}\int_{0+j\chi}^{2\pi+j\chi} e^{-j(\mathsf{R}_v\cdot\boldsymbol{k})\cdot\boldsymbol{r}_A^{pq}} \left[\sum_{n=0}^{L} q_n b_n e^{jn\theta}\right] \mathrm{d}\theta\mathrm{d}\phi. \tag{5.48}$$

The wavevectors $\boldsymbol{k}(\theta + j\chi, \phi) = k\hat{\boldsymbol{k}}(\theta + j\chi, \phi)$ in this expression all share the following properties

$$\Re\left[\hat{\boldsymbol{k}}\right] \cdot \Im\left[\hat{\boldsymbol{k}}\right] = 0, \tag{5.49}$$

$$\Re\left[\hat{\boldsymbol{k}}\right] \cdot \Re\left[\hat{\boldsymbol{k}}\right] = \cosh^2\chi, \tag{5.50}$$

$$\Im\left[\hat{\boldsymbol{k}}\right] \cdot \Im\left[\hat{\boldsymbol{k}}\right] = \sinh^2\chi. \tag{5.51}$$

These properties are invariant under rotations, hence $\mathsf{R}_v \cdot \hat{\boldsymbol{k}}$ also satisfies these properties. Properties (5.49), (5.50) and (5.51) will be used later on as a criterium for the selection of wavevectors. However, expression (5.48) cannot be used immediately in an FMM. It is clear that if this integral is discretized using the uniform points from (5.9) and (5.10)

$$h_0^{(2)}(kr_{pq}) = \frac{\pi}{N_\theta N_\phi}\sum_{n_\theta=1}^{N_\theta}\sum_{n_\phi=1}^{N_\phi} e^{-j\left(\mathsf{R}_v\cdot\boldsymbol{k}\left(\theta_{n_\theta}+j\chi,\phi_{n_\phi}\right)\right)\cdot\boldsymbol{r}_A^{pq}} \left[\sum_{n=0}^{L} q_n b_n e^{jn\theta_{n_\theta}-n\chi}\right], \tag{5.52}$$

the exponential has to be evaluated in the points $\mathsf{R}_v \cdot \boldsymbol{k}\left(\theta_{n_\theta} + j\chi, \phi_{n_\phi}\right)$. Hence, for each translation direction, i.e. for each R_v, the outgoing fields have to be evaluated in another set of points. Obviously this would be very inefficient.

Let us now discuss how this can be avoided. First the exponential $e^{-j(\mathsf{R}_v\cdot\boldsymbol{k})\cdot\boldsymbol{r}_A^{pq}}$ is replaced by $\Psi^q\left(\mathsf{R}_v \cdot \boldsymbol{k}\right)$ which is defined in (5.16) as the product of the outgoing fields of a box and the disaggregation exponential. The function $\Psi^q\left(\boldsymbol{k}\right)$ can be expanded in spherical harmonics

$$\Psi^q\left(\boldsymbol{k}\right) = \sum_{l=0}^{\infty}\sum_{m=-l}^{l} a_{l,m} Y_{l,m}\left(\hat{\boldsymbol{k}}\right), \tag{5.53}$$

where the coefficients $a_{l,m}$ are given by

$$a_{l,m} = 4\pi \sum_p \mathcal{J}_p j^{-l} j_l(kr_A^{pq}) Y_{l,m}^*\left(\hat{\boldsymbol{r}}_A^{pq}\right). \tag{5.54}$$

When applied to wavevectors satisfying (5.49), (5.50) and (5.51), and formula (5.41) is used to determine χ, the infinite summation in (5.53) can be truncated at $l = L$ because the absolute value of the highest order terms is of order ϵ or less (otherwise (5.48) would not achieve the target accuracy). This means that there are, up to an accuracy ϵ, only $(L+1)^2$ degrees of freedom $a_{l,m}$ in $\Psi^q\left(\boldsymbol{k}\right)$. As a consequence, if $(L+1)^2$ samples of $\Psi^q\left(\boldsymbol{k}\right)$ are known, the coefficients $a_{l,m}$ could in principle be computed by solving a system of linear equations. These can in turn be used to obtain $\Psi^q\left(\boldsymbol{k}\right)$ for the other $\boldsymbol{k}$. Of course, care must be taken when choosing these sample points, because the linear system could be ill-conditioned. To this end consider $\mathcal{N}$, with $\mathcal{N} \geq (L+1)^2$, wavevectors $\boldsymbol{k}_n$ $\forall n \in [1, \mathcal{N}]$, satisfying (5.49), (5.50) and (5.51). These conditions are added because all the wavevectors $\mathsf{R}_v \cdot \boldsymbol{k}\left(\theta_{n_\theta} + j\chi, \phi_{n_\phi}\right)$ satisfy them, hence it is sensible to make sure the $\boldsymbol{k}_n$ also satisfy these criteria. Let us also assume that these $\boldsymbol{k}_n$ are chosen such that the samples $\Psi^q\left(\boldsymbol{k}_n\right)$ contain all the information that is necessary for all the translations. This could be accomplished by taking the wavevectors $\mathsf{R}_v \cdot \boldsymbol{k}\left(\theta_{n_\theta} + j\chi, \phi_{n_\phi}\right)$ for all v, n_ϕ, n_θ as the $\boldsymbol{k}_n$. However, this approach would yield a rather large $\mathcal{N}$. In Section 5.8 alternative choices of the $\boldsymbol{k}_n$ will be explored and it will be shown that not that many $\boldsymbol{k}_n$ are needed. Let us define a matrix M and two row vectors $\boldsymbol{a}$ and $\boldsymbol{\Psi}^q$

$$[\mathsf{M}]_{l(l+1)+m+1,n} = j_l(2kr_B) Y_{l,m}\left(\hat{\boldsymbol{k}}_n\right) \ \forall n \in [1,\mathcal{N}], \forall l \in [0, L], \forall m \in [-l, l], \tag{5.55}$$

$$[\boldsymbol{a}]_{l(l+1)+m+1} = \frac{a_{l,m}}{j_l(2kr_B)} \ \forall l \in [0, L], \forall m \in [-l, l], \tag{5.56}$$

$$[\boldsymbol{\Psi}^q]_n = \Psi^q\left(\boldsymbol{k}_n\right) \ \forall n \in [1, \mathcal{N}]. \tag{5.57}$$

The factor $j_l(2kr_B)$ has been introduced for scaling purposes. When applied to the

sample wavevectors $\boldsymbol{k}_n$, (5.53) can be written as

$$\mathsf{M}^T \cdot \boldsymbol{a} = \boldsymbol{\Psi}^q. \tag{5.58}$$

The goal is to select $(L+1)^2$ linearly independent columns from M, such that these columns form a well-conditioned basis for the other columns. This task can be accomplished by means of a QR-algorithm. Here, we will select the columns by means of the usual QR-decomposition with pivoting of the matrix M. This choice is motivated by the fact that the required code is widely available (for example in Matlab or Lapack) and generally delivers good results. If robustness is of the utmost importance, the strong Rank Revealing QR-algorithm proposed in [27] can be used to select the columns. The QR-algorithm with pivoting provides a unitary matrix Q, an upper triangular matrix R and a permutation matrix P. These three matrices are related to M through the following equation:

$$\underbrace{\mathsf{M}}_{(L+1)^2\times\mathcal{N}} \cdot \underbrace{\mathsf{P}}_{\mathcal{N}\times\mathcal{N}} = \underbrace{\mathsf{Q}}_{(L+1)^2\times(L+1)^2} \cdot \underbrace{\mathsf{R}}_{(L+1)^2\times\mathcal{N}} \tag{5.59}$$

The permutation matrix P determines which columns have been selected by the QR-algorithm. The $(L+1)^2$ selected wavevectors $\tilde{\boldsymbol{k}}_{n_s}$ are determined by

$$\tilde{\boldsymbol{k}}_{n_s} = \sum_{n=0}^{\mathcal{N}} \boldsymbol{k}_n \left[\mathsf{P}\right]_{n,n_s} \forall n_s \in [1,(L+1)^2]. \tag{5.60}$$

These wavevectors can now be used as the new discretization for (5.52) instead of $\mathsf{R}_v \cdot \boldsymbol{k}\left(\theta_{n_\theta} + j\chi, \phi_{n_\phi}\right)$. Clearly, this different discretization also requires different translation operators. These will also be computed using the QR-decomposition. For this purpose, Eqn. (5.59) will be rewritten as

$$\begin{bmatrix}\mathsf{M}_{11} & \mathsf{M}_{12}\end{bmatrix} \cdot \begin{bmatrix}\mathsf{P}_{11} & \mathsf{P}_{12} \\ \mathsf{P}_{21} & \mathsf{P}_{22}\end{bmatrix} = \mathsf{Q}_{11} \cdot \begin{bmatrix}\mathsf{R}_{11} & \mathsf{R}_{12}\end{bmatrix}, \tag{5.61}$$

where the submatrices M_{11}, P_{11}, Q_{11} and R_{11} all have dimension $(L+1)^2 \times (L+1)^2$. The values of $\Psi^q(\boldsymbol{k})$ in the selected sample points $\tilde{\boldsymbol{k}}_{n_s}$ are

$$\boldsymbol{\Psi}_s^q = \begin{bmatrix}\mathsf{P}_{11}^T & \mathsf{P}_{21}^T\end{bmatrix} \cdot \boldsymbol{\Psi}^q, \tag{5.62}$$

with the column vector $\left[\boldsymbol{\Psi}_s^q\right]_{n_s} = \Psi^q\left(\tilde{\boldsymbol{k}}_{n_s}\right)$. Combining (5.58) with (5.62) and (5.61) yields

$$\boldsymbol{\Psi}_s^q = \begin{bmatrix}\mathsf{P}_{11}^T & \mathsf{P}_{21}^T\end{bmatrix} \cdot \mathsf{M}^T \cdot \boldsymbol{a} = \left(\mathsf{Q}_{11} \cdot \mathsf{R}_{11}\right)^T \cdot \boldsymbol{a}. \tag{5.63}$$

The coefficients $a_{l,m}$ are easily obtained because Q_{11} is unitary and R_{11} is upper trian-

gular. Moreover, the selection of columns by the QR algorithm makes these operations well-conditioned if a suitable starting set $\boldsymbol{k}_n$ was taken. With

$$[\mathsf{Y}_v]_{l(l+1)+m+1,N_\phi(n_\theta-1)+n_\phi} = j_l(2kr_B)Y_{l,m}\left(\mathsf{R}_v \cdot \hat{\boldsymbol{k}}\left(\theta_{n_\theta} + j\chi, \phi_{n_\phi}\right)\right), \quad (5.64)$$

the function $\Psi^q(\boldsymbol{k})$ can be evaluated in the necessary points

$$\Psi^q\left(\mathsf{R}_v \cdot \boldsymbol{k}\left(\theta_{n_\theta} + j\chi, \phi_{n_\phi}\right)\right) = \mathsf{Y}_v^T \cdot \boldsymbol{a} = \left(\mathsf{R}_{11}^{-1} \cdot \mathsf{Q}_{11}^{-1} \cdot \mathsf{Y}_v\right)^T \cdot \boldsymbol{\Psi}_s^q. \quad (5.65)$$

Now a new translation operator can be constructed, by absorbing the matrix $\mathsf{R}_{11}^{-1} \cdot \mathsf{Q}_{11}^{-1} \cdot \mathsf{Y}_v$ into the translation operator from (5.52)

$$\sum_p \mathcal{J}_p h_0^{(2)}(kr_{pq}) = \frac{\pi}{N_\theta N_\phi}\left(\boldsymbol{\Psi}_s^q\right)^T \cdot \underbrace{\mathsf{R}_{11}^{-1} \cdot \mathsf{Q}_{11}^{-1} \cdot \mathsf{Y}_v \cdot \boldsymbol{T}_z}_{\boldsymbol{T}\text{new}}, \quad (5.66)$$

with the column vector $[\boldsymbol{T}_z]_{N_\phi(n_\theta-1)+n_\phi} = \sum_{n=0}^{L} q_n b_n e^{jn\theta_{n_\theta}} e^{-n\chi}$. If necessary, the column vector $\mathsf{Y}_v \cdot \boldsymbol{T}_z$ can be evaluated more efficiently as follows

$$[\mathsf{Y}_v \cdot \boldsymbol{T}_z]_{l(l+1)+m+1} = C_l \sqrt{\frac{2l+1}{4\pi}} \sum_{m'=-l}^{l} D_{m,m'}^l\left(\mathsf{R}_v\right) \delta_{m',0}, \quad (5.67)$$

with

$$C_l = j_l(2kr_B) N_\phi \sum_{n_\theta=1}^{N_\theta} P_l\left(\cos\left(\theta_{n_\theta} + j\chi\right)\right) \left[\sum_{n=0}^{L} q_n b_n e^{jn\theta_{n_\theta}} e^{-n\chi}\right], \quad (5.68)$$

where the Legendre polynomials $P_l(\cdot)$ and Wigner rotation matrix elements $D_{m,m'}^l(\cdot)$ are defined in Eqns. (A.11) and (A.39). Equation (5.67) can be further simplified by means of (A.12), yielding

$$[\mathsf{Y}_v \cdot \boldsymbol{T}_z]_{l(l+1)+m+1} = C_l Y_{l,m}\left(\mathsf{R}_v \cdot \hat{\boldsymbol{e}}_z\right) = C_l Y_{l,m}\left(\hat{\boldsymbol{r}}_T^v\right). \quad (5.69)$$

By means of this, $\mathsf{Y}_v \cdot \boldsymbol{T}_z$ can be evaluated in $\mathcal{O}\left(L^2\right)$ operations. Since $\mathsf{Y}_v \cdot \boldsymbol{T}_z$ has to be calculated for each possible translation operator, this can yield a significant reduction in CPU time.

With the approach proposed in this section it is possible to do all the necessary translations in a stable manner, using only a minimal set of discretization points. There is a drawback, since this method uses a QR of a matrix of which both dimensions increase quadratically with L. Moreover, as will be seen in Section 5.6, the interpolations required for a multilevel algorithm are full matrices. As a consequence this is an LF technique.

5.6 A multilevel algorithm

It is well known that in the MLFMA interpolation and anterpolation techniques are needed to traverse between levels, and the same holds for the method presented in the previous sections. Indeed, although the bandwidth L_g, determined on level g by means of formula (5.7), becomes nearly constant if the boxes are considerably smaller than the wavelength, interpolation and anterpolation operations are still necessary because the value of χ differs between levels. Also, because the QR-algorithm selects wavevectors in a way that cannot be easily predicted, no special structure can be exploited, requiring a full interpolation matrix. Let the outgoing field of a box with sources $\mathcal{J}_p$ on level g be the column vector $\boldsymbol{\theta}_g$, with elements defined as

$$[\boldsymbol{\theta}_g]_{n_s} = \sum_p \mathcal{J}_p e^{-j\tilde{\boldsymbol{k}}^g_{n_s}\cdot\boldsymbol{a}_p} \; \forall n_s \in [1,(L_g+1)^2]. \tag{5.70}$$

Here $\tilde{\boldsymbol{k}}^g_{n_s}$ are the selected wavevectors on level g. Now define the interpolation matrix I_g that converts this discretized radiation pattern $\boldsymbol{\theta}_g$ into $\boldsymbol{\theta}_{g+1}$, i.e. $\boldsymbol{\theta}_{g+1} = \mathsf{I}_g \cdot \boldsymbol{\theta}_g$. The size of the matrix I_g is $(L_{g+1}+1)^2 \times (L_g+1)^2$. The result from the QR on level g can be used to calculate this matrix. The approach is very similar to the one used in the calculation of the translation operator. Proceeding as in Section 5.5 and defining the matrix S as

$$[\mathsf{S}]_{l(l+1)+m+1,n_s} = j_l(2kr_B)Y_{l,m}\left(\hat{\tilde{\boldsymbol{k}}}^{g+1}_{n_s}\right), \tag{5.71}$$

$\forall n_s \in [1,(L_{g+1}+1)^2], \forall l \in [0,L_g], m \in [-l,l]$, the interpolation matrix becomes

$$\mathsf{I}_g = \left(\mathsf{R}_{11}^{-1}\cdot\mathsf{Q}_{11}^{-1}\cdot\mathsf{S}\right)^T. \tag{5.72}$$

The accuracy of the interpolation will be investigated in Section 5.8. The anterpolations can be done with the transpose of I_g.

As explained in Section 5.5, the computational complexity of the QR-method becomes prohibitive when the boxes become considerably larger than the wavelength. In order to get a multilevel method that can also tackle HF-problems, a switch to the MLFMA should be made at a certain level. This switch is straightforward, since one only has to put χ to zero and use the sample points and interpolations of the MLFMA upward from that level.

5.7 The DC limit

Let us now investigate how the presented method behaves at DC. This involves taking the limit $k \to 0$ and using the asymptotic form (5.80) for χ derived in Appendix 5.A. The addition theorem in the static limit for translations in the z-direction can be

written as an integration over real θ and ϕ as follows

$$\frac{1}{r_{pq}} = \frac{1}{4\pi}\int_0^{2\pi}\int_0^{2\pi} e^{-j\boldsymbol{k}(\theta+j\chi,\phi)\cdot\boldsymbol{r}_A^{pq}}\left[-jk\sum_{n=0}^{L} q_n b_n e^{jn\theta}e^{-n\chi}\right]\mathrm{d}\theta\mathrm{d}\phi. \tag{5.73}$$

The DC-limit of the Fourier coefficients of the one-sided translation operator becomes, for $n \geq 0$

$$\lim_{k\to 0} -jkq_n b_n e^{-n\chi} = \frac{1}{r_T}\frac{j^{-n}n!}{\pi\left[\sqrt[L]{L!}\right]^n}. \tag{5.74}$$

To determine the DC-limit of the plane wave, we need the static limit of $\boldsymbol{k}(\theta+j\chi,\phi)$

$$\lim_{k\to 0}\boldsymbol{k}(\theta+j\chi,\phi) = \lim_{k\to 0} k\begin{bmatrix}\cos\phi\sin(\theta+j\chi)\\ \sin\phi\sin(\theta+j\chi)\\ \cos(\theta+j\chi)\end{bmatrix}^T = e^{-j\theta}\frac{\sqrt[L]{L!}}{r_T}\begin{bmatrix}j\cos\phi\\ j\sin\phi\\ 1\end{bmatrix}^T. \tag{5.75}$$

Since this limit does not vanish, the static 'radiation pattern' of a constellation of sources still contains information about these sources. Equations (5.74) and (5.75) allow a stable translation for the static case in the z-direction. For the other directions, the QR-algorithm is again necessary. This requires the calculation of the matrices M and Y_v, which necessitates taking the DC limit of a spherical harmonic. The result of this calculation is given in Appendix 5.B.

5.8 Results

The accuracy of addition theorem (5.66) will now be investigated. Consider the geometry shown in Figure 5.7. The two boxes have a radius $kr_B = \frac{\sqrt{3}}{20}$. Box 1 contains eight sources with strength 1 that are placed on the vertices (= the $\boldsymbol{r}_1 - \boldsymbol{a}_p$ in (5.66)) of the box. The field due to each of these sources is measured in each of the vertices (= the $\boldsymbol{r}_2 + \boldsymbol{d}_q$ in (5.66)) of box 2. This field is calculated both directly with the spherical Hankel function $h_0^{(2)}(kr_{pq})$ and the addition theorem (5.66). The maximum relative error between these two is

$$\Delta = \max_{pq}\left|\frac{\frac{\pi}{N_\theta N_\phi}\sum_{n_s=1}^{(L+1)^2} e^{-j\tilde{\boldsymbol{k}}_{n_s}\cdot\boldsymbol{r}_A^{pq}}\left[\boldsymbol{T}_{\text{new}}\right]_{n_s}}{h_0^{(2)}(kr_{pq})} - 1\right|. \tag{5.76}$$

In particular, the influence of the choice of the $\boldsymbol{k}_n$ on Δ will be investigated. The numerical tests in Section 5.4 clearly showed that samples of $\Psi^q\left(\boldsymbol{k}\left(\theta_{n_\theta}+j\chi,\phi_{n_\phi}\right)\right)$ carry enough information to do translations in the z-direction accurately. It is easy to

show that these points are also sufficient for translations in the negative z-direction. The obvious question is then if these samples also contain enough information to do the translations in any other direction. It turns out that this is not the case. The first column in Table 5.1(a) lists Δ when the points $\boldsymbol{k}\left(\theta_{n_\theta}+j\chi,\phi_{n_\phi}\right)$ are used as $\boldsymbol{k}_n$. Clearly, the target accuracy is not achieved. Therefore, a better set of points $\boldsymbol{k}_n$ is needed. Note that each translation direction $\mathsf{R}_v\cdot\hat{\boldsymbol{e}}_z$ has its own, 'special', set of wavevectors $\mathsf{R}_v\cdot\boldsymbol{k}\left(\theta_{n_\theta}+j\chi,\phi_{n_\phi}\right)$ of which it is known from Section 5.4 that they guarantee a high accuracy. Therefore the union of all these wavevectors $\mathsf{R}_v\cdot\boldsymbol{k}\left(\theta_{n_\theta}+j\chi,\phi_{n_\phi}\right)$ for all v,n_ϕ,n_θ should certainly contain enough information to do all the translations in a stable manner. In principle it is feasible to do this, since the QR needs to be done only once, and its cost is independent of the problem size N but it still will be unnecessarily computationally intensive. Instead W translation directions will be selected, say $\mathcal{R}_w\cdot\hat{\boldsymbol{e}}_z\ \forall w\in[1,W]$. Figure 5.8 shows the four translation vector constellations that will be investigated here. These constellations, based on the vertices of polyhedra, are aimed to be as spherically symmetric as possible to avoid introducing preferential directions. Table 5.1(a) lists the achieved accuracy using the sets of wavevectors associated with these constellations. The last two sets, labeled with c* and d* use the translation directions from Figures 5.8(c) and 5.8(d) respectively, but they have only approximately one fourth the number of wavevectors per translation direction. This is achieved by setting $N_\theta=N_\phi=L$ in (5.9) and (5.10) when defining the $\boldsymbol{k}_n$. Table 5.1(a) shows that the various sets achieve comparable accuracies, except the one that only uses the z-axis as translation direction. It can be seen that Δ is usually smaller than the target accuracy ϵ and when it is bigger, it is only by a small amount. This validates (5.7) for determining the truncation bound L. The fact that the differences in achieved accuracy between the sets (ignoring Set a) is small, indicates that taking the wavevectors of more translation directions increases the accuracy only marginally. Table 5.1(b) lists the DC limit of Δ for the same geometry as in Figure 5.7. The size of the boxes is of no importance because of the scale invariance. These results confirm the findings from Table 5.1(a) and also clearly show the stability of the proposed algorithm at DC.

Let us now investigate the accuracy of the interpolations as a function of the number of levels n_{level}. The geometry shown in Figure 5.9 is basically the same as in Figure 5.7, but there is only one source and observation point in box 1 and box 2 respectively. Both boxes are divided $n_{\text{level}}-1$ times, on each level only retaining the box containing the source or observation point. The structure that is obtained in this way is a familiar oct-tree of n_{level} levels. The translation is always done on the highest level. The (dis)aggregation is done on the lowest level and traversing up (down) the tree level by level by using interpolations (anterpolations). The target accuracy is $\epsilon=10^{-7}$ and set c* is used as $\boldsymbol{k}_n$. Table 5.2 lists Δ for different numbers of levels. From the results Table 5.2 it can be concluded that the interpolations do not inflict a significant error on the addition theorem. This is to be expected from theo-

(a)

ϵ	Set a	Set b	Set c	Set c*	Set d*
10^{-2}	$1.48\ 10^{-1}$	$4.49\ 10^{-3}$	$2.76\ 10^{-3}$	$5.56\ 10^{-3}$	$3.35\ 10^{-3}$
10^{-3}	$9.69\ 10^{-2}$	$6.90\ 10^{-4}$	$4.65\ 10^{-4}$	$6.82\ 10^{-4}$	$2.55\ 10^{-4}$
10^{-4}	$7.47\ 10^{-1}$	$7.10\ 10^{-5}$	$4.45\ 10^{-5}$	$2.01\ 10^{-4}$	$1.43\ 10^{-4}$
10^{-5}	$1.13\ 10^{-1}$	$1.32\ 10^{-5}$	$4.19\ 10^{-6}$	$8.04\ 10^{-6}$	$5.73\ 10^{-6}$
10^{-6}	$4.03\ 10^{-1}$	$1.18\ 10^{-6}$	$2.38\ 10^{-7}$	$4.34\ 10^{-7}$	$4.35\ 10^{-7}$
10^{-7}	$3.13\ 10^{-1}$	$7.48\ 10^{-8}$	$2.80\ 10^{-8}$	$4.80\ 10^{-8}$	$2.54\ 10^{-8}$

(b)

ϵ	Set a	Set b	Set c	Set c*	Set d*
10^{-2}	$7.83\ 10^{-2}$	$2.55\ 10^{-3}$	$1.98\ 10^{-3}$	$2.80\ 10^{-3}$	$3.21\ 10^{-3}$
10^{-3}	$1.12\ 10^{-1}$	$6.70\ 10^{-4}$	$3.33\ 10^{-4}$	$8.29\ 10^{-4}$	$4.12\ 10^{-4}$
10^{-4}	$7.75\ 10^{-1}$	$5.13\ 10^{-5}$	$3.44\ 10^{-5}$	$2.64\ 10^{-4}$	$1.51\ 10^{-4}$
10^{-5}	$3.50\ 10^{-1}$	$8.42\ 10^{-6}$	$5.96\ 10^{-6}$	$9.73\ 10^{-6}$	$5.41\ 10^{-6}$
10^{-6}	$7.36\ 10^{-1}$	$5.79\ 10^{-7}$	$2.11\ 10^{-7}$	$2.01\ 10^{-7}$	$2.87\ 10^{-7}$
10^{-7}	$3.11\ 10^{+0}$	$1.11\ 10^{-7}$	$1.08\ 10^{-7}$	$1.09\ 10^{-7}$	$6.09\ 10^{-8}$

Table 5.1: The accuracy Δ, defined in (5.76), as a function of the target accuracy ϵ for the various ways of constructing the set of wavevectors $\boldsymbol{k}_n$. These sets are obtained by using the wavevectors associated with the translation directions that are shown in Figure 5.8. Sets labeled with an asterisk $*$ use only approximately one fourth of the wavevectors for each direction. Table 5.0(b)(b) contains similar data for the DC limit.

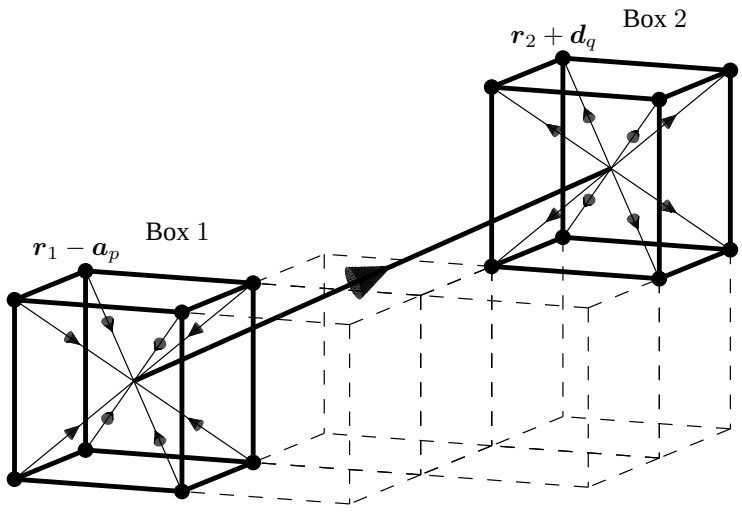

Figure 5.7: The geometry for testing the accuracy of addition theorem (5.66).

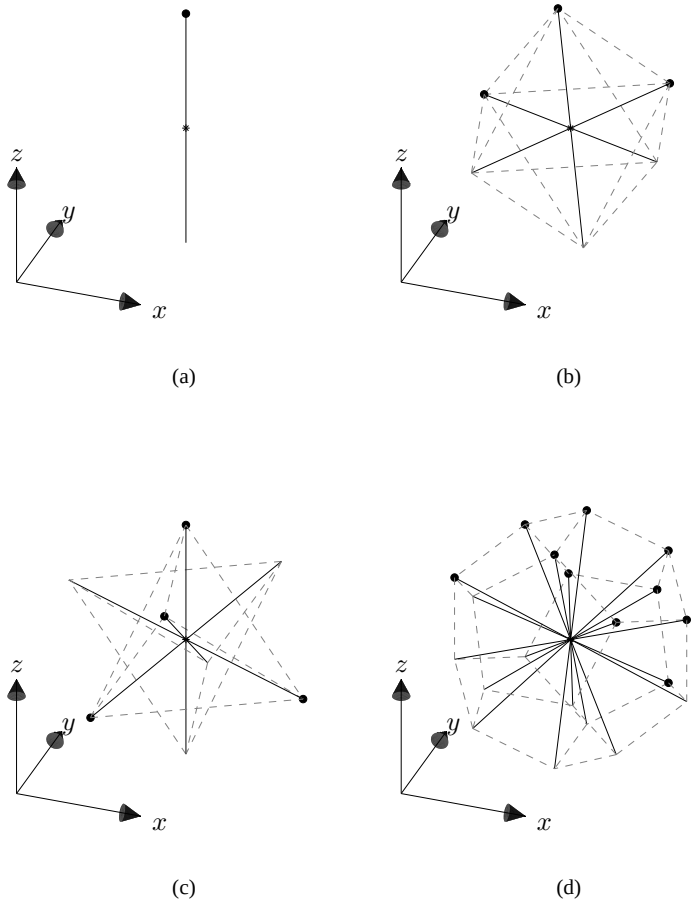

Figure 5.8: Four constellations used for translation directions. The asterisk indicates the origin and the dots indicate the selected translation directions. Constellation 5.8(a) uses the z-axis only, while constellations 5.8(b), 5.8(c) and 5.8(d) use the vertices of an octahedron, tetrahedron and dodecahedron respectively.

n_{level}	Δ
1	$1.22157364\ 10^{-8}$
2	$1.22174995\ 10^{-8}$
3	$1.22172432\ 10^{-8}$
4	$1.22172979\ 10^{-8}$
5	$1.22174006\ 10^{-8}$
6	$1.22174492\ 10^{-8}$
7	$1.22183636\ 10^{-8}$
8	$1.22186867\ 10^{-8}$

Table 5.2: Error for the (dis)aggregation for different numbers of levels n_{level}.

retical grounds. Indeed, a radiation pattern of a box (on level g) that is sampled with $(L_g + 1)^2$ points is oversampled. It is only after multiplication with another exponential during the disaggregation that these $(L_g+1)^2$ points are really required. Therefore the accuracy of an interpolation (anterpolation) can be significantly better than ϵ.

The proposed algorithm will now be tested on a generic three dimensional scattering problem. The scattering of a plane wave at a PEC cube with side 2m (shown as inset in Figure 5.10), is analyzed at frequencies 477MHz ($\lambda = 0.628$m), 47.7MHz ($\lambda = 6.28$m) and 4.77kHz ($\lambda = 62.8$km). The plane wave travels in the positive x-direction and is polarized along the z-axis. The solution is obtained by means of the Magnetic Field Integral Equation (MFIE), discretized using 7200 standard RWG basis functions. The MFIE was used because its condition number converges to a constant value as the frequency decreases, making it the ideal choice to show the LF-stability of the proposed method. The solution of the MFIE was accelerated using a single-level vectorial fast multipole method using the proposed method. The translation operator in the vectorial case is the same as in the scalar case. Although the vectorial aspect requires a small modification to the aggregation (as on page 81 in [16]), it introduces no further new problems, except in the interpolations (which falls outside the scope of this contribution), which is why we opted for a single-level implementation. The size of the boxes is 0.4m, and $\tau_{\min} = 1.732$. The measure of accuracy used here is

$$\kappa = \frac{||\mathsf{J} - \mathsf{J}_{\text{ref}}||}{||\mathsf{J}_{\text{ref}}||} \tag{5.77}$$

where J and J_{ref} are the vectors containing the coefficients of the RWGs for representing the solution current. The reference solution J_{ref} is obtained without any form of acceleration, or equivalently $\tau_{\min} = \infty$. The accuracy κ is plotted as a function of the truncation bandwidth L at the various frequencies in Figure 5.10. For $f = 477$MHz the accuracy of the MLFMA is also plotted. It can be seen that the newly proposed method is slightly less accurate than the MLFMA at 477MHz. However, the MLFMA becomes unstable around $L = 26$ and can thus not be used to achieve higher ac-

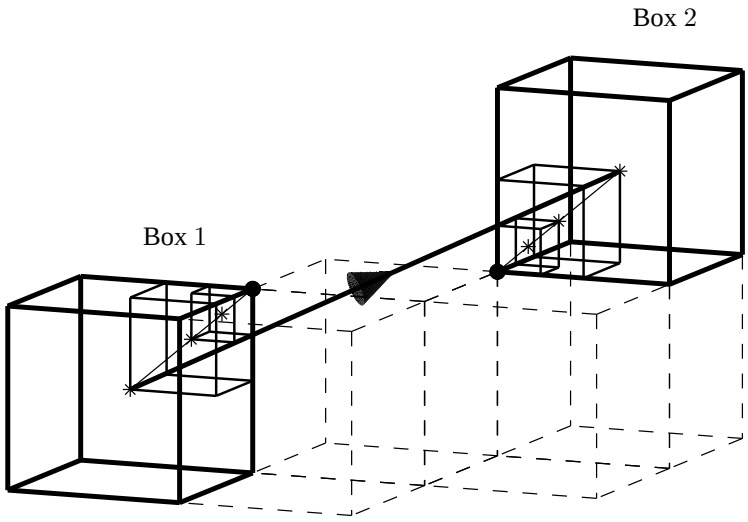

Figure 5.9: An example geometry with three levels, used for investigating the interpolation accuracy. The geometries with more levels are generated by dividing the smallest box into eight smaller boxes of which the one closest to the vertex of the big box is selected. The dots denote the source and observation points, while the asterisks denote the centers of the boxes on the different levels.

curacies. With decreasing frequency, this problem becomes worse quickly. For the cases $f = 47.7$MHz and especially $f = 4.77$kHz no useful accuracy can be obtained anymore with the MLFMA, whereas the novel method remains stable. It should also be noted that once the frequency is sufficiently low, the error curves coincide. This convincingly shows the error-controllability of the proposed method at very low frequencies. Also note that the achievable accuracy is high.

5.9 Conclusion

A novel method, the NSPWMLFMA, was presented to extend the MLFMA to the stable evaluation of LF interactions. It is based on a plane wave expansion, but does not use the spectral representation of the Green function. First, the addition theorem of the MLFMA is used to construct a stable translation along the z-axis. This was made possible by means of a shift of the integration domain into the complex plane. The optimal magnitude of this shift was determined using the closed form expression of the translation operator. A stability criterium was derived and tested with numerical results. Subsequently the method was extended to general translation directions by means of a QR-based method. Interpolations and anterpolations were also provided, allowing a full multilevel algorithm. The novel method uses much of the concepts

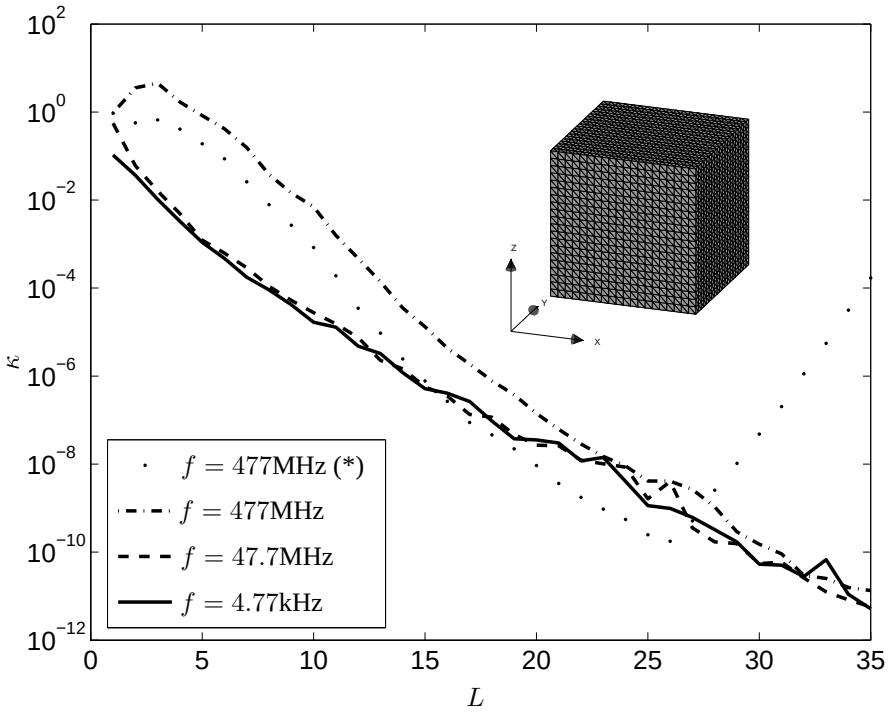

Figure 5.10: The error κ on the solution vector for various frequencies. The curve at 477MHz with the asterisk shows the accuracy of the MLFMA. The surface triangulation of the used PEC cube with side 2m is shown as inset.

that are known from the MLFMA, making it easy to implement in existing MLFMA schemes. Moreover, a coupling of the NSPWMLFMA with the MLFMA is straightforward and yields a broadband MLFMA. The DC limit of the algorithm was also presented and it was shown that the algorithm remains valid for static problems. It was then shown that the algorithm exhibits favorable error-controllability properties as compared to previous methods. Finally, the application of the NSPWMLFMA to a generic scattering problem showed the usefulness of the method to real-life applications.

5.A Region of error-controllability

Here, criterium (5.46) for the region of error-controllability will be derived. The nearest translation is the most critical one, therefore $r_T = 2\tau_{\min} r_B$. Suppose that $2\tau_{\min} k r_B < 1$, such that the spherical Hankel function can be approximated by its asymptotic form. Then by means of (5.31) and (5.33) the following approximation for $n \geq 0$ can be made

$$q_n \left| b_n \right| e^{-n\chi} \approx q_n \frac{1}{2\pi} \frac{(2n-1)!!}{(2\tau_{\min} k r_B)^{n+1}} (2n+1) f_n^n e^{-n\chi}, \tag{5.78}$$

$$\approx \frac{1}{2\pi} \frac{n!}{(\tau_{\min} k r_B)^{n+1}} e^{-n\chi}, \tag{5.79}$$

with this, an asymptotic form for χ can be deduced. With formula (5.41) and (5.79)

$$\chi \approx \frac{1}{L} \ln \left| \frac{L!}{(\tau_{\min} k r_B)^L} \right| \approx \ln \sqrt[L]{L!} - \ln \left(\tau_{\min} k r_B \right). \tag{5.80}$$

In order to assess the loss of accuracy of (5.37) due to the dip in Figure 5.5, it is not sufficient to just look at the maximum difference in magnitude between the Fourier coefficients $q_n b_n e^{-n\chi}$. Indeed, since the high-order coefficients do not contribute so much, the requirements on their precision are less stringent. In a quantitative way, the accuracy of the n-th coefficient should be at least roughly

$$\frac{\epsilon \left| h_0^{(2)}(2\tau_{\min} k r_B) \right|}{(2n+1) j_n(2k r_B) \left| h_n^{(2)}(2\tau_{\min} k r_B) \right|}. \tag{5.81}$$

If the asymptotic expansion of the spherical Hankel function can again be used, this becomes $\epsilon \tau_{\min}^n$. Each coefficient $q_n b_n e^{n\chi}$ should be known with this precision if the addition theorem (5.37) is to obtain accuracy ϵ. The actual accuracy with which the coefficients are known is given by $\delta \frac{\frac{1}{2} b_0}{q_n b_n e^{-n\chi}}$. As a consequence, the following has to

hold for an accurate result

$$\delta \left| \frac{\frac{1}{2}b_0}{q_n b_n e^{-n\chi}} \right| < \epsilon \tau_{\min}^n. \tag{5.82}$$

Together with (5.79) and (5.80), this yields

$$\frac{\delta}{\epsilon} < \frac{n!}{[L!]^{\frac{n}{L}}} \tau_{\min}^n. \tag{5.83}$$

A simple calculation shows that the minimum $n_{\min}$ of the right hand side is located at

$$n_{\min} = \lfloor \frac{\sqrt[L]{L!}}{\tau_{\min}} \rfloor, \tag{5.84}$$

with the floor function $\lfloor \cdot \rfloor$. Upon evaluating (5.83) in $n_{\min}$, and using the fact that ϵ is roughly equal to $\tau_{\min}^{-L}$, the following criterium is obtained

$$\delta < \tau_{\min}^{n_{\min}-L} \frac{(n_{\min})!}{[L!]^{\frac{n_{\min}}{L}}}. \tag{5.85}$$

5.B DC limit of the spherical harmonics

The DC limit of $j_l(2kr_B)Y_{l,m}\left(\hat{\boldsymbol{b}}\right)$, required for the calculation of the matrices M and Y_v in the static case, will be taken here. The vector $\hat{\boldsymbol{b}}$, in its most general form, satisfies the properties shown in (5.49), (5.50) and (5.51). Therefore we can generally write $\hat{\boldsymbol{b}}$ as follows

$$\hat{\boldsymbol{b}} = \cosh\chi \hat{\boldsymbol{b}}_r + j \sinh\chi \hat{\boldsymbol{b}}_i, \tag{5.86}$$

with real unit vectors $\hat{\boldsymbol{b}}_r$ and $\hat{\boldsymbol{b}}_i$ satisfying the condition $\hat{\boldsymbol{b}}_r \cdot \hat{\boldsymbol{b}}_i = 0$. The DC limit of $j_l(2kr_B)Y_{l,m}\left(\hat{\boldsymbol{b}}\right)$ can now be taken by means of the definition of the spherical harmonics (A.1) in Appendix A. Defining $\boldsymbol{B} = \hat{\boldsymbol{b}}_r + j\hat{\boldsymbol{b}}_i$, this becomes

$$\lim_{k\to 0} j_l(2kr_B)Y_{l,m}\left(\hat{\boldsymbol{b}}\right) = \left[\frac{\sqrt[L]{L!}}{\tau_{\min}}\right]^l (-1)^m (B_x + jB_y)^m B_z^{l-m} F_{lm}, \tag{5.87}$$

with

$$F_{lm} = \frac{1}{\sqrt{4\pi(2l+1)(l+m)!(l-m)!}}. \tag{5.88}$$

Using this limit, the DC version of the algorithm from Section 5.5 is easily obtained.

Bibliography

[1] M. Abramowitz and I.A. Stegun. *Handbook of Mathematical Functions with Formulas, Graphs and Mathematical Tables*. Advanced Mathematics. Dover Publications, Inc., New York, 1965.

[2] R.F. Harrington. *Field Computations by Moment Methods*. Macmillan, New York, 1968.

[3] O. Axelsson. *Iterative Solution Methods*. Cambridge University Press, New York, USA, 1995.

[4] L. Greengard and V. Rokhlin. A fast algorithm for particle simulations. *Journal of Computational Physics*, 73(2):325–348, December 1987.

[5] R. Coifman, V. Rokhlin, and S. Wandzura. The fast multipole method for the wave equation: A pedestrian prescription. *IEEE Antennas and Propagation Magazine*, 35(3):7–12, June 1993.

[6] E. Bleszynski, M. Bleszynski, and T. Jaroszewicz. AIM: Adaptive integral method for solving large-scale electromagnetic scattering and radiation problems. *Radio Science*, 31:1225–1252, 1996.

[7] W.C. Chew, J.M. Jin, C.C. Lu, E. Michielssen, and J.M. Song. Fast solution methods in electromagnetics. *IEEE Transactions on Antennas and Propagation*, 45(3):533–543, March 1997.

[8] J.M. Song, C.C. Lu, W.C. Chew, and S.W. Lee. Fast Illinois solver code (FISC). *IEEE Antennas and Propagation Magazine*, 40(3):27–34, June 1998.

[9] E. Darve and P. Havé. Efficient fast multipole method for low-frequency scattering. *Journal of Computational Physics*, 197(1):341–363, June 2004.

[10] D. Vande Ginste, E. Michielssen, F. Olyslager, and D. De Zutter. An efficient perfectly matched layer based multilevel fast multipole algorithm for large planar microwave structures. *IEEE Transactions on Antennas and Propagation*, 54(5):1538–1548, May 2006.

[11] J. Song, C.C. Lu, and W.C. Chew. Multilevel fast multipole algorithm for electromagnetic scattering by large complex objects. *IEEE Transactions on Antennas and Propagation*, 45(10):1488–1493, October 1997.

[12] L.J. Jiang and W.C. Chew. Low-frequency fast inhomogeneous plane-wave algorithm (LF-FIPWA). *Microwave and Optical Technology Letters*, 40(2):117–122, Jan 2004.

[13] H. Cheng, W.Y. Crutchfield, Z. Gimbutas, L.F. Greengard, J.F. Ethridge, J. Huang, V. Rokhlin, N. Yarvin, and J. Zhao. A wideband fast multipole method for the Helmholtz equation in three dimensions. *Journal of Computational Physics*, 216(1):300–325, 2006.

[14] L.J. Jiang and W.C. Chew. A mixed-form fast multipole algorithm. *IEEE Transactions on Antennas and Propagation*, 53(12):4145–4156, Dec 2005.

[15] J.S. Zhao and W.C. Chew. Three dimensional multilevel fast multipole algorithm at very low frequencies. In *Proceedings of the IEEE AP-S International Symposium, Salt Lake City, Utah, USA*, volume 4, pages 1884–1887, July 2000.

[16] W.C. Chew, J.M. Jin, E. Michielssen, and J. Song. *Fast and Efficient Algorithms in Computational Electromagnetics*. Artech House, 2001.

[17] E. Darve and P. Havé. A fast multipole method for Maxwell equations stable at all frequencies. *Philosophical Transactions of the Royal Society A*, 362(1816):603–628, Mar 2004.

[18] N.A. Gumerov and D. Duraiswami. FMM accelerated BEM for 3D Laplace & Helmholtz equations. In *Proceedings of the International Conference on Boundary Element Techniques, Paris, France*, 2006.

[19] I. Bogaert, D. Pissoort, and F. Olyslager. A normalized plane wave method for 2-D Helmholtz problems. *Microwave and Optical Technology Letters*, 48(2):237–243, February 2006.

[20] L. Xuan, A. Zhu, R.J. Adams, and S.D. Gedney. A broadband multilevel fast multipole algorithm. In *Proceedings of the IEEE AP-S International Symposium, Monterey, CA*, volume 2, pages 1195–1198, June 2004.

[21] H. Wallen and J. Sarvas. Translation procedures for broadband MLFMA. *Progress In Electromagnetics Research*, 55:47–78, 2005.

[22] W.J. Wiscombe. Improved mie scattering algorithms. *Applied Optics*, 19, May 1980.

[23] O.M. Bucci and G. Franceschetti. On the spatial bandwidth of scattered fields. *IEEE Transactions on Antennas and Propagation*, 35:1445–1455, Dec 1987.

[24] V. Rokhlin. Sparse diagonal forms for translation operations for the Helmholtz equation in two dimensions. *Research report YALEU/DCS/RR-1095*, Dec 1995.

[25] M.L. Hastriter, S. Ohnuki, and W.C. Chew. Error control of the translation operator in 3D MLFMA. *Microwave and Optical Technology Letters*, 37(3):184–188, May 2003.

[26] J. Sarvas. Performing interpolation and anterpolation entirely by fast Fourier transform in the 3-D multilevel fast multipole algorithm. *SIAM Journal on Numerical Analysis*, 41(6):2180–2196, 2003.

[27] M. Gu and S.C. Eisenstat. Efficient algorithms for computing a strong rank-revealing QR factorization. *SIAM Journal on Scientific Computing*, 17(4):848–869, 1996.

CHAPTER 6

A Low Frequency Stable Plane Wave Addition Theorem

I. Bogaert, and F. Olyslager

Submitted to *Journal of Computational Physics*.

★★★

In the previous chapter, the search for a broadband FMM in 3-D resulted in the semi-analytical NSPWMLFMA. However, it turns out that the stable translation operator in the z-direction can be generalized to all the other directions. This is done by replacing some spherical harmonics in the translation operator by novel so-called pseudospherical harmonics. The pseudospherical harmonics have a diverging Fourier spectrum, forcing them to be interpreted as distributions. Despite this, the use of the pseudospherical harmonics allows the construction of a practical plane wave addition theorem that is numerically stable for low frequencies, in contrast to the MLFMA. However, the diverging Fourier spectrum causes a numerical instability for high frequencies. Therefore, a combination of the traditional MLFMA and the new method should be made to construct a broadband FMM. It should be noted that the discretization points and translation operators are both calculated in closed form, which allows for an easy implementation.

6.1 Introduction

Integral equations containing the Green function of the Helmholtz equation are a very important class of problems in fields such as acoustics and electromagnetics. Usually

these equations are discretized by means of the method of moments [1]. The discretized equation can then be interpreted as a linear system of dimension N, where N is the number of basis functions used to discretize the integral equation. A direct solution (for example by means of an LU decomposition) requires $\mathcal{O}\left(N^3\right)$ operations, therefore this approach rapidly becomes impractical for increasing N. Iterative solution methods can be used to improve on this situation. They only require P matrix-vector multiplications to gradually converge to a solution. If the problem is well conditioned, $P << N$. Of course the matrix-vector multiplications still require $\mathcal{O}\left(N^2\right)$ operations, such that solving the problem requires $\mathcal{O}\left(PN^2\right)$ operations.

A further reduction in operations count can be achieved by applying a so-called Fast Multipole Method (FMM). These methods reduce the complexity of a matrix-vector multiplication from $\mathcal{O}\left(N^2\right)$ to $\mathcal{O}\left(N\right)$ or $\mathcal{O}\left(N \ln N\right)$. The MLFMA is one such method, and is very efficient for structures that do not contain much geometrical detail on a sub-wavelength scale. The efficient simulation of structures that do contain a lot of sub-wavelength geometrical detail, however, is prevented by the so-called LF breakdown. The LF breakdown of the MLFMA [2] is not of mathematical origin but is caused by the inevitable numerical roundoff error on a finite-precision computer. Hence, broadband simulations require the integration of the MLFMA with another method that efficiently takes care of the sub-wavelength geometrical detail. In [3] the MLFMA is used in conjunction with a multipole based method. Although this multipole based method achieves computational complexity $\mathcal{O}\left(N\right)$, the translations in this method are not diagonal, resulting in a relatively slow algorithm. In [4] the spectral representation of the Green function is used, which leads to diagonal translation operators. Unfortunately the spectral representation of the Green function converges in only one halfspace, thereby imposing the need for six radiation patterns. This causes the factor hidden in the $\mathcal{O}\left(N\right)$ or $\mathcal{O}\left(N \ln N\right)$ to be quite large. In addition, it is stated in [4] that "the CPU time requirements of the scheme are minimized when HF techniques are used wherever possible". The term 'HF techniques' refers to the MLFMA.

All this obviates the need for an addition theorem that is stable at LF and similar to the one used in the MLFMA. The first steps in the search for such an addition theorem were taken in the Uniform Multilevel Fast Multipole Algorithm (UMLFMA) [5]. In the UMLFMA, the integration path is shifted into the complex plane so as to include more near field information in the radiation pattern. However, the translation operators are to be calculated numerically. The achievable accuracy is also rather limited [6]. Recently a novel method, the Nondirective Stable Plane Wave Multilevel Fast Multipole Algorithm (NSPWMLFMA [7]), has been proposed which does not suffer from these drawbacks. It also uses a shift into the complex plane but instead of numerically constructing the translation operators, they are obtained from a QR decomposition of an analytically known matrix. The discretization points for the radiation patterns are also selected using QR decomposition, which guarantees a high accuracy. However, the fact that the discretization points are selected using the QR algorithm also destroys

any symmetry properties of the discretization points. Therefore, inter- and anterpolations must be done using dense matrices, making these operations a more costly part of the algorithm for high accuracies. In this paper a novel addition theorem will be derived that is completely known in closed form, i.e. explicit formulas for the translation operators and discretization points will be given. As in the UMLFMA, a shift of the integration path into the complex plane will then be used to make it numerically stable at LF. A heuristic algorithm for the calculation of the complex shift will be given and the limits to the error-controllability will be explored. In addition it will be shown that the inter- and anterpolations can be performed efficiently using FFTs.

In this work, the norm of a vector is denoted by the same symbol as the vector, but without boldface: $v = \sqrt{\boldsymbol{v} \cdot \boldsymbol{v}}$. Unit vectors are denoted with a hat $\hat{\boldsymbol{v}} = \frac{\boldsymbol{v}}{v}$. An asterisk $*$ denotes complex conjugation. In the MLFMA, the two most important vectors are the translation vector $\boldsymbol{r}_T$ and the vector $\boldsymbol{r}_A$ (see Figure 6.1). The vector $\boldsymbol{r}_A = \boldsymbol{r}_a - \boldsymbol{r}_d$ actually consists of a part coming from the aggregation $\boldsymbol{r}_a = \boldsymbol{R}_1 - \boldsymbol{r}_1$ and a part from the disaggregation $\boldsymbol{r}_d = \boldsymbol{R}_2 - \boldsymbol{r}_2$. The translation vector $\boldsymbol{r}_T$ is given by $\boldsymbol{R}_2 - \boldsymbol{R}_1$ such that $\boldsymbol{r} = \boldsymbol{r}_2 - \boldsymbol{r}_1 = \boldsymbol{r}_A + \boldsymbol{r}_T$.

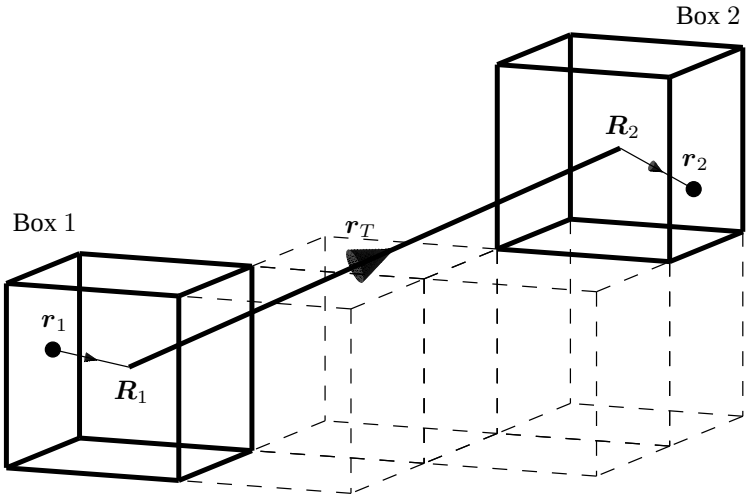

Figure 6.1: A typical configuration in the MLFMA.

6.2 A general form of the addition theorem of the MLFMA

The addition theorem of the MLFMA is well known [8]. However, it is not unique in its usefulness to FMM as will be proven in Subsection 6.2.1. In fact there may be

an infinite number of possible addition theorems, all of which equally valid for the construction of an FMM (although they might be numerically unstable). In the subsequent subsections three special cases will be discussed. Two of them will be shown to reduce to known results from the literature, among which the usual addition theorem of the MLFMA. These two special cases do not allow stable translation operators for LF. The third case is based on a novel set of distributions, the so-called pseudospherical harmonics, and will be used in the next sections to construct LF stable translation operators.

6.2.1 A more general addition theorem

The starting point of the derivation is the addition theorem for the spherical Hankel function of the zeroth order and second kind

$$h_0^{(2)}(kr) = \frac{e^{-jkr}}{-jkr} = \sum_{l=0}^{L} (-1)^l (2l+1) j_l(kr_A) h_l^{(2)}(kr_T) P_l\left(\hat{\boldsymbol{r}}_A \cdot \hat{\boldsymbol{r}}_T\right), \tag{6.1}$$

which converges absolutely if $r_T > r_T$. This equation can be found in [9], Eqns. (10.1.5) and (10.1.6). The function $P_l(\cdot)$ is the Legendre polynomial of degree l, while $Y_{l,m}(\theta,\phi)$ is a spherical harmonic of degree l and order m. Both are defined in Appendix A. The truncation bound L is determined such that the relative error introduced by the truncation of (6.1) is lower than a given threshold ϵ

$$(2L+3) j_{L+1}(kr_A) \left| h_{L+1}^{(2)}(kr_T) \right| \leq \epsilon \left| h_0^{(2)}(kr_T) \right|. \tag{6.2}$$

To avoid the possibility of using (6.2) near a zero of the spherical Bessel function, the condition $L+1 > kr_A$ should be added. Now consider any set of functions $f_{l,m}(\theta,\phi)$ such that the following property holds

$$\iint_D f_{l,m}(\theta,\phi) Y_{l',m'}^*(\theta,\phi)\, w(\theta,\phi) \mathrm{d}\theta \mathrm{d}\phi = \delta_{l,l'} \delta_{m,m'}, \tag{6.3}$$

for some integration domain D and weight distribution $w(\theta,\phi)$. By means of (6.3), (A.10) and the expansion of a plane wave

$$e^{-j\boldsymbol{k}(\theta,\phi)\cdot\boldsymbol{r}_A} = \sum_{l=0}^{\infty} (2l+1) j^{-l} j_l(kr_A) P_l\left(\hat{\boldsymbol{k}}(\theta,\phi) \cdot \hat{\boldsymbol{r}}_A\right), \tag{6.4}$$

the spherical Hankel function $h_0^{(2)}(kr)$ can be written as

$$h_0^{(2)}(kr) = \frac{1}{4\pi} \iint_D e^{-j\boldsymbol{k}(\theta,\phi)\cdot\boldsymbol{r}_A} T(k\boldsymbol{r}_T,\theta,\phi) w(\theta,\phi) \mathrm{d}\theta \mathrm{d}\phi, \tag{6.5}$$

with

$$T(k\boldsymbol{r}_T,\theta,\phi)=4\pi\sum_{l=0}^{L}\sum_{m=-l}^{l}j^{-l}h_l^{(2)}\left(kr_T\right)f_{l,m}(\theta,\phi)Y_{l,m}^{*}\left(\theta_T,\phi_T\right), \tag{6.6}$$

and $\boldsymbol{k}\left(\theta,\phi\right)=k\hat{\boldsymbol{k}}\left(\theta,\phi\right)$, with $\hat{\boldsymbol{k}}\left(\theta,\phi\right)=\cos\phi\sin\theta\hat{\boldsymbol{x}}+\sin\phi\sin\theta\hat{\boldsymbol{y}}+\cos\theta\hat{\boldsymbol{z}}$ and k the wavenumber. Three valid choices for $f_{l,m}$, D and w will now be given. The first two have already been described in the literature and are widely known and used. However, no simple method exists to make these two translation operators numerically stable at LF. The third choice uses a novel set of functions, the so-called pseudospherical harmonics, for $f_{l,m}$. In contrast to the first two choices, the addition theorem corresponding to this third choice can be made numerically stable for LF.

6.2.2 Choice 1: the MLFMA

By choosing

$$f_{l,m}(\theta,\phi)=Y_{l,m}\left(\theta,\phi\right), \tag{6.7}$$
$$w(\theta,\phi)=\sin\theta, \tag{6.8}$$
$$D=[0,2\pi]\otimes[0,\pi], \tag{6.9}$$

Eqn. (6.5) reduces to the traditional addition theorem of the MLFMA

$$h_0^{(2)}\left(kr\right)=\frac{1}{4\pi}\int_0^{2\pi}\int_0^{\pi}e^{-j\boldsymbol{k}(\theta,\phi)\cdot\boldsymbol{r}_A}T(k\boldsymbol{r}_T,\theta,\phi)\sin\theta\mathrm{d}\theta\mathrm{d}\phi, \tag{6.10}$$

with the translation operator being defined as

$$T(k\boldsymbol{r}_T,\theta,\phi)=\sum_{l=0}^{L}(2l+1)j^{-l}h_l^{(2)}\left(kr_T\right)P_l\left(\hat{\boldsymbol{k}}\left(\theta,\phi\right)\cdot\hat{\boldsymbol{r}}_T\right). \tag{6.11}$$

The addition theorem of the MLFMA is usually discretized using Gauss-Legendre quadrature points [10].

6.2.3 Choice 2: the MLFMA with uniform discretization

In [11], Sarvas presented an approach corresponding to the following choices

$$f_{l,m}(\theta,\phi)=\frac{1}{2}Y_{l,m}\left(\theta,\phi\right)\left|\sin\theta\right|, \tag{6.12}$$
$$w(\theta,\phi)=1, \tag{6.13}$$
$$D=[0,2\pi]\otimes[0,2\pi], \tag{6.14}$$

Proving that this choice satisfies (6.3) is straightforward when given Eqn. (A.7) of Appendix A. The integration domain runs over a full period of the integrand in both θ and ϕ. Therefore the integration in (6.5) can be efficiently performed using uniformly sampled points in both the θ and ϕ direction provided that the Fourier series of $f_{l,m}(\theta,\phi)$ in both θ and ϕ are truncated at bandwidth L (a smoothing operation).

$$\theta_{n_\theta} = \frac{2\pi}{N_\theta} n_\theta, \;\; \forall n_\theta \in [1, N_\theta], \tag{6.15}$$

$$\phi_{n_\phi} = \frac{2\pi}{N_\phi} n_\phi, \;\; \forall n_\phi \in [1, N_\phi], \tag{6.16}$$

with $N_\theta = 2L+1$. The uniform sampling allows inter- and anterpolations to be done entirely with FFTs. Moreover if N_ϕ is even, Eqn. (A.7) allows a reduction of the number of discretization points by a factor two, therefore $N_\phi = 2L+2$.

6.2.4 Choice 3: pseudospherical harmonics

We propose the following novel choice

$$f_{l,m}(\theta,\phi) = \begin{cases} \frac{1}{2} U_{l,m}(\theta,\phi)\sin\theta \;\; \forall m \geq 0 \\ \frac{1}{2}(-1)^m U^*_{l,-m}(\theta,\phi)\sin\theta \;\; \forall m < 0 \end{cases}, \tag{6.17}$$

$$w(\theta,\phi) = 1, \tag{6.18}$$

$$D = [0, 2\pi] \otimes [0, 2\pi]. \tag{6.19}$$

The $U_{l,m}(\theta,\phi)$ are distributions which are conveniently called "the pseudospherical harmonics", defined in Appendix 6.A. Proving that this choice satisfies (6.3) is equivalent to proving Theorem 6.A.1 as is done in Appendix 6.A. As in the previous subsection, the integration in (6.5) can be efficiently performed using a uniform discretization, this time with $N_\phi = N_\theta = 2L_d + 1$. The number of points is calculated based on L_d, not L itself, for reasons that will be explained in Section 6.3. Also, it will become clear in Section 6.4 that a reduction of the number of discretization points, as was possible in Subsection 6.2.3, is not possible anymore. Therefore, there is no need to make the number of points in the ϕ direction even, hence $N_\phi = 2L_d + 1$ A uniform discretization again necessitates a smoothing of $U_{l,m}(\theta,\phi)\sin\theta$ to bandwidth L_d. Therefore the Fourier spectrum of $U_{l,m}(\theta,\phi)\sin\theta$ will be determined in Section 6.3. The special properties of the Fourier spectrum of $U_{l,m}(\theta,\phi)\sin\theta$ will then for the first time allow the construction of analytically known LF stable translation operators.

6.3 The pseudospherical harmonics as a Fourier series

The addition theorem following from the choice for $f_{l,m}$, D and w in Subsection 6.2.4 is

$$h_0^{(2)}(kr) = \frac{1}{4\pi}\int_0^{2\pi}\int_0^{2\pi} e^{-j\boldsymbol{k}(\theta,\phi)\cdot\boldsymbol{r}_A} T(k\boldsymbol{r}_T,\theta,\phi)\mathrm{d}\theta\mathrm{d}\phi, \tag{6.20}$$

with the translation operator

$$T(k\boldsymbol{r}_T,\theta,\phi) = 2\pi\sin\theta\sum_{l=0}^{L} j^{-l}h_l^{(2)}(kr_T)\sum_{m=0}^{l} s_m\left[Y_{l,m}^*(\theta_T,\phi_T)\,U_{l,m}(\theta,\phi) + Y_{l,m}(\theta_T,\phi_T)\,U_{l,m}^*(\theta,\phi)\right], \tag{6.21}$$

with $s_m = 1 - \frac{1}{2}\delta_{m,0}$ and the fact that $U_{l,0}^*(\theta,\phi) = U_{l,0}(\theta,\phi)$. The uniform discretization proposed in Subsection 6.2.4 allows the exact integration of a function with bandwidth $2L_d$. Because the translation operator shares this bandwidth with the plane wave in (6.20), it must be smoothed to a bandwidth L_d. In practice, this amounts to calculating the Fourier series of $U_{l,m}(\theta,\phi)\sin\theta$ for $m \geq 0$, i.e. writing it as

$$U_{l,m}(\theta,\phi)\sin\theta = e^{jm\phi}\sum_{n=-\infty}^{\infty} u_{l,m}^n e^{jn\theta} \tag{6.22}$$

and truncating the summation to the range $[-L_d, L_d]$. It is worthwhile to point out that property (6.54) of Appendix 6.A yields a condition on the Fourier coefficients, namely

$$u_{l,m}^{-n} = (-1)^m u_{l,m}^n. \tag{6.23}$$

The calculation of $u_{l,m}^n$ can be done by using Theorem 6.B.2

$$U_{l,m}(\theta,\phi)\sin\theta = K_{l,m}e^{jm\phi}\sin^{m+1}\theta\frac{2^{m+1}}{\sqrt{\pi}}\sum_{p=0}^{\infty}\lambda_{l,m}^p\sin\left[(l+m+2p+1)\theta\right], \tag{6.24}$$

with Theorem 6.B.2 proven, $K_{l,m}$ defined in Appendix A and $\lambda_{l,m}^p$ defined in Appendix 6.B. It is shown in Lemma 6.B.3 that if $\lambda_{l,m}^p$ is interpreted as $\lim_{x\to p}\lambda_{l,m}^x$,

then

$$\lambda_{l,m}^{p} = -\lambda_{l,m}^{-p-l-m-1}. \tag{6.25}$$

Furthermore, using (6.63), it is easily seen that

$$\lambda_{l,m}^{p} = 0 \;\; \forall p \in [-l-m, -1]. \tag{6.26}$$

As a consequence Eqn. (6.24) can be rewritten as

$$U_{l,m}(\theta,\phi)\sin\theta = -jK_{l,m}e^{jm\phi}\sin^{m+1}\theta\frac{2^m}{\sqrt{\pi}}\sum_{p=-\infty}^{\infty}\lambda_{l,m}^{p}e^{j(l+m+2p+1)\theta}. \tag{6.27}$$

Because $m \geq 0$ in (6.21), it is possible to expand $\sin^{m+1}\theta$ using the binomial theorem. Absorbing the result into the summation over p yields the following closed form

$$u_{l,m}^{n} = \begin{cases} \frac{1}{2}\frac{K_{l,m}(-j)^m}{\sqrt{\pi}}\sum_{q=0}^{m+1}(-1)^{m-q}\binom{m+1}{q}\lambda_{l,m}^{\frac{n-l}{2}-q} & \forall n-l \text{ even} \\ 0 & \forall n-l \text{ odd} \end{cases}, \tag{6.28}$$

with the binomial coefficient

$$\binom{m+1}{q} = \frac{(m+1)!}{q!(m+1-q)!}. \tag{6.29}$$

The $u_{l,m}^{n}$ satisfy the following curious property

Lemma 6.3.1 *For any integer n, $l \geq 0$ and $m \in [-l, l]$ the following holds*

$$u_{l,m}^{n} = 0 \;\; \forall l > |n|. \tag{6.30}$$

Proof The inequality $l > |n|$ and the summation bounds for q in Eqn. (6.28) yield the following two inequalities

$$-l < \frac{n-l}{2} < 0, \tag{6.31}$$

$$-m-1 \leq -q \leq 0. \tag{6.32}$$

The sum of Eqns. (6.31) and (6.32) yields

$$-l-m-1 < \frac{n-l}{2} - q < 0, \tag{6.33}$$

which proves by means of Eqn. (6.26), that all the terms in summation (6.28) are zero, concluding the proof. □

It can also be verified that $u_{l,m}^n$ diverges as a function of n if $m > 2$. However, as mentioned before, the pseudospherical harmonics are distributions, therefore (6.22) does not have to converge. Provided the distribution is integrated with a function that has a Fourier spectrum that decays fast enough to compensate the divergence, a well defined result is obtained. Equation (6.28) makes it easy to calculate the smoothed translation operator

$$\begin{aligned}
&\tilde{T}(k\boldsymbol{r}_T, \theta, \phi) \\
&\quad = 2\pi \sum_{n=-L_d}^{L_d} \sum_{m=0}^{L} \sum_{l=m}^{L} j^{-l} h_l^{(2)}(kr_T)\, s_m \\
&\qquad\qquad \times \left[Y_{l,m}^*(\theta_T, \phi_T)\, e^{jm\phi} + Y_{l,m}(\theta_T, \phi_T)\, e^{-jm\phi} \right] u_{l,m}^n e^{jn\theta}, \quad (6.34) \\
&\quad = \sum_{n=-L_d}^{L_d} \sum_{m=-L}^{L} t_{n,m} e^{jn\theta} e^{jm\phi}, \quad (6.35)
\end{aligned}$$

with

$$t_{n,m} = 2\pi \sum_{l=|m|}^{\min(|n|,L)} j^{-l-m+|m|} h_l^{(2)}(kr_T)\, Y_{l,m}^*(\theta_T, \phi_T)\, u_{l,|m|}^n, \quad (6.36)$$

where Lemma 6.3.1 was used to establish the upper bound for the summation over l. The two outer sums can be performed using the FFT algorithm, due to the uniform discretization. Assuming that L_d does not differ too much from L, the calculation of the smoothed translation operator $\tilde{T}(k\boldsymbol{r}_T, \theta, \phi)$ requires the evaluation of $u_{l,m}^n$ in $\mathcal{O}\left(L^3\right)$ different arguments. The evaluation of $u_{l,m}^n$ itself costs $\mathcal{O}(L)$ operations hence the calculation of the smoothed translation operator is dominated by the $\mathcal{O}\left(L^4\right)$ scaling of calculating the various $u_{l,m}^n$. Although this problem is not that severe because the $u_{l,m}^n$ can be reused for all the different translation directions, in Appendix 6.C we supply a more efficient recursive calculation method that yields an $\mathcal{O}\left(L^3\right)$ calculation of all required $u_{l,m}^n$.

Using the uniform discretization from Eqns. (6.15) and (6.16), the smoothed translation operator can be directly discretized

$$h_0^{(2)}(kr) = \frac{\pi}{N_\theta N_\phi} \sum_{n_\theta=1}^{N_\theta} \sum_{n_\phi=1}^{N_\phi} \tilde{T}(k\boldsymbol{r}_T, \theta_{n_\theta}, \phi_{n_\phi}) e^{-j\boldsymbol{k}\left(\theta_{n_\theta}, \phi_{n_\phi}\right) \cdot \boldsymbol{r}_A}. \quad (6.37)$$

An error analysis will now be performed to control the discretization error and determine the value of L_d. In this analysis the effects of roundoff error will be ignored, a subject being studied in the next section. The uniform discretization exactly integrates every function of bandwidth $2L_d$. Because in the translation operator, the spectrum of pseudospherical harmonics has been truncated to bandwidth L_d, the orthogonality

property (6.A.1) between pseudospherical harmonics and spherical harmonics holds after discretization if $l_2 \leq L_d$. The plane wave, however, contains spherical harmonics with all orders, such that this inequality will be violated. Therefore, (6.37) becomes

$$h_0^{(2)}(kr) = \sum_{l=0}^{L}(-1)^l(2l+1)j_l(kr_A)h_l^{(2)}(kr_T)P_l\left(\hat{\boldsymbol{r}}_A \cdot \hat{\boldsymbol{r}}_T\right) \tag{6.38}$$

$$+ \frac{\pi}{N_\theta N_\phi}\sum_{n_\theta=1}^{N_\theta}\sum_{n_\phi=1}^{N_\phi}\tilde{T}(k\boldsymbol{r}_T,\theta_{n_\theta},\phi_{n_\phi}) \times \sum_{l=L_d+1}^{\infty}(2l+1)j^{-l}j_l(kr_A)P_l\left(\hat{\boldsymbol{k}}\left(\theta_{n_\theta},\phi_{n_\phi}\right)\cdot\hat{\boldsymbol{r}}_A\right). \tag{6.39}$$

Since L has been chosen to satisfy (6.1) with an accuracy ϵ, we can conclude that the second term must be reduced below the same accuracy threshold to safeguard the error-controllability of the method. In the MLFMA, this condition is automatically satisfied because the Fourier series of spherical harmonics converges. In the method proposed here, however, the diverging nature of the Fourier series of the pseudospherical harmonics blows up the second term. However, it can be suppressed by choosing L_d sufficiently large. Indeed, without taking into account numerical roundoff error, it is possible to make this term arbitrarily small because the lowest-order spherical Bessel function is $j_{L_d+1}(kr_A)$, which converges super-exponentially if $L_d > kr_A$. For the same reason the value of L_d approaches L if the frequency drops. For situations where kr_A has a value around or above unity, however, the difference between L_d and L can be significant. Numerical experiments can be used to determine a suitable value for L_d by starting at $L_d = L + 1$ and gradually increasing L_d. For this the translation operator with translation direction $\hat{\boldsymbol{e}}_x$ should be used. This choice can be understood by looking at translations close to the z-axis. Indeed, for these translations the factor $\sin^{|m|}\theta_T$ contained within $Y_{L,m}^*(\theta_T,\phi_T)$ becomes dominant over the diverging behavior of $u_{l,m}^n$. Hence, their Fourier spectrum does not increase as fast as the Fourier spectrum of other translation operators. For translations far enough away from the z-axis, this suppression of the divergence becomes less and less strong, and disappears completely in the xy-plane (where $\theta_T = \frac{\pi}{2}$). Therefore the translations in the xy-plane should have approximately the fastest increasing Fourier spectrum, yielding a worst case scenario for the determination of L_d. To avoid having to take into account the various possible $\boldsymbol{r}_A$, the following inequality is useful

$$\left|\sum_{m=-l}^{l}a_{l,m}Y_{l,m}(\theta,\phi)\right| \leq \sqrt{\frac{2l+1}{4\pi}}\sqrt{\sum_{m=-l}^{l}|a_{l,m}|^2}. \tag{6.40}$$

As a consequence, when $a_{l,m}$ is defined as

$$a_{l,m} = j^{-l} j_l(kr_A) \frac{4\pi^2}{N_\theta N_\phi} \sum_{n_\theta=1}^{N_\theta} \sum_{n_\phi=1}^{N_\phi} \tilde{T}(kr_T \hat{\boldsymbol{e}}_x, \theta_{n_\theta}, \phi_{n_\phi}) Y_{l,m}\left(\theta_{n_\theta}, \phi_{n_\phi}\right), \quad (6.41)$$

the following inequality must be satisfied to obtain a relative accuracy ϵ

$$\sum_{l=L_d+1}^{\infty} \sqrt{\frac{2l+1}{4\pi}} \sqrt{\sum_{m=-l}^{l} |a_{l,m}|^2} < \epsilon h_0^{(2)}(kr). \quad (6.42)$$

6.4 A normalized translation operator

The translation operator derived in the previous section is neither LF-stable nor HF-stable. The instability for the HF case is caused by the exponential divergence of $u_{l,m}^n$ as a function of n and cannot be easily remedied. However, for the LF case L becomes fixed as the frequency drops, and the numerical instability associated with the diverging $u_{l,m}^n$ becomes fixed as well. The instability due to the super-exponential increase of the spherical Hankel functions, on the other hand, becomes more and more of a problem as the frequency drops. In this section the elimination of this LF instability of the translation operator will be discussed.

The smoothed translation operator as it was derived in the previous section (6.35) has two very peculiar properties. First, the spectrum $t_{n,m}$ is zero whenever $|m| > |n|$ or $|m| > L$ so that when a dot is placed at every nonzero Fourier coefficient an hourglass shaped figure is obtained. Second, the coefficient $t_{n,m}$ contains only Hankel functions of order $|n|$ or lower. These properties are not shared by the translation operators of 6.2.2 and 6.2.3. They will enable us to construct a translation operator that remains valid at very low frequencies and even has a DC limit. The drawback is a failure due to numerical roundoff error at HF.

The first part of the derivation entails a further manipulation of the smoothed translation operator. Consider a translation operator defined as follows

$$\hat{T}(k\boldsymbol{r}_T, \theta, \phi) = \sum_{n=0}^{L_d} \sum_{m=-L}^{L} 2 s_n t_{n,m} e^{jn\theta} e^{jm\phi}. \quad (6.43)$$

Note that the summation over n starts at 0 instead of $-L_d$. We will call $\hat{T}(k\boldsymbol{r}_T, \theta, \phi)$ the triangular translation operator, since its spectrum is more or less triangle shaped. It is easily seen that this translation operator is a valid one for use in (6.20) since the plane wave $e^{-j\boldsymbol{k}(\theta,\phi)\cdot\boldsymbol{r}_A}$ is invariant under the transformation $(\theta, \phi) \rightarrow (2\pi - \theta, \phi + \pi)$

and $(-1)^m t_{-n,m} = t_{n,m}$

$$\begin{aligned}
&\frac{1}{4\pi}\int_0^{2\pi}\int_0^{2\pi} e^{-j\boldsymbol{k}(\theta,\phi)\cdot\boldsymbol{r}_A}\hat{T}(k\boldsymbol{r}_T,\theta,\phi)\mathrm{d}\theta\mathrm{d}\phi \\
&\quad= \frac{1}{4\pi}\int_0^{2\pi}\int_0^{2\pi} e^{-j\boldsymbol{k}(\theta,\phi)\cdot\boldsymbol{r}_A}\sum_{n=0}^{L_d}\sum_{m=-L}^{L} t_{n,m}e^{jn\theta}e^{jm\phi}\mathrm{d}\theta\mathrm{d}\phi \\
&\quad+ \frac{1}{4\pi}\int_0^{2\pi}\int_0^{2\pi} e^{-j\boldsymbol{k}(\theta,\phi)\cdot\boldsymbol{r}_A}\sum_{n=1}^{L_d}\sum_{m=-L}^{L} t_{n,m}e^{jn\theta}e^{jm\phi}\mathrm{d}\theta\mathrm{d}\phi, \\
&\quad= \frac{1}{4\pi}\int_0^{2\pi}\int_0^{2\pi} e^{-j\boldsymbol{k}(\theta,\phi)\cdot\boldsymbol{r}_A}\sum_{n=0}^{L_d}\sum_{m=-L}^{L} t_{n,m}e^{jn\theta}e^{jm\phi}\mathrm{d}\theta\mathrm{d}\phi \\
&\quad+ \frac{1}{4\pi}\int_0^{2\pi}\int_0^{2\pi} e^{-j\boldsymbol{k}(\theta,\phi)\cdot\boldsymbol{r}_A}\sum_{n=-L_d}^{-1}\sum_{m=-L}^{L} (-1)^m t_{-n,m}e^{jn\theta}e^{jm\phi}\mathrm{d}\theta\mathrm{d}\phi, \\
&\quad= \frac{1}{4\pi}\int_0^{2\pi}\int_0^{2\pi} e^{-j\boldsymbol{k}(\theta,\phi)\cdot\boldsymbol{r}_A}\tilde{T}(k\boldsymbol{r}_T,\theta,\phi)\mathrm{d}\theta\mathrm{d}\phi. \qquad (6.44)
\end{aligned}$$

The second part of the derivation of LF-stable translation operators consists of shifting the integration path along the θ direction into the complex plane

$$h_0^{(2)}(kr) = \frac{1}{4\pi}\int_0^{2\pi}\int_{j\chi}^{2\pi+j\chi} e^{-j\boldsymbol{k}(\theta,\phi)\cdot\boldsymbol{r}_A}\hat{T}(k\boldsymbol{r}_T,\theta,\phi)\mathrm{d}\theta\mathrm{d}\phi. \qquad (6.45)$$

Figure 6.2 shows the old and new integration paths, i.e. C_0 and C_2 respectively. The integrated function is analytical, hence the contributions from C_0 and $C_1+C_2+C_3$ are equal. The integrated function is also periodic with period 2π, hence the contributions from C_1 and C_3 cancel each other, legitimating the shift in Eqn. (6.45). A shift into the complex plane simply multiplies the Fourier coefficients $2s_n t_{n,m}$ with a factor $e^{-n\chi}$. The two outer sums in (6.43) can thus still be performed using the FFT algorithm. A side effect of the complex shift is that the symmetry of the plane wave under the transformation $(\theta,\phi) \rightarrow (2\pi-\theta,\phi+\pi)$ can no longer be used to reduce the number of points in a radiation pattern. Indeed, $(\theta+j\chi,\phi)$ maps into $(2\pi-\theta-j\chi,\phi+\pi)$ which is not a point in the integration domain.

In order to make Eqn. (6.45) numerically stable for low frequencies, the complex shift must be tailored to compensate the divergent behavior of the spectrum of the triangular translation operator. In [7], a similar problem is encountered. However, only translations in the z-direction were stabilized. For this special case, the value of χ was chosen by imposing the condition that, after the application of the complex shift, no Fourier coefficient (of the translation operator) should have a magnitude larger than the magnitude of the lowest order coefficient $t_{0,0}$. The aim of this was to avoid that the highest order coefficients, which contribute the least in the addition theorem, numeri-

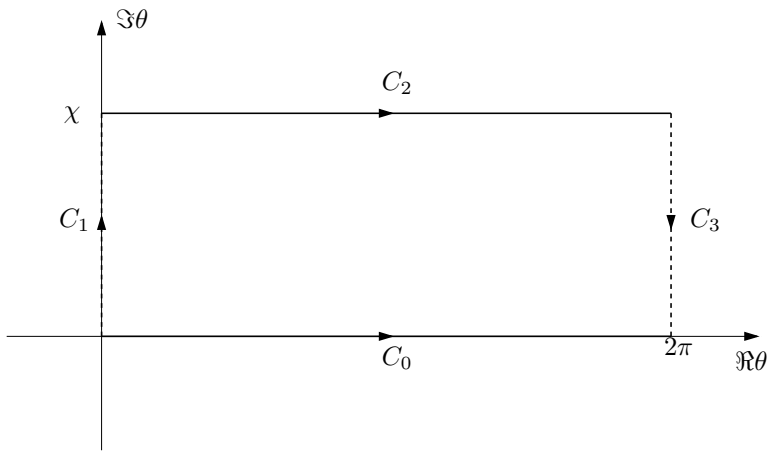

Figure 6.2: Shifting the integration path C_0 into the complex plane. The new integration path is C_2.

cally overwhelm the low order terms. A similar reasoning will be applied here, with the generalization that the selected value of χ must work for all translation directions. We propose the following algorithm for calculating χ:

1: Calculate $2s_n t_{n,m}, \forall n \in [0, L_d], m \in [-L, L]$ for a translation vector $\boldsymbol{r}_T = r_T^{\min} \hat{\boldsymbol{e}}_x$.
2: Determine the maximum over all m: $t_n = \max_m(|2s_n t_{n,m}|), \forall n \in [0, L_d]$.
3: $\chi = 0$
4: **repeat**
5: Determine $n_{\max}$ such that $|t_{n_{\max}}| \geq |t_n|, \forall n \in [0, L_d]$
6: **if** $n_{\max} = 0$ **then**
7: $\delta = 0$
8: **else**
9: $\delta = \frac{1}{n_{\max}} \ln \left| \frac{t_{n_{\max}}}{t_0} \right|$
10: **end if**
11: $t_n = e^{-n\delta} t_n, \forall n \in [0, L_d]$
12: $\chi = \chi + \delta$
13: **until** $|\delta| < \epsilon$
14: **return** χ

with ϵ a small number (e.g. 10^{-12} in double precision), for determining whether $|\delta|$ is close enough to zero. Upon termination this algorithm yields a complex shift that is suitable for all translations in the xy-plane, since the chosen translation direction is $\hat{\boldsymbol{e}}_x$ and $|2s_n t_{n,m}|$ does not depend on ϕ_T. It can, however, also be used for the other translation directions. This can be understood by means of the same argument as the one used for the calculation of L_d. The translations in the xy-plane usually have

the Fourier coefficients with the largest magnitude, hence the value of χ obtained by means of the algorithm can be used for the other translations too. Although this argument is tenuous and does not actually prove that the selected χ also works for translation directions that are neither close to the xy-plane nor to the z-axis, numerical experiments (see Section 6.6) indicate that it is at least approximately valid.

The translation distance used in the algorithm is $r_T^{\min}$. The superscript $\min$ is introduced to indicate that the shortest translation distance should be used. If (6.45) is used in an FMM, many different translation distances are encountered. As was explained in [7], the shortest used translation distance should in this case be used in the calculation of χ. This rule stems from the fact that the shortest translation requires the most near-field information. Therefore, if χ is adequate for the shortest translation, the longer translations should also be accurate.

6.5 Transitions between levels

In a full multilevel scheme, a procedure must be devised for calculating the radiation pattern of a box on level $p+1$ from the radiation patterns of its child boxes on level p. In the MLFMA this procedure boils down to an interpolation of the radiation pattern. The transposed procedure, corresponding to an anterpolation in the MLFMA, is required while going down in the tree. The method proposed here has, in the LF case, an almost constant number of samples. However, procedures similar to inter- and anterpolations are still necessary because the value of the complex shift χ changes between levels. We will call these the extrapolations, since the integration domains $[0,2\pi]\otimes[0,2\pi]+j\chi_p$ and $[0,2\pi]\otimes[0,2\pi]+j\chi_{p+1}$ are disjoint, where χ_p is the value of the complex shift on level p. As was noted in [6], these extrapolations can be done using the FFT algorithm. However, this turned out to be significantly less accurate than a procedure based on least-squares fits. The least-squares technique, however, has the disadvantage that dense matrices need to be multiplied. In the following we will propose an modified FFT based method that allows accurate extrapolations. This allows for a very efficient transition between the levels.

Let $\Psi(\theta+j\chi_p,\phi)$ be the radiation pattern of a box on level p, discretized with $2L_d^p+1$ points in θ and ϕ. Then the extrapolation starts with the calculation, by means of FFT, of the spectrum of $\Psi(\theta+j\chi_p,\phi)$

$$\Psi(\theta+j\chi_p,\phi)=\sum_{n=-L_d^p}^{L_d^p}\sum_{m=-L_d^p}^{L_d^p}c_{n,m}e^{jn\theta-n\chi_p}e^{jm\phi}=\sum_{n=-L_d^p}^{L_d^p}\sum_{m=-L_d^p}^{L_d^p}d_{n,m}^p e^{jn\theta}e^{jm\phi} \tag{6.46}$$

The spectrum $c_{n,m}$ can be seen as the spectrum of $\Psi(\theta,\phi)$. Because $\Psi(\theta,\phi)=$

$\Psi(2\pi - \theta, \phi + \pi)$, this spectrum satisfies the following property

$$c_{n,m} = (-1)^m c_{-n,m}. \tag{6.47}$$

Also, $d^p_{n,m} = c_{n,m} e^{-n\chi_p}$. This means that the spectrum $d^p_{n,m}$ of $\Psi(\theta + j\chi_p, \phi)$ has a large magnitude for negative n and a small magnitude for positive n. From this it immediately follows that $d^p_{|n|,m}$ is known with much less accuracy than $d^p_{-|n|,m}$. It now turns out that changing χ actually amplifies these errors. Indeed, the effect of the changing the complex shift from χ_p to χ_{p+1} is that the spectrum $d^p_{n,m}$ is multiplied with $e^{n(\chi_p - \chi_{p+1})}$. Since $\chi_p > \chi_{p+1}$, this blows up the small $d^p_{n,m}$ and shrinks the large $d^p_{n,m}$. Hence the large relative error on the small coefficients is amplified as well. This can be avoided by explicitly using the symmetry relation (6.47), leading to the following formula

$$d^{p+1}_{n,m} = \begin{cases} n \leq 0 : d^p_{n,m} e^{n(\chi_p - \chi_{p+1})} \\ n > 0 : (-1)^m d^p_{-n,m} e^{-n(\chi_p + \chi_{p+1})} \end{cases} \tag{6.48}$$

In this way, the entire spectrum of $\Psi(\theta + j\chi_{p+1}, \phi)$ is calculated from $d^p_{n,m}$ with negative n. Hence they are known with a good accuracy. The radiation pattern on level $p+1$ can then be obtained by means of FFTs.

When going down in the tree, the transposed extrapolation must be used. This transpose can be taken by writing all operations (FFTs, calculation of $d^{p+1}_{n,m}$ with (6.48)) as the multiplication of a matrix and taking the transpose of the entire product. The computational cost of this procedure is the same as the original extrapolation, since the Fourier matrix is its own transpose.

6.6 Numerical results

6.6.1 Single level results

In the previous sections, a closed form expression for the translation operator was derived, as well as a way to determine the parameters L, L_d and χ. In this section we will investigate how well this ensemble of methods works. All calculations were carried out in Matlab, in double precision. In the first test the frequency is varied for a fixed configuration of boxes. The used configuration is the one seen in Figure 6.1, except that there are sources on all the vertices $\boldsymbol{R}_1 - \boldsymbol{r}^p_a$ of box 1 and receivers on all the vertices $\boldsymbol{R}_2 - \boldsymbol{r}^q_d$ of box 2. The 64 interactions are all calculated both directly and using the addition theorem. The error measure Δ is then calculated as the maximum relative error (over the 64 interactions) between the numerically calculated and exact

spherical Hankel function

$$\Delta = \max_{pq} \left| \frac{h^{(2)}_{0,\text{num.}}\left(k\left|\boldsymbol{r}_T + \boldsymbol{r}^p_a - \boldsymbol{r}^q_d\right|\right)}{h^{(2)}_0\left(k\left|\boldsymbol{r}_T + \boldsymbol{r}^p_a - \boldsymbol{r}^q_d\right|\right)} - 1 \right|. \tag{6.49}$$

with

$$h^{(2)}_{0,\text{num.}}\left(k\left|\boldsymbol{r}\right|\right) = \frac{\pi}{N_\theta N_\phi} \sum_{n_\theta=1}^{N_\theta} \sum_{n_\phi=1}^{N_\phi} \hat{T}(k\boldsymbol{r}_T, \theta_{n_\theta} + j\chi, \phi_{n_\phi}) e^{-j\boldsymbol{k}\left(\theta_{n_\theta}+j\chi,\phi_{n_\phi}\right)\cdot\boldsymbol{r}} \tag{6.50}$$

The sides of the boxes are 1m. The maximum relative error is shown in Figure 6.3, for various target accuracies ϵ. It can be seen that the error is always below the target acuracy, except for the rightmost points on the curve with target accuracy 10^{-8}. This failure can be traced back to the HF-breakdown of the addition theorem. This breakdown is seen earliest in the highest-accuracy curve because both L is higher and smaller errors are visible. However, at the highest shown frequency the boxes have a side of 1.6 wavelengths, which is already quite large for a method which is essentially HF unstable. According to [4], the sides of the boxes may be as small as 0.25 wavelengths for 10^{-3} accuracy with the MLFMA. This opens up the possibility of making a switch to the MLFMA with uniform discretization, once the boxes reach a certain size, yielding a broadband method.

The results from the first test show that the proposed mechanisms for determining L, L_d and χ are adequate if used for one translation. In the second test we will show that these parameters also work when many different translations have to be performed, as is the case in an FMM. Since the calculation of both L_d and χ was based on translations in the xy-plane, we will be mostly interested in the error controllability of the method for θ_T differing much from $\frac{\pi}{2}$. The translations under consideration are therefore defined by the following formula

$$\boldsymbol{r}_T = r_T^{\min}(1 + \frac{n_r}{4}) \left[\sin\left(\frac{\pi n_t}{30}\right)\hat{\boldsymbol{e}}_x + \cos\left(\frac{\pi n_t}{30}\right)\hat{\boldsymbol{e}}_z\right], \quad \forall n_r \in [0,4], n_t \in [0,30]. \tag{6.51}$$

and shown in Figure 6.4. A further reason to omit a dependence on ϕ_T is that the values of L_d and χ do not depend on ϕ_T, even if we would use a general translation operator in the xy-plane for their calculation. In addition, both the simple dependence on ϕ_T of the translation operator and numerical tests indicate that the error is relatively invariant under rotations around the z-axis. The accuracy results are summarized in Figures 6.5(a) and 6.5(b). For both figures the target accuracy was 10^{-5}, the sides of the boxes were 1m and the shortest translation distance $r_T^{\min}$ was 3m. The frequency for Figure 6.5(a) was 4.77kHz, while the frequency for Figure 6.5(b) was 239MHz.

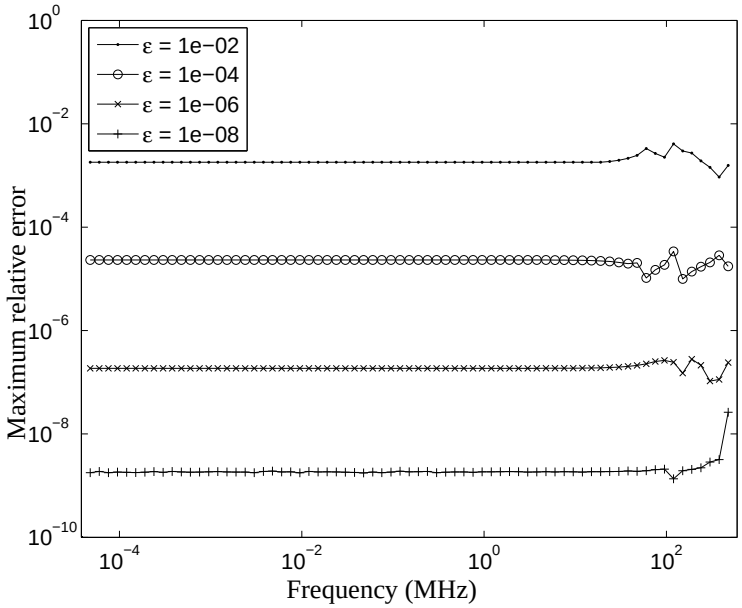

Figure 6.3: The maximum relative error Δ as a function of frequency.

This leads to the parameters $L = 20$, $L_d = 21$ and $\chi = 11.51098$ for Figure 6.5(a) and $L = 24$, $L_d = 32$ and $\chi = 1.03578$ for Figure 6.5(b). From these figures, it is clear that the accuracy requirements are fulfilled for all the tested translations. Therefore, this validates the heuristic algorithms devised for calculating L_d and χ and shows the usefulness of the new addition theorem in an FMM.

6.6.2 Multilevel results

The extrapolation procedure outlined in Section 6.5 and its transpose were also implemented in Matlab and tested on a geometry as shown in Figure 6.6. The largest boxes have sides 1m, the frequency is 477MHz and the target accuracy is 10^{-6}. The largest boxes are divided $n_{\text{level}} - 1$ times and the error of the addition theorem is again calculated as the maximum error over the 64 combinations of vertices. Table 6.1 shows the obtained accuracy for various numbers of levels. These results clearly demonstrate the error-controllability of the total algorithm.

6.7 Conclusion

A novel plane wave addition theorem has been presented. It was constructed by judiciously replacing spherical harmonics in the translation operator of the MLFMA

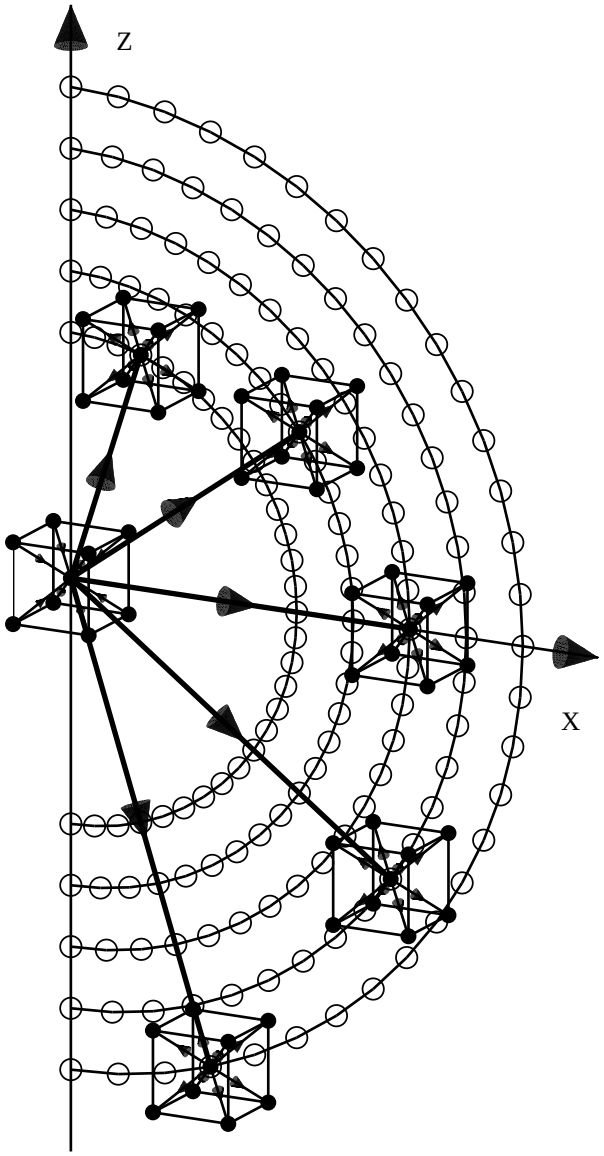

Figure 6.4: The tested translations. For each translation distance, only one of the 31 translations is depicted.

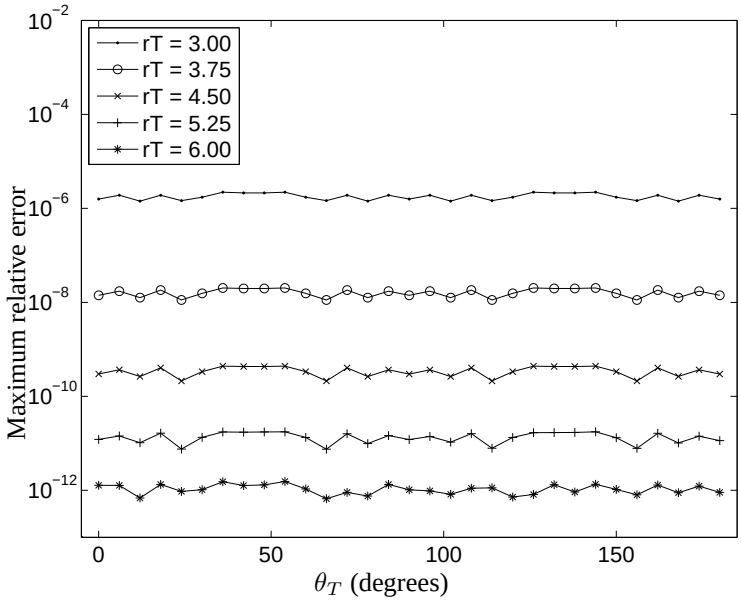

(a)

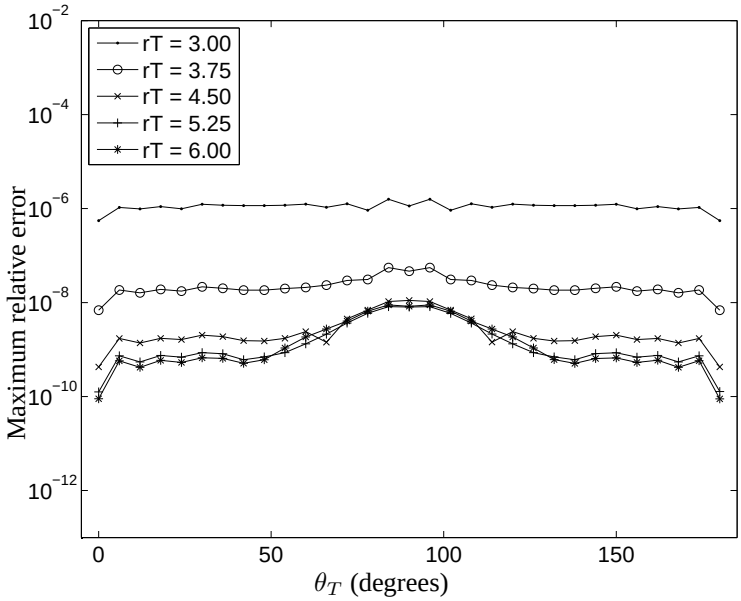

(b)

Figure 6.5: The maximum relative error as a function of θ_T.

n_{level}	Accuracy
1	$2.430667966162078\ 10^{-7}$
2	$1.970807036056693\ 10^{-7}$
3	$1.970906654170130\ 10^{-7}$
4	$1.970871348190628\ 10^{-7}$
5	$1.970960996697772\ 10^{-7}$
6	$1.969563794810023\ 10^{-7}$
7	$1.970044079688026\ 10^{-7}$
8	$1.968621907003791\ 10^{-7}$
9	$1.968419081134079\ 10^{-7}$
10	$1.968573919736930\ 10^{-7}$

Table 6.1: Error on the addition theorem in a multilevel environment, for different numbers of levels n_{level}.

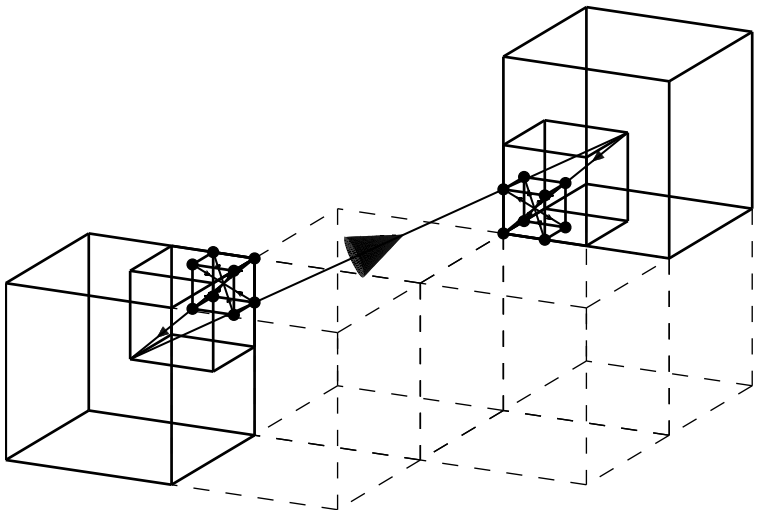

Figure 6.6: One of the geometries used for testing the accuracy of the interpolations. The number of levels n_{level} determines how deeply the largest boxes are divided. This particular geometry has three levels.

with pseudospherical harmonics. Although these novel distributions have a diverging Fourier spectrum, truncation of the spectrum yields a finite and valid translation operator. However, the divergence of the spectrum makes it impossible to choose the truncation bound arbitrarily large, without leading to an HF numerical instability. A fast algorithm for calculating the Fourier spectrum has been provided. For LF, the specific form of the Fourier spectrum of the pseudospherical harmonics has allowed us to find a complex shift that is capable of compensating most of the divergence of the spherical Hankel function, thereby eliminating the LF instability. In addition, the transitions between levels can be done very efficiently using FFTs. To the best knowledge of the authors, this is the first analytically known plane wave addition theorem that is numerically stable in the quasi static regime. Moreover, the numerical results show that it is error controllable for sufficiently high frequencies. Therefore a hybrid method with the usual MLFMA is straightforward, yielding a broadband method.

6.A Pseudospherical harmonics

The so-called pseudospherical harmonics $U_{l,m}(\theta,\phi)$ used in this paper are defined as

$$U_{l,m}(\theta,\phi) = K_{lm} e^{jm\phi} \frac{\sin^m\theta}{2^l l!} \left(\frac{1}{\sin\theta}\frac{\mathrm{d}}{\mathrm{d}\theta}\right)^{l+m} \left[S(\theta)\sin^{2l}\theta\right], \tag{6.52}$$

with $S(\theta) = \frac{|\sin\theta|}{\sin\theta}$ a piecewise constant function that has value $+1$ for $\theta \in]0,\pi[$ and has value -1 for $\theta \in]\pi,2\pi[$. The derivatives in (6.52) must be interpreted in a distributional sense, since $U_{l,m}(\theta,\phi)$ contains Dirac delta distributions and derivatives thereof. Therefore the pseudospherical harmonics only have meaning when they are integrated with sufficiently smooth functions.

The following properties of the pseudospherical harmonics are very similar to properties (A.6) and (A.7) of the spherical harmonics

$$U_{l,m}(\pi-\theta,\phi+\pi) = (-1)^l U_{l,m}(\theta,\phi), \tag{6.53}$$

$$U_{l,m}(2\pi-\theta,\phi+\pi) = -U_{l,m}(\theta,\phi). \tag{6.54}$$

However, property (A.8) nor an orthogonality relation like (A.17) exist for the pseudospherical harmonics. Instead the following orthogonality relation holds

Theorem 6.A.1 *For any integers l_1, l_2 and m_1, m_2 satisfying $l_j \geq 0$ and $-l_j \leq m_j \leq l_j$ the following holds*

$$\int_0^{2\pi}\int_0^{2\pi} U_{l_1,m_1}(\theta,\phi)\, Y^*_{l_2,m_2}(\theta,\phi)\sin\theta \mathrm{d}\theta\mathrm{d}\phi = 2\delta_{l_1,l_2}\delta_{m_1,m_2}. \tag{6.55}$$

Proof Let Q denote the left hand side of Eqn. (6.55). To prove Theorem 6.A.1, first

replace $Y^*_{l_2,m_2}(\theta,\phi)$ by $(-1)^{m_2}Y_{l_2,-m_2}(\theta,\phi)$ and integrate over ϕ

$$Q = 2\pi\delta_{m1,m2}(-1)^{m_2}\frac{K_{l_1,m_1}}{2^{l_1}l_1!}\frac{K_{l_2,-m_2}}{2^{l_2}l_2!} \times \int_0^{2\pi}\left(\frac{1}{\sin\theta}\frac{\mathrm{d}}{\mathrm{d}\theta}\right)^{l_1+m_1}\left[S(\theta)\sin^{2l_1}\theta\right]\left(\frac{1}{\sin\theta}\frac{\mathrm{d}}{\mathrm{d}\theta}\right)^{l_2-m_1}\left[\sin^{2l_2}\theta\right]\sin\theta\mathrm{d}\theta. \tag{6.56}$$

The integral can be transformed into a well-defined integral by performing partial integration l_1+m_1 times

$$(-1)^{l_1+m_1}\int_0^{2\pi} S(\theta)\sin^{2l_1}\theta\left(\frac{1}{\sin\theta}\frac{\mathrm{d}}{\mathrm{d}\theta}\right)^{l_2+l_1}\left[\sin^{2l_2}\theta\right]\sin\theta\mathrm{d}\theta. \tag{6.57}$$

Due to the definition of $S(\theta)$, the product $S(\theta)\sin\theta$ becomes $|\sin\theta|$. At this point the symmetry of the integrand can be used to reduce the integration domain to $[0,\pi]$. This brings a factor $1+(-1)^{l_1+l_2}$ in front of the integral. Then partial integration can again be performed l_1+m_1 times, yielding an integral that is very similar to the orthogonality integral of the spherical harmonics

$$(1+(-1)^{l_1+l_2})\int_0^{\pi}\left(\frac{1}{\sin\theta}\frac{\mathrm{d}}{\mathrm{d}\theta}\right)^{l_1+m_1}\left[\sin^{2l_1}\theta\right]\left(\frac{1}{\sin\theta}\frac{\mathrm{d}}{\mathrm{d}\theta}\right)^{l_2-m_1}\left[\sin^{2l_2}\theta\right]\sin\theta\mathrm{d}\theta. \tag{6.58}$$

As a consequence Eqn. (6.56) becomes

$$Q = (1+(-1)^{l_1+l_2})\int_0^{2\pi}\int_0^{\pi} Y_{l_1,m_1}(\theta,\phi)\,Y^*_{l_2,m_2}(\theta,\phi)\sin\theta\mathrm{d}\theta\mathrm{d}\phi = 2\delta_{l_1,l_2}\delta_{m_1,m_2}. \tag{6.59}$$

This conludes the proof of (6.55). □

6.B Useful properties of the pseudospherical harmonics

In this appendix, some properties will be proven that are necessary for calculating the Fourier spectrum of the pseudospherical harmonics. First we will prove the following lemma

Lemma 6.B.1 *For any integer l satisfying $l \geq 0$ the following holds*

$$S(\theta)\sin^{2l}\theta = \frac{2(-1)^l\Gamma(2l+1)}{2^{2l}\pi}\sum_{p=0}^{\infty}\frac{\Gamma\left(p-l+\frac{1}{2}\right)}{\Gamma\left(p+l+\frac{3}{2}\right)}\sin\left[(2p+1)\theta\right] \tag{6.60}$$

Proof It is easily verified that the result holds for $l = 0$. It then remains to be proven from induction that if (6.60) is correct for a certain $l \geq 0$, it is correct for $l+1$. Therefore the product of the right hand side of (6.60) with $\sin^2\theta$ must be investigated.

$$\begin{aligned}
&\sin^2\theta\frac{2(-1)^l\Gamma(2l+1)}{2^{2l}\pi}\sum_{p=0}^{\infty}\frac{\Gamma\left(p-l+\frac{1}{2}\right)}{\Gamma\left(p+l+\frac{3}{2}\right)}\sin\left[(2p+1)\theta\right]\\
&\quad=\frac{(-1)^l\Gamma(2l+1)}{2^{2l+1}\pi}\sum_{p=0}^{\infty}\frac{\Gamma\left(p-l+\frac{1}{2}\right)}{\Gamma\left(p+l+\frac{3}{2}\right)}\\
&\qquad\qquad\times\left\{2\sin\left[(2p+1)\theta\right]-\sin\left[(2p+3)\theta\right]-\sin\left[(2p-1)\theta\right]\right\}\\
&\quad=-\frac{(-1)^l\Gamma(2l+1)}{2^{2l+1}\pi}\sum_{p=0}^{\infty}2(l+1)(2l+1)\frac{\Gamma\left(p-l-\frac{1}{2}\right)}{\Gamma\left(p+l+\frac{5}{2}\right)}\sin\left[(2p+1)\theta\right]\\
&\quad=\frac{2(-1)^{l+1}\Gamma(2(l+1)+1)}{2^{2(l+1)}\pi}\sum_{p=0}^{\infty}\frac{\Gamma\left(p-(l+1)+\frac{1}{2}\right)}{\Gamma\left(p+(l+1)+\frac{3}{2}\right)}\sin\left[(2p+1)\theta\right],
\end{aligned} \tag{6.61}$$

which concludes the proof. □

Now we move on to proving the wanted equality

Theorem 6.B.2 *For any integers l and m satisfying $l \geq 0$ and $-l \leq m \leq l$ the following holds*

$$\left(\frac{1}{\sin\theta}\frac{\mathrm{d}}{\mathrm{d}\theta}\right)^{l+m}\left[S(\theta)\sin^{2l}\theta\right] = \frac{2^{l+m+1}\Gamma(l+1)}{\sqrt{\pi}}\sum_{p=0}^{\infty}\lambda_{l,m}^{p}\sin\left[(l+m+2p+1)\theta\right], \tag{6.62}$$

with

$$\lambda_{l,m}^{p} = \frac{\Gamma\left(p+m+\frac{1}{2}\right)\Gamma(l+m+p+1)}{\Gamma\left(m+\frac{1}{2}\right)\Gamma\left(l+p+\frac{3}{2}\right)\Gamma(p+1)}. \tag{6.63}$$

Proof This proof will also be done using induction. By means of Lemma 6.B.1 and

$$\frac{\Gamma(l+1)}{\Gamma\left(-l+\frac{1}{2}\right)} = \frac{(-1)^l\Gamma(2l+1)}{2^{2l}\sqrt{\pi}}, \tag{6.64}$$

it is easy to prove (6.62) for the special case $m = -l$. Now assume that (6.62) holds

for a certain $m \in [-l, l[$, then we have to prove that it also holds for $m+1$

$$\left(\frac{1}{\sin\theta}\frac{\mathrm{d}}{\mathrm{d}\theta}\right)^{l+m+1}\left[S(\theta)\sin^{2l}\theta\right]$$
$$= \left(\frac{1}{\sin\theta}\frac{\mathrm{d}}{\mathrm{d}\theta}\right)\frac{2^{l+m+1}\Gamma(l+1)}{\sqrt{\pi}}\sum_{p=0}^{\infty}\lambda_{l,m}^{p}\sin\left[(l+m+2p+1)\theta\right] \tag{6.65}$$
$$= \frac{1}{\sin\theta}\frac{2^{l+m+1}\Gamma(l+1)}{\sqrt{\pi}}\sum_{p=0}^{\infty}(l+m+2p+1)\lambda_{l,m}^{p}\cos\left[(l+m+2p+1)\theta\right]. \tag{6.66}$$

The factor $(l+m+2p+1)\lambda_{l,m}^{p}$ can be dealt with by means of the following identity

$$(l+m+2p+1)\lambda_{l,m}^{p} = \lambda_{l,m+1}^{p} - \lambda_{l,m+1}^{p-1}. \tag{6.67}$$

This identity is still valid in the special case where $p=0$ because $\frac{1}{\Gamma(0)}=0$. Equation (6.65) then becomes

$$\frac{1}{\sin\theta}\frac{2^{l+m+1}\Gamma(l+1)}{\sqrt{\pi}}\sum_{p=0}^{\infty}\left(\lambda_{l,m+1}^{p}-\lambda_{l,m+1}^{p-1}\right)\cos\left[(l+m+2p+1)\theta\right]$$
$$= \frac{2^{l+m+2}\Gamma(l+1)}{\sqrt{\pi}}\sum_{p=0}^{\infty}\lambda_{l,m+1}^{p}\sin\left[(l+m+2p+2)\theta\right]. \tag{6.68}$$

which concludes the proof. □

For completeness, the following property of $\lambda_{l,m}^{p}$ will also be shown:

Lemma 6.B.3 *For any x and any integer $p \geq 0$, $l \geq 0$ and $m \in [-l, l]$ the following holds*

$$\lim_{x\to p}\left[\lambda_{l,m}^{x} + \lambda_{l,m}^{-x-l-m-1}\right] = 0. \tag{6.69}$$

Proof Using the definition (6.63) for $\lambda_{l,m}^{-x-l-m-1}$ yields

$$\lambda_{l,m}^{-x-l-m-1} = \frac{\Gamma\left(-x-l-\frac{1}{2}\right)\Gamma(-x)}{\Gamma\left(m+\frac{1}{2}\right)\Gamma\left(-x-m+\frac{1}{2}\right)\Gamma(-x-l-m)},$$
$$= \frac{\sin(\pi(x+l+m))\sin(\pi(x+m-\frac{1}{2}))}{\sin(\pi x)\sin(\pi(x+l+\frac{1}{2}))}\lambda_{l,m}^{x}. \tag{6.70}$$

The following form of the functional equation of the Gamma function was used to

obtain this result

$$\Gamma(-z)\,\Gamma(z+1) = -\frac{\pi}{\sin(\pi z)}. \tag{6.71}$$

By means of Eqn. (6.70), the limit reduces to

$$\lim_{x\to p}\left[\lambda_{l,m}^{x} + \lambda_{l,m}^{-x-l-m-1}\right] = \lambda_{l,m}^{p}\left[1 + (-1)^{l+m}\frac{(-1)^{p+m+1}}{(-1)^{p+l}}\right] = 0, \tag{6.72}$$

where we used l'Hôspital's rule. □

6.C Recursive calculation of $u_{l,m}^n$

Here we will supply a recurrence formula and an algorithm that can be used for an $\mathcal{O}\left(L^2\right)$ calculation of $u_{l,m}^n$, with $n, l \in [0, L]$ and m fixed. The values of $u_{l,m}^n$ for negative n can be obtained by means of Eqn. (6.23). The recurrence is proven in the following Lemma:

Lemma 6.C.1 *For any integer n, $l \geq 0$ and $m \in [-l, l]$ the following holds*

$$\frac{2l+1}{2}\left[\tilde{u}_{l,m}^{n+2} + \tilde{u}_{l,m}^{n}\right] = (l+m)\tilde{u}_{l-1,m}^{n+1} + (l-m+1)\tilde{u}_{l+1,m}^{n+1}, \tag{6.73}$$

with $\tilde{u}_{l,m}^n = \frac{u_{l,m}^n}{K_{l,m}}$.

Proof We start with the following identity

$$\frac{2l+1}{2}\left[\lambda_{l,m}^{p+1} + \lambda_{l,m}^{p}\right] = (l+m)\lambda_{l-1,m}^{p+1} + (l-m+1)\lambda_{l+1,m}^{p}. \tag{6.74}$$

The proof of this using Eqn. (6.63) is tedious but straightforward. Now we replace p with $\frac{n-l}{2} - q$ to obtain

$$\frac{2l+1}{2}\left[\lambda_{l,m}^{\frac{(n+2)-l}{2}-q} + \lambda_{l,m}^{\frac{n-l}{2}-q}\right] = (l+m)\lambda_{l-1,m}^{\frac{n+1-(l-1)}{2}-q} + (l-m+1)\lambda_{l+1,m}^{\frac{n+1-(l+1)}{2}-q}. \tag{6.75}$$

Applying the sum operator $\frac{(-j)^m}{2\sqrt{\pi}}\sum_{q=0}^{m+1}(-1)^{m-q}\binom{m+1}{q}$ to this entire equation yields Eqn. (6.73) which concludes the proof. □

For the special case when $n = l - 2$, Lemma 6.3.1 reduces the recurrence to the simpler form

$$\tilde{u}_{l,m}^{l} = \frac{2(l+m)}{2l+1}\tilde{u}_{l-1,m}^{l-1}. \tag{6.76}$$

The following algorithm can now be used to calculate all the $\tilde{u}^n_{l,m}$ for a fixed m:

1: Calculate $\tilde{u}^n_{m,m} \forall n \in [m, L]$ and $\tilde{u}^n_{m+1,m} \forall n \in [m+1, L]$ using the direct formula (6.28)
2: **for** $l = m + 2$ to L **do**
3: Calculate $\tilde{u}^l_{l,m}$ from $\tilde{u}^{l-1}_{l-1,m}$ by means of (6.76)
4: **end for**
5: **for** $h = 0$ by 2 to $L - m - 4$ **do**
6: **for** $l = m + 2$ to $L - h - 2$ **do**
7: $n = l + h$
8: Calculate $\tilde{u}^{n+2}_{l,m}$ from $\tilde{u}^n_{l,m}$, $\tilde{u}^{n+1}_{l-1,m}$ and $\tilde{u}^{n+1}_{l+1,m}$ by means of (6.73)
9: **end for**
10: **end for**

Bibliography

[1] R.F. Harrington. *Field Computations by Moment Methods*. Macmillan, New York, 1968.

[2] L.J. Jiang and W.C. Chew. Low-frequency fast inhomogeneous plane-wave algorithm (LF-FIPWA). *Microwave and Optical Technology Letters*, 40(2):117–122, Jan 2004.

[3] L.J. Jiang and W.C. Chew. A mixed-form fast multipole algorithm. *IEEE Transactions on Antennas and Propagation*, 53(12):4145–4156, Dec 2005.

[4] H. Cheng, W.Y. Crutchfield, Z. Gimbutas, L.F. Greengard, J.F. Ethridge, J. Huang, V. Rokhlin, N. Yarvin, and J. Zhao. A wideband fast multipole method for the Helmholtz equation in three dimensions. *Journal of Computational Physics*, 216(1):300–325, 2006.

[5] L. Xuan, A. Zhu, R.J. Adams, and S.D. Gedney. A broadband multilevel fast multipole algorithm. In *Proceedings of the IEEE AP-S International Symposium, Monterey, CA*, volume 2, pages 1195–1198, June 2004.

[6] H. Wallen and J. Sarvas. Translation procedures for broadband MLFMA. *Progress In Electromagnetics Research*, 55:47–78, 2005.

[7] I. Bogaert, J. Peeters, and F. Olyslager. A nondirective plane wave MLFMA stable at low frequencies. *Accepted for IEEE Transactions on Antennas and Propagation*, 2008.

[8] W.C. Chew, S. Koc, J.M. Song, C.C. Lu, and E. Michielssen. A succinct way to diagonalize the translation matrix in three dimensions. *Microwave and Optical Technology Letters*, 15(3):144–147, December 1998.

[9] M. Abramowitz and I.A. Stegun. *Handbook of Mathematical Functions with Formulas, Graphs and Mathematical Tables*. Advanced Mathematics. Dover Publications, Inc., New York, 1965.

[10] W.C. Chew, J.M. Jin, E. Michielssen, and J. Song. *Fast and Efficient Algorithms in Computational Electromagnetics*. Artech House, 2001.

[11] J. Sarvas. Performing interpolation and anterpolation entirely by fast Fourier transform in the 3-D multilevel fast multipole algorithm. *SIAM Journal on Numerical Analysis*, 41(6):2180–2196, 2003.

CHAPTER 7

Homogenization of Metamaterials Using Full-Wave Simulations

I. Bogaert, J. Peeters, and F. Olyslager

Provisionally accepted for the new Elsevier journal *Metamaterials* (Invited).

★★★

Here, the broadband FMMs developed in the chapters 3 and 5 are applied to the simulation of metamaterials. Metamaterials are structures consisting of a large number of more or less homogeneously distributed particles with specific properties. Because the inhomogeneities are at a scale much smaller than the wavelength, these structures can be treated as homogeneous effective materials. These artificial materials may have properties that are not found in natural materials, for example a negative index of refraction. The simulation of metamaterials is a broadband problem. Indeed, by definition the wavelength is larger than the smallest geometrical detail (the particles), and at the same time the wavelength is usually smaller than the entire piece of metamaterial, as for example in 7.4.1. The simulation method consists of the multiple scattering equation from 2.4.3, accelerated by means of the SPWMLFMA [9] and the technique described in Chapter 3. The determination of the T-matrix of one particle is done by means of a Method of Moments surface integral equation solver that is accelerated with the NSPWMLFMA from Chapter 5. In addition to simulating the metamaterials, we also present closed-form full-wave homogenization formulas to extract the effective material parameters from the T-matrix of a spherical piece of metamaterial. Examples verify the accuracy and limitations of the method.

7.1 Introduction

In this paper we want to explore the possibilities of full-wave electromagnetic field simulations to find effective material parameters of metamaterials, i.e. we try to solve the homogenization problem using accurate field simulations. By a metamaterial we understand, in this paper, a random mixture of inclusions embedded in a host medium. The inclusions, called particles in this paper, can have any geometry and any linear material properties.

Although we see more and more full-wave simulations of the scattering of fields at finite pieces of metamaterials in literature, using full-wave simulations to come to effective parameters has been explored only limitedly. Early efforts have been done by Whites using a Method of Moments (MoM) thin wire integral equation simulation for chiral materials [1], [2] and [3]. In those publications spherical ensembles of chiral wire particles were considered. The most advanced effort was done in [4] which considered a spherical ensemble of dielectric spheres and used the T-matrix method [5] to come to effective permittivities. In [6] the homogenization of a mixture of metal needles was considered, also using a Method of Moments (MoM) thin wire integral equation simulation method. In that paper not only spherical but also cylindrical ensembles were considered.

In the present contribution we will also use the T-matrix method and a spherical ensemble of particles to obtain effective material parameters. In order to be able to simulate a large number of particles we accelerate the T-matrix method with a Fast Multipole Method (FMM) [7]. In [8] also a T-matrix method was used to calculate the scattering at a large ensemble of spheres (not the homogenization) in the realm of metamaterials. It was accelerated compared to [4] by using a Single Level FMM.

One of the most widely known FMMs is the Multilevel Fast Multipole Algorithm (MLFMA). However, the problem at hand is difficult to handle with the propagating plane wave based MLFMA because it contains much geometrical detail, i.e. the particles, that are small compared to the wavelength. To overcome this problem we resort to the Stable Plane Wave MLFMA (SPWMLFMA) [9] which is further accelerated by the method described in [10].

Unlike in [4] and [8] we will not limit the analysis to spherical particles but consider generally shaped particles. The T-matrix of each particle is determined using a MoM technique based on a surface integral equation. The MoM to analyze one particle is also accelerated by an FMM. Again one faces the problem that the MLFMA is not suitable and now we resort to the recently developed non-directive SPWMLFMA (NSPWMLFMA) [11].

Generally shaped particles which are randomly ordered and oriented lead in the most general form to a bi-isotropic material. If the particles have handedness then the material will be chiral. As said above we will use a spherical ensemble of particles and compare this ensemble with an effective homogeneous bi-isotropic sphere with

the same radius. In [3] and [4] the average of a Monte Carlo scattering simulation over a number of different random ensembles is considered. In [6] the average is taken over different angles of incidence for the same ensemble of spheres. In both cases this result is then fitted to the Mie series of an isotropic sphere. Here we use a sufficiently large ensemble such that an average over different angles of incidence is again suitable for homogenization. However, this is not accomplished by doing several scattering simulations but immediately by considering a summing operation on the T-matrix of the entire ensemble. We also do not use a fitting technique to find the effective parameters but develop a new closed form formula, based on recursive properties of spherical Bessel functions, to derive the effective parameters directly form the T-matrix.

This paper is organized as follows. First we develop the homogenization assuming that the T-matrix of the entire ensemble is known. Then we give some details about the numerical simulation technique to obtain the T-matrix of one particle and the T-matrix of the entire ensemble. In Section 4 we verify the method and also discuss some problems and limitations. Finally, a number of examples illustrate the method. In the last section we will also look at a general scattering experiment, as in [8], without considering homogenization. We consider examples with about 350000 unknowns. First results of this work have been reported in [12] and [13].

7.2 Homogenization

7.2.1 Field expansion in a bi-isotropic medium

Let us first find a general field solution in a sourceless homogeneous bi-isotropic medium using vector multipoles. The Maxwell curl equation in a bi-isotropic medium, using an $e^{j\omega t}$ time dependence, are given by [14]

$$\check{\boldsymbol{\nabla}} \times \begin{bmatrix} \boldsymbol{e}(\boldsymbol{r}) \\ \boldsymbol{h}(\boldsymbol{r}) \end{bmatrix} = j\omega \begin{bmatrix} -\zeta & -\mu \\ \varepsilon & \xi \end{bmatrix} \cdot \begin{bmatrix} \boldsymbol{e}(\boldsymbol{r}) \\ \boldsymbol{h}(\boldsymbol{r}) \end{bmatrix}. \tag{7.1}$$

We assume that the material parameter matrix can be diagonalized using an eigenvalue decomposition as follows

$$j\omega \begin{bmatrix} -\zeta & -\mu \\ \varepsilon & \xi \end{bmatrix} = \mathsf{V} \cdot \begin{bmatrix} k_1 & 0 \\ 0 & k_2 \end{bmatrix} \cdot \mathsf{V}^{-1}, \tag{7.2}$$

where k_1 and k_2 are the eigenvalues and where the matrix V contains the corresponding eigenvectors. The eigenvalues k_1 and k_2 are the wavenumbers of the medium.

Invoking a Beltrami decomposition [15] yields decoupled curl equations

$$\check{\boldsymbol{\nabla}} \times \begin{bmatrix} \boldsymbol{\Theta}(\boldsymbol{r}) \\ \boldsymbol{\Phi}(\boldsymbol{r}) \end{bmatrix} = \begin{bmatrix} k_1 & 0 \\ 0 & k_2 \end{bmatrix} \cdot \begin{bmatrix} \boldsymbol{\Theta}(\boldsymbol{r}) \\ \boldsymbol{\Phi}(\boldsymbol{r}) \end{bmatrix}, \tag{7.3}$$

with $\boldsymbol{\Theta}(\boldsymbol{r})$ and $\boldsymbol{\Phi}(\boldsymbol{r})$ the so-called Beltrami fields that are related to the $\boldsymbol{e}(\boldsymbol{r})$ and $\boldsymbol{h}(\boldsymbol{r})$ fields through

$$\begin{bmatrix} \boldsymbol{\Theta}(\boldsymbol{r}) \\ \boldsymbol{\Phi}(\boldsymbol{r}) \end{bmatrix} = \mathsf{V}^{-1} \cdot \begin{bmatrix} \boldsymbol{e}(\boldsymbol{r}) \\ \boldsymbol{h}(\boldsymbol{r}) \end{bmatrix}. \tag{7.4}$$

The vector multipoles are defined as

$$\boldsymbol{M}^f_{l,m}(k\boldsymbol{r}) = \frac{f_l(kr)}{\sqrt{l(l+1)}}(-j\boldsymbol{r} \times \check{\boldsymbol{\nabla}}) Y_{l,m}(\hat{\boldsymbol{r}}), \tag{7.5}$$

$$\boldsymbol{N}^f_{l,m}(k\boldsymbol{r}) = \frac{1}{k}\check{\boldsymbol{\nabla}} \times \boldsymbol{M}^f_{l,m}(k\boldsymbol{r}), \tag{7.6}$$

with integer $l \in [0, \infty]$ and $m \in [-l, l]$. The spherical harmonics $Y_{l,m}(\hat{\boldsymbol{r}})$ are defined in Appendix A and the unit vector $\hat{\boldsymbol{r}}$ is given by $\frac{\boldsymbol{r}}{r}$. The function $f_l(\cdot)$ and the superscript f in the vector multipoles denote any of the spherical Bessel functions of order l. Due to the properties of the vector multipoles, the field $\boldsymbol{S}^f_{l,m}(k\boldsymbol{r})$, defined as $\boldsymbol{M}^f_{l,m}(k\boldsymbol{r}) + \boldsymbol{N}^f_{l,m}(k\boldsymbol{r})$, satisfies

$$\check{\boldsymbol{\nabla}} \times \boldsymbol{S}^f_{l,m}(k\boldsymbol{r}) = k\boldsymbol{S}^f_{l,m}(k\boldsymbol{r}), \tag{7.7}$$

which means that $\boldsymbol{S}^f_{l,m}(k\boldsymbol{r})$ are the eigenfunctions of the curl operator corresponding to the eigenvalue k. A general field can now be expressed as

$$\boldsymbol{\Theta}(\boldsymbol{r}) = \sum_{l,m} \left[a^1_{l,m} \boldsymbol{S}^j_{l,m}(k_1\boldsymbol{r}) + b^1_{l,m} \boldsymbol{S}^h_{l,m}(k_1\boldsymbol{r}) \right], \tag{7.8}$$

$$\boldsymbol{\Phi}(\boldsymbol{r}) = \sum_{l,m} \left[a^2_{l,m} \boldsymbol{S}^j_{l,m}(k_2\boldsymbol{r}) + b^2_{l,m} \boldsymbol{S}^h_{l,m}(k_2\boldsymbol{r}) \right], \tag{7.9}$$

where in the first term $f_l(\cdot)$ is replaced by the spherical Bessel functions $j_l(\cdot)$ and in the second term by the spherical Bessel function $h_l(\cdot)$ that is defined as

$$h_l(kr) = [s(k)]^l h^{(2)}_l(s(k)kr), \tag{7.10}$$

with $s(k) = -\mathrm{sign}(\Im(k))$ and $h^{(2)}_l(\cdot)$ the spherical Hankel function of second kind and order l.

7.2.2 T-matrix of a bi-isotropic sphere

Consider a homogeneous bi-isotropic sphere with radius a and parameters $(\varepsilon, \mu, \xi, \zeta)$ embedded in free space with parameters (ε_0, μ_0). Suppose the fields outside the sphere are represented by

$$\begin{bmatrix} \boldsymbol{e}^o(\boldsymbol{r}) \\ \boldsymbol{h}^o(\boldsymbol{r}) \end{bmatrix} = \mathsf{V}^o \cdot \begin{bmatrix} \sum_{l,m} \left[a^1_{l,m} \boldsymbol{S}^j_{l,m}\left(k^o_1 \boldsymbol{r}\right) + b^1_{l,m} \boldsymbol{S}^h_{l,m}\left(k^o_1 \boldsymbol{r}\right) \right] \\ \sum_{l,m} \left[a^2_{l,m} \boldsymbol{S}^j_{l,m}\left(k^o_2 \boldsymbol{r}\right) + b^2_{l,m} \boldsymbol{S}^h_{l,m}\left(k^o_2 \boldsymbol{r}\right) \right] \end{bmatrix}, \tag{7.11}$$

with V^o, k^o_1 and k^o_2 resulting from the diagonalization (7.2) for free space parameters. The sphere will impose a relation between the coefficients $(b^1_{l,m}, b^2_{l,m})$ and $(a^1_{l,m}, a^2_{l,m})$. We define this relation as the T-matrix $\mathsf{T}^B_{l,m;l',m'}$ for the Beltrami fields, i.e.

$$\begin{bmatrix} b^1_{l,m} \\ b^2_{l,m} \end{bmatrix} = \sum_{l',m'} \mathsf{T}^B_{l,m;l',m'} \cdot \begin{bmatrix} a^1_{l',m'} \\ a^2_{l',m'} \end{bmatrix}. \tag{7.12}$$

The usual T-matrix $\mathsf{T}_{l,m;l',m'}$ for the fields [5] is then given by $\mathsf{T}_{l,m;l',m'} = \left(\mathsf{V}^o\right)^{-1} \cdot \mathsf{T}^B_{l,m;l',m'} \cdot \mathsf{V}^o$. The fields inside the sphere are

$$\begin{bmatrix} \boldsymbol{e}^i(\boldsymbol{r}) \\ \boldsymbol{h}^i(\boldsymbol{r}) \end{bmatrix} = \mathsf{V}^i \cdot \begin{bmatrix} \sum_{l,m} c^1_{l,m} \boldsymbol{S}^j_{l,m}\left(k^i_1 \boldsymbol{r}\right) \\ \sum_{l,m} c^2_{l,m} \boldsymbol{S}^j_{l,m}\left(k^i_2 \boldsymbol{r}\right) \end{bmatrix}, \tag{7.13}$$

with V^i, k^i_1 and k^i_2 resulting from the diagonalization (7.2) for the parameters of the sphere.

The continuity of the tangential electric and magnetic fields at the boundary of the sphere can be expressed as

$$\mathsf{V}^i \cdot \mathsf{j}^i_l \cdot \begin{bmatrix} c^1_{l,m} \\ c^2_{l,m} \end{bmatrix} = \mathsf{V}^o \cdot \mathsf{j}^o_l \cdot \begin{bmatrix} a^1_{l,m} \\ a^2_{l,m} \end{bmatrix} + \mathsf{V}^o \cdot \mathsf{h}^o_l \cdot \begin{bmatrix} b^1_{l,m} \\ b^2_{l,m} \end{bmatrix}, \tag{7.14}$$

$$\mathsf{V}^i \cdot \tilde{\mathsf{j}}^i_l \cdot \begin{bmatrix} c^1_{l,m} \\ c^2_{l,m} \end{bmatrix} = \mathsf{V}^o \cdot \tilde{\mathsf{j}}^o_l \cdot \begin{bmatrix} a^1_{l,m} \\ a^2_{l,m} \end{bmatrix} + \mathsf{V}^o \cdot \tilde{\mathsf{h}}^o_l \cdot \begin{bmatrix} b^1_{l,m} \\ b^2_{l,m} \end{bmatrix}, \tag{7.15}$$

with

$$\mathsf{j}^o_l = \begin{bmatrix} j_l\left(k^o_1 a\right) & 0 \\ 0 & j_l\left(k^o_2 a\right) \end{bmatrix}, \qquad \tilde{\mathsf{j}}^o_l = \begin{bmatrix} \mathcal{J}_l\left(k^o_1 a\right) & 0 \\ 0 & \mathcal{J}_l\left(k^o_2 a\right) \end{bmatrix}, \tag{7.16}$$

$$\mathsf{h}^o_l = \begin{bmatrix} h_l\left(k^o_1 a\right) & 0 \\ 0 & h_l\left(k^o_2 a\right) \end{bmatrix}, \qquad \tilde{\mathsf{h}}^o_l = \begin{bmatrix} \mathcal{H}_l\left(k^o_1 a\right) & 0 \\ 0 & \mathcal{H}_l\left(k^o_2 a\right) \end{bmatrix}, \tag{7.17}$$

$$\mathsf{j}^i_l = \begin{bmatrix} j_l\left(k^i_1 a\right) & 0 \\ 0 & j_l\left(k^i_2 a\right) \end{bmatrix}, \qquad \tilde{\mathsf{j}}^i_l = \begin{bmatrix} \mathcal{J}_l\left(k^i_1 a\right) & 0 \\ 0 & \mathcal{J}_l\left(k^i_2 a\right) \end{bmatrix}, \tag{7.18}$$

and

$$\mathcal{J}_l(x) = \frac{1}{x}\frac{d}{dx}[x j_l(x)] = j_{l-1}(x) - \frac{l}{x} j_l(x) \tag{7.19}$$

$$\mathcal{H}_l(x) = \frac{1}{x}\frac{d}{dx}[x h_l(x)] = h_{l-1}(x) - \frac{l}{x} h_l(x). \tag{7.20}$$

It can be immediately seen from the system (7.14) and (7.15) that the T-matrix must have a block diagonal form $\mathsf{T}^B_{l,m;l',m'} = \mathsf{T}^B_l \delta_{l,l'}\delta_{m,m'}$, where the 2 by 2 diagonal blocks $\mathsf{T}^B_{l,m;l,m}$ were denoted by T^B_l. This special form of the T-matrix can be traced back to the rotational invariance of the bi-isotropic sphere. Solution of the system (7.14) and (7.15) finally leads to

$$\begin{aligned}\mathsf{T}^B_l = &\left[\left(\tilde{\mathsf{j}}^i_l\right)^{-1}\cdot\left(\mathsf{V}^i\right)^{-1}\cdot\mathsf{V}^o\cdot\tilde{\mathsf{h}}^o_l - \left(\mathsf{j}^i_l\right)^{-1}\cdot\left(\mathsf{V}^i\right)^{-1}\cdot\mathsf{V}^o\cdot\mathsf{h}^o_l\right]^{-1}\\ &\cdot\left[\left(\mathsf{j}^i_l\right)^{-1}\cdot\left(\mathsf{V}^i\right)^{-1}\cdot\mathsf{V}^o\cdot\mathsf{j}^o_l - \left(\tilde{\mathsf{j}}^i_l\right)^{-1}\cdot\left(\mathsf{V}^i\right)^{-1}\cdot\mathsf{V}^o\cdot\tilde{\mathsf{j}}^o_l\right].\end{aligned} \tag{7.21}$$

7.2.3 Homogenization

Consider a spherical piece of metamaterial with radius a embedded in free space for which we have determined the T-matrix $\mathsf{T}^C_{l,m;l',m'}$. How this is done will be explained in the next section. We will now show that it is possible to determine the material parameters ε, μ, ζ and ξ in closed form of an equivalent homogeneous sphere. Hence, we assume that it is possible to homogenize the piece of metamaterial and that it is possible to fit the T-matrix of a homogeneous sphere to $\mathsf{T}^C_{l,m;l',m'}$.

The T-matrix of a bi-isotropic sphere is block diagonal (with 2 by 2 blocks) due to spherical symmetry. However, the matrix $\mathsf{T}^C_{l,m;l',m'}$ which resulted from the simulation of a random ensemble of particles will not be entirely block diagonal. From $\mathsf{T}^C_{l,m;l',m'}$ a block diagonal matrix $\hat{\mathsf{T}}^C_{l,m;l',m'}$ is obtained by averaging over all spatial rotations. This is, as explained in [5], accomplished by

$$\hat{\mathsf{T}}^C_{l,m;l',m'} = \hat{\mathsf{T}}^C_l \delta_{l,l'}\delta_{m,m'} = \delta_{l,l'}\delta_{m,m'}\sum_{m=-l}^{l}\mathsf{T}^C_{l,m;l,m}, \tag{7.22}$$

where again the shorthand notation $\hat{\mathsf{T}}^C_l$ was introduced to indicate the diagonal blocks of $\hat{\mathsf{T}}^C_{l,m;l',m'}$. In a next step we transform $\hat{\mathsf{T}}^C_l$ to the corresponding T-matrix $\hat{T}^{C,B}_l$ for the Beltrami fields of free space

$$\hat{\mathsf{T}}^{C,B}_l = \mathsf{V}^o\cdot\hat{\mathsf{T}}^C_l\cdot(\mathsf{V}^o)^{-1}. \tag{7.23}$$

If we now identify $\hat{\mathsf{T}}_l^{C,B}$ with T_l^B from (7.21) we find after some manipulations

$$\mathsf{V}^i \cdot \mathsf{j}_l^i \cdot \left(\tilde{\mathsf{j}}_l^i\right)^{-1} \cdot \left(\mathsf{V}^i\right)^{-1} = [\mathsf{V}^o \cdot \mathsf{j}_l^o + \mathsf{V}^o \cdot \mathsf{h}_l^o \cdot \hat{\mathsf{T}}_l^{C,B}] \cdot [\mathsf{V}^o \cdot \tilde{\mathsf{j}}_l^o + \mathsf{V}^o \cdot \tilde{\mathsf{h}}_l^o \cdot \hat{\mathsf{T}}_l^{C,B}]^{-1}. \quad (7.24)$$

The quantities on the right-hand side are known, those on the left-hand side are sought for. An eigenvalue decomposition, i.e. a diagonalization, of the right-hand side yields the matrices V_i with the eigenvectors and the diagonal matrix $\mathsf{j}_l^i \cdot \left(\tilde{\mathsf{j}}_l^i\right)^{-1}$ with the eigenvalues denoted as $y_{l,1}$ and $y_{l,2}$. Now we have to determine the wavenumbers k_1^i and k_2^i by solving the equation

$$y_{l,k} = \frac{\mathcal{J}_l\left(k_k^i a\right)}{j_l(k_k^i a)} = \frac{j_{l-1}(k_k^i a)}{j_l(k_k^i a)} - \frac{l}{k_k^i a}, \quad (7.25)$$

for $k = 1, 2$. This can be done in an elegant manner in closed form without having to solve a transcendental equation. Invoking a recursion relation for spherical Bessel functions

$$\frac{j_{l-1}(x)}{j_l(x)} + \frac{1}{\frac{j_l(x)}{j_{l+1}(x)}} = \frac{2l+1}{x}, \quad (7.26)$$

allows us to write the following quadratic equation for k_k^i, $k = 1, 2$,

$$y_{l,k} + \frac{l}{k_k^i a} + \frac{1}{y_{l+1,k} + \frac{l+1}{k_k^i a}} = \frac{2l+1}{k_k^i a}. \quad (7.27)$$

Of the two roots, one can be rejected by substituting the solution back in (7.25) and checking which root is best. From the knowledge of k_1^i and k_2^i and V^i the equivalent material parameters are eventually found using (7.2).

In this derivation we have tacitly assumed that the algorithm yields values k_1^i and k_2^i and V^i, i.e. equivalent material parameters, that are independent of l. In practice this will not be the case and for different values of l different equivalent material parameters will be found. However, if a homogenization of the piece of metamaterial is to make sense, then it is to be expected that the variation on the material parameters for small values of l will be small. Or stated differently the variation on the material parameters will provide an error estimate for these material parameters.

7.3 Simulation technique

This section explains how we calculate the T-matrix of a spherical random ensemble of particles. This is done in two stages. First we determine the T-matrix of one particle using a MoM scattering simulation technique considering different incident fields. Then we determine the T-matrix of the ensemble using an SPWMLFMA T-matrix method.

The T-matrix method requires that the circumscribing spheres of none of the particles overlap. This puts some limitations on the density of the particles. Generating random ensembles of spheres comprising a given volume fraction is not that straightforward. We opted for the following method. First we place one particle at a random position in the spherical piece of material, then we add a second particle at another random position. If the circumscribing spheres do not overlap we leave the second particle, otherwise we generate another random position for the particle. This process is continued iteratively until the desired volume fraction of particles is obtained. This algorithm has its limitations because it does not allow very high volume fractions of particles and because it has an exponential CPU-complexity as a function of the volume fraction. If the considered particles have no spherical symmetry then one also needs to generate a random orientation for each particle in order to obtain an isotropic metamaterial.

A random direction (θ, ϕ) for a particle is found by using $\phi = 2\pi\nu_1$ and $\theta = \cos^{-1}(2\nu_2 - 1)$ with ν_1 and ν_2 uniformly distributed over $[0, 1]$. The particle is then oriented along this direction and rotated around this direction by a random angle $\psi = 2\pi\nu_3$, with ν_3 uniformly distributed over $[0, 1]$. A random position (r, θ, ϕ) for the particle is found by again generating a random direction (θ, ϕ) and a random radial coordinate $r = a\nu_4^{1/3}$ with a the radius of the ensemble and ν_4 uniformly distributed over $[0, 1]$.

7.3.1 T-matrix of one particle

In this section we will present a brief overview of the simulation method used to determine the T-matrix of a single particle. The T-matrix is found from calculating the scattering of vector multipoles with $f_l(\cdot) = j_l(\cdot)$ and evaluating the field in a set of points on a sphere surrounding the particle. This field is then projected back on the vector multipoles as in Eqns. (2.51), (2.52), (2.53) and (2.54).

For the present discussion we assume that the particle is a PEC object with an arbitrary shape. Non-PEC particles consisting of different isotropic materials can be treated in a similar way [17]. We use an Electric Field Integral Equation (EFIE) for the PEC particles considered here. The integral equations are solved using a Galerkin MoM in which the unknown surface current density is discretized on a triangular mesh with Rao-Wilton-Glisson vectorial basis functions. To achieve high accuracy the singular part of the Green functions is extracted for both the self-patch and neighbor-patch integrations. These integrations over the singular part are all being evaluated in closed form.

For particles with a complex geometry the number of unknowns n to discretize the surface current density can be very large. A direct solution of the MoM problem requires $\mathcal{O}\left(n^3\right)$ CPU-time and soon becomes unpractical. For that reason we resort to an FMM that has an $\mathcal{O}\left(n \log n\right)$ complexity. We assume the reader to be

familiar with the basics of FMMs, for an introduction see [7]. The classical plane wave based MLFMA breaks down at low frequencies due to loss of numerical accuracy. This means that the boxes on the lowest level in the MLFMA for structures containing significant sub-wavelength geometrical detail, as will be the case for particles with complex geometries, will contain a considerable number of unknowns. Several attempts have been proposed to remedy this problem without having to resort to non-diagonal translation operators. The crux is to incorporate more near-field information in the plane wave spectrum. This can be done by incorporating evanescent plane waves leading to the Stable Plane Wave MLFMA (SPWMLFMA) [9] which needs 6 radiation patterns along 6 different directions. Recently a new method, the non-directional SPWMLFMA (NSPWMLFMA), was devised [11] that avoids these 6 different directions.

Often a particle will contain symmetries where two pairs of interacting triangles are geometrically equal which means that the corresponding two elements in the MoM matrix are equal. In [16] and [17] we have shown that a splay tree [18] allows to extract these geometrical symmetries in $\mathcal{O}(n \log n)$ computational complexity, where n are the number of unknowns. Even for structures with limited symmetry this method yields savings in CPU-time. The extra memory needed for the splay tree is only required during the set-up phase of the NSPWMLFMA. An implementation of the NSPWMLFMA is available as open-source software from [19]. This also considers non-PEC objects and includes an asynchronous parallelization of the algorithm for distributed memory GRID environments connected by gigabit Ethernet.

7.3.2 T-matrix of an ensemble

To determine the T-matrix of an ensemble of N particles from the T-matrices of these particles we will use the T-matrix approach as described in e.g. 2.4.3 or [5]. If each T-matrix contains M^2 elements then this requires the solution of a linear system of NM unknowns. Since N will be large it is not possible to use a direct or even an iterative solution of this system. The constituents are small compared to wavelength, although the ensemble can be several wavelengths in size. This means that the numerical problem is at the same time a low- and a high-frequency problem. The solution of the linear system can again be accelerated using an FMM technique. In order to be able to use small boxes and to fully exploit the potential of the FMM we will again resort to the SPWMLFMA as derived by [9]. In this way it becomes possible to obtain a computational and memory complexity of $\mathcal{O}(NM \log NM)$. The SPWMLFMA requires the conversion of the vectorial multipoles into evanescent plane waves along 6 different directions. In [10] a method has been devised that reduces the computational complexity of this conversion by a factor of 6.

7.4 Verification

7.4.1 Lüneburg lens

A Lüneburg lens is a spherical object of which the permittivity has a radial dependence given by $\varepsilon(r) = \varepsilon_0(2 - \frac{r^2}{a^2})$ with a the radius of the lens [20]. It has the property to focus an incident plane wave at a point on the surface of the lens, at least in the geometric optics regime. Let us now consider a metamaterial Lüneburg lens with $a = 8\lambda$ built from a large number of spherical particles with increasing density towards to the center of the lens. The density as a function of the radius was guessed from the Maxwell-Garnett approximation [20] which yields a radial dependence of the volume fraction of inclusions given by

$$f(r) = \frac{1 - \frac{r^2}{a^2}}{4 - \frac{r^2}{a^2}} \frac{\varepsilon_{r,incl} + 2}{\varepsilon_{r,incl} - 1}. \tag{7.28}$$

The wavelength is 2m, the particles have a diameter of 0.12λ and a relative permittivity of $\varepsilon_{r,incl} = 12$. In the example $N = 42899$ particles and $M = 6$ vector multipoles per particle were considered leading to 257394 unknowns. Figure 1 shows the focusing of the amplitude of the field when a plane wave is incident on the lens from the right. The example proves the validity of homogenization using Maxwell-Garnett and the accuracy of the simulation method.

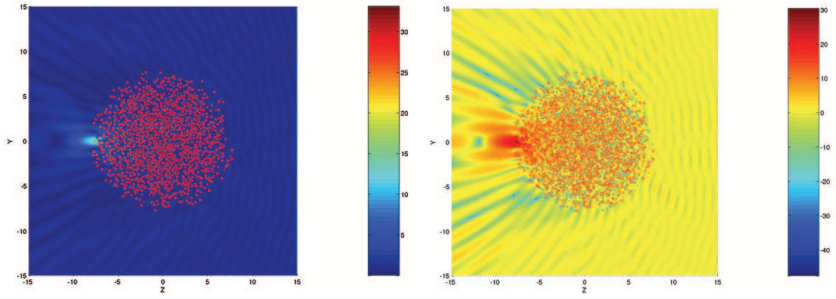

(a) (b)

Figure 7.1: Amplitude of the field in a metamaterial Lüneburg lens illuminated by a plane wave from the right. The right figure shows the amplitude is in dB.

7.4.2 Influence of the radius a

Simulations to obtain effective material parameters show similarities with deriving material parameters from measurements. We will illustrate one of these similarities here: the influence of resonances of the set-up. Let us consider a spherical arrange-

ment with radius $a = 0.2$m of $N = 2409$ dielectric spherical particles with radius 0.01m and relative permittivity 20. Figure 2 shows the effective relative permittivity and permeability as a function of frequency obtained for $l = 1$ (left) and $l = 2$ (right). We note several resonances in the curve which correspond to zeroes of $j_l\,(ka)$ (solid vertical lines) and $\mathcal{J}_l\,(ka)$ (dashed vertical lines). By considering different l-values or spherical arrangements of different radii the effect of these resonances can be eliminated.

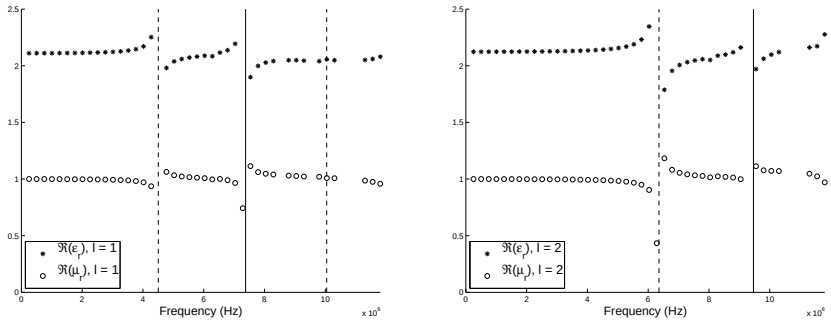

(a) (b)

Figure 7.2: Effective relative permittivity and permeability as a function of frequency for $l = 1$ (left) and $l = 2$ (right).

7.4.3 Limitations

The FMM algorithm is based on an iterative solution of the linear system of equations that results from the T-matrix method. It provides a fast matrix-vector multiplication in each iteration. However, an FMM will only be successful if the number of iterations remains much smaller than the number of unknowns NM. The number of iterations needed in iterative solvers is related to the condition number of the linear system of equations [21].

Let us consider a small spherical ensemble with $N = 125$ spherical particles with $M = 30$, i.e. $NM = 3750$ unknowns. The spherical ensemble has a radius $a = 0.082$m and the particles have a radius of 0.0112m. We chose a frequency of $f = 900$MHz. Figure 3 shows the number of iterations N_{it} needed to obtain a relative accuracy of 10^{-7} in the BICGSTAB iterative solution method [21] as a function of the parameter t. The parameter t determines the material parameters of the spherical inclusions. The number of iterations was limited to 4000.

We note that when the relative permittivity and/or the permeability of the inclusions drops below a value of -0.75 the number of iterations increases fast. This limits the use of the method as discussed in this paper for negative index materials or plasmonic materials. Things are somewhat better than illustrated here because we did not

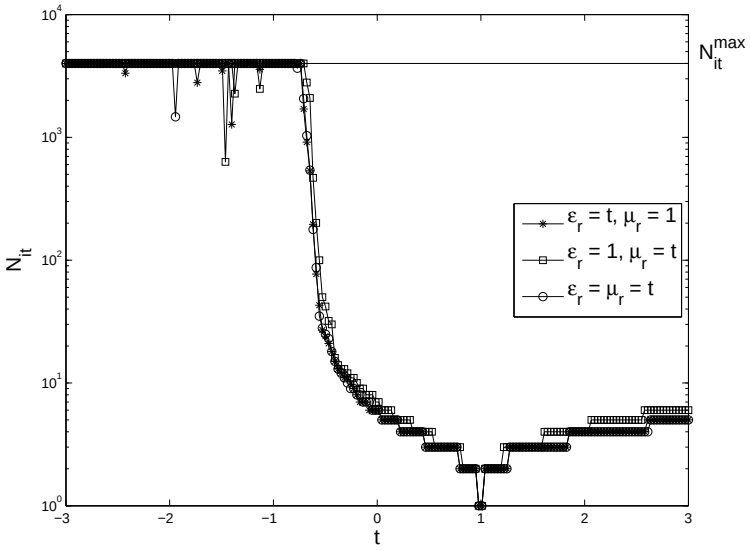

Figure 7.3: Number of iterations as a function of material parameters of the inclusions.

include losses. Losses will reduce the condition number and the number of iterations. An example of a negative index medium with losses simulated with our method was presented in [12] and verified with Maxwell-Garnett mixing rules.

To get an idea of the origin of these condition number problems let us consider the Mie scattering at a homogeneous negative index sphere with a radius $a = 8$m, a relative permittivity $\varepsilon_r = -1.5$ and a relative permeability $\mu_r = -1$ at a frequency $f = 47.7$MHz. Figure 4 shows the amplitude and phase of the electric field component along the direction corresponding to the linear polarization of the incident plane wave in the cross-section of the sphere. We note very high field intensities at the surface of the sphere that decay quickly even for moderate $|\varepsilon_r|$ and $|\mu_r|$. If we consider a spherical arrangement of particles to achieve this behavior this means that intricate interactions between the particles are necessary. Note also the reversal of the phase inside the sphere as expected for a negative index material.

In principle, the condition problem can be resolved by using an adequate preconditioner. For periodic arrangements of scatterers, such as in the realm of electromagnetic crystals, successful preconditioners have been devised [22]. Due to the random arrangement of particles these cannot be applied here. In [8] a symmetric Gauss-Seidel preconditioner is used for particles with positive permittivity and permeability. This preconditioning problem is focus of further challenging research.

There are also other limitations on the applicability of this method. One such limitation has to do with the fundamental limitations of homogenization. Suppose having a periodic arrangement of particles that form an electromagnetic crystal then it is not

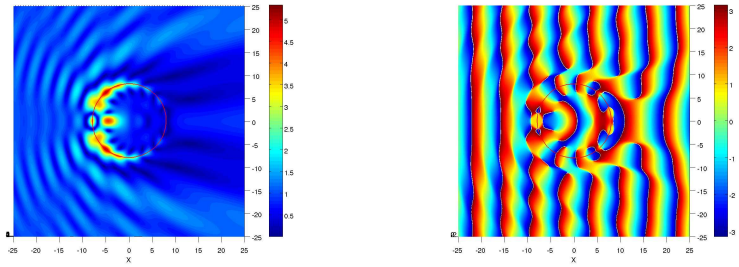

(a) (b)

Figure 7.4: Plane wave incident on a homogeneous negative index sphere. The left figure shows the amplitude and the right figure the phase of the component of the electric field along the polarization of the incident plane wave.

obvious what homogenization means. It is to be expected that when the particles are moved randomly from the periodic lattice homogenization will not suddenly become meaningful. It is our belief that one has to resort to particles that are small compared to the wavelength.

7.5 Numerical results

7.5.1 A non-chiral particle

Consider a spherical ensemble of loop-wire PEC particles. Figure 5 (left) shows the current density on the particle, as well as the triangular mesh for the MoM simulation. The diameter of the inclusions is 2.202mm and the diameter of the wires is 0.2mm. The number of unknowns per inclusion in the MoM was $n = 4316$. We consider spherical ensembles with N equal to 126, 248, 501, 1016 and 1981 particles with a particle density of 0.0345mm^{-3} and a frequency of 5.98GHz. Homogenization yields the following material parameters (average over the 5 different ensembles)

$$\begin{bmatrix} \frac{\zeta}{\sqrt{\varepsilon_0\mu_0}} & \frac{\mu}{\mu_0} \\ \frac{\varepsilon}{\varepsilon_0} & \frac{\xi}{\sqrt{\varepsilon_0\mu_0}} \end{bmatrix} = \begin{bmatrix} 0.00000003 + 0.000005j & 0.9428 - 0.00001j \\ 1.26427 - 0.00005j & -0.00000008 - 0.000005j \end{bmatrix}. \tag{7.29}$$

Note that, as expected, no chirality is found and that the losses are extremely small. Tables 1 and 2 show the material parameters for the 5 ensembles as a function of the parameter l used in the homogenization procedure of Section 2.3. We only see very small variations in the material parameters as a function of l and N.

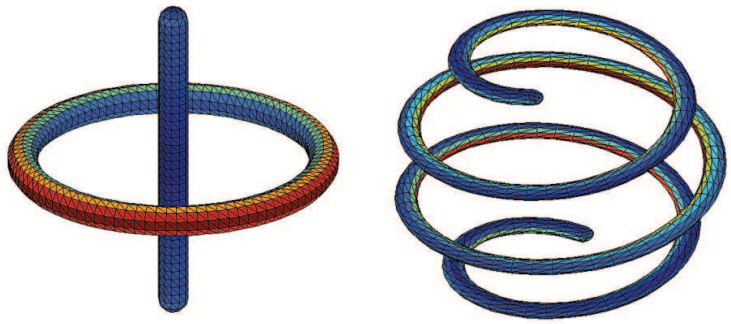

(a) (b)

Figure 7.5: Current density on a wire-loop particle (left) and a chiral particle (right).

$l\backslash N$	126	248	501	1016	1981
1	1.2686	1.2627	1.2686	1.2509	1.2610
2	1.2631	1.2621	1.2642	1.2697	1.2656
3	1.2599	1.2639	1.2632	1.2728	1.2624
4	1.2593	1.2665	1.2633	1.2763	1.2616

Table 1: Effective relative permittivity as a function of l and N for the wire-loop particle of Fig. 5 (left).

$l\backslash N$	126	248	501	1016	1981
1	0.94117	0.94271	0.94079	0.95330	0.94356
2	0.94263	0.94275	0.94199	0.94129	0.94018
3	0.94399	0.94267	0.94228	0.94091	0.94235
4	0.94474	0.94262	0.94246	0.94066	0.94302

Table 2: Effective relative permeability as a function of l and N for the wire-loop particle of Fig. 5 (left).

7.5.2 A chiral particle

As a last example we consider an ensemble of spiral PEC particles. Figure 5 (right) shows the current density on the particle, as well as the triangular mesh for the MoM simulation. The diameter of the inclusions is 2.202mm and the wire has an elliptical cross-section with major diameter 0.14mm and minor diameter 0.07mm. The number of unknowns per inclusion in the MoM was $n = 4584$. We consider spherical ensembles with N equal to 126, 248, 501, 1016 and 1981 particles with a particle density of 0.0345mm^{-3} and a frequency of 5.98GHz. Homogenization yields the following material parameters (average over the 5 different ensembles)

$$\begin{bmatrix} \frac{\zeta}{\sqrt{\varepsilon_0\mu_0}} & \frac{\mu}{\mu_0} \\ \frac{\varepsilon}{\varepsilon_0} & \frac{\xi}{\sqrt{\varepsilon_0\mu_0}} \end{bmatrix} = \begin{bmatrix} 0.0007 + 0.2033j & 1.1072 - 0.0004j \\ 1.6347 - 0.0014j & -0.0007 - 0.2032j \end{bmatrix}. \tag{7.30}$$

We find lossless reciprocal bi-isotropic, i.e. chiral, material parameters as expected.

Now consider a rectangular block of this metamaterial of size $2\lambda \times 2\lambda \times \lambda$ with an inclusion density of 0.023mm^{-3} at a frequency of 5.98GHz. This means that there are $N = 11580$ inclusions. We take $M = 30$ vector multipoles per particle leading to $NM = 347400$ unknowns in the T-matrix method. Using a brute-force MoM analysis, as e.g. in [3], of this sample would result in a problem of $Nn = 53082720$ unknowns. Although currently no such large MoM problems have been solved it is likely to happen in the foreseeable future [23] and [24].

We excite the block of metamaterial in two ways. Once using a dipole in the symmetry plane of the block (Fig. 6, left) (symmetric configuration) and once using a dipole in the top plane of the block (Fig. 6, right) (asymmetric configuration). Figure 7 shows the amplitude of the magnetic field in the xy-plane of the block for both situations. Note the symmetry of the field for the symmetric configuration and the asymmetry for the asymmetric configuration.

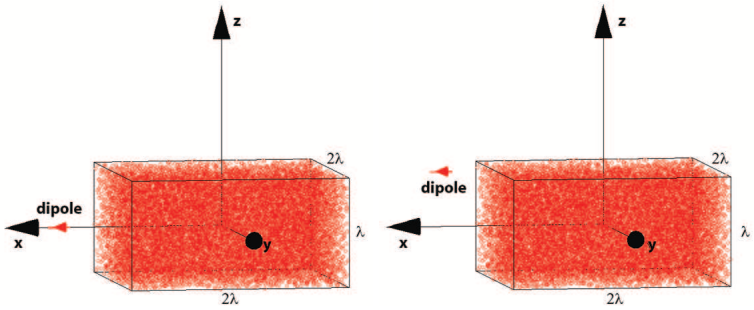

(a) (b)

Figure 7.6: Rectangular block of chiral metamaterial excited by a dipole in a symmetry plane (left) an outside a symmetry plane (right).

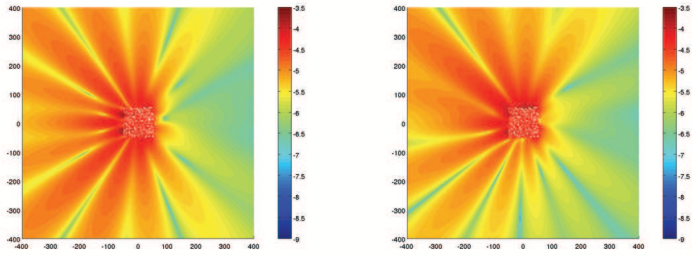

(a) (b)

Figure 7.7: Amplitude of the x-component of the magnetic field in the xy-plane corresponding to the configurations of Fig. 6.

Now we proceed as follows. First we again determine the effective material parameters for a spherical ensemble of these particles and this density. Then we use the bi-isotropic version of the Maxwell-Garnett mixing rule [20] to determine the material parameters of equivalent homogeneous chiral spherical particles of the same size and density that yield the same effective material parameters. Finally we use these spherical chiral particles in the asymmetric configuration of Fig. 6 of the rectangular block. The amplitude of the magnetic field in the symmetry plane is shown on the left of Fig. 8. Note the similarity with the left figure of Fig. 7. Finally we put the chirality to zero in our spherical particle and perform again the same simulation. The result on the right of Fig. 8 now is symmetric proving that the asymmetry in the right figure of Fig. 7 and the left figure of Fig. 8 indeed is due to chirality.

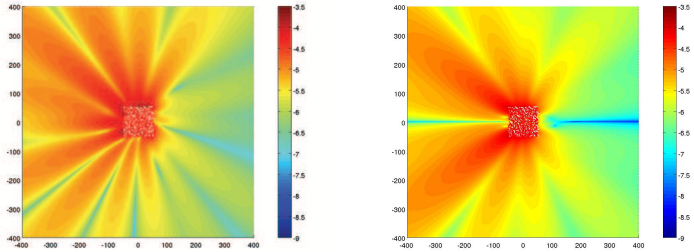

(a) (b)

Figure 7.8: Amplitude of the x-component of the magnetic field in the xy-plane for the configuration on the right of Fig. 6 when considering equivalent spherical chiral particles and non-chiral particles.

7.6 Conclusions

It was shown that recent advances in computational electromagnetics allow full-wave simulations of finite pieces of metamaterials comprising tens of thousands of inclusions. In particular the use of the NSPWMLFMA MOM combined with the SPWMLFMA T-matrix method was shown to be capable of deriving effective material parameters of metamaterials. We also derived a closed form formula to find the effective material parameters from the full-wave simulations without requiring fitting algorithms and Monte Carlo simulations. Finally some limitations of the method have been highlighted, some of which, hopefully, will be alleviated during further research.

Bibliography

[1] K. Whites, "Surmounting numerical limitations in the full-wave simulation of chiral materials," *Proceedings 1993 URSI Radio Science Meeting*, Ann Arbor, Michigan, p. 243, 1993.

[2] K. Whites, "Host effects on the constitutive parameters for synthetic chiral media," *Proceedings of the Chiral '94 Symposium*, Périgueux, France, pp. 77–82, 1994.

[3] K. Whites, "Full-wave computation of constitutive parameters for lossless composite chiral materials," *IEEE Transactions on Antennas and Propagation*, Vol. 43, pp. 376–384, 1995.

[4] P.R. Siqueira and K. Sarabandi, "T-matrix determination of the effective permittivity for three-dimensional dense random media," *IEEE Transactions on Antennas and Propagation*, Vol. 48, pp. 317–327, 2000.

[5] M.I. Mishchenko, J.W. Hovenier, and L.D. Travis, *Light Scattering by Nonspherical Particles: Theory, Measurements, and Applications*, Academic Press, San Diego, 2000.

[6] S. Van Damme and A. Franchois, "A full-wave homogenization technique for steel fiber reinforced concrete," *Electromagnetics*, Vol. 26, pp. 301–314, 2006.

[7] W.C. Chew, J.M. Jin, E. Michielssen, and J. Song, *Fast and Efficient Algorithms in Computational Electromagnetics*, Artech House, Boston, 2001.

[8] C. Meiners and A.F. Jacob, "Scattering from thin layers of composite materials: a numerical approach," *Electromagnetics*, Vol. 26, pp. 235–246, 2006.

[9] E. Darve and P. Havé, "A fast multipole method for Maxwell equations stable at all frequencies," *Phil. Trans. R. Soc. Lond. A*, Vol. 362, pp. 603–628, 2004.

[10] I. Bogaert, D. Pissoort, and F. Olyslager, "A fast aggregation for 3-D fast evanescent wave solvers using rotations," *Journal of Computational Physics*, Vol. 227, pp. 557–573, 2007.

[11] I. Bogaert, J. Peeters, and F. Olyslager, "A nondirective plane wave MLFMA stable at low frequencies," Submitted to *IEEE Transactions on Antennas and Propagation*.

[12] I. Bogaert and F. Olyslager, "Exact modelling of a finite sample of metamaterial," Proceedings of the *ACES 2007 Symposium*, Verona, Italy, 2007.

[13] I. Bogaert and F. Olyslager, "Exact full-wave simulation of finite pieces of metamaterials and extraction of effective material parameters," *Proceedings Metamaterials 2007*, Roma, Italy, pp. 609–612, 2007.

[14] I.V. Lindell, *Methods for Electromagnetic Field Analysis*, 2nd ed., Oxford: University Press, 1995.

[15] A. Lakhtakia, V.K. Varadan, and V.V. Varadan, *Time-Harmonic Electromagnetic Fields in Chiral Media*, Springer Verlag, New York, 1989.

[16] F. Olyslager, J. Fostier, J. Peeters, and D. De Zutter, "Fast and accurate evaluation of enclosures with the method of moments by using splay trees," in *Proc. 18th International Zurich Symposium on Electromagnetic Compatibility*, Munich, Germany, pp. 87–90, 2006.

[17] J. Peeters, I. Bogaert, J. Fostier, and F. Olyslager, "Accurate wideband evaluation of the shielding effectiveness of complex enclosures using an asynchronous parallel NSPWMLFMA," Submitted to the *19th International Zurich Symposium on Electromagnetic Compatibility*, Singapore, May 2008.

[18] D.D. Sleator and R.E. Tarjan, "Self-adjusting binary search trees," *Journal of the ACM*, Vol. 32, pp. 652–686, July 1985.

[19] J. Fostier, J. Peeters, and F. Olyslager, "Open FMM", [Online]. Available: http://openfmm.intec.ugent.be.

[20] I.V. Lindell, I.V. Sihvola, A.H. Tretyakov, and A.J. Viitanen, *Electromagnetic Waves in Chiral and Bi-isotropic Media*, Artech House, Boston, 1994.

[21] G.H. Golub and C.F. Van Loan, *Matrix Computations*, 3rd ed., The Johns Hopkins University Press, Baltimore, 1996.

[22] D. Pissoort, E. Michielssen, D. Vande Ginste, and F. Olyslager, "A rank-revealing preconditioner for the fast integral-equation-based characterization of electromagnetic crystal devices," *Microwave and Optical Technology Letters* Vol. 48, no. 4, pp. 783–798, 2006.

[23] J. Fostier and F. Olyslager, "An asynchronous parallel MLFMA for scattering at multiple dielectric objects," Accepted for *IEEE Transactions on Antennas and Propagation*, 2008.

[24] L. Gürel and Ö. Ergül, "Fast and accurate solutions of extremely large integral-equation problems discretised with tens of millions of unknowns," *Electronics Letters*, Vol. 43, pp. 499–500, 2007.

Conclusion and future research

In this work, a number of novel techniques have been developed that can be used to efficiently simulate LF and broadband FMMs. For example, the techniques introduced in Chapter 3 yield an acceleration of at most a factor 6 for the (dis)aggregation stage in FMMs based on the spectral decomposition of the Green function. This was shown using theoretical as well as experimental grounds. The Beltrami decomposition technique is very interesting in this respect because it is not limited to FMMs that use the spectral decomposition. Indeed, it can be applied to any vectorial FMM, thereby yielding an acceleration of a factor 2 in the (dis)aggregation stage.

In Chapter 4 a stabilized two dimensional addition theorem was introduced. This addition theorem is found by diagonalizing the multipole addition theorem, but only after a normalization factor has been introduced. This approach yields a decomposition of the Green function that remains numerically stable for all frequencies. Also it has the additional advantage that the region of converge is the complement of a circular disk which, compared to FMMs using the spectral decomposition, results in a much simpler tree. A fully broadband FMM can be constructed using this new addition theorem. Furthermore, it was shown that this decomposition is more optimal for use in an FMM than the multipole expansion. A disadvantage is the fact that the method requires two radiation patterns. Future research will mainly focus on the reduction of this number to one.

A three dimensional generalization, the NSPWMLFMA, of the technique proposed in Chapter 4 was introduced in Chapter 5. As in the two dimensional case, the resulting addition theorem is LF stable and converges in a region that is the complement of a sphere. A disadvantage is the fact that it requires a QR to determine the discretization points, which has the immediate consequence of dense interpolation matrices. Because of this, the NSPWMLFMA is not broadband in its own right. However, it is possible to construct a broadband FMM by coupling the NSPWMLFMA with the MLFMA. This hybrid has been implemented in the parallel framework OpenFMM [1] and the Method of Moments solver Cassandra. An example of the capabilities of this solver is shown in Figure 7.9. This simulation was performed using the combined field integral equation, by means of 341541 RWG basis functions. The number of required iterations was 151 to converge to $\epsilon = 10^{-3}$. The simulation was run on 16 processors, and each iteration took 20s to complete. The Thunderbird 2 is 14.15m long and

the wavelength of the impinging plane wave is 6.28m. Clearly this is a broadband problem. The upper level of the FMM was done using the MLFMA, while the levels below that are handled by the NSPWMLFMA. Future research will focus on finding a way to do the interpolations of the NSPWMLFMA in a fast way. This would allow the method to be used for all frequencies, not just LF. Another interesting topic is the study of the distribution of the discretization points that are selected by the QR. It might for example be possible to find a criterium that these points have to satisfy in order to get a numerically stable decomposition. Another interesting question is whether the NSPWMLFMA can be made even more accurate or not, i.e. are there fundamental limits to its accuracy ?

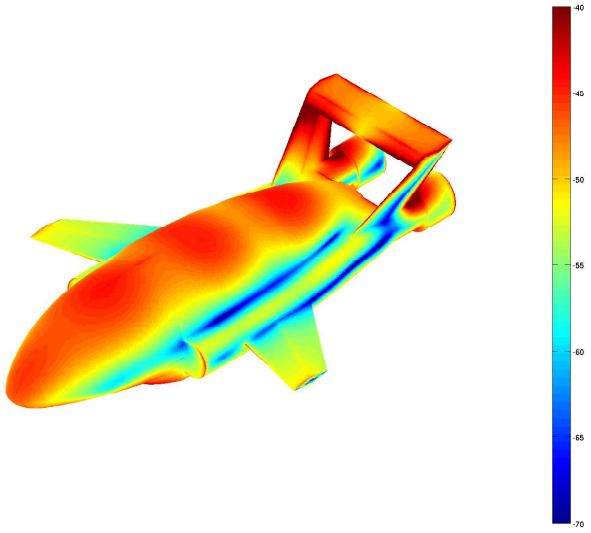

Figure 7.9: The magnitude (dB) of the electric currents on a PEC Thunderbird 2, illuminated by a frontally impinging plane wave.

Compared to the NSPWMLFMA, the fully analytical LF stable FMM introduced in Chapter 6 has the advantage that the interpolations can be done using FFTs, but the disadvantage that it generally uses four times more discretization points. For the rest it offers similar capabilities as the NSPWMLFMA. Indeed, although the fast interpolations would in principle allow a fully broadband algorithm, this is prevented by an HF numerical instability in the addition theorem. Therefore a coupling with the MLFMA is required, as for the NSPWMLFMA. Future research on this analytical FMM will largely coincide with the research on the NSPWMLFMA. Indeed, these two lines of research both search for the holy grail of FMM research: an analytically

known plane wave decomposition of the Green function that is stable for all frequencies, can achieve very high accuracies and yields an FMM that is as efficient as the MLFMA would be without numerical roundoff errors. Such an algorithm would, apart from being very efficient and much more elegant than a hybrid method, allow an easy implementation since no ad hoc criteria are needed that determine when to switch between algorithms. Such a fully broadband algorithm would also be invaluable for the construction of a broadband time domain algorithm. Indeed, if the algorithm depends on the frequency in a smooth way, the inverse Fourier transform can be taken efficiently.

In Chapter 7, the methods developed in Chapters 5 and 6 have been used to determine the T-matrix of an entire spherical sample of metamaterial. This T-matrix was then compared to the analytical expression of the T-matrix of a homogeneous bi-isotropic sphere. The resulting equations have been shown to reduce to a simple quadratic equation in the effective material parameters, which is easily solved. The effectiveness of the approach has been demonstrated by means of numerical tests on a number of metamaterials. Some limitations of the technique were also encountered. For example, when the particles that constitute the metamaterial are highly resonant or comprised of a material with a negative ε or μ, the iterative solver converges very slowly. Therefore, future research will consist of a search for effective preconditioners for this kind of problems.

Bibliography

[1] J. Fostier, J. Peeters, and F. Olyslager. Open FMM.

APPENDICES

APPENDIX A

Scalar and vector spherical harmonics and wave operators

A.1 Scalar spherical harmonics

Here the spherical harmonics will be introduced. The spherical harmonics are functions on the unit sphere, therefore they are usually defined with the spherical coordinates θ and ϕ as arguments. However, here it is convenient to use an equivalent definition, which simplifies the notation when rotations are considered. It uses a unit vector $\hat{\boldsymbol{r}} = \frac{\boldsymbol{r}}{r}$ as argument, whose components $\hat{x} = \frac{x}{r}$, $\hat{y} = \frac{y}{r}$ and $\hat{z} = \frac{z}{r}$ obviously satisfy $\hat{x}^2 + \hat{y}^2 + \hat{z}^2 = 1$. Then the definition is

$$Y_{l,m}\left(\hat{\boldsymbol{r}}\right) = (-1)^m \frac{K_{l,m}}{2^l l!} \left(\hat{x} + j\hat{y}\right)^m \mathcal{P}_l^m\left(\hat{z}\right), \quad \forall l \in [0, \infty], \; \forall m \in [-l, l]. \tag{A.1}$$

For integer l and m so that $l \in [0, \infty]$ and $m \in [-l, l]$. The function $\mathcal{P}_l^m\left(\cdot\right)$ is defined as

$$\mathcal{P}_l^m\left(t\right) = \left(\frac{\mathrm{d}}{\mathrm{d}t}\right)^{l+m} \left[t^2 - 1\right]^l, \tag{A.2}$$

and

$$K_{l,m} = \sqrt{\frac{2l+1}{4\pi} \frac{(l-m)!}{(l+m)!}}. \tag{A.3}$$

The index l is called the degree and m is called the order of the spherical harmonic. Sometimes it is convenient to use the usual (θ, ϕ) form of the spherical harmonics. In

that case the notation should be interpreted as follows

$$Y_{l,m}(\theta,\phi) = Y_{l,m}(\hat{\boldsymbol{r}}(\theta,\phi)), \tag{A.4}$$

with

$$\hat{\boldsymbol{r}}(\theta,\phi) = \cos\phi\sin\theta\hat{\boldsymbol{e}}_x + \sin\phi\sin\theta\hat{\boldsymbol{e}}_y + \cos\theta\hat{\boldsymbol{e}}_z. \tag{A.5}$$

A.1.1 Properties

Using definitions (A.1) and (A.4), the following properties of the spherical harmonics are easily proven

$$Y_{l,m}(-\hat{\boldsymbol{r}}) = (-1)^l Y_{l,m}(\hat{\boldsymbol{r}}), \tag{A.6}$$

$$Y_{l,m}(2\pi-\theta,\phi+\pi) = Y_{l,m}(\theta,\phi). \tag{A.7}$$

For real arguments the following holds

$$(-1)^m Y_{l,-m}(\hat{\boldsymbol{r}}) = Y^*_{l,m}(\hat{\boldsymbol{r}}). \tag{A.8}$$

For complex arguments this has to be generalized to

$$(-1)^m Y_{l,-m}(\hat{\boldsymbol{r}}) = Y^*_{l,m}(\hat{\boldsymbol{r}}^*), \tag{A.9}$$

such that the complex conjugation of the entire function offsets the conjugation of the argument. The so-called spherical harmonic addition theorem is given by

$$P_l(\hat{\boldsymbol{r}}_1\cdot\hat{\boldsymbol{r}}_2) = \frac{4\pi}{2l+1}\sum_{m=-l}^{l}(-1)^m Y_{l,-m}(\hat{\boldsymbol{r}}_1)\,Y_{l,m}(\hat{\boldsymbol{r}}_2), \tag{A.10}$$

with the Legendre polynomials defined as

$$P_l(t) = \frac{1}{2^l l!}\left(\frac{\mathrm{d}}{\mathrm{d}t}\right)^l\left[t^2-1\right]^l. \tag{A.11}$$

Another useful property is

$$Y_{l,m}(\hat{\boldsymbol{e}}_z) = \sqrt{\frac{2l+1}{4\pi}}\delta_{m,0}. \tag{A.12}$$

Furthermore the spherical harmonics are closely connected to the angular momentum operator $\check{\boldsymbol{L}}$

$$\check{\boldsymbol{L}} = -j\boldsymbol{r}\times\check{\boldsymbol{\nabla}} = j\left[\hat{\boldsymbol{e}}_\theta\frac{1}{\sin\theta}\partial_\phi - \hat{\boldsymbol{e}}_\phi\partial_\theta\right]. \tag{A.13}$$

Indeed, the spherical harmonics are eigenfunctions of the operators $\check{\boldsymbol{L}}^2$ and $\check{L}_z = \hat{\boldsymbol{e}}_z \cdot \check{\boldsymbol{L}}$

$$\check{\boldsymbol{L}}^2 Y_{l,m}(\hat{\boldsymbol{r}}) = l(l+1) Y_{l,m}(\hat{\boldsymbol{r}}), \tag{A.14}$$

$$\check{L}_z Y_{l,m}(\hat{\boldsymbol{r}}) = m Y_{l,m}(\hat{\boldsymbol{r}}). \tag{A.15}$$

When the integration over the unit sphere is defined as

$$\int_{\mathcal{S}_2} F(\hat{\boldsymbol{r}}) \mathrm{d}\hat{\boldsymbol{r}} = \int_0^{2\pi} \int_0^{\pi} F(\hat{\boldsymbol{r}}(\theta,\phi)) \sin\theta \mathrm{d}\theta \mathrm{d}\phi, \tag{A.16}$$

with $\hat{\boldsymbol{r}}(\theta,\phi)$ given by (A.5), the operators $\check{\boldsymbol{L}}^2$ and $\check{L}_z = \hat{\boldsymbol{e}}_z \cdot \check{\boldsymbol{L}}$ are Hermitian operators with respect to the dot product defined by this integration. Therefore, the spherical harmonics are orthogonal with respect to this dot product. Due to the specific choice for $K_{l,m}$, they are also normalized, leading to the following orthonormality relation

$$\int_{\mathcal{S}_2} Y_{l_1,m_1}(\hat{\boldsymbol{r}}) Y^*_{l_2,m_2}(\hat{\boldsymbol{r}}) \, \mathrm{d}\hat{\boldsymbol{r}} = \delta_{l_1,l_2} \delta_{m_1,m_2}. \tag{A.17}$$

In addition, the spherical harmonics are also complete, i.e.

$$\sum_{l=0}^{\infty} \sum_{m=-l}^{l} Y_{l,m}(\hat{\boldsymbol{r}}') \int_{\mathcal{S}_2} F(\hat{\boldsymbol{r}}) Y^*_{l,m}(\hat{\boldsymbol{r}}) \, \mathrm{d}\hat{\boldsymbol{r}} = F(\hat{\boldsymbol{r}}'). \tag{A.18}$$

Other useful identities contain the so-called ladder operators

$$\check{L}_{\pm} = \check{L}_x \pm j\check{L}_y = (\hat{\boldsymbol{e}}_x \pm j\hat{\boldsymbol{e}}_y) \cdot \check{\boldsymbol{L}}, \tag{A.19}$$

with the following properties

$$\check{L}_{\pm} Y_{l,m}(\hat{\boldsymbol{r}}) = \lambda^{\pm}_{l,m} Y_{l,m\pm1}(\hat{\boldsymbol{r}}), \tag{A.20}$$

and

$$\lambda^{\pm}_{l,m} = \sqrt{(l \pm m + 1)(l \mp m)}. \tag{A.21}$$

Recurrence relations constitute another set of useful identities. With the special cases

$$Y_{1,-1}(\hat{\boldsymbol{r}}) = \sqrt{\frac{3}{8\pi}}(\hat{x} - j\hat{y}), \tag{A.22a}$$

$$Y_{1,0}(\hat{\boldsymbol{r}}) = \sqrt{\frac{3}{4\pi}}\hat{z}, \tag{A.22b}$$

$$Y_{1,+1}(\hat{\boldsymbol{r}}) = -\sqrt{\frac{3}{8\pi}}(\hat{x} + j\hat{y}). \tag{A.22c}$$

the following holds

$$Y_{1,-1}(\hat{\boldsymbol{r}})\,Y_{l,m}(\hat{\boldsymbol{r}}) = -B_l^m Y_{l-1,m-1}(\hat{\boldsymbol{r}}) + B_{l+1}^{-m+1} Y_{l+1,m-1}(\hat{\boldsymbol{r}}), \tag{A.23a}$$

$$Y_{1,0}(\hat{\boldsymbol{r}})\,Y_{l,m}(\hat{\boldsymbol{r}}) = A_l^m Y_{l-1,m}(\hat{\boldsymbol{r}}) + A_{l+1}^m Y_{l+1,m}(\hat{\boldsymbol{r}}), \tag{A.23b}$$

$$Y_{1,+1}(\hat{\boldsymbol{r}})\,Y_{l,m}(\hat{\boldsymbol{r}}) = -B_l^{-m} Y_{l-1,m+1}(\hat{\boldsymbol{r}}) + B_{l+1}^{m+1} Y_{l+1,m+1}(\hat{\boldsymbol{r}}), \tag{A.23c}$$

with A_l^m en B_l^m given by

$$A_l^m = \sqrt{\frac{3}{4\pi}}\sqrt{\frac{(l+m)(l-m)}{(2l+1)(2l-1)}}, \tag{A.24}$$

$$B_l^m = \sqrt{\frac{3}{4\pi}}\sqrt{\frac{(l+m)(l+m-1)}{2(2l+1)(2l-1)}}. \tag{A.25}$$

These properties can be proven by induction, or they can be seen as a special case of the more general formula

$$Y_{l_1,m_1}(\hat{\boldsymbol{r}})\,Y_{l_2,m_2}(\hat{\boldsymbol{r}}) = \sum_{l_3,m_3} \mathcal{A}_{l_1,m_1;l_2,m_2;l_3,m_3} Y^*_{l_3,m_3}(\hat{\boldsymbol{r}}), \tag{A.26}$$

with

$$\begin{aligned}
&\mathcal{A}_{l_1,m_1;l_2,m_2;l_3,m_3} \\
&\quad = \int_{\mathcal{S}_2} Y_{l_1,m_1}(\hat{\boldsymbol{r}})\,Y_{l_2,m_2}(\hat{\boldsymbol{r}})\,Y_{l_3,m_3}(\hat{\boldsymbol{r}})\,\mathrm{d}\hat{\boldsymbol{r}} && \text{(A.27)} \\
&\quad = \sqrt{\frac{(2l_1+1)(2l_2+1)(2l_3+1)}{4\pi}} \begin{pmatrix} l_1 & l_2 & l_3 \\ 0 & 0 & 0 \end{pmatrix} \begin{pmatrix} l_1 & l_2 & l_3 \\ m_1 & m_2 & m_3 \end{pmatrix}. && \text{(A.28)}
\end{aligned}$$

The expressions between brackets are the $3j$-Wigner symbols. Another useful recurrence is

$$(\hat{x} - j\hat{y})\lambda_{lm}^{+} Y_{l,m+1}(\hat{\boldsymbol{r}}) + 2m\hat{z} Y_{l,m}(\hat{\boldsymbol{r}}) + \lambda_{lm}^{-}(\hat{x} + j\hat{y}) Y_{l,m-1}(\hat{\boldsymbol{r}}) = 0. \tag{A.29}$$

This relation is the manifestation of the operator equality

$$(\hat{x} - j\hat{y})\check{L}_{+} + 2\hat{z}\check{L}_z + (\hat{x} + j\hat{y})\check{L}_{-} = 2\hat{\boldsymbol{r}} \cdot \check{\boldsymbol{L}} = 0 \tag{A.30}$$

A.1.2 Efficient calculation

The recurrence relations (A.23) can be used to efficiently calculate the spherical harmonics. The required values for $Y_{1,m}(\hat{\boldsymbol{r}})$ are provided in (A.22). First substitute

$m = l$ in (A.23c) and $m = -l$ in (A.23a) to obtain

$$Y_{l+1,l+1}\left(\hat{\boldsymbol{r}}\right) = \sqrt{\frac{2l+3}{l+1}}\sqrt{\frac{4\pi}{3}}Y_{1,1}\left(\hat{\boldsymbol{r}}\right)Y_{l,l}\left(\hat{\boldsymbol{r}}\right), \tag{A.31}$$

$$Y_{l+1,-(l+1)}\left(\hat{\boldsymbol{r}}\right) = \sqrt{\frac{2l+3}{l+1}}\sqrt{\frac{4\pi}{3}}Y_{1,-1}\left(\hat{\boldsymbol{r}}\right)Y_{l,-l}\left(\hat{\boldsymbol{r}}\right). \tag{A.32}$$

With these equations the spherical harmonics with $m = \pm l$ can be calculated from the starting value $Y_{0,0}\left(\hat{\boldsymbol{r}}\right) = \frac{1}{\sqrt{4\pi}}$. Subsequently, for every m, the recurrence (A.23b) over l

$$Y_{l+1,m}\left(\hat{\boldsymbol{r}}\right) = \frac{1}{A_{l+1}^{m}}\left[Y_{1,0}\left(\hat{\boldsymbol{r}}\right)Y_{l,m}\left(\hat{\boldsymbol{r}}\right) - A_{l}^{m}Y_{l-1,m}\left(\hat{\boldsymbol{r}}\right)\right], \tag{A.33}$$

is used to calculate all necessary spherical harmonics. For the special case where $l = |m|$, this equation reduces to the simpler form

$$Y_{|m|+1,m}\left(\hat{\boldsymbol{r}}\right) = Y_{1,0}\left(\hat{\boldsymbol{r}}\right)Y_{|m|,m}\left(\hat{\boldsymbol{r}}\right)\sqrt{2\left|m\right|+3}\sqrt{\frac{4\pi}{3}}. \tag{A.34}$$

All the recurrences in this process are stable in the direction in which they are used. Moreover, the calculation of the coefficients A_l^m and B_l^m requires $\mathcal{O}\left(1\right)$ operations. Therefore the calculation of all the L^2 spherical harmonics of degree lower than L requires $\mathcal{O}\left(L^2\right)$ operations, which is clearly the best possible complexity.

A.2 Wigner rotation matrices

Now the transformation properties under rotations of the spherical harmonics will be given. We assume the rotation to be defined in terms of an orthogonal rotation matrix R, such that a unit vector $\hat{\boldsymbol{r}}$ is rotated into $\hat{\boldsymbol{r}}' = \mathsf{R}\cdot\hat{\boldsymbol{r}}$ when the rotation is applied. A general rotation can also be represented by means of a rotation axis $\hat{\boldsymbol{a}}$ and a rotation angle α. In that case the rotation matrix will acquire $\hat{\boldsymbol{a}}$ and α as arguments. Some details of this representation and a way to calculate $\mathsf{R}(\hat{\boldsymbol{a}},\alpha)$ can be found in A.2.3. The most general expansion of a rotated spherical harmonic is given by

$$Y_{l_1,m_1}\left(\mathsf{R}\cdot\hat{\boldsymbol{r}}\right) = \sum_{l_2=0}^{\infty}\sum_{m_2=-l_2}^{l_2} d_{m_1,m_2}^{l_1,l_2}(\mathsf{R})Y_{l_2,m_2}\left(\hat{\boldsymbol{r}}\right) \tag{A.35}$$

The operator $\check{\boldsymbol{L}}^2 = \check{\boldsymbol{L}}\cdot\check{\boldsymbol{L}}$ is rotationally invariant due to the scalar product (this can also be proven directly by means of (A.13)), therefore it can be easily applied to both

sides of (A.35)

$$l_1(l_1+1)Y_{l_1,m_1}\left(\mathsf{R}\cdot\hat{\boldsymbol{r}}\right)=\sum_{l_2=0}^{\infty}\sum_{m_2=-l_2}^{l_2}l_2(l_2+1)d^{l_1,l_2}_{m_1,m_2}(\mathsf{R})Y_{l_2,m_2}\left(\hat{\boldsymbol{r}}\right) \tag{A.36}$$

Expanding $Y_{l_1,m_1}\left(\mathsf{R}\cdot\hat{\boldsymbol{r}}\right)$ by means of (A.35) and integrating over the unit sphere with $Y^*_{l_3,m_3}\left(\hat{\boldsymbol{r}}\right)$ yields

$$l_1(l_1+1)d^{l_1,l_3}_{m_1,m_3}(\mathsf{R})=l_3(l_3+1)d^{l_1,l_3}_{m_1,m_3}(\mathsf{R}) \tag{A.37}$$

Or more explicitly

$$d^{l_1,l_3}_{m_1,m_3}(\mathsf{R})=0\ \ \forall l_1\neq l_3 \tag{A.38}$$

Apparently, spherical harmonics of degree l are transformed into a sum of spherical harmonics of the same degree. Therefore Eqn. (A.35) can be written as

$$Y_{l,m_1}\left(\mathsf{R}\cdot\hat{\boldsymbol{r}}\right)=\sum_{m_2=-l}^{l}D^{l}_{m_1,m_2}\left(\mathsf{R}\right)Y_{l,m_2}\left(\hat{\boldsymbol{r}}\right) \tag{A.39}$$

The matrices $D^{l}_{m_1,m_2}\left(\mathsf{R}\right)$ (labeled with l and function of R) are widely known as the Wigner rotation matrices, or simply Wigner matrices.

A.2.1 Properties

Since integration over the unit sphere is rotationally invariant

$$\int_{\mathcal{S}_2}Y_{l_1,m_1}\left(\hat{\boldsymbol{r}}\right)Y^*_{l_2,m_2}\left(\mathsf{R}\cdot\hat{\boldsymbol{r}}\right)\mathrm{d}\hat{\boldsymbol{r}}=\int_{\mathcal{S}_2}Y_{l_1,m_1}\left(\mathsf{R}^{-1}\cdot\hat{\boldsymbol{r}}\right)Y^*_{l_2,m_2}\left(\hat{\boldsymbol{r}}\right)\mathrm{d}\hat{\boldsymbol{r}}, \tag{A.40}$$

the Wigner matrices are unitary

$$D^{l*}_{m_2,m_1}\left(\mathsf{R}\right)=D^{l}_{m_1,m_2}\left(\mathsf{R}^{-1}\right). \tag{A.41}$$

Or more explicitly

$$\sum_{m=-l}^{l}D^{l*}_{m,m_1}\left(\mathsf{R}\right)D^{l}_{m,m_2}\left(\mathsf{R}\right)=\delta_{m_1,m_2}. \tag{A.42}$$

Another property is given by

$$D^{l}_{m_1,0}\left(\mathsf{R}\right)=\sum_{m_2=-l}^{l}D^{l}_{m_1,m_2}\left(\mathsf{R}\right)\delta_{m_2,0}=\sqrt{\frac{4\pi}{2l+1}}Y_{l,m_1}\left(\mathsf{R}\cdot\hat{\boldsymbol{e}}_z\right). \tag{A.43}$$

Therefore the spherical harmonics are a special case of the Wigner matrices. Another special case of the Wigner matrices occurs when a rotation around the z-axis over an angle β is used

$$D^l_{m_1,m_2}\left(\mathsf{R}(\hat{\boldsymbol{e}}_z,\beta)\right) = e^{jm_1\beta}\delta_{m_1,m_2}, \tag{A.44}$$

with

$$\mathsf{R}(\hat{\boldsymbol{e}}_z,\beta) = \begin{bmatrix}\cos\beta & -\sin\beta & 0\\ \sin\beta & \cos\beta & 0\\ 0 & 0 & 1\end{bmatrix}. \tag{A.45}$$

A.2.2 Efficient calculation of the Wigner matrices

For the efficient calculation of the Wigner matrices, the approach advocated in [1] will be adopted. The Wigner matrix for $l = 0$ is trivially 1. The Wigner matrix D^1 for $l = 1$

$$\mathsf{D}^1 = \begin{bmatrix}D^1_{-1,-1}(\mathsf{R}) & D^1_{-1,0}(\mathsf{R}) & D^1_{-1,1}(\mathsf{R})\\ D^1_{0,-1}(\mathsf{R}) & D^1_{0,0}(\mathsf{R}) & D^1_{0,1}(\mathsf{R})\\ D^1_{1,-1}(\mathsf{R}) & D^1_{1,0}(\mathsf{R}) & D^1_{1,1}(\mathsf{R})\end{bmatrix}, \tag{A.46}$$

can be easily calculated from R. Starting from Eqns. (A.22)

$$\begin{bmatrix}Y_{1,-1}(\hat{\boldsymbol{r}})\\ Y_{1,0}(\hat{\boldsymbol{r}})\\ Y_{1,1}(\hat{\boldsymbol{r}})\end{bmatrix} = \frac{1}{2}\sqrt{\frac{3}{\pi}}\begin{bmatrix}\frac{\hat{x}-j\hat{y}}{\sqrt{2}}\\ \hat{z}\\ -\frac{\hat{x}+j\hat{y}}{\sqrt{2}}\end{bmatrix} = \frac{1}{2}\sqrt{\frac{3}{\pi}}\underbrace{\begin{bmatrix}\frac{1}{\sqrt{2}} & -\frac{j}{\sqrt{2}} & 0\\ 0 & 0 & 1\\ -\frac{1}{\sqrt{2}} & -\frac{j}{\sqrt{2}} & 0\end{bmatrix}}_{\mathsf{M}}\begin{bmatrix}\hat{x}\\ \hat{y}\\ \hat{z}\end{bmatrix}, \tag{A.47}$$

it is easily seen that

$$\frac{1}{2}\sqrt{\frac{3}{\pi}}\mathsf{M}\cdot\mathsf{R}\cdot\begin{bmatrix}\hat{x}\\ \hat{y}\\ \hat{z}\end{bmatrix} = \begin{bmatrix}Y_{1,-1}(\mathsf{R}\cdot\hat{\boldsymbol{r}})\\ Y_{1,0}(\mathsf{R}\cdot\hat{\boldsymbol{r}})\\ Y_{1,1}(\mathsf{R}\cdot\hat{\boldsymbol{r}})\end{bmatrix} = \frac{1}{2}\sqrt{\frac{3}{\pi}}\mathsf{D}^1\cdot\mathsf{M}\cdot\begin{bmatrix}\hat{x}\\ \hat{y}\\ \hat{z}\end{bmatrix}. \tag{A.48}$$

Therefore the Wigner matrix is given by

$$\mathsf{D}^1 = \mathsf{M}\cdot\mathsf{R}\cdot\mathsf{M}^H, \tag{A.49}$$

since the matrix M is unitary. Recurrences will now be deduced that allow the Wigner matrices for $l > 1$ to be calculated recursively. Let Q denote the following

$$Q = \begin{bmatrix}Y_{1,-1}(\mathsf{R}\cdot\hat{\boldsymbol{r}})\\ Y_{1,0}(\mathsf{R}\cdot\hat{\boldsymbol{r}})\\ Y_{1,1}(\mathsf{R}\cdot\hat{\boldsymbol{r}})\end{bmatrix} Y_{l,m}(\mathsf{R}\cdot\hat{\boldsymbol{r}}). \tag{A.50}$$

Then the rotated version of (A.23) is

$$Q = \begin{bmatrix} -B_l^m Y_{l-1,m-1}\left(\mathsf{R}\cdot\hat{\boldsymbol{r}}\right) + B_{l+1}^{-m+1} Y_{l+1,m-1}\left(\mathsf{R}\cdot\hat{\boldsymbol{r}}\right) \\ A_l^m Y_{l-1,m}\left(\mathsf{R}\cdot\hat{\boldsymbol{r}}\right) + A_{l+1}^m Y_{l+1,m}\left(\mathsf{R}\cdot\hat{\boldsymbol{r}}\right) \\ -B_l^{-m} Y_{l-1,m+1}\left(\mathsf{R}\cdot\hat{\boldsymbol{r}}\right) + B_{l+1}^{m+1} Y_{l+1,m+1}\left(\mathsf{R}\cdot\hat{\boldsymbol{r}}\right) \end{bmatrix}. \tag{A.51}$$

Q can also be expanded as follows

$$Q = \sum_{m'=-l}^{l} D_{m,m'}^l\left(\mathsf{R}\right)\mathsf{D}^1 \cdot \begin{bmatrix} Y_{1,-1}\left(\hat{\boldsymbol{r}}\right) \\ Y_{1,0}\left(\hat{\boldsymbol{r}}\right) \\ Y_{1,1}\left(\hat{\boldsymbol{r}}\right) \end{bmatrix} Y_{l,m'}\left(\hat{\boldsymbol{r}}\right), \tag{A.52}$$

which, using Eqns. (A.23), leads to

$$Q = \sum_{m'=-l}^{l} D_{m,m'}^l\left(\mathsf{R}\right)\mathsf{D}^1 \cdot \begin{bmatrix} -B_l^{m'} Y_{l-1,m'-1}\left(\hat{\boldsymbol{r}}\right) + B_{l+1}^{-m'+1} Y_{l+1,m'-1}\left(\hat{\boldsymbol{r}}\right) \\ A_l^{m'} Y_{l-1,m'}\left(\hat{\boldsymbol{r}}\right) + A_{l+1}^{m'} Y_{l+1,m'}\left(\hat{\boldsymbol{r}}\right) \\ -B_l^{-m'} Y_{l-1,m'+1}\left(\hat{\boldsymbol{r}}\right) + B_{l+1}^{m'+1} Y_{l+1,m'+1}\left(\hat{\boldsymbol{r}}\right) \end{bmatrix}. \tag{A.53}$$

Now integrate the two expression for Q, namely (A.51) and (A.53), with $Y_{l+1,m_1}\left(\hat{\boldsymbol{r}}\right)$ over the unit sphere. This yields, after a tedious calculation

$$\mathsf{D}^1 \cdot \begin{bmatrix} B_{l+1}^{-m_1} D_{m,m_1+1}^l\left(\mathsf{R}\right) \\ A_{l+1}^{m_1} D_{m,m_1}^l\left(\mathsf{R}\right) \\ B_{l+1}^{m_1} D_{m,m_1-1}^l\left(\mathsf{R}\right) \end{bmatrix} = \begin{bmatrix} B_{l+1}^{-m+1} D_{m-1,m_1}^{l+1}\left(\mathsf{R}\right) \\ A_{l+1}^m D_{m,m_1}^{l+1}\left(\mathsf{R}\right) \\ B_{l+1}^{m+1} D_{m+1,m_1}^{l+1}\left(\mathsf{R}\right) \end{bmatrix}. \tag{A.54}$$

This equation thus yields a means of calculating the Wigner matrix for degree $l+1$ from the Wigner matrix for degree l. In practice the second component of Eqn. (A.54) is used to calculate all $D_{m,m_1}^{l+1}\left(\mathsf{R}\right)$ for all m_1 and for $m \in [-l, l]$. Then the first and third components are used to calculate all $D_{m,m_1}^{l+1}\left(\mathsf{R}\right)$ for all m_1 and for $m = -l-1$ and $m = l+1$ respectively.

A.2.3 Rotations defined by axis and angle

Sometimes, it is more convenient to represent a rotation as the couple $(\hat{\boldsymbol{a}}, \alpha)$. Here the unit vector $\hat{\boldsymbol{a}}$ denotes the axis around which the rotation is performed and α is the rotation angle. The direction of the rotation is determined by means of the right hand rule. When the rotation has to be performed on a vector $\boldsymbol{v}$, the result $\boldsymbol{v}'$ can be easily obtained by means of quaternions. Indeed, when the vector $\boldsymbol{v}$ is encoded in the quaternion c as follows

$$c = \begin{bmatrix} 0 & v_x & v_y & v_z \end{bmatrix}, \tag{A.55}$$

and the unit quaternion q contains the rotation parameters as follows,

$$q = \begin{bmatrix} \cos\frac{\alpha}{2} & \hat{\boldsymbol{a}} \cdot \hat{\boldsymbol{e}}_x \sin\frac{\alpha}{2} & \hat{\boldsymbol{a}} \cdot \hat{\boldsymbol{e}}_y \sin\frac{\alpha}{2} & \hat{\boldsymbol{a}} \cdot \hat{\boldsymbol{e}}_z \sin\frac{\alpha}{2} \end{bmatrix}, \tag{A.56}$$

then $\boldsymbol{v}'$ can be found by means of

$$c' = \begin{bmatrix} 0 & v'_x & v'_y & v'_z \end{bmatrix} = q \times c \times q^{-1}. \tag{A.57}$$

Here, $\times$ denotes quaternion multiplication and $q \times q^{-1} = \begin{bmatrix} 1 & 0 & 0 & 0 \end{bmatrix}$. When the rotation matrix $\mathsf{R}(\hat{\boldsymbol{a}}, \alpha)$ corresponding to the rotation is required, it can be obtained by using (A.57) on the three Cartesian unit vectors.

A.3 Vector spherical harmonics

The vector spherical harmonics $\boldsymbol{X}_{l,m}(\hat{\boldsymbol{r}})$ and $\boldsymbol{W}_{l,m}(\hat{\boldsymbol{r}})$ are defined as follows

$$\boldsymbol{X}_{l,m}(\hat{\boldsymbol{r}}) = \frac{\check{\boldsymbol{L}} Y_{l,m}(\hat{\boldsymbol{r}})}{\sqrt{l(l+1)}}, \tag{A.58}$$

$$\boldsymbol{W}_{l,m}(\hat{\boldsymbol{r}}) = \hat{\boldsymbol{r}} \times \boldsymbol{X}_{l,m}(\hat{\boldsymbol{r}}). \tag{A.59}$$

A.3.1 Properties

The vector spherical harmonics satisfy many properties akin to those satisfied by the spherical harmonics. Among these are the transformation properties under inversion

$$\boldsymbol{X}_{l,m}(-\hat{\boldsymbol{r}}) = (-1)^l \boldsymbol{X}_{l,m}(\hat{\boldsymbol{r}}), \tag{A.60}$$

$$\boldsymbol{W}_{l,m}(-\hat{\boldsymbol{r}}) = (-1)^{l+1} \boldsymbol{W}_{l,m}(\hat{\boldsymbol{r}}), \tag{A.61}$$

and under complex conjugation

$$\boldsymbol{X}^*_{l,m}(\hat{\boldsymbol{r}}^*) = (-1)^{m+1} \boldsymbol{X}_{l,-m}(\hat{\boldsymbol{r}}), \tag{A.62}$$

$$\boldsymbol{W}^*_{l,m}(\hat{\boldsymbol{r}}^*) = (-1)^{m+1} \boldsymbol{W}_{l,-m}(\hat{\boldsymbol{r}}). \tag{A.63}$$

The vector spherical harmonics do not have a radial component

$$\hat{\boldsymbol{r}} \cdot \boldsymbol{X}_{l,m}(\hat{\boldsymbol{r}}) = 0, \tag{A.64}$$

$$\hat{\boldsymbol{r}} \cdot \boldsymbol{W}_{l,m}(\hat{\boldsymbol{r}}) = 0, \tag{A.65}$$

which is readily proven by means of the definition (A.58) and (A.59). The following properties are also useful and easily proven with elementary vector algebra

$$\boldsymbol{W}_{l,m}\left(\hat{\boldsymbol{r}}\right)\cdot\boldsymbol{W}_{l',m'}\left(\hat{\boldsymbol{r}}\right)=\boldsymbol{X}_{l,m}\left(\hat{\boldsymbol{r}}\right)\cdot\boldsymbol{X}_{l',m'}\left(\hat{\boldsymbol{r}}\right), \tag{A.66}$$

$$\boldsymbol{W}_{l,m}\left(\hat{\boldsymbol{r}}\right)\cdot\boldsymbol{X}_{l',m'}\left(\hat{\boldsymbol{r}}\right)=-\boldsymbol{X}_{l,m}\left(\hat{\boldsymbol{r}}\right)\cdot\boldsymbol{W}_{l',m'}\left(\hat{\boldsymbol{r}}\right). \tag{A.67}$$

The following orthogonality properties hold

$$\int_{\mathcal{S}_2}\boldsymbol{X}_{l_1,m_1}\left(\hat{\boldsymbol{r}}\right)\cdot\boldsymbol{X}^*_{l_2,m_2}\left(\hat{\boldsymbol{r}}\right)\mathrm{d}\hat{\boldsymbol{r}}=\delta_{l_1,l_2}\delta_{m_1,m_2}, \tag{A.68}$$

$$\int_{\mathcal{S}_2}\boldsymbol{W}_{l_1,m_1}\left(\hat{\boldsymbol{r}}\right)\cdot\boldsymbol{W}^*_{l_2,m_2}\left(\hat{\boldsymbol{r}}\right)\mathrm{d}\hat{\boldsymbol{r}}=\delta_{l_1,l_2}\delta_{m_1,m_2}, \tag{A.69}$$

$$\int_{\mathcal{S}_2}\boldsymbol{X}_{l_1,m_1}\left(\hat{\boldsymbol{r}}\right)\cdot\boldsymbol{W}^*_{l_2,m_2}\left(\hat{\boldsymbol{r}}\right)\mathrm{d}\hat{\boldsymbol{r}}=0, \tag{A.70}$$

$$\int_{\mathcal{S}_2}\boldsymbol{W}_{l_1,m_1}\left(\hat{\boldsymbol{r}}\right)\cdot\boldsymbol{X}^*_{l_2,m_2}\left(\hat{\boldsymbol{r}}\right)\mathrm{d}\hat{\boldsymbol{r}}=0. \tag{A.71}$$

Equations (A.68) and (A.69) are easily proven using the orthonormality of the spherical harmonics and the fact that $\check{\boldsymbol{L}}$ is Hermitian. Equations (A.70) and (A.71) are proven by means of $\check{\boldsymbol{L}}\cdot\check{\boldsymbol{\nabla}}Y_{l,m}\left(\hat{\boldsymbol{r}}\right)=0$. The completeness relation is given by

$$\sum_{l,m}\int_{\mathcal{S}_2}\left[\boldsymbol{X}_{l,m}\left(\hat{\boldsymbol{r}}\right)\boldsymbol{X}^*_{l,m}\left(\hat{\boldsymbol{r}}'\right)+\boldsymbol{W}_{l,m}\left(\hat{\boldsymbol{r}}\right)\boldsymbol{W}^*_{l,m}\left(\hat{\boldsymbol{r}}'\right)\right]\cdot\boldsymbol{F}(\hat{\boldsymbol{r}}')\mathrm{d}\hat{\boldsymbol{r}}'$$
$$=\left[\mathbb{1}-\hat{\boldsymbol{r}}\hat{\boldsymbol{r}}\right]\cdot\boldsymbol{F}(\hat{\boldsymbol{r}}), \tag{A.72}$$

It can be seen that the radial component of $\boldsymbol{F}(\hat{\boldsymbol{r}})$ is lost. This is obviously caused by the fact that the vector spherical harmonics are purely tangential. To get a complete basis, a third set of vector spherical harmonics that has a radial component must be added. This set is given by $\hat{\boldsymbol{r}}Y_{l,m}\left(\hat{\boldsymbol{r}}\right)$. The additional orthonormality properties are easily shown, however, we will not further elaborate on this third set since it is not required in this work.

Under rotations, the vector spherical harmonics transform in the same manner as the spherical harmonics, i.e.

$$\mathsf{R}^{-1}\boldsymbol{X}_{l,m_1}\left(\mathsf{R}\cdot\hat{\boldsymbol{r}}\right)=\sum_{m_2=-l}^{l}D^l_{m_1,m_2}\left(\mathsf{R}\right)\boldsymbol{X}_{l,m_2}\left(\hat{\boldsymbol{r}}\right), \tag{A.73}$$

$$\mathsf{R}^{-1}\boldsymbol{W}_{l,m_1}\left(\mathsf{R}\cdot\hat{\boldsymbol{r}}\right)=\sum_{m_2=-l}^{l}D^l_{m_1,m_2}\left(\mathsf{R}\right)\boldsymbol{W}_{l,m_2}\left(\hat{\boldsymbol{r}}\right). \tag{A.74}$$

This can be proven for $\boldsymbol{X}_{l,m_1}(\mathsf{R}\cdot\hat{\boldsymbol{r}})$ as follows

$$\mathsf{R}^{-1}\boldsymbol{X}_{l,m_1}(\mathsf{R}\cdot\hat{\boldsymbol{r}}) = -j\mathsf{R}^{-1}\cdot\left[(\mathsf{R}\cdot\boldsymbol{r})\times(\mathsf{R}\cdot\check{\boldsymbol{\nabla}})\right]Y_{l,m_1}(\mathsf{R}\hat{\boldsymbol{r}})\frac{1}{\sqrt{l(l+1)}} \tag{A.75}$$

Because the cross product of two rotated vectors is the rotated cross product , this can be simplified to

$$\begin{aligned}\mathsf{R}^{-1}\boldsymbol{X}_{l,m_1}(\mathsf{R}\cdot\hat{\boldsymbol{r}}) &= \frac{\check{\boldsymbol{L}}Y_{l,m_1}(\mathsf{R}\hat{\boldsymbol{r}})}{\sqrt{l(l+1)}}\\ &= \sum_{m_2=-l}^{l} D^l_{m_1,m_2}(\mathsf{R})\boldsymbol{X}_{l,m_2}(\hat{\boldsymbol{r}})\end{aligned} \tag{A.76}$$

and likewise for $\boldsymbol{W}_{l,m_1}(\mathsf{R}\cdot\hat{\boldsymbol{r}})$

$$\begin{aligned}\mathsf{R}^{-1}\boldsymbol{W}_{l,m_1}(\mathsf{R}\cdot\hat{\boldsymbol{r}}) &= \mathsf{R}^{-1}\cdot[(\mathsf{R}\cdot\hat{\boldsymbol{r}})\times\boldsymbol{X}_{l,m_1}(\mathsf{R}\cdot\hat{\boldsymbol{r}})]\\ &= \hat{\boldsymbol{r}}\times\left[\mathsf{R}^{-1}\boldsymbol{X}_{l,m_1}(\mathsf{R}\cdot\hat{\boldsymbol{r}})\right]\\ &= \sum_{m_2=-l}^{l} D^l_{m_1,m_2}(\mathsf{R})\boldsymbol{W}_{l,m_2}(\hat{\boldsymbol{r}})\,.\end{aligned} \tag{A.77}$$

A recurrence over m for the vector spherical harmonics can be found by applying $\check{\boldsymbol{L}}$ to Eqn. (A.29), yielding

$$\begin{aligned}&2j\boldsymbol{W}_{l,m}(\hat{\boldsymbol{r}})\\ &\quad= (\hat{x}-j\hat{y})\lambda^{+}_{lm}\boldsymbol{X}_{l,m+1}(\hat{\boldsymbol{r}}) + 2m\hat{z}\boldsymbol{X}_{l,m}(\hat{\boldsymbol{r}}) + \lambda^{-}_{lm}(\hat{x}+j\hat{y})\boldsymbol{X}_{l,m-1}(\hat{\boldsymbol{r}})\,.\end{aligned} \tag{A.78}$$

Taking the cross product with $\hat{\boldsymbol{r}}$ yields a similar expression

$$\begin{aligned}&-2j\boldsymbol{X}_{l,m}(\hat{\boldsymbol{r}})\\ &\quad= (\hat{x}-j\hat{y})\lambda^{+}_{lm}\boldsymbol{W}_{l,m+1}(\hat{\boldsymbol{r}}) + 2m\hat{z}\boldsymbol{W}_{l,m}(\hat{\boldsymbol{r}}) + \lambda^{-}_{lm}(\hat{x}+j\hat{y})\boldsymbol{W}_{l,m-1}(\hat{\boldsymbol{r}})\,.\end{aligned} \tag{A.79}$$

Expressions (A.78) and (A.79) are coupled recurrences. They can be decoupled by using the linear combinations

$$\boldsymbol{V}^{\pm}_{l,m}(\hat{\boldsymbol{r}}) = \boldsymbol{X}_{l,m}(\hat{\boldsymbol{r}}) \pm j\boldsymbol{W}_{l,m}(\hat{\boldsymbol{r}})\,. \tag{A.80}$$

Equations (A.78) and (A.79) then become

$$\pm 2\boldsymbol{V}^{\pm}_{l,m}\left(\hat{\boldsymbol{r}}\right) = (\hat{x}-j\hat{y})\lambda^{+}_{lm}\boldsymbol{V}^{\pm}_{l,m+1}\left(\hat{\boldsymbol{r}}\right) + 2m\hat{z}\boldsymbol{V}^{\pm}_{l,m}\left(\hat{\boldsymbol{r}}\right) + \lambda^{-}_{lm}(\hat{x}+j\hat{y})\boldsymbol{V}^{\pm}_{l,m-1}\left(\hat{\boldsymbol{r}}\right). \tag{A.81}$$

The vector spherical harmonics also satisfy the following easily proven identities

$$\boldsymbol{X}_{l_1,m_1}\left(\hat{\boldsymbol{k}}\right)\cdot\boldsymbol{X}_{l_2,m_2}\left(\hat{\boldsymbol{k}}\right) = \frac{\check{\boldsymbol{L}}^2 - l_1(l_1+1) - l_2(l_2+1)}{2\sqrt{l_1(l_1+1)l_2(l_2+1)}}Y_{l_2,m_2}\left(\hat{\boldsymbol{k}}\right)Y_{l_1,m_1}\left(\hat{\boldsymbol{k}}\right), \tag{A.82}$$

$$\boldsymbol{X}_{l_1,m_1}\left(\hat{\boldsymbol{k}}\right)\cdot\boldsymbol{W}_{l_2,m_2}\left(\hat{\boldsymbol{k}}\right) = \frac{-jr\check{\boldsymbol{\nabla}}}{\sqrt{l_1(l_1+1)}}\cdot\left[Y_{l_1,m_1}\left(\hat{\boldsymbol{k}}\right)\boldsymbol{X}_{l_2,m_2}\left(\hat{\boldsymbol{k}}\right)\right]. \tag{A.83}$$

Equation (A.82) can be used to show that

$$\begin{aligned}\mathcal{B}_{l_1,m_1;l_2,m_2;l_3,m_3} &= \int_{\mathcal{S}_2}\left[\boldsymbol{X}_{l_1,m_1}\left(\hat{\boldsymbol{r}}\right)\cdot\boldsymbol{X}_{l_2,m_2}\left(\hat{\boldsymbol{r}}\right)\right]Y_{l_3,m_3}\left(\hat{\boldsymbol{r}}\right)\mathrm{d}\hat{\boldsymbol{r}}\\ &= \frac{l_3(l_3+1)-l_1(l_1+1)-l_2(l_2+1)}{2\sqrt{l_1(l_1+1)l_2(l_2+1)}}\mathcal{A}_{l_1,m_1;l_2,m_2;l_3,m_3}\end{aligned} \tag{A.84}$$

A.3.2 Efficient calculation

The $\boldsymbol{X}_{l,m}\left(\hat{\boldsymbol{r}}\right)$ can be expressed in term of the spherical harmonics by means of the ladder operators (A.19)

$$\boldsymbol{X}_{l,m}\left(\hat{\boldsymbol{r}}\right) = \frac{1}{\sqrt{l(l+1)}}\left[\frac{1}{2}(\hat{\boldsymbol{e}}_x - j\hat{\boldsymbol{e}}_y)\check{L}_+ + \frac{1}{2}(\hat{\boldsymbol{e}}_x + j\hat{\boldsymbol{e}}_y)\check{L}_- + \hat{\boldsymbol{e}}_z\check{L}_z\right]Y_{l,m}\left(\hat{\boldsymbol{r}}\right), \tag{A.85}$$

which, by means of (A.20), evaluates to

$$\boldsymbol{X}_{l,m}\left(\hat{\boldsymbol{r}}\right) = \frac{1}{\sqrt{l(l+1)}}\mathsf{M}^H\cdot\begin{bmatrix}\frac{\lambda^{-}_{lm}}{\sqrt{2}}Y_{l,m-1}\left(\hat{\boldsymbol{r}}\right)\\ mY_{l,m}\left(\hat{\boldsymbol{r}}\right)\\ -\frac{\lambda^{+}_{lm}}{\sqrt{2}}Y_{l,m+1}\left(\hat{\boldsymbol{r}}\right)\end{bmatrix}, \tag{A.86}$$

with M defined in (A.47). This expression immediately allows the efficient calculation of $\boldsymbol{X}_{l,m}\left(\hat{\boldsymbol{r}}\right)$ from the spherical harmonics. The spherical harmonics themselves can in turn be calculated efficiently by means of the algorithm described in A.1.2. With $\boldsymbol{X}_{l,m}\left(\hat{\boldsymbol{r}}\right)$ known, $\boldsymbol{W}_{l,m}\left(\hat{\boldsymbol{r}}\right)$ is rapidly obtained by means of Eqn. (A.59). An alternative expression is obtained when the cross product with $\hat{\boldsymbol{r}}$ is explicitly calculated, after

which the factors x, y and z are absorbed into the spherical harmonics using (A.23). This is a tedious calculation and we give only the result

$$\begin{aligned}&\boldsymbol{W}_{l,m}(\hat{\boldsymbol{r}})\\&= \sqrt{\frac{4\pi}{3}}\frac{(-j)}{\sqrt{l(l+1)}}\mathsf{M}^H \cdot \begin{bmatrix}(l+1)B_l^m Y_{l-1,m-1}(\hat{\boldsymbol{r}}) + lB_{l+1}^{-m+1}Y_{l+1,m-1}(\hat{\boldsymbol{r}})\\ -(l+1)A_l^m Y_{l-1,m}(\hat{\boldsymbol{r}}) + lA_{l+1}^m Y_{l+1,m}(\hat{\boldsymbol{r}})\\ (l+1)B_l^{-m}Y_{l-1,m+1}(\hat{\boldsymbol{r}}) + lB_{l+1}^{m+1}Y_{l+1,m+1}(\hat{\boldsymbol{r}})\end{bmatrix},\end{aligned} \tag{A.87}$$

with A_l^m and B_l^m defined in (A.24) abd (A.25).

A.4 Scalar and vector spherical wave operators

The scalar spherical wave operators, introduced in [2], are defined by substituting $\hat{\boldsymbol{r}}$ with $\frac{\check{\boldsymbol{\nabla}}}{-jk}$ in the definition of the spherical harmonics

$$Y_{l,m}\left(\frac{\check{\boldsymbol{\nabla}}}{-jk}\right) = \left(\frac{-j}{k}\right)^m \frac{K_{l,m}}{2^l l!}\left(\frac{\partial}{\partial x} + j\frac{\partial}{\partial y}\right)^m \mathcal{P}_l^m\left(\frac{1}{-jk}\frac{\partial}{\partial z}\right), \tag{A.88}$$

with $\mathcal{P}_l^m(\cdot)$ defined in (A.2). For example, the following explicit formula for $l = 1$ can be found

$$\begin{bmatrix}Y_{1,-1}\left(\frac{\check{\boldsymbol{\nabla}}}{-jk}\right)\\ Y_{1,0}\left(\frac{\check{\boldsymbol{\nabla}}}{-jk}\right)\\ Y_{1,1}\left(\frac{\check{\boldsymbol{\nabla}}}{-jk}\right)\end{bmatrix} = \frac{1}{-2jk}\sqrt{\frac{3}{\pi}}\mathsf{M}\cdot\check{\boldsymbol{\nabla}}. \tag{A.89}$$

With the scalar spherical wave operators defined, the definition of the vector spherical wave operators is trivial: simply replace $\hat{\boldsymbol{r}}$ by $\frac{\check{\boldsymbol{\nabla}}}{-jk}$ in (A.86) and (A.87). When applied to a plane wave with wavevector $\boldsymbol{k}$ with $\boldsymbol{k}\cdot\boldsymbol{k} = k^2$, the scalar spherical wave operators can be immediately evaluated

$$Y_{l,m}\left(\frac{\check{\boldsymbol{\nabla}}}{-jk}\right)e^{-j\boldsymbol{k}\cdot\boldsymbol{r}} = Y_{l,m}\left(\hat{\boldsymbol{k}}\right)e^{-j\boldsymbol{k}\cdot\boldsymbol{r}}. \tag{A.90}$$

Because every field $w(\boldsymbol{r})$ satisfying the Helmholtz equation

$$\check{\boldsymbol{\nabla}}^2 w(\boldsymbol{r}) + k^2 w(\boldsymbol{r}) = 0 \tag{A.91}$$

can be written as a superposition of such plane waves, the scalar spherical wave operators satisfy the following property

$$Y_{l_1,m_1}\left(\frac{\check{\boldsymbol{\nabla}}}{-jk}\right)Y_{l_2,m_2}\left(\frac{\check{\boldsymbol{\nabla}}}{-jk}\right)w(\boldsymbol{r}) = \sum_{l_3=0}^{\infty}\sum_{m_3=-l_3}^{l_3} A_{L_1,L_2,L_3}(-1)^m Y_{l_3,-m_3}\left(\frac{\check{\boldsymbol{\nabla}}}{-jk}\right)w(\boldsymbol{r}). \quad \text{(A.92)}$$

Equation (A.23) has a similar analogue.

Bibliography

[1] C.H. Choi, J. Ivanic, M.S. Gordon, and K. Ruedenberg. Rapid and stable determination of rotation matrices between spherical harmonics by direct recursion. *Journal of Chemical Physics*, 111(19):8825–8831, Nov 1999.

[2] R.C. Wittmann. Spherical wave operators and the translation formulas. *IEEE Transactions on Antennas and Propagation*, 36(8):1078–1087, Aug 1988.

APPENDIX B

Spherical Bessel functions

B.1 Spherical Bessel functions

A spherical Bessel function $f_l(x)$ is defined as the solution of the spherical Bessel differential equation

$$\frac{\mathrm{d}}{\mathrm{d}x}\left(x^2\frac{\mathrm{d}}{\mathrm{d}x}f_l(x)\right)+\left[x^2-l(l+1)\right]f_l(x)=0. \tag{B.1}$$

This is a second-order differential equation, hence there are two linearly independent solutions. There are an infinite number of linear combinations of these solutions, but we will mainly use the following two

$$j_l\left(x\right)=\sqrt{\frac{\pi}{2x}}J_{l+\frac{1}{2}}\left(x\right), \tag{B.2}$$

$$h_l^{(2)}\left(x\right)=\sqrt{\frac{\pi}{2x}}H^{(2)}_{l+\frac{1}{2}}\left(x\right). \tag{B.3}$$

The functions $J_\nu\left(x\right)$ and $H_\nu^{(2)}\left(x\right)$ are the cylindrical Bessel functions, defined in [1].

B.1.1 Properties

The spherical Bessel functions satisfy two recurrence relations

$$\frac{2l+1}{x}f_l(x)=f_{l-1}(x)+f_{l+1}(x), \tag{B.4a}$$

$$(2l+1)\frac{\mathrm{d}}{\mathrm{d}x}f_l(x)=lf_{l-1}(x)-(l+1)f_{l+1}(x), \tag{B.4b}$$

which can also be written as

$$\frac{\mathrm{d}}{\mathrm{d}x} f_l(x) = f_{l-1}(x) - \frac{l+1}{x} f_l(x), \tag{B.5a}$$

$$\frac{\mathrm{d}}{\mathrm{d}x} f_l(x) = \frac{l}{x} f_l(x) - f_{l+1}(x). \tag{B.5b}$$

The following cross product formula is also useful

$$j_l\left(x\right) h_{l-1}^{(2)}\left(x\right) - j_{l-1}\left(x\right) h_l^{(2)}\left(x\right) = -\frac{j}{x^2}. \tag{B.6}$$

The spherical Bessel functions naturally arise in the solution of the three dimensional scalar Helmholtz equation.

B.1.2 A special identity

Here we will prove the following Theorem

Theorem B.1.1 *For every integer $l \in [0, \infty]$ and $m \in [-l, l]$, the following holds*

$$Z_{l,m}^f\left(k\boldsymbol{r}\right) = j^l Y_{l,m}\left(\frac{\check{\boldsymbol{\nabla}}}{-jk}\right) f_0(kr), \tag{B.7}$$

with

$$Z_{l,m}^f\left(k\boldsymbol{r}\right) = f_l(kr) Y_{l,m}\left(\hat{\boldsymbol{r}}\right), \tag{B.8}$$

where $f_l(x)$ is a spherical Bessel function, i.e. a function satisfying (B.1). The differential operator $Y_{l,m}\left(\frac{\check{\boldsymbol{\nabla}}}{-jk}\right)$ is defined in A.4.

Before proving Theorem B.1.1, the following lemma will first be proven

Lemma B.1.2 *For every integer $l \in [0, \infty]$ and $m \in [-l, l]$, the following holds*

$$\begin{bmatrix} Y_{1,-1}\left(\frac{\check{\boldsymbol{\nabla}}}{-jk}\right) \\ Y_{1,0}\left(\frac{\check{\boldsymbol{\nabla}}}{-jk}\right) \\ Y_{1,1}\left(\frac{\check{\boldsymbol{\nabla}}}{-jk}\right) \end{bmatrix} Z_{l,m}^f\left(k\boldsymbol{r}\right) = -j \begin{bmatrix} B_l^m Z_{l-1,m-1}^f\left(k\boldsymbol{r}\right) + B_{l+1}^{-m+1} Z_{l+1,m-1}^f\left(k\boldsymbol{r}\right) \\ -A_l^m Z_{l-1,m}^f\left(k\boldsymbol{r}\right) + A_{l+1}^m Z_{l+1,m}^f\left(k\boldsymbol{r}\right) \\ B_l^{-m} Z_{l-1,m+1}^f\left(k\boldsymbol{r}\right) + B_{l+1}^{m+1} Z_{l+1,m+1}^f\left(k\boldsymbol{r}\right) \end{bmatrix}, \tag{B.9}$$

with A_l^m and B_l^m defined in (A.24) and (A.25).

Proof Let Q denote the left hand side of (B.9). Then the following is easily shown

$$Q = \frac{1}{-2jk}\sqrt{\frac{3}{\pi}}\mathsf{M}\cdot\check{\boldsymbol{\nabla}}Z^f_{l,m}\left(k\boldsymbol{r}\right) \tag{B.10}$$

$$= \frac{j}{k}\sqrt{\frac{3}{4\pi}}\mathsf{M}\cdot\left[f_l(kr)\check{\boldsymbol{\nabla}}Y_{l,m}\left(\hat{\boldsymbol{r}}\right) + Y_{l,m}\left(\hat{\boldsymbol{r}}\right)\check{\boldsymbol{\nabla}}f_l(kr)\right] \tag{B.11}$$

$$= \frac{j}{k}\sqrt{\frac{3}{4\pi}}\mathsf{M}\cdot\left[-f_l(kr)\hat{\boldsymbol{r}}\times\left[\hat{\boldsymbol{r}}\times\check{\boldsymbol{\nabla}}Y_{l,m}\left(\hat{\boldsymbol{r}}\right)\right] + Y_{l,m}\left(\hat{\boldsymbol{r}}\right)\hat{\boldsymbol{r}}\frac{\mathrm{d}}{\mathrm{d}r}f_l(kr)\right]. \tag{B.12}$$

Or by means of the definition of M and $\boldsymbol{W}_{l,m}\left(\hat{\boldsymbol{r}}\right)$ in (A.47) and (A.59) respectively

$$Q = \sqrt{\frac{3}{4\pi}}\frac{f_l(kr)}{kr}\mathsf{M}\cdot\boldsymbol{W}_{l,m}\left(\hat{\boldsymbol{r}}\right)\sqrt{l(l+1)} + jY_{l,m}\left(\hat{\boldsymbol{r}}\right)\begin{bmatrix}Y_{1,-1}\left(\hat{\boldsymbol{r}}\right)\\ Y_{1,0}\left(\hat{\boldsymbol{r}}\right)\\ Y_{1,1}\left(\hat{\boldsymbol{r}}\right)\end{bmatrix}\frac{\mathrm{d}}{\mathrm{d}(kr)}f_l(kr). \tag{B.13}$$

By means of (A.87), the first term becomes

$$\sqrt{\frac{3}{4\pi}}\frac{f_l(kr)}{kr}\mathsf{M}\cdot\boldsymbol{W}_{l,m}\left(\hat{\boldsymbol{r}}\right)\sqrt{l(l+1)}$$
$$= j\frac{f_l(kr)}{kr}\begin{bmatrix}-(l+1)B^m_l Y_{l-1,m-1}\left(\hat{\boldsymbol{r}}\right) - lB^{-m+1}_{l+1}Y_{l+1,m-1}\left(\hat{\boldsymbol{r}}\right)\\ (l+1)A^m_l Y_{l-1,m}\left(\hat{\boldsymbol{r}}\right) - lA^m_{l+1}Y_{l+1,m}\left(\hat{\boldsymbol{r}}\right)\\ -(l+1)B^{-m}_l Y_{l-1,m+1}\left(\hat{\boldsymbol{r}}\right) - lB^{m+1}_{l+1}Y_{l+1,m+1}\left(\hat{\boldsymbol{r}}\right)\end{bmatrix}, \tag{B.14}$$

while, by means of (A.23), the second term becomes

$$jY_{l,m}\left(\hat{\boldsymbol{r}}\right)\begin{bmatrix}Y_{1,-1}\left(\hat{\boldsymbol{r}}\right)\\ Y_{1,0}\left(\hat{\boldsymbol{r}}\right)\\ Y_{1,1}\left(\hat{\boldsymbol{r}}\right)\end{bmatrix}\frac{\mathrm{d}}{\mathrm{d}(kr)}f_l(kr)$$
$$= j\frac{\mathrm{d}}{\mathrm{d}(kr)}f_l(kr)\begin{bmatrix}-B^m_l Y_{l-1,m-1}\left(\hat{\boldsymbol{r}}\right) + B^{-m+1}_{l+1}Y_{l+1,m-1}\left(\hat{\boldsymbol{r}}\right)\\ A^m_l Y_{l-1,m}\left(\hat{\boldsymbol{r}}\right) + A^m_{l+1}Y_{l+1,m}\left(\hat{\boldsymbol{r}}\right)\\ -B^{-m}_l Y_{l-1,m+1}\left(\hat{\boldsymbol{r}}\right) + B^{m+1}_{l+1}Y_{l+1,m+1}\left(\hat{\boldsymbol{r}}\right)\end{bmatrix}. \tag{B.15}$$

The derivative of the spherical Bessel function in Eqn. (B.15) can now be expanded by means of recurrences (B.5). For the part containing spherical harmonics of degree $l-1$, recurrence (B.5a) should be used while (B.5b) should be used for the degree $l+1$ harmonics. It is easily seen that, after this substitution, the terms containing $\frac{f_l(kr)}{kr}$ are canceled by (B.14). Therefore

$$Q = -j\begin{bmatrix}B^m_l f_{l-1}(kr)Y_{l-1,m-1}\left(\hat{\boldsymbol{r}}\right) + B^{-m+1}_{l+1}f_{l+1}(kr)Y_{l+1,m-1}\left(\hat{\boldsymbol{r}}\right)\\ -A^m_l f_{l-1}(kr)Y_{l-1,m}\left(\hat{\boldsymbol{r}}\right) + A^m_{l+1}f_{l+1}(kr)Y_{l+1,m}\left(\hat{\boldsymbol{r}}\right)\\ B^{-m}_l f_{l-1}(kr)Y_{l-1,m+1}\left(\hat{\boldsymbol{r}}\right) + B^{m+1}_{l+1}f_{l+1}(kr)Y_{l+1,m+1}\left(\hat{\boldsymbol{r}}\right)\end{bmatrix}, \tag{B.16}$$

which concludes the proof of Lemma B.1.2. □

Theorem B.1.1 will now be proven

Proof Equation (B.7) is trivially true for $l = 0$. The case $l = 1$ can be proven by replacing l in Eqn. (B.13) by zero. Since $\boldsymbol{W}_{0,0}(\hat{\boldsymbol{r}})$ is identically zero and $\frac{\mathrm{d}}{\mathrm{d}x} f_0(x) = -f_1(x)$, this leads to the required result. An inductive argument will now be used to prove (B.7) for higher l. Assume that (B.7) holds $\forall l \leq L$. Then

$$\begin{bmatrix} Y_{1,-1}\left(\frac{\check{\boldsymbol{\nabla}}}{-jk}\right) \\ Y_{1,0}\left(\frac{\check{\boldsymbol{\nabla}}}{-jk}\right) \\ Y_{1,1}\left(\frac{\check{\boldsymbol{\nabla}}}{-jk}\right) \end{bmatrix} Z^f_{L,m}(k\boldsymbol{r}) = j^L \begin{bmatrix} Y_{1,-1}\left(\frac{\check{\boldsymbol{\nabla}}}{-jk}\right) \\ Y_{1,0}\left(\frac{\check{\boldsymbol{\nabla}}}{-jk}\right) \\ Y_{1,1}\left(\frac{\check{\boldsymbol{\nabla}}}{-jk}\right) \end{bmatrix} Y_{L,m}\left(\frac{\check{\boldsymbol{\nabla}}}{-jk}\right) f_0(kr) \tag{B.17}$$

Let Q denote the left hand side of Eqn. (B.17). Since $f_0(kr)$ is a solution of the Helmholtz equation, recurrences (A.23) also hold for the scalar spherical wave operators

$$Q = j^L \begin{bmatrix} -B^m_L Y_{L-1,m-1}\left(\frac{\check{\boldsymbol{\nabla}}}{-jk}\right) + B^{-m+1}_{L+1} Y_{L+1,m-1}\left(\frac{\check{\boldsymbol{\nabla}}}{-jk}\right) \\ A^m_L Y_{L-1,m}\left(\frac{\check{\boldsymbol{\nabla}}}{-jk}\right) + A^m_{L+1} Y_{L+1,m}\left(\frac{\check{\boldsymbol{\nabla}}}{-jk}\right) \\ -B^{-m}_L Y_{L-1,m+1}\left(\frac{\check{\boldsymbol{\nabla}}}{-jk}\right) + B^{m+1}_{L+1} Y_{L+1,m+1}\left(\frac{\check{\boldsymbol{\nabla}}}{-jk}\right) \end{bmatrix} f_0(kr) \tag{B.18}$$

$$= j \begin{bmatrix} -B^m_L Z^f_{L-1,m-1}(k\boldsymbol{r}) - B^{-m+1}_{L+1} j^{L+1} Y_{L+1,m-1}\left(\frac{\check{\boldsymbol{\nabla}}}{-jk}\right) f_0(kr) \\ A^m_L Z^f_{L-1,m}(k\boldsymbol{r}) - A^m_{L+1} j^{L+1} Y_{L+1,m}\left(\frac{\check{\boldsymbol{\nabla}}}{-jk}\right) f_0(kr) \\ -B^{-m}_L Z^f_{L-1,m+1}(k\boldsymbol{r}) - B^{m+1}_{L+1} j^{L+1} Y_{L+1,m+1}\left(\frac{\check{\boldsymbol{\nabla}}}{-jk}\right) f_0(kr) \end{bmatrix}. \tag{B.19}$$

According to Lemma B.1.2, Q is also given by

$$Q = j \begin{bmatrix} -B^m_L Z^f_{L-1,m-1}(k\boldsymbol{r}) - B^{-m+1}_{L+1} Z^f_{L+1,m-1}(k\boldsymbol{r}) \\ A^m_L Z^f_{L-1,m}(k\boldsymbol{r}) - A^m_{L+1} Z^f_{L+1,m}(k\boldsymbol{r}) \\ -B^{-m}_L Z^f_{L-1,m+1}(k\boldsymbol{r}) - B^{m+1}_{L+1} Z^f_{L+1,m+1}(k\boldsymbol{r}) \end{bmatrix}, \tag{B.20}$$

Comparing (B.19) and (B.20) yields

$$-B^{-m+1}_{L+1} j^{L+1} Y_{L+1,m-1}\left(\frac{\check{\boldsymbol{\nabla}}}{-jk}\right) f_0(kr) = -B^{-m+1}_{L+1} Z^f_{L+1,m-1}(k\boldsymbol{r}), \tag{B.21a}$$

$$-A^m_{L+1} j^{L+1} Y_{L+1,m}\left(\frac{\check{\boldsymbol{\nabla}}}{-jk}\right) f_0(kr) = -A^m_{L+1} Z^f_{L+1,m}(k\boldsymbol{r}), \tag{B.21b}$$

$$-B^{m+1}_{L+1} j^{L+1} Y_{L+1,m+1}\left(\frac{\check{\boldsymbol{\nabla}}}{-jk}\right) f_0(kr) = -B^{m+1}_{L+1} Z^f_{L+1,m+1}(k\boldsymbol{r}). \tag{B.21c}$$

Since $A^m_{L+1} \neq 0$ if $|m| \neq L+1$, the equality of $j^{L+1} Y_{L+1,m}\left(\frac{\check{\boldsymbol{\nabla}}}{-jk}\right) f_0(kr)$ and

$Z^f_{L+1,m}(k\boldsymbol{r})$ under the same conditions on m can be proven using (B.21b). For proving the cases $m = L + 1$ and $m = -L - 1$, Eqns. (B.21c) respectively (B.21a) can be used. As a consequence (B.7) holds $\forall l \leq L + 1$, which concludes the proof by induction. $\square$

Bibliography

[1] M. Abramowitz and I.A. Stegun. *Handbook of Mathematical Functions with Formulas, Graphs and Mathematical Tables*. Advanced Mathematics. Dover Publications, Inc., New York, 1965.

APPENDIX C

Conference papers

C.1 Exact Modeling of a Finite Sample of Metamaterial

I. Bogaert and F. Olyslager

Abstract: Metamaterials are electromagnetically complex structures. In this contribution we present a technique that allows for a detailed analysis of a finite sample of metamaterial incorporating all electromagnetic interactions. To this end we use a full-wave T-matrix formalism. To accelerate the simulations we use the Stable Plane Wave Multilevel Fast Multipole Method. We also present a direct method to derive the effective material parameters from the T-matrix of a spherical sample of metamaterial.

Keywords: metamaterials, fast multipole methods

C.1.1 Introduction

Metamaterials consist of a large number of constituents embedded in a host medium. Each constituent can have a complex structure and e.g. consist of printed ring resonators and dipoles. When considering a finite piece of metamaterial one is interested in the overall effective medium parameters of this piece. These effective parameters are usually estimated from the polarizabilities of a constituent using homogenization formulas such as Maxwell-Garnett or Bruggeman [1].

In this paper we want to use another approach. We aim at performing a full-wave numerical simulation of a finite sample of metamaterial and then derive the effective parameters from these scattering simulations by comparison with a homogeneous sample of material with the same geometry. In this way all the electromagnetic interactions are taken into account. This approach allows us to check the validity of the homogenization formulas. Such formulas fail when the density of the constituents become high and these formulas also assume a material of infinite extent. This also

means that the dependence of the geometry of the sample on the effective parameters only can be estimated using a full-wave simulation.

To solve the scattering problem we will use the T-matrix approach [2]. We will first determine the T-matrix of each constituent and then considering the interactions between all the T-matrices. If there are N constituents, and if each T-matrix contains M^2 elements then this requires the solution of a linear system of NM unknowns. Since N will be large it is not possible to use a direct or even an iterative solution of this system. The constituents are small compared to wavelength, although the sample can be several wavelengths in size. This means that the numerical problem is at the same time a low- and high-frequency problem. The solution of the linear system can be accelerated using a multilevel fast multipole technique but this technique needs to be valid for high as well as low frequencies. For this purpose we opted the use of the Stable Plane Wave Method as derived by [3]. In this way it becomes possible to obtain a computational and memory complexity of $O(NM)$. We also use an acceleration to convert multipoles into evanescent plane waves as has been derived recently in [4].

To derive the effective parameters of a metamaterial we will consider a spherical sample. From the T-matrix of the individual constituents we can derive the T-matrix of the entire sample using the Stable Plane Wave Method. Then we compare this T-matrix with the T-matrix of a homogeneous sphere to identify the effective material parameters. It turns out this can be done in a very elegant way using a recurrence relation of Bessel functions.

C.1.2 Analysis

The examples will consider a spherical sample consisting of spherical inclusions. Spherical inclusions have an analytical T-matrix. We will show the validity of the Maxwell-Garnett and Bruggeman formula and show the possibility to derive a negative index material for an example proposed in [5]. First we determine the T-matrix of the constituents of the metamaterial. This starts from the illumination of the constituent by incoming fields of the following forms

$$\boldsymbol{E}_{lm}^{inc,1}(\boldsymbol{r}) = \frac{\check{\boldsymbol{L}}\left[j_l\left(kr\right)Y_{l,m}\left(\boldsymbol{r}\right)\right]}{\sqrt{l(l+1)}} \qquad \boldsymbol{E}_{lm}^{inc,2}(\boldsymbol{r}) = \frac{1}{k}\check{\boldsymbol{\nabla}} \times \boldsymbol{E}_{lm}^{inc,1}(\boldsymbol{r}), \quad \text{(C.1)}$$

where k is the wavenumber, $Y_{lm}(\boldsymbol{r})$ are the scalar spherical harmonics and where $\hat{\boldsymbol{L}}$ is the angular momentum operator

$$\check{\boldsymbol{L}} = -j\boldsymbol{r} \times \check{\boldsymbol{\nabla}} = j\left[\boldsymbol{e}_\theta \frac{1}{\sin\theta}\frac{d}{d\theta} - \boldsymbol{e}_\phi \frac{d}{d\phi}\right]. \quad \text{(C.2)}$$

The resulting scattered fields can be decomposed into functions similar to (C.1), but with spherical Hankel functions instead of spherical Bessel functions. The coeffi-

cients arising in this decomposition can be interpreted as entries of the T-matrix of the constituent. All scattering information of the constituent is contained in the T-matrix.

In the next step the T-matrix of the entire spherical sample is determined. This is done using the Stable Plane Wave Method as developed in [3]. We will not go into the details of this multilevel fast multipole technique but suffice to say that the method remains stable at low frequencies by also incorporating evanescent plane waves in addition to propagating plane waves. In the disaggregation and aggregation steps it is necessary to transform the vectorial spherical harmonics expansion of the T-matrix into plane waves. For the evanescent plane waves this requires 6 different expansions along the $\pm x$-, $\pm y$- and the $\pm z$-axis. Recently [4] a new method was derived to reduce the workload of this process by a factor of 6.

In the final step the T-matrix of the entire sample is matched to the analytical T-matrix of an homogeneous sphere. This T-matrix is diagonal and the diagonal elements are given by

$$T^1_{l,m} = -\frac{Z_i \frac{\mathcal{J}_l(k_o a)}{j_l(k_o a)} - Z_o \frac{\mathcal{J}_l(k_i a)}{j_l(k_i a)}}{Z_i \frac{\mathcal{H}^{(2)}_l(k_o a)}{j_l(k_o a)} - Z_o \frac{\mathcal{J}_l(k_i a)}{j_l(k_i a)} \frac{h^{(2)}_l(k_o a)}{j_l(k_o a)}}, \tag{C.3}$$

$$T^2_{l,m} = -\frac{Z_o \frac{\mathcal{J}_l(k_o a)}{j_l(k_o a)} - Z_i \frac{\mathcal{J}_l(k_i a)}{j_l(k_i a)}}{Z_o \frac{\mathcal{H}^{(2)}_l(k_o a)}{j_l(k_o a)} - Z_i \frac{\mathcal{J}_l(k_i a)}{j_l(k_i a)} \frac{h^{(2)}_l(k_o a)}{j_l(k_o a)}}. \tag{C.4}$$

Here, $\mathcal{J}_l(x) = \frac{1}{x}\frac{d}{dx}\left[x j_l(x)\right]$ and $\mathcal{H}^{(2)}_l(x) = \frac{1}{x}\frac{d}{dx}\left[x h^{(2)}_l(x)\right]$. The unknowns are Z_i and k_i, the impedance and wavenumber inside the sphere. The left hand sides of both of these equations are known as are the radius of the piece of metamaterial and the parameters of the surrounding host medium. Therefore these equations can be solved for the two quantities $\frac{Z_o}{Z_i}$ (thus yielding Z_i) and $A_l = \frac{\mathcal{J}_l(k_i a)}{j_l(k_i a)}$. From the latter, a unique value for $k_i a$ is not easily found, but since this quantity is known for a whole series of l, the recurrences of the Bessel functions can be used to obtain the following quadratic equation which can be solved easily

$$-\left(\frac{l+1}{k_i a}\right)^2 + (A_l - A_{l+1})\frac{l+1}{k_i a} + A_l A_{l+1} + 1 = 0. \tag{C.5}$$

Determining which one of the two roots to choose is done by calculating these roots for various l and checking which one is consistent.

C.1.3 Numerical example

As an example we consider a spherical sample with radius $R = 1.477\text{m}$ at a frequency of 25MHz, hence the spheres have a diameter of about one quarter of a wavelength

in free space. The host medium has a relative permittivity $\varepsilon_r = -1.5 + j$ and a relative permeability $\mu_r = 2.0 + 1.2j$. In the host medium spheres with a radius of $r = 0.1$m are embedded. These spheres have a relative permittivity $\varepsilon_r = -6 + 0.9j$ and a relative permeability $\mu_r = 1.5 + 0.2j$. By varying the number of spheres we vary the volume fraction of the inclusions. To obtain high volume fractions we invert the medium by interchanging the material parameters of the spheres and the host medium. Figure C.1 shows a volume fraction of 16% obtained by randomly placing 500 spheres in the spherical host medium. Figures C.2 and C.3 respectively show

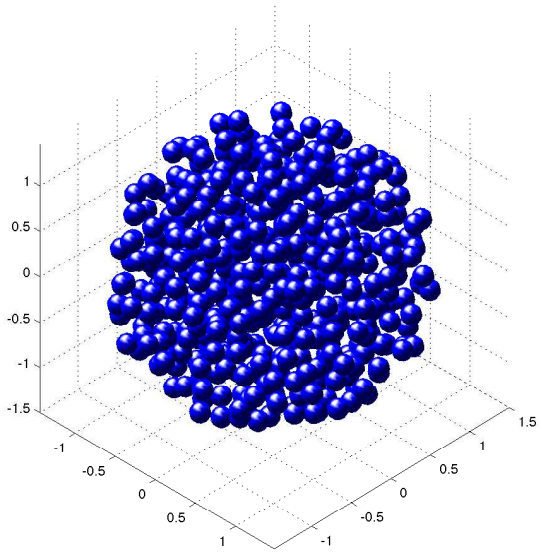

Figure C.1: A spherical sample with 500 spheres.

the real and imaginary part of the effective relative permittivity. The result predicted in [5] using the Bruggeman homogenization formula (indicated as "Mackay" on the figures)are also shown as well as the results of the Maxwell-Garnett formula. As can be seen the Maxwell-Garnett formula is more accurate than the Bruggeman formula. Similar conclusions can be drawn from the real and imaginary part of the effective permeability as shown in Figures C.4 and C.5.

For each volume fraction we only considered one realization of the medium. Nevertheless the simulated results show a very smooth behavior indicating that the medium really can be considered homogeneous. Using (C.5) we can derive the effective medium parameters also for various values of l. It turns out that our results are independent of l again confirming previous conclusion. This conclusion will be less evident if one considers higher frequencies. Then the effective parameters will depend on the radius of the spherical example and different realizations will yield

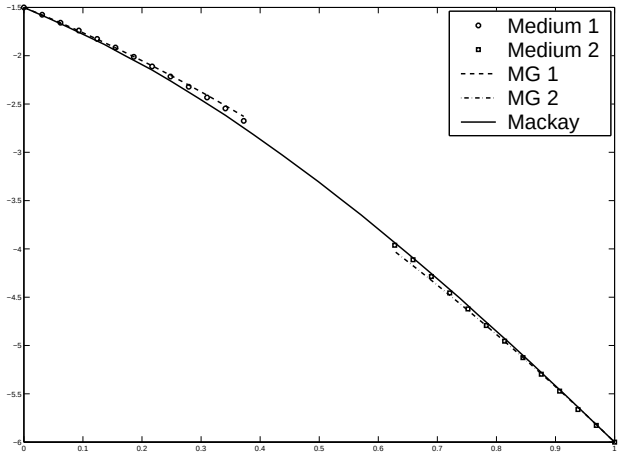

Figure C.2: Real part of the effective permittivity.

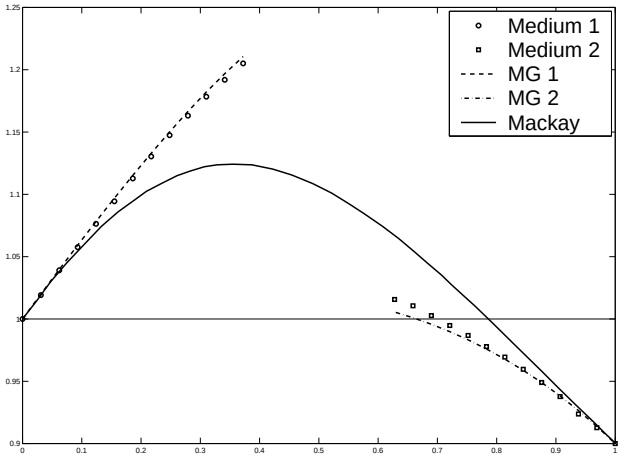

Figure C.3: Imaginary part of the effective permittivity.

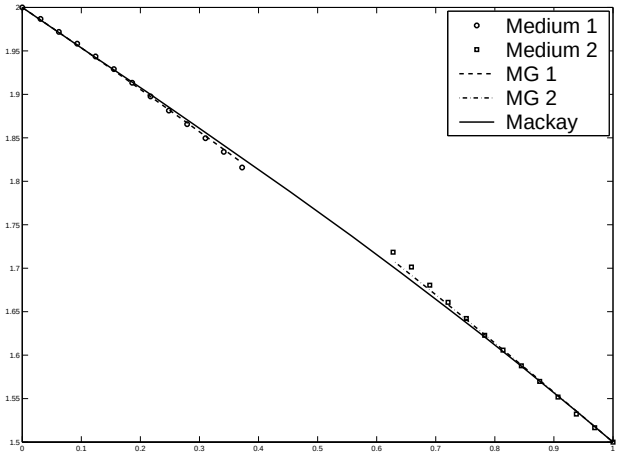

Figure C.4: Real part of the effective permeability.

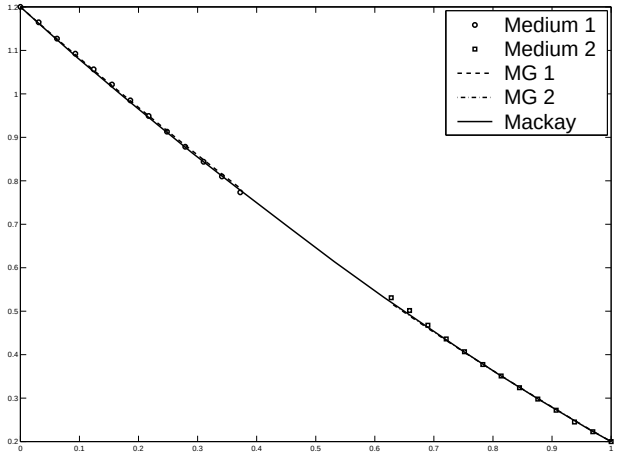

Figure C.5: Imaginary part of the effective permeability.

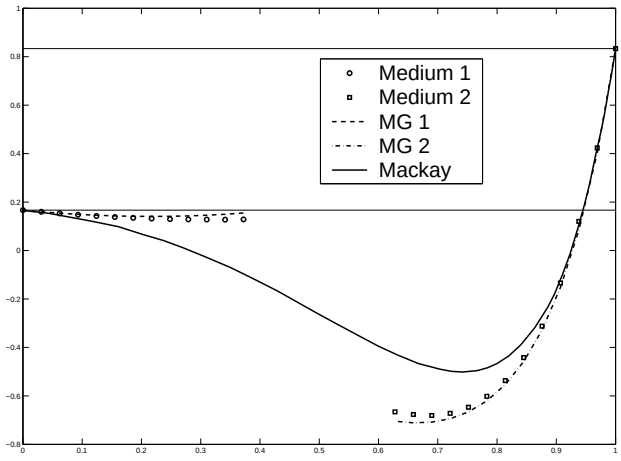

Figure C.6: Negative phase velocity parameter.

different effective parameters.

For the example considered here we also calculated the negative phase velocity parameter ρ_{NPV} given by [5]

$$\rho_{NPV} = \frac{\Re[\varepsilon_{eff}]}{\Im[\varepsilon_{eff}]} + \frac{\Re[\mu_{eff}]}{\Im[\mu_{eff}]}. \tag{C.6}$$

For a negative index medium this parameter has to be negative. The curve in Figure C.6 indeed shows a region of volume fractions corresponding to a negative index medium.

C.1.4 Conclusions

It is shown that using a multilevel fast multipole method including evanescent and propagating plane waves such as the stable plane wave method allows for the accurate simulation of a finite piece of metamaterial. These simulations allow to check the validity of the homogenization assumption as well as of homogenization formulas. We also presented a new direct method to obtain the effective parameters from a spherical sample.

C.2 Efficient Calculation of Moment Integrals for Tensor Product Basis Functions

I. Bogaert, L. Knockaert, and F. Olyslager

Abstract: The calculation of moment integrals for the solution of integral equations is still an arduous task. A considerable amount of literature exists concerning the treatment of the various singularities, but it is usually focussed on one type of basis function and one Green function. Moreover, the number of successive quadratures in a moment integral can be rather large, in particular for 3-D volume integral equations (VIEs). A more general approach will be presented here for tensor product basis functions. This type of basis function often arises in volume integral equations. The new approach is based on the known Abel transform properties of the Green function, which provide a way to expand the Green function of general dimension into a superposition of Gaussians. This allows the quadratures over the different dimensions to be decoupled, which enhances the computational efficiency. A further simplification of the moment integral to only a single integration can be attained when the basis functions are polynomial, which is usually the case.

C.2.1 Method of moments in electromagnetics

Consider e.g. the following VIE in $\mathbb{R}^d$:

$$u(\boldsymbol{r}) = \int K(\boldsymbol{r}, \boldsymbol{r}')v(\boldsymbol{r}')\mathrm{d}\boldsymbol{r}' \tag{C.7}$$

with $\mathrm{d}\boldsymbol{r} = \mathrm{d}x_1 ... \mathrm{d}x_d$. Equation (C.7) can be converted into linear equations by means of the method of moments which consists in expanding $v(\boldsymbol{r}')$ into a suitable set of N basis functions $A_n(\boldsymbol{r}')$:

$$v(\boldsymbol{r}') = \sum_{n=1}^{N} v_n A_n(\boldsymbol{r}') \tag{C.8}$$

and integrating (C.7) with N, possibly different, test functions $B_m(\boldsymbol{r})$. The resulting linear system of equations is given by:

$$\int B_m(\boldsymbol{r})u(\boldsymbol{r})\mathrm{d}\boldsymbol{r} = \sum_{n=1}^{N} Z_{mn}v_n, \;\; m = 1, ..., N \tag{C.9}$$

with the so-called moment matrix given by

$$Z_{mn} = \int\int B_m(\boldsymbol{r})K(\boldsymbol{r}, \boldsymbol{r}')A_n(\boldsymbol{r}')\mathrm{d}\boldsymbol{r}\mathrm{d}\boldsymbol{r}', \;\; m, n = 1, ..., N \tag{C.10}$$

For electromagnetic applications, $K(\boldsymbol{r}, \boldsymbol{r}')$ is usually the free-space Green function in d dimensions:

$$K(\boldsymbol{r}, \boldsymbol{r}') = g_d(k, |\boldsymbol{r} - \boldsymbol{r}'|) \tag{C.11}$$

where k is the wavenumber and $g_d(\cdot, \cdot)$ is defined in (C.14). Since the Green function exhibits a singularity, the calculation of these integrals is not obvious if the basis and test functions $B_m(\boldsymbol{r})$ and $A_n(\boldsymbol{r})$ have overlapping support. The most widely used method to perform the quadrature is extracting the singular part of the Green function and integrating that part analytically. However, the resulting analytical expressions can be very complicated and some limit cases may also need special attention. Moreover, these expressions are specific to the Green function that is used. Going from 2-D to 3-D, for example, will alter the expressions considerably. In addition, the numerical evaluation of the remaining nonsingular part of the integral can require a large number of Green function evaluations. When q is the number of quadrature nodes per dimension, $\mathcal{O}(q^{2d})$ Green function evaluations are needed for (C.10). For 3-D VIEs, this results in $\mathcal{O}(q^6)$ evaluations. It would therefore be desirable to have a method with a lower computational cost which works for any dimension d and for any overlap the support of the basis and test functions might have. In this paper, such a method will be presented for tensor product basis functions. This means basis and test functions can be written as

$$F(\boldsymbol{r}) = \prod_{w=1}^{d} f_w(x_w) \tag{C.12}$$

C.2.2 The Green function as a superposition of Gaussians

The d-dimensional Green function is the fundamental solution of the Helmholtz equation in $\mathbb{R}^d$:

$$\check{\boldsymbol{\nabla}}^2 g_d(k, |\boldsymbol{r}|) + k^2 g_d(k, |\boldsymbol{r}|) = \delta(\boldsymbol{r}) \tag{C.13}$$

and is given by [6]:

$$g_d(k, r) = \frac{j}{4}\left(\frac{k}{2\pi r}\right)^{\frac{d-2}{2}} H^{(2)}_{\frac{d-2}{2}}(kr) \tag{C.14}$$

where $H^{(2)}_n(\cdot)$ is the Hankel function of the second kind. A very interesting property of the Green function was presented in [7], in connection with the Abel transform of $g_d(k, r)$. The Abel transform is defined as

$$\Phi(r) = \mathcal{A}f(r) = \int_{-\infty}^{\infty} f(\sqrt{r^2 + x^2})\mathrm{d}x \tag{C.15}$$

By applying the Abel transform to (C.13), it is easy to show that $\mathcal{A}g_d(k,r) = g_{d-1}(k,r)$. Also, the Abel transform has a continuous set of Gaussian eigenfunctions

$$\mathcal{A}e^{-\sigma r^2} = \sqrt{\frac{\pi}{\sigma}}e^{-\sigma r^2} \quad \Re\sigma > 0. \tag{C.16}$$

It can be readily verified that

$$g_1(k,r) = \frac{j}{2k}e^{-jkr} = -\frac{1}{2\pi\sqrt{\alpha}}\int_0^\infty e^{-\pi\alpha\frac{r^2}{\rho^2}}e^{-\frac{\beta\rho^2}{4\pi}}\mathrm{d}\rho \tag{C.17}$$

where $\Re\alpha > 0$, $\Re\beta > 0$ and $jk = \sqrt{\alpha\beta}$. As a consequence, the 1-dimensional Green function can be seen as a continuous superposition of Gaussians. Together with (C.16), this yields an expression for all the higher-dimensional Green functions:

$$g_d(k,r) = -\frac{1}{2\pi\sqrt{\alpha}}\int_0^\infty \left(\frac{\sqrt{\alpha}}{\rho}\right)^{d-1} e^{-\pi\alpha\frac{r^2}{\rho^2}}e^{-\frac{\beta\rho^2}{4\pi}}\mathrm{d}\rho \tag{C.18}$$

It should be noted that the requirements for α and β can only be met for lossy media. As a consequence, (C.18) is invalid if there are no losses. However, this can be easily remedied by moving the integration path of (C.18) into the complex plane.

C.2.3 Calculating the moment integral

We now substitute expression (C.18) in the moment integral (C.10):

$$Z_{mn} = -\frac{1}{2\pi\sqrt{\alpha}}\int_0^\infty \left(\frac{\sqrt{\alpha}}{\rho}\right)^{d-1} e^{-\frac{\beta\rho^2}{4\pi}}Q_{mn}(\rho)\mathrm{d}\rho \tag{C.19}$$

where

$$Q_{mn}(\rho) = \int\int B_m(\boldsymbol{r})e^{-\frac{\pi\alpha}{\rho^2}\sum_{w=1}^{d}\left(x_w - x'_w\right)^2}A_n(\boldsymbol{r'})\mathrm{d}\boldsymbol{r}\mathrm{d}\boldsymbol{r'} \tag{C.20}$$

The integral in (C.19) can be evaluated easily with an adaptive Gauss-Legendre quadrature routine. Although the original moment integral had a singularity, this singularity does not appear in $Q_{mn}(\rho)$, and with Gauss-Legendre quadrature, $Q_{mn}(0)$ never needs to be evaluated. Hence, it becomes very easy to achieve any desired accuracy. Note that adding another integral will not in general reduce the workload. However, if we suppose the basis functions are separable, then the quadratures over the different dimensions become separated, i.e.

$$Q_{mn}(\rho) = \prod_{w=1}^{d}\int\int b_{w,m}(x_w)e^{-\frac{\pi\alpha}{\rho^2}\left(x_w - x'_w\right)^2}a_{w,n}(x'_w)\mathrm{d}x_w\mathrm{d}x'_w \tag{C.21}$$

Hence the $2d$ quadratures have been replaced by 3 successive quadratures, thereby lowering the computational complexity to $\mathcal{O}(dq^2P)$, where P is the number of nodes for the quadrature of (C.19). Usually, the $b_{w,m}(x_w)$ and $a_{w,n}(x'_w)$ are piecewise polynomials, so the double quadratures in (C.21) can be done analytically by means of the Error function, reducing the number of quadratures to only one, and the computational complexity to $\mathcal{O}(dP)$! This method is very useful for moment integrals arising in VIEs for electromagnetic inversion problems. These integral equations typically have polynomial basis functions on a rectangular mesh [8, 9] because the exact geometry of the problem is not known a priori. Since any polynomial can be written as a sum of tensor products, the method presented here can be used to efficiently calculate these moment integrals.

C.2.4 Example: 2-D volume integral equation

The proposed method has been applied to the two-dimensional TM-scattering by a square region (see Figure C.7) with relative permittivity 2.0. The sides of the square are one wavelength long and the incoming field is a plane wave $\boldsymbol{E}^{inc} = \boldsymbol{u}_z e^{-jkx}$. The following VIE for the TM case was used:

$$\boldsymbol{E}^{tot}(\boldsymbol{r}) = \boldsymbol{E}^{inc}(\boldsymbol{r}) - k^2(\varepsilon_r - 1)\int_{-1}^{1}\int_{-1}^{1} g_2(k, |\boldsymbol{r} - \boldsymbol{r}'|)\boldsymbol{E}^{tot}(\boldsymbol{r}')\mathrm{d}x\mathrm{d}y \quad \text{(C.22)}$$

where k is the wavenumber of free space and ε_r is the relative permittivity of the medium in the square. As basis and test functions the Chebyshev polynomials $T(n, x) = \cos(n \arccos x)$ were used up to degree 15 in both x and y directions, i.e. $A_{m_1,m_2}(\boldsymbol{r}) = B_{m_1,m_2}(\boldsymbol{r}) = T(m_1, x)T(m_2, y)$. Chebyshev polynomials were chosen because of their nice interpolatory properties. The resulting electric field from this

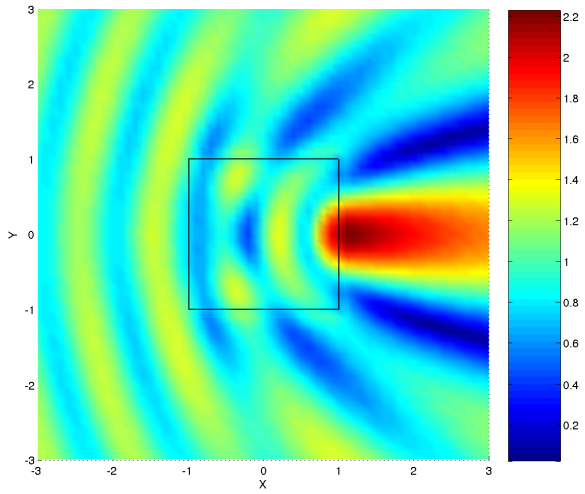

Figure C.7: Total electric field for scattering by a $\varepsilon_r = 2$ square.

calculation is shown in Figure C.7. This result has been validated with the result from a boundary integral equation.

C.2.5 Conclusion

A novel method for efficiently calculating moment integrals, based on the Abel transform properties of the Green function, has been presented. It is applicable to any tensor product basis function. If, in addition, the basis functions are polynomial, the moment integrals can be calculated with just one numerical quadrature.

C.3 Fast Full-Wave Validation of a Metamaterial Lüneburg Lens

I. Bogaert, L. Meert, and F. Olyslager

Abstract: Metamaterials have received much attention in the past. The possibility of creating a metamaterial with just the required properties for some given application is tantalizing. However, designing a metamaterial application usually entails making assumptions, concerning for example the homogeneity of the metamaterial. Only the experiment or a full-wave analysis of the design, which also incorporates the detailed structure of the metamaterial, can justify these assumptions and validate a design. In this paper, a stable plane wave fast multipole method for simulating a metamaterial consisting of a collection of spheres will be presented. As an illustrative example, this method will then be used to simulate a Lüneburg lens which was designed using the Maxwell-Garnett approximation formula.

C.3.1 The Lüneburg lens

The classic Lüneburg lens [10, 11] of radius a is a spherically symmetric lens which has an index of refraction given by:

$$n(r) = \sqrt{2 - \frac{r^2}{a^2}} \tag{C.23}$$

with r the distance to the centre of the lens. If a plane wave impinges on the lens, a focal point exists at the far side of the surface of the lens. This property is often used in so-called Lüneburg reflectors, which have a good conductor covering part of the lens. The continuous variation of the index of refraction is usually approximated

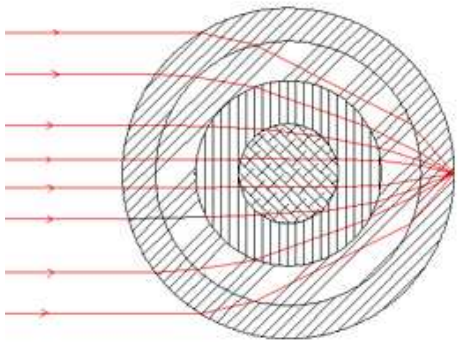

Figure C.8: Lüneburg lens with homogeneous concentric shells.

using homogeneous concentric shells (see Figure C.8) but, at least theoretically, it can also be done using a collection of electrically small dielectric spherical inclusions in a host medium with a variable inclusion density. For such a metamaterial, the Maxwell-Garnett homogenization formula [1] predicts the following relative permittivity:

$$\varepsilon_r = 1 + \frac{f(r)\alpha}{1 - \frac{1}{3}f(r)\alpha}. \tag{C.24}$$

Here, $f(r)$ is the sphere density (the number of spheres per cubic meter) and α is the polarizability of one sphere, given by:

$$\alpha = 3V\frac{\varepsilon_s - 1}{\varepsilon_s + 2} \tag{C.25}$$

with ε_s and V respectively the relative permittivity and volume of each of the spheres. By equation (C.23) the relative permittivity is known and this permits the calculation of the sphere density as a function of the distance to the centre:

$$f(r) = \frac{3}{\alpha}\frac{1 - \frac{r^2}{a^2}}{4 - \frac{r^2}{a^2}} \tag{C.26}$$

C.3.2 Simulation method

In order to simulate a large number of spheres, the T-matrix method is used. In this method the incoming and scattered electric field of every sphere is expressed in terms of the vectormultipoles [12]:

$$\boldsymbol{E}^{inc}(\boldsymbol{r}) = \sum_{l=0}^{L}\sum_{m=-l}^{l}\left[a_{lm}^{inc}\boldsymbol{M}_{lm}^{j}(\boldsymbol{r}) + b_{lm}^{inc}\boldsymbol{N}_{lm}^{j}(\boldsymbol{r})\right] \tag{C.27}$$

$$\boldsymbol{E}^{sc}(\boldsymbol{r}) = \sum_{l=0}^{L}\sum_{m=-l}^{l}\left[a_{lm}^{sc}\boldsymbol{M}_{lm}^{h^{(2)}}(\boldsymbol{r}) + b_{lm}^{sc}\boldsymbol{N}_{lm}^{h^{(2)}}(\boldsymbol{r})\right] \tag{C.28}$$

where

$$\boldsymbol{M}_{lm}^{f}(\boldsymbol{r}) = \frac{\check{\boldsymbol{L}}\left[f_l(kr)Y_{lm}(\boldsymbol{r})\right]}{\sqrt{l(l+1)}} \qquad \boldsymbol{N}_{lm}^{f}(\boldsymbol{r}) = \frac{1}{k}\check{\boldsymbol{\nabla}} \times \boldsymbol{M}_{lm}^{f}(\boldsymbol{r}) \tag{C.29}$$

with $j_l(\cdot)$ and $h_l^{(2)}(\cdot)$ respectively the spherical Bessel function and the spherical Hankel function of the second kind. The angular momentum operator $\hat{\boldsymbol{L}}$ is given by:

$$\check{\boldsymbol{L}} = -j\boldsymbol{r} \times \check{\boldsymbol{\nabla}} = j\left[\boldsymbol{e}_\theta \frac{1}{\sin\theta}\frac{d}{d\theta} - \boldsymbol{e}_\phi \frac{d}{d\phi}\right] \tag{C.30}$$

The total field impinging on the kth sphere is the field generated by the source plus the scattered fields of all the other spheres. Mathematically, this can be expressed as follows:

$$\begin{bmatrix} a_{lm}^{inc,k} \\ b_{lm}^{inc,k} \end{bmatrix} = \sum_{j \neq k} \sum_{l',m'} \begin{bmatrix} \alpha_{lm,l'm'}^{MM}(\boldsymbol{r}_{jk}) & \alpha_{lm,l'm'}^{MN}(\boldsymbol{r}_{jk}) \\ \alpha_{lm,l'm'}^{MN}(\boldsymbol{r}_{jk}) & \alpha_{lm,l'm'}^{MM}(\boldsymbol{r}_{jk}) \end{bmatrix} \cdot \begin{bmatrix} a_{l'm'}^{sc,j} \\ b_{l'm'}^{sc,j} \end{bmatrix} + \begin{bmatrix} a_{lm}^{so,k} \\ b_{lm}^{so,k} \end{bmatrix} \quad \text{(C.31)}$$

The α-matrices are the translation matrices for the vectormultipoles [12]. To get a solvable linear system of equations, another relation between the scattered and incoming field of the spheres is required. This relation is provided by means of the so-called T-matrix of the spheres. The T-matrix of a sphere converts an incoming field, expressed as a vector of multipole coefficients, into the corresponding scattered field:

$$\begin{bmatrix} a_{l'm'}^{sc,k} \\ b_{l'm'}^{sc,k} \end{bmatrix} = \sum_{l=0}^{L} \sum_{m=-l}^{l} \mathsf{T}_{l'm',lm}^{k} \cdot \begin{bmatrix} a_{lm}^{inc,k} \\ b_{lm}^{inc,k} \end{bmatrix} \quad \text{(C.32)}$$

For a homogeneous sphere $\mathsf{T}_{l'm',lm}^{k}$ is a diagonal matrix and it can be computed analytically. For more complex geometries, it can be calculated numerically. Multiplying (C.31) with $\mathsf{T}_{l'm',lm}^{k}$ yields a matrix equation which only contains the scattered fields.

Solving this matrix equation can be done using an LU-decomposition, but this requires $\mathcal{O}(N^3)$ multiplications and $\mathcal{O}(N^2)$ memory size. For large problems, this is unacceptable. However, using an iterative technique in combination with a fast multipole method (FMM) for the matrix-vector multiplications, the computational complexity and memory requirements can both be reduced to $\mathcal{O}(N)$. The geometrical detail of metamaterials is smaller than the wavelength while a piece of metamaterial is usually larger than the wavelength. Therefore, the FMM for the simulation of metamaterials must work for both low-frequency (LF) as high-frequency (HF) problems. The Stable Plane Wave Method (SPWM) [13] satisfies this requirement. It incorporates propagating as well as evanescent plane waves by means of the following spectral representation of the Green function:

$$h_0^{(2)}(\gamma r) = \frac{1}{2\pi} \int_{-\infty}^{\infty} \int_{-\infty}^{\infty} e^{\mp j \boldsymbol{k} \cdot \boldsymbol{r}} \frac{\mathrm{d}k_x \mathrm{d}k_y}{\gamma k_z(\gamma, K)}, \; z = \boldsymbol{u}_z \cdot \boldsymbol{r} \gtrless 0. \quad \text{(C.33)}$$

Here, k_z is a quantity depending on γ and $K = \sqrt{k_x^2 + k_y^2}$, defined as

$$k_z(\gamma, K) = \begin{cases} \sqrt{\gamma^2 - K^2}, & \gamma \geq K \\ -j\sqrt{K^2 - \gamma^2}, & K > \gamma \end{cases} \quad \text{(C.34)}$$

Unfortunately, equation (C.33) is valid only if $z \gtrless 0$. This is caused by the fact that evanescent waves grow exponentially if this condition is not satisfied, causing the in-

tegral representation (C.33) to diverge. Similar expressions for the other half-spaces are easily obtained, but the fact that six different representations ($x, y, z \gtrless 0$) are needed means a serious reduction of the efficiency of the method. The aggregations and disaggregations are the dominant computational costs. However, it has been recently shown [4] that the (dis)aggregation from (to) multipoles to (from) the six plane wave patterns can be accelerated by using the symmetry of the aggregation matrices. This acceleration has been used here.

C.3.3 Results

A Lüneburg lens with a diameter of 8 wavelengths was simulated. The wavelength is 2m, the radius of the spheres is 0.12m, and their relative permittivity is 12. The total number of spheres is 42899, which results in 257394 unknowns if only the dipole scattering term is taken into account. The incoming field is a plane wave traveling in the negative z-direction: $\boldsymbol{E}^{inc}(\boldsymbol{r}) = \boldsymbol{u}_x e^{j\boldsymbol{k}\cdot\boldsymbol{r}}$. The simulation was run on a computer with 4 Opteron 270 processors. Multithreading was only used for the (dis)aggregation stage. Memory usage was approximately 7Gb and the simulation took 10 hours. In figures C.9(a) and C.9(b), the amplitude and phase of $\boldsymbol{u}_x \cdot \boldsymbol{E}^{tot}(\boldsymbol{r})$ are plotted in the plane $x = 0$. In C.9(a) the spheres intersecting with this plane are also shown, while in C.9(b) the contour of the lens is shown. The focussing effect of the lens is clearly visible in both plots, thereby validating the design and the simulation method.

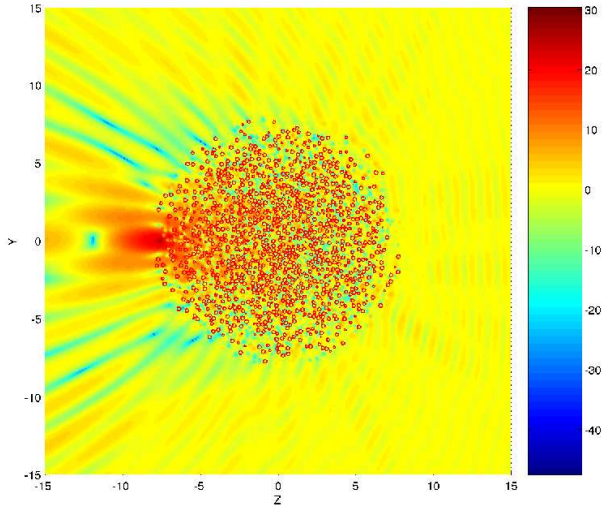

(a) Amplitude (dB)

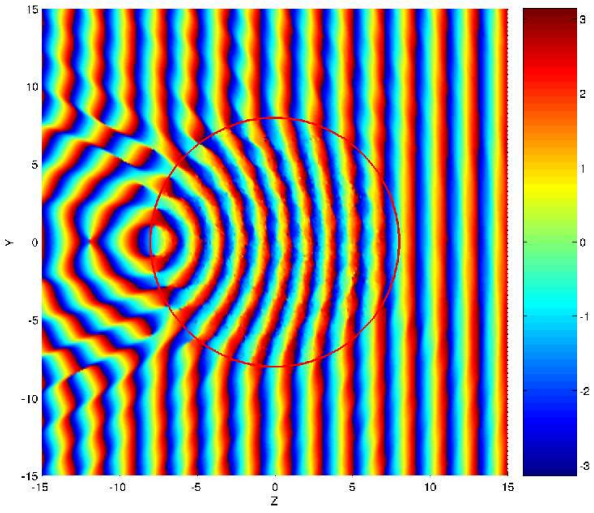

(b) Phase (rad)

Figure C.9: Amplitude and phase of the x-component of the electric field in the Lüneburg lens.

C.4 Exact full-wave simulation of finite pieces of metamaterials and extraction of effective material parameters

I. Bogaert and F. Olyslager

Abstract: A stable plane wave multilevel fast multipole method (SPWMLFMA) is presented for the simulation of the scattering at a very large number of scatterers using the T-matrix method. The method is used to accurately simulate the interaction of an incident field with a piece of metamaterial consisting of a large number of particles embedded in a host medium. From the scattering data it is possible to derive effective material parameters of the piece of metamaterial. We will show two examples. The first one consists of a metamaterial Lüneburg lens and illustrates the interaction of the incident field with a large number of scatterers and the second one is a chiral medium composed from a large number of metal spiral like objects and illustrates the extraction of effective parameters.

C.4.1 Introduction

The T-matrix of a particle relates incoming and scattered vectorial spherical harmonic coefficients of the fields. Knowing the T-matrix for each particle in a cloud allows the construction of a linear system of equations describing the interaction of an incoming field with the cloud. The dimension N of the system is equal to the number of particles multiplied by the number of spherical harmonics per particle. Typically the size of the particles will be small and the size of the cloud will be large compared to wavelength. To solve this system efficiently we will use the SPWMLFMA [13] which is valid in the low and the high frequency regime. We have further accelerated and optimized this method [14].

The T-matrix of an individual particle is evaluated analytically in the case of a sphere or using a detailed Method of Moments integral equation analysis in the case of a more complex particle. For metal particles we use an electric field integral equation.

To extract the effective material parameters of a metamaterial composed of a cloud of particles a spherical cloud is considered and the T-matrix of the total cloud is calculated. From that an analytical technique is used to extract effective material parameters. I.e. material parameters of a homogeneous sphere are determined that produce the same T-matrix as the spherical cloud. Since different spherical harmonics can be compared we have a check for the accuracy. In practise we will take the average of the result of four to five such spherical harmonics.

C.4.2 A Lüneburg lens

As a first example we consider a Lüneburg lens of 8λ diameter build from a large number of spherical particles with increasing density towards to the center of the lens. The density as a function of radius was guessed from the Maxwell-Garnett approximation. The particles have a diameter of 0.12λ and a relative permittivity of 12. In the example $N = 257394$ for 42899 spherical particles. Figure C.10 shows the focussing of the amplitude of the field when a plane wave is incident on the lens from the right. The example proves the validity of homogenization using Maxwell-Garnett and the accuracy of the simulation method.

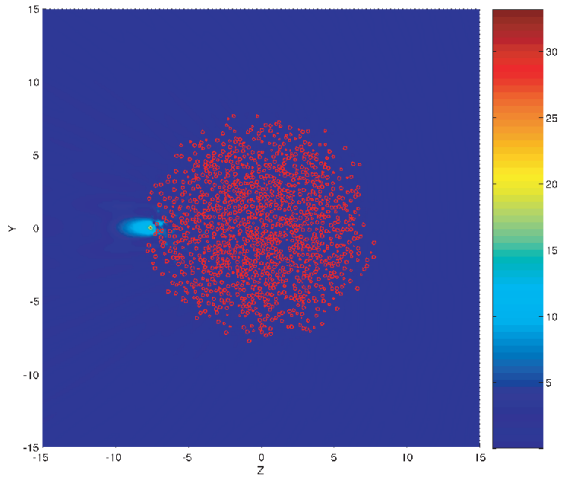

Figure C.10: Plane wave incident on a metamaterial Lüneburg lens.

C.4.3 A chiral medium

Now we consider particles that are metal spirals as shown in Figure C.11. The diameter of a particle is 2.202mm and the perfectly conducting wire has an elliptical cross-section with a major diameter of 0.14mm and a minor diameter of 0.07mm. The surface current density on the wire is discretized using 4584 Rao-Wilton-Glisson basis functions. Figure C.11 shows the current density on the wire when a plane wave is incident at a frequency of 5.98GHz.

Spherical clouds composed of randomly positioned and randomly oriented particles are build. We consider clouds consisting of 125, 250, 500, 1000 and 2000 particles each with a density of 0.0345 particles per mm^3. The centers of two particles are at least separated by 2.6mm. In each case we determined the effective material parameters by comparing the total T-matrix with that of a homogeneous bi-isotropic

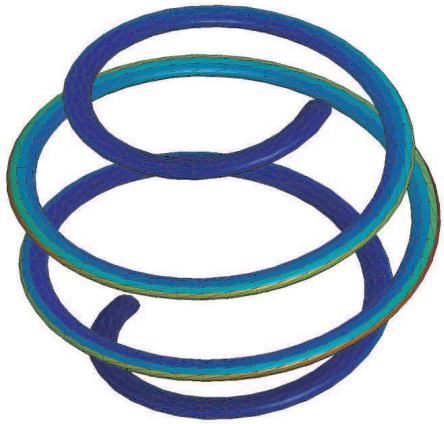

Figure C.11: Surface current density on a perfectly conducting chiral particle.

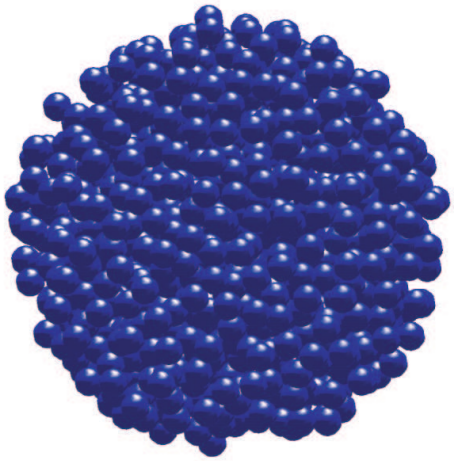

Figure C.12: Spherical cloud with 1000 particles.

sphere. We took the average of the effective material parameters of each of these five constellations and we found

$$\begin{bmatrix} \frac{\zeta}{\sqrt{\varepsilon_0\mu_0}} & \frac{\mu}{\mu_0} \\ \frac{\varepsilon}{\varepsilon_0} & \frac{\xi}{\sqrt{\varepsilon_0\mu_0}} \end{bmatrix} = \begin{bmatrix} 0.0007 + 0.2033j & 1.1072 - 0.0004j \\ 1.6347 - 0.0014j & -0.0007 - 0.2032j \end{bmatrix}. \tag{C.35}$$

where we used the material parameter definitions of a bi-isotropic medium as defined in [15]. As $\zeta = -\xi$ we indeed recover a reciprocal bi-isotropic medium, i.e. a chiral medium. Also note that the numerical simulations give rise to a lossless medium within numerical accuracy. The variance on the matrix elements derived from the effective parameters of the five constellations is

$$\begin{bmatrix} 0.0043j & 0.011 \\ 0.022 & 0.0040j \end{bmatrix}. \tag{C.36}$$

Hence, an accuracy between 1% and 2% on the effective parameters is obtained.

A spherical cloud with 1000 particles is shown in Figure C.12. Each small sphere on this figure represents a spiral like particle as shown in Figure C.11.

C.4.4 Conclusion

We show that using advanced fast multipole methods it becomes possible the simulate finite pieces of metamaterial comprising a very large number of scattering particles. We demonstrated that this method allows for the extraction of effective parameters from a finite piece of metamaterial.

C.5 Accurate Wideband Evaluation of the Shielding Effectiveness of Complex Enclosures Using an Asynchronous Parallel NSPWMLFMA

J. Peeters, I. Bogaert, J. Fostier, and F. Olyslager

Abstract: We present the application of the Non-directive Stable Plane Wave Multilevel Fast Multipole Algorithm (NSPWMLFMA) to the simulation of the shielding effectiveness of enclosures with complex fillings. The method is parallelized with an asynchronous algorithm in order to allow highly efficient simulations in an inexpensive GRID computing environment. The whole method is fully error controlled. Further increased efficiency is obtained by using Block-Jacobi preconditioners, splay trees (STs) to extract symmetries in the geometry and careful evaluation of self-patch and neighbor-patch integrals. Numerical examples of enclosures with and without equipment illustrate the method. We will also focus on the use of lossy materials to increase the shielding efficiency of metal enclosures around resonance frequencies.

C.5.1 Introduction

In [16] a detailed study was made on the shielding performance of metallic enclosures. The simulation of the shielding effectiveness of an enclosure remains a difficult task because of two main reasons. First, the accuracy of the simulations needs to be very high. This requires high precision calculations and very fine discretizations both leading to high computational costs. Second, every geometric detail in the enclosure is of importance. Taking into account this detail again puts high demands on the computational complexity. In [16] a Method of Moments (MoM) based code [17] was used in order to achieve the required accuracy. The high computational cost limited the simulations to low frequencies and simple geometries.

We have already shown that the Multilevel Fast Multipole Algorithm (MLFMA) [18] is especially suited for evaluation of the shielding performance of enclosures. This method combines a high accuracy with limited computational cost. If N represents the number of unknowns to discretize the unknown (equivalent) electric and magnetic current densities on surfaces then the computational cost of the MLFMA is $\mathcal{O}\left(N \log N\right)$. For three-dimensional problems, involving considerable geometrical detail and/or of several wavelengths in size, N will grow rapidly requiring considerable computer resources even when using MLFMA.

Two-dimensional simulations of shielding enclosures using a boundary integral equation accelerated with MLFMA were presented in [19] and [20]. In these contributions we demonstrated the importance of the accuracy in self-patch and neighbor-patch integrations, the importance of preconditioning and the use of STs to efficiently extract symmetry. In [21] we presented an asynchronous parallelized MLFMA that allows for efficient parallelization of the MLFMA method on inexpensive GRID computer en-

vironments connected by a slow switch. The asynchronous algorithm is also highly performant compared to existing synchronous parallelizations of the MLFMA when considering multiple object scattering as is encountered in the evaluation of shielding enclosures comprising realistic hardware. An implementation of this two-dimensional parallel MLFMA is available as open source software from [22]. Applications of this method reach far beyond EMC problems, see e.g. [23].

In [21] we already mentioned the possibility to extend this algorithm to three dimensions by considering elementary three-dimensional scattering examples. This paper wants to further explore this and show its abilities to evaluate realistic shielding problems. We apply the MLFMA on different surface integral equations to calculate the scattering at multiple homogeneous dielectric or perfectly conducting (PEC) objects. Since the classical plane wave based MLFMA breaks down at low frequencies it is not very suitable to simulate objects with sub-wavelength detail. However, recently a very efficient new plane wave based MLFMA, the NSPWMLFMA, has been developed [24] that remains stable at low frequencies. In [24] NSPWMLFMA was developed for scalar wave propagation problems, here we for the first time apply it for vectorial wave propagation.

The asynchronous parallelization scheme developed in [21] for two-dimensional problems is shown to be fully applicable for the three-dimensional NSPWMLFMA as will be illustrated here for the first time. As in the two-dimensional case we will devote special attention to preconditioning, accurate evaluation of self-patch and neighbor-patch integrations and the use of STs. In particular the performance in three-dimensions of STs [25] deserves special attention.

In [16] it was argued that shielding at resonance frequencies of enclosures benefits from the use of absorbing materials. We will show that the asynchronous parallel NSPWMLFMA is capable to include lossy objects without losing accuracy. As we did for the two-dimensional implementation we also made this three-dimensional implementation available as open-source software from [22].

The scope of this paper does not allow us to give a detailed description of all the elements of the asynchronous parallel NSPWMLFMA. We will suffice with a brief discussion of each of these elements with the relevant references, where possible, and rather focus on the simulation results. We will compare results with results obtained in [16], show results of the shielding efficiency of a typical personal computer tower and illustrate the effect of absorbing materials. More results will be shown during the presentation at the conference.

C.5.2 Theory

Surface integral equations

The geometry that we consider consists of a number of homogeneous isotropic dielectric objects, each characterized by its complex permittivity and permeability, and of

PEC objects both embedded in an isotropic background, usually free space. Objects can be embedded into other objects and objects can touch each other creating lines where three or more materials come together.

The scattering at such geometries is evaluated by surface integral equations with as unknowns the (equivalent) electric and magnetic surface current densities on the boundaries of each object. Several integral equations are possible, for an overview we refer to [26]. We use a combination of different types of integral equations depending on the type of objects and the frequencies involved. For open PEC objects, such as enclosures with apertures, we use the Electric Field Integral Equation (EFIE), for closed objects we use EFIE below the first resonance frequency of the object and the Combined Field Integral Equation (CFIE) above that frequency. For very low frequencies we resort to the Magnetic Field Integral Equation (MFIE) in stead of EFIE because it is better conditioned at low frequencies. For dielectrics we use the Müller integral equation at low frequencies and the Poggio-Miller-Chang-Harrington-Wu-Tsai (PMCHWT) formulation at high frequencies.

Method of Moments

We use a Galerkin MoM where the surface current densities are discretized on a triangular mesh with Rao-Wilton-Glisson vectorial basis functions. To achieve high accuracy the singular part of the Green functions is extracted for both the self-patch and neighbor-patch integrations. These integrations over the singular part are all being done in closed form. The remaining regular part of the Green function and the integrations for interactions that are nor self-patch nor neighbor-patch are done numerically using Gaussian quadrature rules defined on a triangle [27].

Special care is taken when objects are touching. In the past two touching objects were often simulated by including a very small gap between them. While this simplifies the implementation and does not lead to significant error, it does involve twice as many unknowns along the touching surface as strictly necessary. We opted for a more cumbersome implementation, as described in [28], that avoids including these gaps and extra unknowns and that at the same time remains a full Galerkin scheme, which avoids half basis functions at lines where three or more materials come together.

Splay Trees

Often large structures contain symmetries where two pairs of interacting triangles are geometrically equal which means that the corresponding two elements in the MoM matrix are equal. In [20] we have shown for two-dimensional problems that a ST [25] allows to extract these geometrical symmetries for the near interactions in $\mathcal{O}(N \log N)$ time complexity, making it compatible with the MLFMA. Also for three-dimensional problems the ST method can be used efficiently, again leading to an $\mathcal{O}(N \log N)$ complexity. Because the near interactions are relatively more impor-

tant in three than in two dimensions, the savings by using STs are even more profound. Even for structures with limited symmetry some savings are seen which shows that the overhead imposed by unsuccessful search operations is limited. The extra memory needed for the ST is only needed during the set-up phase of the MLFMA.

NSPWMLFMA

The classical plane wave based MLFMA breaks down at low frequencies due to loss of numerical accuracy. This means that the boxes on the lowest level in the MLFMA for structures containing significant sub-wavelength geometrical detail will contain a considerable number of unknowns. Several attempts have been proposed to remedy this problem without having to resort to non-diagonal translation operators. The crux is to incorporate more near-field information in the plane wave spectrum. This can be done by incorporating evanescent plane waves leading to the Stable Plane Wave MLFMA [3] which needs 6 radiation patterns along 6 different directions. Recently a new method, the NSPWMLFMA, was devised [24] that avoids these 6 different directions for scalar wave propagation problems. In this contribution we for the first time report results obtained with the NSPWMLFMA for vectorial wave propagation. The NSPWMLFMA is easily incorporated in and is fully compatible with the classical MLFMA.

Asynchronous parallelization

In [21] it was announced that the asynchronous parallelization developed for two-dimensional MLFMA was mutatis-mutandis applicable for the three-dimensional case. In this contribution we, for the first time, present results obtained in three dimensions. The asynchronous parallelization uses a space filling curve to assign different boxes in the MLFMA to different processors. The workload is then divided in small packets which are arranged in a priority queue. The priority queue is built using an advanced heuristic and avoids communication bursts between processors as would be the case in synchronous parallelization. This makes this method highly suitable for low cost GRID computing environments connected by standard gigabit Ethernet. It is also very favorable when scattering at multiple objects is considered as is the case for shielding effectiveness evaluations.

C.5.3 Shielding problems

As a verification we first consider the cubical brass box of dimensions 50cm by 50cm by 50cm that was also extensively investigated in [16]. The front panel of the box is interchangeable and here we will consider a front panel with a slit of 5cm by 20cm in the center of the box. As a reference solution we consider a box without a front panel. The box is perpendicularly illuminated by a plane wave with the electric field

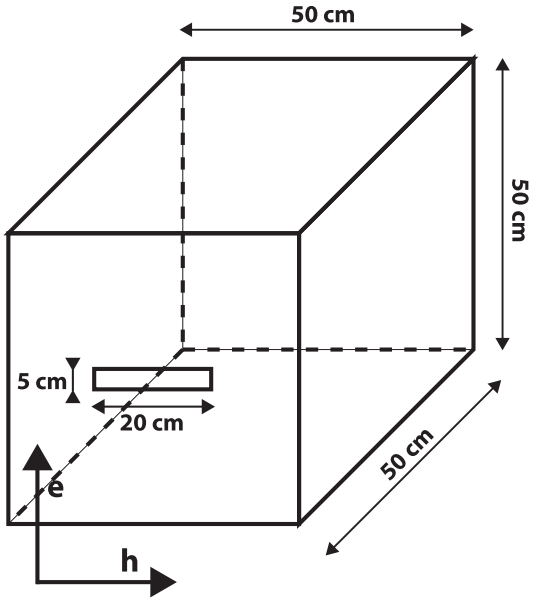

Figure C.13: Cubic box with slit illuminated by a plane wave.

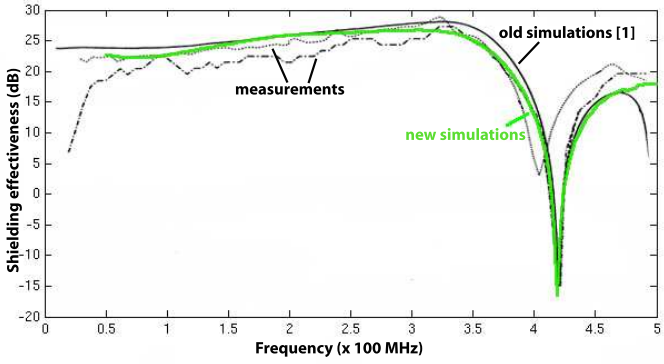

Figure C.14: Shielding effectiveness of the box in Fig. C.13.

polarized orthogonal to the slit. The electric field is measured in the center of the box. The set-up is shown in Fig. C.13.

Figure C.14 shows the shielding efficiency of the box when the box without front panel is used as reference. As a comparison also results from [16] are shown which consist both of measurements and simulations. As can be seen the new simulations are somewhat closer to the measurements than the simulations in [16]. This is due to the fact that the number of unknowns $N = 11744$ is about ten times higher than was possible in [16].

In [16] it was mentioned that the application of absorbing materials in a shielding enclosure could help improving the shielding efficiency around resonance frequencies. To illustrate this effect we place an absorbing plate of 46cm by 46cm by 2cm at a distance of 2cm from the bottom in the cubic enclosure. Horizontally the plate is centered in the box. The complex relative permittivity of the plate is $2 - 2j$. As a comparison we also consider a lossless plate with the same dimensions but with a relative permittivity of 2. The entire structure is meshed using $N = 38951$ unknowns. Figure C.15 shows the shielding efficiency as a function of frequency with lossy plate, with lossless plate and without plate. The reference always is the enclosure with open front and without plate. We note as expected an increase in shielding efficiency around resonances. Also note that the losses of the plate indeed are responsible for an increased shielding efficiency. In Fig. C.17 the amplitude of the vertical component of the electric field is shown in a vertical cross-sectional plane of the enclosure at the first resonance. The figure on the left corresponds with the lossless plate and the figure on the right with the lossy plate. Note the substantial decrease in field amplitudes inside the enclosure due to the losses.

As a final example we consider a personal computer filled with a number of objects and a number of holes in the casing. Figures C.17 and C.18 give an idea of the mesh which resulted in $N = 44852$ unknowns. With $N = 44852$ the problem was simulated on 16 processors (8 dual core 2GHz AMD 64 bit processors connected by a 1GBit Ethernet switch) using 3.2GByte of memory when using STs and 1.6GByte without using STs. At 250MHz the setup time reduced from 960s to 526s due to the use of STs. The NSPWMLFMA required 0.5s per iteration for a total of 251 iterations. Figure C.19 shows the shielding efficiency as a function of frequency when considering an incident plane wave with the electric field polarized along the height of the case. Three different discretizations are considered resulting in $N = 15495$, $N = 33394$ and $N = 66980$. The small difference in shielding efficiency at low frequencies is due to a reduction of numerical leakage through the walls when using finer meshes. The amplitude of the vertical electric field component in the central vertical cross-section at a resonance at 1GHz is shown in Fig. C.20.

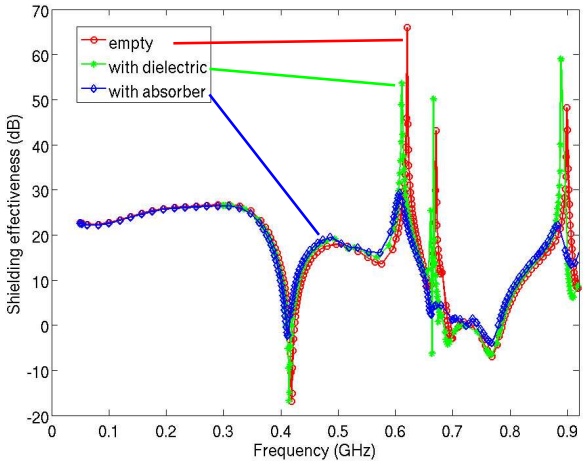

Figure C.15: Shielding effectiveness of the box in Fig. C.13 with a lossy plate (diamonds), with a lossless plate (stars) and without a plate (circles).

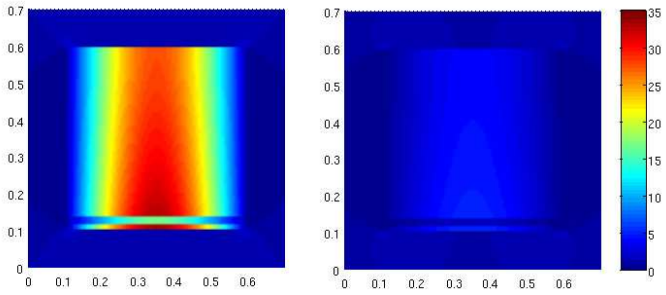

Figure C.16: Field distribution at first resonance in the box of Fig. C.13 with lossless (left) and lossy (right) plate.

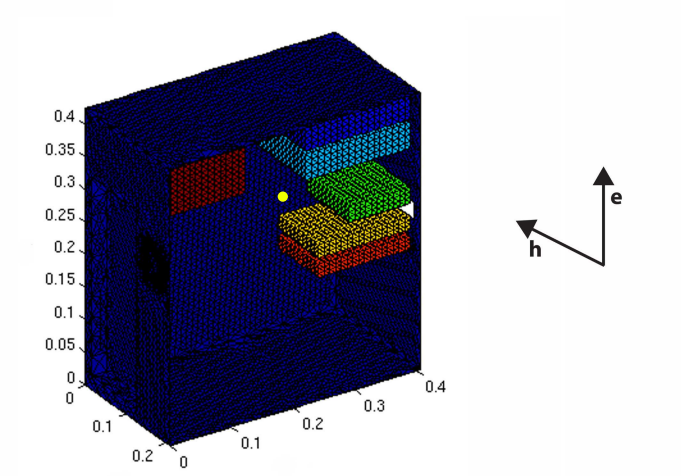

Figure C.17: Internal view of a personal computer. Dimensions are in m and the yellow dot indicates the measure point.

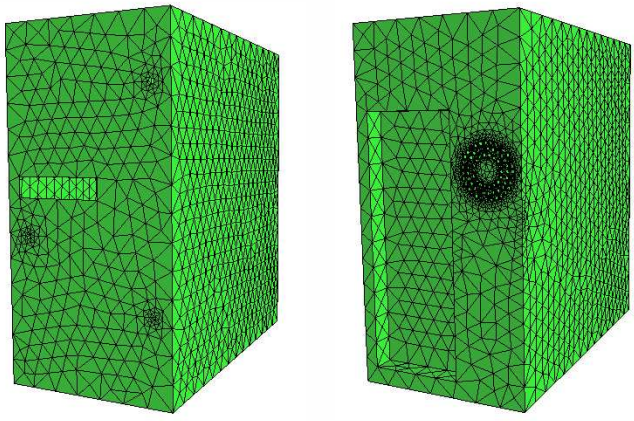

Figure C.18: Front (left) and rear (right) view of the external mesh of a personal computer.

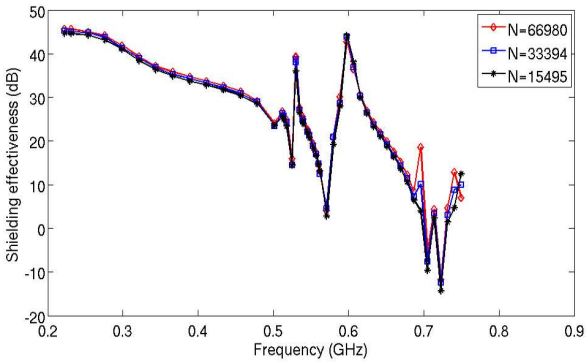

Figure C.19: Shielding effectiveness of the enclosure of Figs. C.17 and C.18.

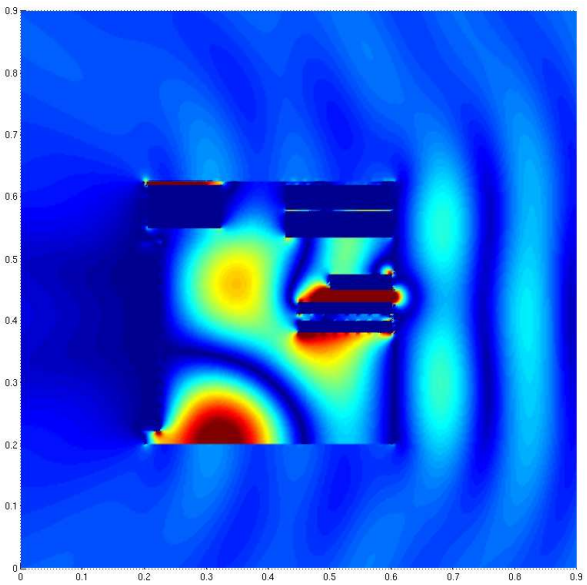

Figure C.20: Amplitude of the vertical electric field component in the cross section of the enclosure of Figs. C.17 and C.18 at 250MHz.

C.5.4 Conclusions

We demonstrated the use of a non-directional plane wave based MLFMA stable at low frequencies for the simulation of complex shielding problems. An advanced asynchronous parallel implementation of the MLFMA allows for efficient simulations on inexpensive GRID computing environments. Further research will focus on better preconditioners to reduce the number of iterations and towards further acceleration of the algorithms in order to be able to simulate even more complex structures with reasonable computational effort.

C.6 Recent Advances in Fast Multipole Methods to Simulate Ever Larger and More Complex Structures

F. Olyslager, K. Cools, J. Peeters, I. Bogaert, J. Fostier, J. Peeters, F.P. Andriulli and E. Michielssen

Abstract: In this paper we wish to focus on some recent advances in the Multilevel Fast Multipole Algorithm (MLFMA). Three different topics will be discussed briefly: a seamless extension of the MLFMA to low frequencies, an asynchronous parallelization of the MLFMA suitable for grid computing environments and a new Calderón based preconditioner for the Electric Field Integral Equation (EFIE). This will be illustrated by three scattering examples in frequency and time domain.

C.6.1 Introduction

Since the introduction of the MLFMA the use of integral equations has seen a new impetus [18]. The MLFMA drastically reduces the computational and memory complexity of Method of Moments (MoM) discretizations for boundary integral equations from $\mathcal{O}\left(N^2\right)$ to $\mathcal{O}\left(N \log N\right)$ with N the number of unknowns in the discretization. At the same time the numerical error is fully controlled in MLFMA. The MLFMA has been used to simulate problems involving several millions of unknowns [29], [21] and in two dimensions problems of tens of thousands wavelengths in size [30].

In [31] we have concentrated on the application of MLFMA for EMC shielding problems. Here, we will focus on a number of recent advances in the MLFMA. First we will investigate a stable and seamless extension [24] of the classical MLFMA to low frequencies resulting in the first truly broadband MLFMA that does not rely on directional translation operators. As a second extension we briefly discuss a new parallelization scheme [21] for the MLFMA. Contrary to existing schemes the new scheme is asynchronous and very well suited to handle multiple object scattering. Finally we discuss a new preconditioning method based on the Calderón identities for the Electric Field Integral Equation (EFIE) [32], [33]. This method was introduced for time domain integral equations but is also suited for low frequency EFIE frequency domain problems.

We will illustrate these advances by a few numerical examples in two and three dimensions and in frequency and time domain. For more examples we refer to the presentation during the conference and to the cited literature. Most of the code that was implemented to test these new advances is available as open source software under GPL licence [22].

C.6.2 The NSPWMLFMA

The Nondirective Stable Plane Wave Multilevel Fast Multipole Algorithm (NSPWMLFMA [24]) is a novel method for calculating the low frequency (LF) interactions that cannot be handled by the classical MLFMA. An interaction is called LF if the source and observer are closer to each other than approximately one wavelength. To expand fields this close to the source into plane waves in a stable manner, evanescent plane waves are necessary. The MLFMA uses only propagating plane waves and therefore succumbs to a severe numerical instability when dealing with LF interactions. Alternative algorithms can be used to deal with the LF interactions. The most widely used ones are based on multipoles [34] or the spectral decomposition of the Green function [3, 35]. However, the former has the disadvantage that the translations are not diagonal and the latter needs six radiation patterns to cover all possible translation directions. As a consequence these methods are computationally suboptimal.

The NSPWMLFMA aims to combine the strengths of the multipole and spectral methods and do away with the weaknesses. It does so by using a novel LF-stable addition theorem for translations in the z-direction. This addition theorem employs evanescent plane waves, hence its stability. However, in contrast to the spectral methods, it is still based on the same fundamental formula as the one underlying the MLFMA. Therefore it shares the MLFMA's convergence characteristics and requires only one radiation pattern. There is one problem with this addition theorem, though. It is numerically stable only for translations in z-direction. Therefore it is necessary to rotate the coordinate system such that the vector connecting the centers of the interacting source and observer boxes is parallel to the z-axis. This causes the radiation patterns to be rotated too, and this in turn causes the discretization points of the radiation patterns to be different for every translation direction. This problem is solved by using the QR-algorithm to select a special set of sample points (wave vectors in which to evaluate the radiation pattern). These sample points are chosen such that the samples contain sufficient information to fully describe the radiation pattern, i.e. the samples can be solved for the multipole coefficients of the radiation pattern. The QR selection procedure of the sample points makes sure that this operation is well conditioned. The knowledge of the multipole coefficients then allows the calculation of the radiation pattern in all other possible sample points. This enables the construction of an interpolation matrix that converts the selected samples of the radiation pattern into the required sample points for a certain translation. This matrix is then absorbed into the translation operator for this direction. In this way, numerically stable translation operators are found for all translation directions. The set of selected sample points defines the single radiation pattern.

The LF equivalents of inter- and anterpolations are done by means of dense matrices. This is a disadvantage of the NSPWMLFMA since the size of these matrices grows quadratically with the electric size of the boxes. Therefore, the NSPWMLFMA is an LF technique. It can, however, be easily coupled seamlessly with the MLFMA

to obtain a broadband method. Also, the DC limit of the algorithm exists, which clearly shows its LF stability. It is noteworthy that recently a new version of the NSPWMLFMA was created that uses translation operators that are known in closed form [36].

C.6.3 Asynchronous Parallelization

The current trend in computer architecture is to incorporate several "cores" into a single processing unit (CPU) [37]. These cores run independently and can hence be seen as a parallel system. With the ever dropping hardware prices, several computers can be connected using a cheap but fast interconnection network such as Gigabit Ethernet. It is clear that, in order to take advantage of this increase of computational power, the traditional serial algorithms need to be modified to run in such a distributed environment.

Previous efforts towards distributed parallel MLFMA were largely focused on scattering from very large 3-D PEC objects. Using advanced load balancing schemes and fast interconnection networks, problems with a very large number of unknowns have been demonstrated [29]. These implementations are essentially synchronous and are characterized by alternating phases of calculation and communication. Attempts for such an approach on Gigabit Ethernet networks led to a poor efficiency.

Recently, we proposed an asynchronous approach to the parallelization of the MLFMA [21]. The term "asynchronous" denotes that different processes can execute different types of operations at a given point in time. While some nodes are communicating, others could be calculating, leading to a better spreading of communication through time. This alleviates the need for expensive interconnection networks and avoids communication in bursts. Furthermore, this approach allows for an efficient parallelization of simulations that comprise multiple dielectric objects. The asynchronous MLFMA has been applied to both two dimensional (TE/TM) and three dimensional problems. The source code of these solvers can be obtained free of charge [22].

C.6.4 Preconditioning

The linear systems of equations resulting from the discretization of integral equations are often ill-conditioned. This is especially cumbersome for the application of MLFMA since it will drastically increase the number of iterations in the iterative solution process. Hence, reducing the condition number by using preconditioning strategies is of paramount importance when wishing to reduce the computational load of MLFMA. Ill-conditioned systems can stem from different origins. On the one hand the physical geometry of the scatterer itself can induce high condition numbers. This will be the case when strong interference effects are encountered such as in e.g. photonic crystals. Dedicated preconditioners can be developed to reduce the condition

number [38]. On the other hand the used integral equation itself can be the cause of large condition numbers. This is e.g. the case with the EFIE when increasing the density of the mesh. This is especially worrysome when simulations over wide frequency bands are necessary with a constant mesh or when dealing with non-uniform meshes.

The condition number of EFIE can be improved by constructing a so-called Calderón preconditioner (see e.g. [39]). If $T[\boldsymbol{j}]$ represents the integral operator in the EFIE acting on the unknown current density $\#j$ on the surface of the scatterer then the integral equation can be written compactly as $0 = \boldsymbol{u}_n \times \boldsymbol{e}^i(\boldsymbol{r}) + T[\boldsymbol{j}](\boldsymbol{r})$ for a PEC with $\boldsymbol{e}^i$ the incident electric field and $\boldsymbol{u}_n$ the unit vector normal to the scatterer's surface. Calderón preconditioning amounts to operating T on this EFIE resulting in the Calderón preconditioned EFIE (CP-EFIE) $0 = T[\boldsymbol{u}_n \times \boldsymbol{e}^i](\boldsymbol{r}) + T^2[\boldsymbol{j}](\boldsymbol{r})$. It can be shown using the Calderón identities that T^2 has a bounded singular value spectrum when the frequency or the mesh density decreases.

Discretizing the T^2 operator by a direct Galerkin method is impractical. Therefore a discretization is used that considers a product of two discretized operators T. In the classical MoM for the EFIE the domain of T is discretized using RWG basis functions and the rang using curl-conforming RWG basis functions (i.e. $\boldsymbol{u}_n \times RWG$ basis functions). This cannot be used twice for T^2 since a singular Gram matrix is encountered when projecting the range of the first operator on the domain of the second operator. Recently, [32,33,40], it was shown that this can be resolved elegantly by discretizing the domain of the second T operator in so-called Buffa-Christiansen basis functions (BC basis functions) [40] and the range in $\boldsymbol{u}_n \times BC$ basis functions.

C.6.5 2D frequency domain example

As a two dimensional example, we consider an indoor propagation example. The geometry consists of a wooden ($\epsilon_r = 3.5$) office cubicle with metal (PEC) supports in which metal (PEC) cupboards have been placed. The size of each cubicle is 2m by 2m. A TM line current operating at 6GHz is used to excite the structure. The total number of unknowns using a $\frac{\lambda}{10}$ discretization is $48\,045$. Using four AMD Opteron 270 cores, the iterative solution took 258s and 726 iterations to converge to a tolerance of 10^{-3}. A $1\lambda \times 1\lambda$ block-Jacobi preconditioner was used. Fig. C.21 shows the electrical field density inside the cubicle. Although the number of unknowns is rather modest in this example we have used the same technique to simulate problems with $15\,000\,000$ of unknowns [21]. We have also used it for passive optical set-ups [23].

C.6.6 3-D frequency domain example

As a three dimensional example, we consider the broadband scattering at PEC objects, in casu "Thunderbird 2". First we illuminate a formation of three Thunderbirds with a frontal linearly polarized wave at a frequency such that the length of a Thunderbird

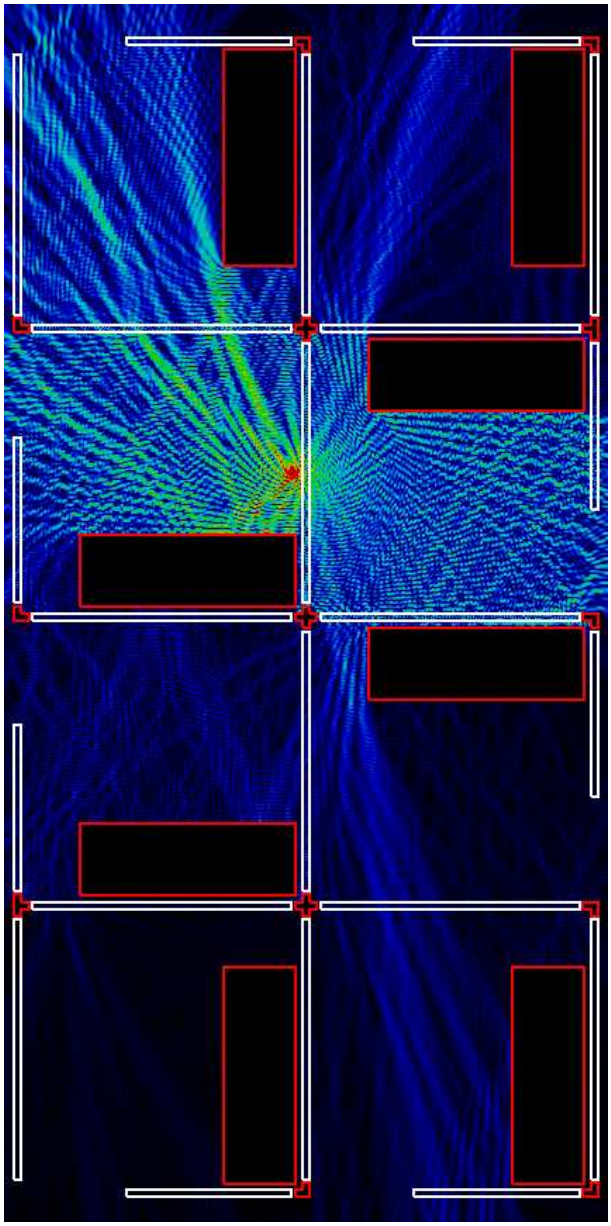

Figure C.21: Electric field density in an office cubicle.

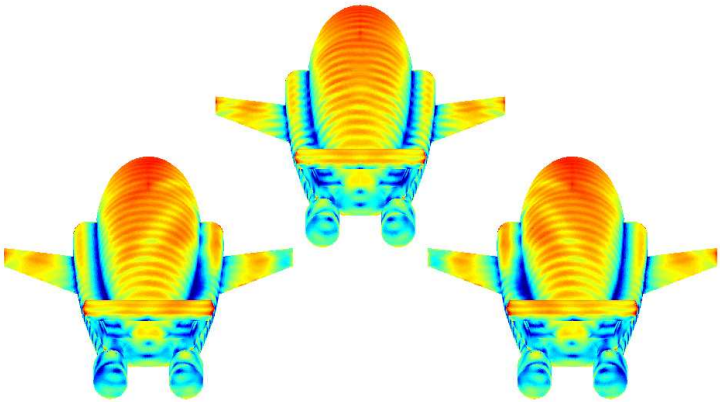

Figure C.22: HF current densities on the surface of a formation of three Thunderbirds.

corresponds to 15 wavelengths. The electric component of the incident wave is orthogonal to the wings, i.e. vertical. This problem is simulated with the CFIE to avoid spurious reflections and discretized using $1\,025\,559$ unknowns. It was simulated in about 100 iterations on 20 AMD Opteron 270 cores to a tolerance of 10^{-3}. The problem required 20 times 1.2GByte of memory and each iteration lasted 28s. Fig. C.22 shows the current distribution on the surface of the formation.

To demonstrate the efficacy of the NSPWMLFMA one single Thunderbird was illuminated by the same plane wave but now at a frequency where the length of the Thunderbird is 0.014 wavelengths. For stability reasons a MFIE was used that was discretized with $101\,466$ unknowns. Using 12 processors each iteration took 20s and convergence to a tolerance of 10^{-3} was reached after 21 iterations. Fig. C.23 shows the current distribution.

C.6.7 3-D time domain example

As a last example we consider a 3-D scattering problem in time domain. A plane wave time pulse is incident on the PEC structure of Fig. C.24. This problem is analyzed with a time domain EFIE and illustrates the capabilities of a Calderón preconditioner and the use of BC basis functions. Without preconditioner this problem requires 300 iterations per time step and with preconditioner this reduces to 15 iterations. A typical time response for the current density on the structure is shown in Fig. C.25. We see that the result of the non-preconditioned and preconditioned solution coincide. The frequency response is shown in Fig. C.26. Note the two adjacent resonances that cause the beating phenomenon in Fig. C.25. For more information and other examples we refer to [32] and [33].

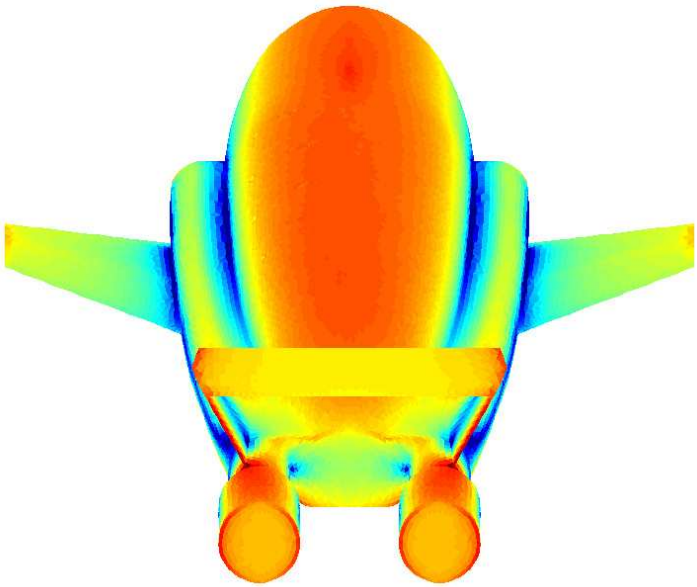

Figure C.23: LF current densities on the surface of one Thunderbird.

C.6.8 Conclusions

Three different recent advances in the development of the MLFMA have been illustrated. We are convinced that further challenging advances in the MLFMA will ultimately result in a broadband parallel algorithm that allows for the simulation of three-dimensional problems of thousands of wavelengths in size comprising several billions of unknowns on affordable computer networks.

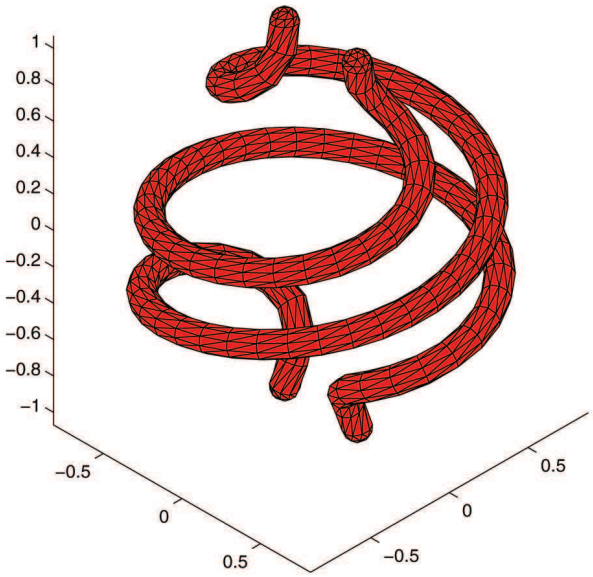

Figure C.24: Geometry and mesh of two intertwined spiral conductors.

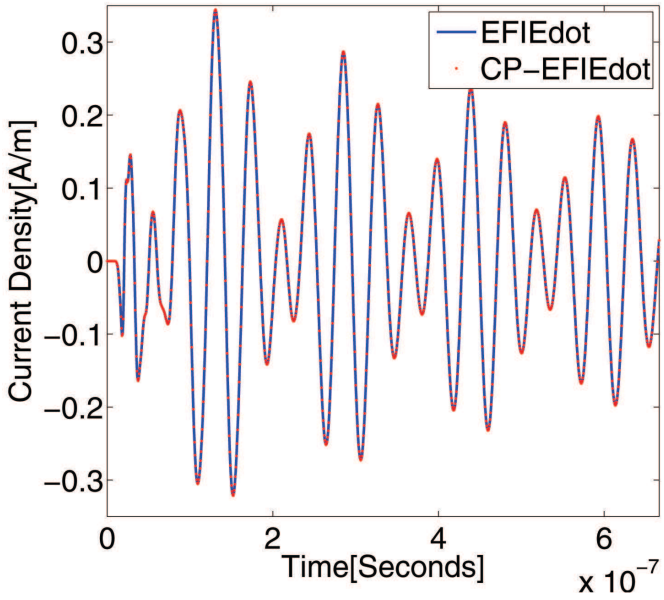

Figure C.25: Time response of the current density due to a pulse incident on the structure of Fig. C.24.

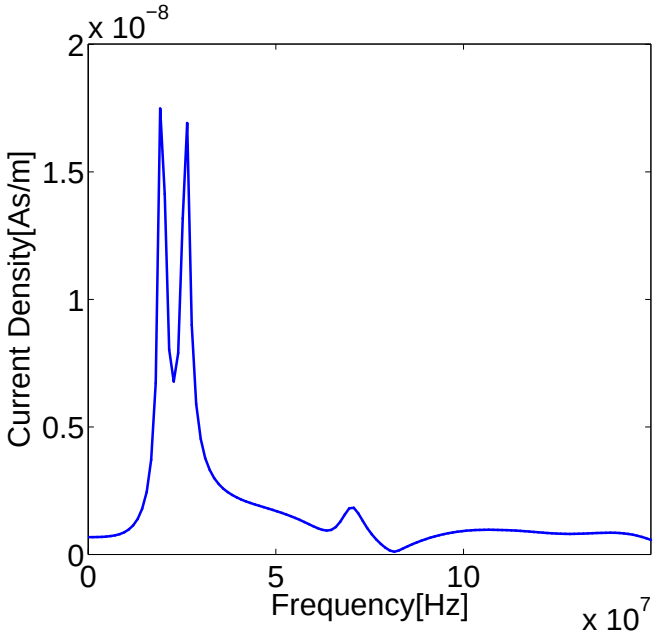

Figure C.26: Frequency response of Fig. C.24.

C.7 NSPWMLFMA: A Low Frequency Stable Formulation of the MLFMA in Three Dimensions

I. Bogaert, J. Peeters, J. Fostier, and F. Olyslager

Abstract: The iterative solution of integral equations containing the Green function of the Helmholtz equation as the integration kernel requires repeated matrix-vector products. These products can be accelerated by means of a so-called fast multipole method (FMM). Of the many fast multipole methods in use today, the Multilevel Fast Multipole Algorithm (MLFMA) is arguably among the most successful ones. It allows the simulation of electrically large structures that are intractable with direct or unaccelerated iterative solvers. Testimony to the MLFMAs myriad uses is its implementation in various commercial EM software packages such as FEKO and CST Microwave studio. However, the MLFMA has one big drawback: a numerical instability prevents the method from being used on low frequency (LF) interactions, i.e. interactions between sources and observers that are less than approximately one wavelength apart. As a consequence configurations containing significant subwavelength geometrical detail cannot be efficiently treated using the MLFMA alone and a hybrid method is necessary. However, the LF methods in use today are generally less efficient due to non-diagonal translation operators (multipole methods) or the need for six radiation patterns (spectral methods). In this contribution a novel algorithm, called the Nondirective Stable Plane Wave Multilevel Fast Multipole Algorithm (NSPWMLFMA) [24], will be presented that is stable at LF, exhibits diagonal translation operators and requires only one radiation pattern. The method is based on an analytical expression for a translation operator in the z-direction. This translation operator is made numerically stable using a shift of the integration path into the complex plane. It even has a DC-limit. A QR-based method is then used to extend the applicability to all the other translation directions. The algorithm has also been parallelized using Open FMM [22]. Finally some numerical results will be shown.

C.7.1 The LF breakdown of the MLFMA

The LF breakdown can be understood by looking at the translation operator of the MLFMA

$$T(k\boldsymbol{r}_T,\theta,\phi)=\sum_{l=0}^{L}(2l+1)j^{-l}h_l^{(2)}\left(kr_T\right)P_l\left(\hat{\boldsymbol{k}}\left(\theta,\phi\right)\cdot\hat{\boldsymbol{r}}_T\right), \tag{C.37}$$

with k the wavenumber, $\boldsymbol{r}_T=r_T\hat{\boldsymbol{r}}_T$ the translation vector and $\hat{\boldsymbol{k}}\left(\theta,\phi\right)=\cos\phi\sin\theta\hat{\boldsymbol{x}}+\sin\phi\sin\theta\hat{\boldsymbol{y}}+\cos\theta\hat{\boldsymbol{z}}$. The functions $P_l\left(\cdot\right)$ are the Legendre polynomials. Because the spherical Hankel function $h_l^{(2)}\left(kr_T\right)$ increases exponentially as a function of l if $l>kr_T$, the terms with a low l are eventually swamped in the high order terms. Obvi-

ously, the loss of the low order terms is catastrophic because they contribute the most to the addition theorem.

Various approaches have been explored to deal with this problem. Maybe the most radical approach is to replace the MLFMA with a method based on the spectral representation of the Green function [3]. Another approach is to construct a hybrid method where the LF interactions are treated using a multipole [34] or spectral representation [35] based method. However, the multipole based method does not exhibit diagonal translation operators and the spectral methods require six radiation patterns for each box, making all these approaches less efficient than the MLFMA, if it were not numerically unstable. Indeed, it is stated in [35] that the high frequency technique (MLFMA) should be used whenever possible. Hence, a formulation of the MLFMA that is stable at LF is desirable. A first attempt to obtain such a formulation can be found in [41], where a complex shift of the integration path is performed and the translation operators are found numerically. However, the achievable accuracy is rather limited [42].

C.7.2 A stable translation in the z-direction

The method presented here is based on a uniform discretization of the addition theorem, as described in [43]. This means that the double Fourier spectrum of the translation operator times $|\sin\theta|$ has to be truncated at a bandwidth L. For a translation in the z-direction, the truncated translation operator $\tilde{T}(kr_T\hat{\boldsymbol{e}}_z,\theta,\phi)$ depends only on θ and can be written as follows

$$\tilde{T}(kr_T\hat{\boldsymbol{e}}_z,\theta,\phi) = \sum_{n=-L}^{L} b_n e^{jn\theta}, \tag{C.38}$$

$$b_n = \frac{1}{2\pi}\sum_{l=0}^{L}(2l+1)j^{-l}h_l^{(2)}(kr_T)f_n^l. \tag{C.39}$$

The coefficients f_n^l can be calculated analytically and have the crucial property that $f_n^l = 0 \;\forall -l < n < l$. Through a series of further manipulations and a shift of the integration path into the complex plane, this allows the construction of a numerically stable translation in the z-direction. The analytical expression for f_n^l and an explicit formula for the magnitude of the complex shift can be found in [24].

C.7.3 Stable translations in the other directions

In order to obtain stable translations in a general direction $\boldsymbol{r}_T = r_T\mathsf{R}\cdot\boldsymbol{e}_z$ with R a 3×3 rotation matrix, it is necessary to express it as a translation in the z-direction

$$h_0^{(2)}(k\,||\boldsymbol{r}_A+\boldsymbol{r}_T||) = \frac{1}{4\pi}\int_0^{2\pi}\int_0^{\pi} e^{-j(\mathsf{R}\cdot\boldsymbol{k})\cdot\boldsymbol{r}_A}T(kr_T\boldsymbol{e}_z,\theta,\phi)\sin\theta\mathrm{d}\theta\mathrm{d}\phi. \tag{C.40}$$

The key problem is that the discretization points of the radiation pattern are rotated differently for each translation direction. Therefore we would need a separate set of plane waves for each different translation, which would be very inefficient. To avoid this, a QR is used to select the least dependent plane waves, such that they constitute a basis for the other plane waves. This process then allows the stable translation operators in the z-direction to be transformed such that they can be used on the selected plane waves.

C.7.4 Numerical results

The accuracy of the proposed method was tested on the configuration shown in Figure C.27. The sides of the boxes are 1m long. Figure C.28 shows the obtained accuracy as a function of the frequency. The accuracy is defined as the maximum relative error of all the 64 interactions between the vertices of box 1 and box 2.

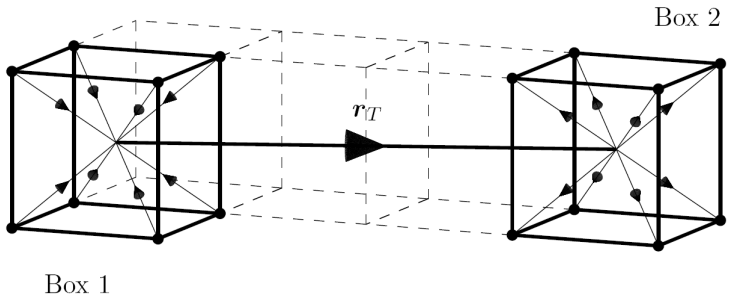

Figure C.27: The geometry for testing the accuracy.

As can be seen, the method keeps on working fine even for very low frequencies. In fact the method remains stable all the way down to DC. This limit is derived in [24]. For high frequencies the error increases because the required L for a certain accuracy increases. As for simulation results, Figure C.29 shows simulations of a plane wave impinging on an A380 airplane. These simulations were performed using an asynchronously parallelized [21, 22] vectorial version of the hybrid MLFMA - NSPWMLFMA.

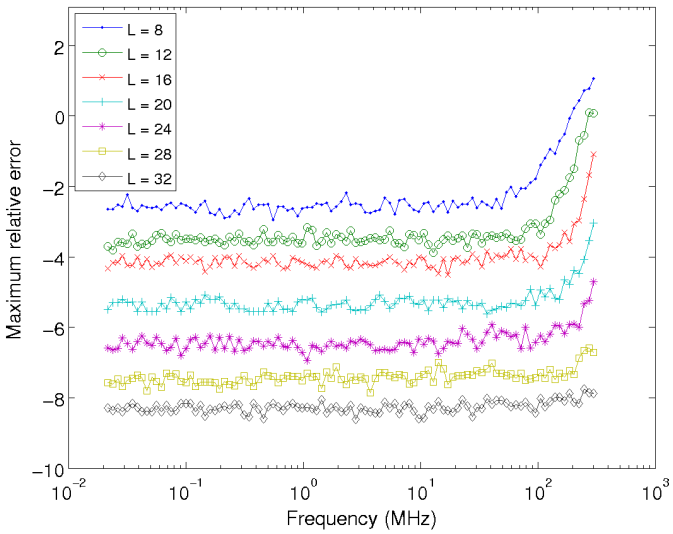

Figure C.28: The maximum relative error as a function of the frequency for various truncation bounds L.

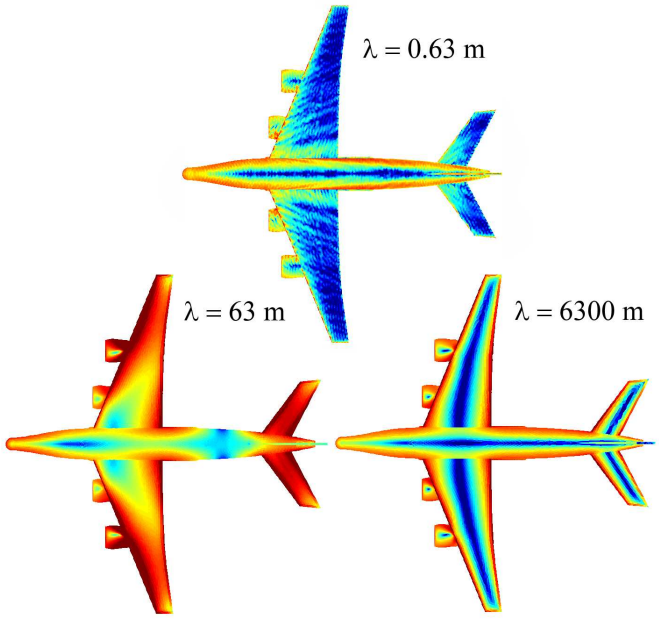

Figure C.29: Currents on the A380 airplane for plane waves impinging from the left. The wavelengths are 0.63m (top), 63m (bottom left) and 6300m (bottom right) respectively. The number of unknowns is 500000 (top) and 117000 (bottom left and right).

C.8 New Plane Wave Addition Theorems

I. Bogaert, and F. Olyslager

Integral equations containing the Green function of the Helmholtz equation play an important role in computational acoustics and electromagnetics. Numerical discretization of these equations results in a linear system of dimension N, where N is the number of basis functions used to discretize the integral equation. For large N a direct solution of the system soon becomes impractical and one has to resort to an iterative solution technique where the matrix vector product in each iteration step still requires $\mathcal{O}\left(N^2\right)$ operations.

The Multilevel Fast Multipole Algorithm (MLFMA) [18] reduces the computational complexity of the matrix vector product to $\mathcal{O}\left(N \ln N\right)$. The MLFMA is based on a plane wave addition theorem for the Green function where the Green function is written as an integral over the Ewald sphere and where the integrand is written as a product of a long range translation operator and a short range factor.

It turns out that this expansion of the Green function is not unique and that several types of plane wave addition theorems are possible. Actually a general formalism can be developed from which several new addition theorems can be conceived. The classic addition theorem used for the MLFMA is not stable when considering distances small compared to wavelength, i.e. when the argument of the Green function becomes small. This phenomenon is called the Low Frequency (LF) breakdown of the addition theorem. The new formalism allows to develop addition theorems that avoid this LF breakdown.

The starting point of the derivation is the addition theorem for the spherical Hankel function of the zeroth order and second kind

$$h_0^{(2)}\left(kr\right) = \frac{e^{-jkr}}{-jkr} = \sum_{l=0}^{L} (-1)^l (2l+1) j_l(kr_A) h_l^{(2)}(kr_T) P_l\left(\hat{\boldsymbol{r}}_A \cdot \hat{\boldsymbol{r}}_T\right), \qquad \text{(C.41)}$$

where $r = |\boldsymbol{r}|$ and $\boldsymbol{r} = \boldsymbol{r}_A + \boldsymbol{r}_T$. This addition theorem converges absolutely if $r_T > r_A$. The function $P_l\left(\cdot\right)$ is the Legendre polynomial of degree l, while $Y_{l,m}\left(\theta,\phi\right)$ is a spherical harmonic of degree l and order m. Now consider any set of functions $f_{l,m}(\theta,\phi)$ such that the following property holds

$$\iint\limits_D f_{l,m}(\theta,\phi) Y^*_{l',m'}\left(\theta,\phi\right) w(\theta,\phi) \mathrm{d}\theta \mathrm{d}\phi = \delta_{l,l'}\delta_{m,m'}, \qquad \text{(C.42)}$$

for some integration domain D and weight distribution $w(\theta,\phi)$. By means of (C.42),

properties of the Legendre functions and the expansion of a plane wave

$$e^{-j\boldsymbol{k}(\theta,\phi)\cdot\boldsymbol{r}_A} = \sum_{l=0}^{\infty}(2l+1)j^{-l}j_l(kr)P_l\left(\hat{\boldsymbol{k}}\left(\theta,\phi\right)\cdot\hat{\boldsymbol{r}}_A\right), \tag{C.43}$$

the spherical hankel function $h_0^{(2)}\left(kr\right)$ can be written as

$$h_0^{(2)}\left(kr\right) = \frac{1}{4\pi}\iint\limits_D e^{-j\boldsymbol{k}(\theta,\phi)\cdot\boldsymbol{r}_A}T(k\boldsymbol{r}_T,\theta,\phi)w(\theta,\phi)\mathrm{d}\theta\mathrm{d}\phi, \tag{C.44}$$

with a translation operator defined through

$$T(k\boldsymbol{r}_T,\theta,\phi) = 4\pi\sum_{l=0}^{L}\sum_{m=-l}^{l}j^{-l}h_l^{(2)}\left(kr_T\right)f_{l,m}(\theta,\phi)Y_{l,m}^{*}\left(\theta_T,\phi_T\right), \tag{C.45}$$

and $\boldsymbol{k}\left(\theta,\phi\right) = k\hat{\boldsymbol{k}}\left(\theta,\phi\right)$, with $\hat{\boldsymbol{k}}\left(\theta,\phi\right) = \cos\phi\sin\theta\hat{\boldsymbol{x}} + \sin\phi\sin\theta\hat{\boldsymbol{y}} + \cos\theta\hat{\boldsymbol{z}}$ and k the wavenumber.

In this contribution we will consider three valid choices for $f_{l,m}$, D and w. Let us now very briefly discuss these three choices. An in depth mathematical analysis will be given during the presentation and in the full paper.

By choosing

$$f_{l,m}(\theta,\phi) = Y_{l,m}\left(\theta,\phi\right), \tag{C.46}$$
$$w(\theta,\phi) = \sin\theta, \tag{C.47}$$
$$D = [0,2\pi]\otimes[0,\pi], \tag{C.48}$$

(C.44) reduces to the classic addition theorem of the MLFMA which faces the problem of not being stable when $kr << 1$. The integration over the domain D requires Gauss-Legendre quadrature points.

The following choice, already proposed in [43],

$$f_{l,m}(\theta,\phi) = \frac{1}{2}Y_{l,m}\left(\theta,\phi\right)\left|\sin\theta\right|, \tag{C.49}$$
$$w(\theta,\phi) = 1, \tag{C.50}$$
$$D = [0,2\pi]\otimes[0,2\pi], \tag{C.51}$$

allows a Fast Fourier Transform (FFT) based evaluation of the integration over the domain D provided that the Fourier series of $f_{l,m}(\theta,\phi)$ in both θ and ϕ are truncated at bandwidth L (a smoothing operation).

We propose the following novel choice

$$f_{l,m}(\theta,\phi) = \begin{cases} \frac{1}{2} U_{l,m}(\theta,\phi)\sin\theta \ \ \forall m \geq 0 \\ \frac{1}{2}(-1)^m U^*_{l,-m}(\theta,\phi)\sin\theta \ \ \forall m < 0 \end{cases}, \tag{C.52}$$

$$w(\theta,\phi) = 1, \tag{C.53}$$

$$D = [0,2\pi] \otimes [0,2\pi]. \tag{C.54}$$

The $U_{l,m}(\theta,\phi)$ are distributions which are conveniently called "the pseudospherical harmonics" defined as

$$U_{l,m}(\theta,\phi) = \sqrt{\frac{2l+1}{4\pi}\frac{(l-m)!}{(l+m)!}} e^{im\phi} \frac{\sin^m\theta}{2^l l!} \left(\frac{1}{\sin\theta}\frac{\mathrm{d}}{\mathrm{d}\theta}\right)^{l+m} \left[\frac{|\sin\theta|}{\sin\theta}\sin^{2l}\theta\right]. \tag{C.55}$$

As in the previous choice it can be shown that smoothing allows FFT integration but in addition it yields LF stable analytical translation operators.

Bibliography

[1] A. Sihvola. *Electromagnetic Mixing Formulas and Applications*. The Institution of Electrical Engineers, London, 1999.

[2] M.I. Mishchenko, J.W. Hovenier, and L.D. Travis. *Light Scattering by Nonspherical Particles: Theory, Measurements, and Applications*. Academic Press, San Diego, 2000.

[3] E. Darve and P. Havé. A fast multipole method for Maxwell equations stable at all frequencies. *Philosophical Transactions of the Royal Society A*, 362(1816):603–628, Mar 2004.

[4] I. Bogaert, D. Pissoort, and F. Olyslager. Accelerating the aggregation and disaggregation in the stable plane wave method. In *Proceedings of the USNC/URSI National Radio Science Meeting*, page 302, Albuquerque, USA, 9-14 July 2006.

[5] T.G. Mackay and A. Lakhtakia. Negative phase velocity in isotropic dielectric-magnetic mediums via homogenization. *Microwave and Optical Technology Letters*, 47:313, 2005.

[6] L. Knockaert, F. Olyslager, and D. Vande Ginste. On the evaluation of self-patch integrals in the method of moments. *Microwave and Optical Technology Letters*, 47(1):22–26, Oct. 2005.

[7] L. Knockaert. Abel, gauss and related transforms for electromagnetic applications. In *Proceedings of ICEEA-EESC*, Torino, Italy, June 2005.

[8] J.D. Zaeytijd, A. Franchois, C. Eyraud, and J.M. Geffrin. Full-wave three-dimensional microwave imaging with a regularized gauss-newton method–theory and experiment. *IEEE Transactions on Antennas and Propagation*, 55(11):3279–3292, Nov. 2007.

[9] P. Zwamborn and P. van den Berg. The three-dimensional weak form of the conjugate gradient fft method for solving scattering problems. *IEEE Transactions on Microwave Theory and Techniques*, 40(9), Sept. 1992.

[10] R.K. Luneburg. *Mathematical Theory of Optics*. Brown University, Providence, Rhode Island, 1944.

[11] A.F. Kay. Spherically symmetric lenses. *IEEE Transactions on Antennas and Propagation*, 7(1):32–38, Jan. 1959.

[12] R.C. Wittmann. Spherical wave operators and the translation formulas. *IEEE Transactions on Antennas and Propagation*, 36(8):1078–1087, Aug 1988.

[13] E. Darve and P. Havé. Efficient fast multipole method for low-frequency scattering. *Journal of Computational Physics*, 197(1):341–363, June 2004.

[14] I. Bogaert, D. Pissoort, and F. Olyslager. A faster aggregation for 3-D fast evanescent wave solvers using rotations. *Journal of Computational Physics*, 227(1):557–573, November 2007.

[15] I.V. Lindell. *Methods for Electromagnetic Field Analysis*. Oxford University Press, Oxford, 1991.

[16] F. Olyslager, E. Laermans, D. De Zutter, S. Criel, R. De Smedt, N. Lietaert, and A. De Clercq. Numerical and experimental study of the shielding effectiveness of a metallic enclosure. *IEEE Transactions on Electromagnetic Compatibility*, 41(3):202–213, Aug. 1999.

[17] T. Mader and H.D. Brüns. Efie analysis of arbitrary metallic structures in the area of electromagnetic compatibility. In *Proceedings of the 9th International Symposium on Electromagnetic Compatibility*, Zürich, Switzerland, Mar. 1991.

[18] W.C. Chew, J. Jin, E. Michielssen, and J. Song. *Fast and Efficient Algorithms in Computational Electromagnetics*. Artech House, 2001.

[19] F. Olyslager and J. Fostier. Fast and accurate evaluation of the shielding effectiveness of complex enclosures. In *Proceedings of the 17th International Zürich Symposium on Electromagnetic Compatibility*, pages 30–33, Singapore, Feb. 2006.

[20] F. Olyslager, J. Fostier, J. Peeters, and D. De Zutter. Fast and accurate evaluation of enclosures with the method of moments by using splay trees. In *Proceedings of the 18th International Zürich Symposium on Electromagnetic Compatibility*, pages 87–90, Munich, Germany, Sept. 2006.

[21] J. Fostier and F. Olyslager. An asynchronous parallel mlfma for scattering at multiple dielectric objects. *Accepted for IEEE Transactions on Antennas and Propagation*.

[22] J. Fostier, J. Peeters, and F. Olyslager. Open FMM.

[23] J. Fostier and F. Olyslager. A grid computer implementation of the multilevel fast multipole algorithm for full-wave analysis of optical devices. *IEICE Transactions on Communications*, E90-B(9):2430–2438, Sept. 2007.

[24] I. Bogaert, J. Peeters, and F. Olyslager. A nondirective plane wave MLFMA stable at low frequencies. *Accepted for IEEE Transactions on Antennas and Propagation*, 2008.

[25] D.D. Sleator and R.E. Tarjan. Self-adjusting binary search trees. *Journal of the ACM*, 32:652–686, July. 1985.

[26] P. Yla-Oijala, M. Taskinen, and S. Jarvenpaa. Surface integral equation formulations for solving electromagnetic scattering problems with iterative methods. *Radio Science*, 40(RS6002).

[27] M.A. Taylor, B.A. Wingate, and L.P. Bos. Several new quadrature formulas for polynomial integration in the triangle. Feb. 2007. [Online]. Available: http://arxiv.org/PS_cache/math/pdf/0501/0501496v2.pdf.

[28] P. Yla-Oijala, M. Taskinen, and J. Sarvas. Surface integral equation method for general composite metallic and dielectric structures with junctions. *PIER*, 52:81–108, 2005.

[29] L. Gürel and Ö. Ergül. Fast and accurate solutions of extremely large integral-equation problems discretised with tens of millions of unknowns. *Eletronics Letters*, 43(9):499–500, April 2007.

[30] J. Fostier and F. Olyslager. A fast 2.5d parallel multilevel fast multipole algorithm solver. *Submitted to Radio Science*, 2008.

[31] J. Peeters, I. Bogaert, J. Fostier, and F. Olyslager. Accurate wideband evaluation of the shielding effectiveness of complex enclosures using an asynchronous parallel NSPWMLFMA. In *Accepted for the 19th International Zurich Symposium on Electromagnetic Compatibility*, Singapore, 19-23 May 2008.

[32] K. Cools, F. P. Andriulli, F. Olyslager, and E. Michielssen. "time-domain calderón identities and their application to the transient analysis of scattering by 3d pec objects part i: Preconditioning". *submitted to IEEE Transactions on Antennas and Propagation*, 2007.

[33] F. P. Andriulli, K. Cools, F. Olyslager, and E. Michielssen. "time-domain calderón identities and their application to the transient analysis of scattering by 3d pec objects part ii: Stabilization". *submitted to IEEE Transactions on Antennas and Propagation*, 2007.

[34] L.J. Jiang and W.C. Chew. A mixed-form fast multipole algorithm. *IEEE Transactions on Antennas and Propagation*, 53(12):4145–4156, Dec 2005.

[35] H. Cheng, W.Y. Crutchfield, Z. Gimbutas, L.F. Greengard, J.F. Ethridge, J. Huang, V. Rokhlin, N. Yarvin, and J. Zhao. A wideband fast multipole

method for the Helmholtz equation in three dimensions. *Journal of Computational Physics*, 216(1):300–325, 2006.

[36] I. Bogaert and F. Olyslager. A low frequency stable plane wave addition theorem. *Submitted to Journal of Computational Physics*.

[37] P.F. Gorder. Multicore processors for science and engineering. *IEEE Comput. Sci. Eng.*, 9(2):3–7, 2007.

[38] D. Pissoort, E. Michielssen, D. Vande Ginste, and F. Olyslager. A rank-revealing preconditioner for the fast integral-equation-based characterization of electromagnetic crystal devices. *Microwave and Optical Technology Letters*, 48(4):783–798, April 2006.

[39] R. Adams and N. Champagne. A numerical implementation of a modified form of the electric field integral equation. *IEEE Transactions on Antennas and Propagation*, 52(9):2262–2266, Sept. 2004.

[40] A. Buffa and S.H. Christiansen. A dual finite element complex on the barycentric refinement. *Tech. Report PV-18 IMATI-CNR*, 2005.

[41] L. Xuan, A. Zhu, R.J. Adams, and S.D. Gedney. A broadband multilevel fast multipole algorithm. In *Proceedings of the IEEE AP-S International Symposium, Monterey, CA*, volume 2, pages 1195–1198, June 2004.

[42] H. Wallen and J. Sarvas. Translation procedures for broadband MLFMA. *Progress In Electromagnetics Research*, 55:47–78, 2005.

[43] J. Sarvas. Performing interpolation and anterpolation entirely by fast Fourier transform in the 3-D multilevel fast multipole algorithm. *SIAM Journal on Numerical Analysis*, 41(6):2180–2196, 2003.

Research funded by a Ph.D grant of the Institute for the Promotion of Innovation through Science and Technology in Flanders (IWT-Vlaanderen).